R-98-15

System and safety studies of accelerator driven transmutation systems

Annual Report 1998

Jan Wallenius, Waclaw Gudowski,
Johan Carlsson, Marcus Eriksson, Kamil Tucek

Department of Nuclear and Reactor Physics
Royal Institue of Technology

December 1998

Svensk Kärnbränslehantering AB
Swedish Nuclear Fuel
and Waste Management Co
Box 5864
SE-102 40 Stockholm Sweden
Tel 08-459 84 00
+46 8 459 84 00
Fax 08-661 57 19
+46 8 661 57 19

ISSN 1402-3091
SKB Rapport R-98-15

System and safety studies of accelerator driven transmutation systems

Annual Report 1998

Jan Wallenius, Waclaw Gudowski,
Johan Carlsson, Marcus Eriksson, Kamil Tucek

Department of Nuclear and Reactor Physics
Royal Institute of Technology

December 1998

ABSTRACT

This annual report describes the accelerator-driven transmutation project conducted at the Department of Nuclear and Reactor Physics at the Royal Institute of Technology. The main results are:

- development of the simulation tools for accelerator-driven transmutation calculations including an integrated Monte-Carlo burnup module and improvements of neutron energy fission yield simulations ,
- processing of the evacuated nuclear data files including preparation of the temperature dependent neutron cross-sections, development of nuclear data for a medium energy range for some isotopes,
- development of the models and codes for radiation damage simulations,
- system studies for the spent fuel transmuter, based on heavy metal coolant and advanced nuclear fuel,
- contribution to the spallation target design being manufactured in IPPE, Obninsk
- accelerator reliability studies.

Moreover a lot of efforts were put to further develop existing international collaboration with the most active research groups in the world together with educational activities in Sweden including a number of meetings and workshops and a graduate course in transmutation.

This project has been conducted in close collaboration with the EC-project "Impact of the Accelerator Based Technologies on Nuclear Fission Safety" - IABAT and in bilateral cooperation with different foreign research groups.

TABLE OF CONTENTS

Transmutation ADS-Benchmark (stage 2)", presented at the meeting of the IAEA Coordinated Research Project (CRP) - Use of Th-based Fuel Cycle in Accelerator Driven Systems (ADS) to Incinerate Pu and to Reduce Long-term Waste Toxicities in Petten, The Netherlands (December 1998), to be published.

3. Marcus Eriksson and Christopher Piaszczyk, "Reliability Assessment of the LANSCE Accelerator System", OECD workshop on Reliability of High Power Accelerators, Tokai (October 1999)

4. Marcus Eriksson, "Reliability Assessment of the LANSCE Accelerator System", MSc thesis, Royal Institute of Technology (1998)

5. Charlotta Sanders, "Reactor Neutron induced Material Damage in Subcritical Systems", Licentiate thesis, Royal Institute of Technology (1998)

1 INTRODUCTION

In November 1996, SKB started financing of the project "System and safety studies of accelerator driven transmutation systems and development of a spallation target". The aim of the project was stated as:

- Development of a complete code for simulation of transmutation processes in an accelerator driven system. Application of the code for analysis of neutron flux, transmutation rates, reactivity changes, toxicity and radiation damages in the transmutation core.
- Build up of competence regarding issues related to spallation targets, development of research activities regarding relevant material issues. Performing of basic experiments in order to investigate the adequacy of using the spallation target as a neutron source for a transmutation system, and participation in the planning and implementation of an international demonstration experiment.

In the present report, activities within the framework of the project performed at the department of Nuclear and Reactor Physics at the Royal Institute of Technology during 1998, are accounted for.

Moreover, Charlotta Sanders, PhD student financed separately by Studsvik Nuclear, participated in the studies on radiation damages.

2 CODES AND DATA FOR SIMULATION OF ACCELERATOR DRIVEN SYSTEMS

Detailed system studies of accelerator-driven systems require a vast amount of nuclear data in order to get reliable assessment results and to guide an optimized engineering design. Moreover, integration of existing codes for modelling of spallation, neutronics and burnup is essential in order to avoid problems with basic data discrepancies and neutron spectrum changes during burnup. This part of the project was performed in collaboration with our international partners including guest scientist Jerzy Cetnar (Technical University "Akademia Gorniczo-Hutnicza" in Krakow), Yuri Shubin (Institute of Physics and Power Engineering in Obninsk), Aleksander Polanski (Institute of Nuclear Research, Swierk), Vladilen Barashenkov (Joint Institute for Nuclear Research, Dubna), Anatoliy Grashin and his group (Moscow Institute of Physics and Power Engineering). Also close collaboration with Los Alamos National Laboratory (Accelerator -Transmutation of Waste and Accelerator Production of Tritium groups) was indispensable for the outcome of the work.

2.1 SPALLATION

Los Alamos National Laboratory (LANL)released version 2 of MCNPX [Hugh97], a Monte Carlo code that fully integrates the high energy particle transport capabilities of LAHET [Prae89] with the "low energy" neutron transport code MCNP [Brie97]. Our collaborator A. Polanski contributed with new theoretically calculated cross sections for spallation processes that improve the ability of the code to predict residual element production. The perhaps most important feature of MCNPX from the ADS perspective is the continuous tracking of neutrons appearing in proton induced spallation having kinetic energies up to several GeV, to the instant of absorption in fuel and construction materials of the system. In comparison with a similar code developed by the Emerging Energy Technology group of CERN (EET), MCNPX has a distinct advantage in its ability to utilize evaluated cross section data libraries in the energy region 20 - 150 MeV, where it is known that calculated cross sections are less reliable. For this purpose, LANL produced evaluations of cross section data for construction material elements like iron and aluminum (see chapter on Nuclear Data) .

MCNPX itself was evaluated at KTH in a simulation of proton and neutron flux in a subcritical system designed for transmutation of non-recycled waste from Swedish light water reactors. A core with hexagonal geometry was set up as shown in Figure 1.

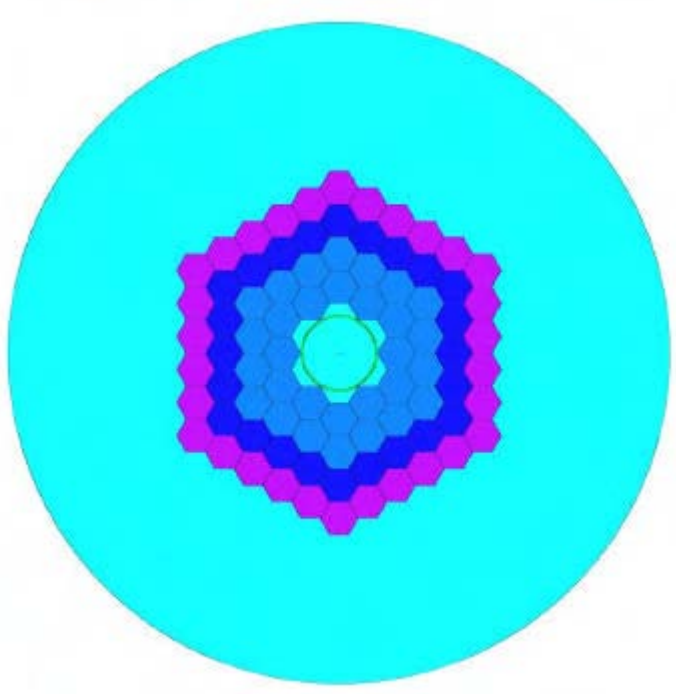

Figure 1: Geometry set up of SSC - a subcritical core designed for transmutation of nuclear waste from Swedish light water reactors. The cylindrical spallation target wall is shown in green, while different TRU-enrichments in the nitride fuel elements are denoted by different shades of blue.

The radius of the liquid lead/bismuth spallation target turns out to be determined by the largest cylindrical tube that can be fitted into the empty space created by leaving out the seven central fuel bundles of a traditional fast reactor core. Since the flat to flat distance of the fuel bundle duct is given by reactor physics considerations mostly decoupled from the spallation source, optimization of spallation neutron yield will not be a determining factor in the design of the target. Generally, duct flat to flat distances (FTF) vary between 10 to 20 cm. The maximal target outer radius

$$R_{target} = \frac{2}{\sqrt{3}} FTF$$

is then confined to the interval 11.5 to 23.0 cm. The high energy tail of the spallation neutron spectrum that will contribute to material damage in construction materials constitutes a relatively smaller fraction of the total flux as distance from the centerline of the target grows. Thus this contribution was investigated for the smallest configuration being of interest in realistic designs, i.e. an outer target radius of 11.5 cm. The cylindrical target wall was assumed to have a thickness of 5 mm and to be composed of a 90% iron, 10% chromium steel approximating the ferritic martensitic steels that are compatible with liquid lead/bismuth environments. The accelerator beam tube had a radius of 5 cm and the point of proton impact was set to 12 cm above mid plane, in order to achieve an even distribution of primary source neutron absorptions along the z-coordinate of the fuel elements. It was shown that virtually no protons

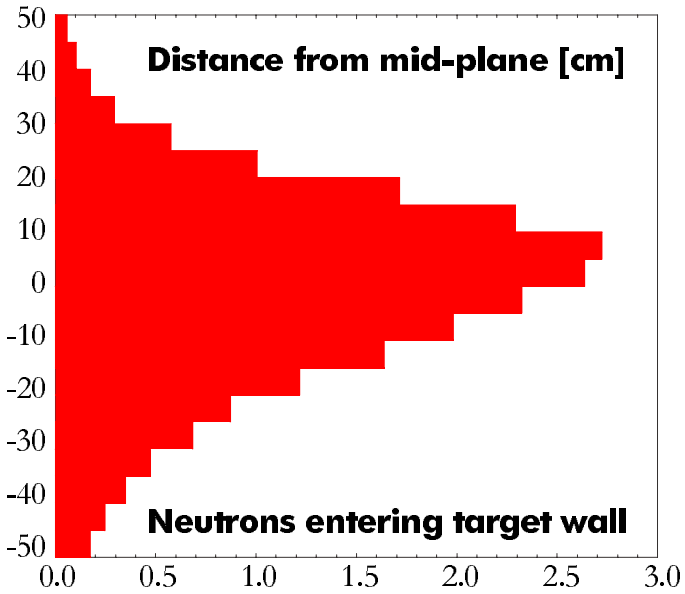

Figure 2: Spatial distribution of spallation neutrons entering the target wall within the vertical range of the surrounding core. The wall was divided into 5 cm wide bins. The impact of the 1 GeV proton beam was set to 12 cm above midplane. Totally 21.5 neutrons per incident proton entered the target wall. Of these 10.0 entered below midplane, and 11.5 above.

leave the lead/bismuth target. Figure 2 shows the distribution of spallation and other secondary neutrons traversing the target wall .

The fraction of spallation neutron flux above 20 MeV entering the target wall is displayed in Figure 3. It can be seen that it constitutes merely 1.4% of the total flux. This fraction diminishes further out in the core.

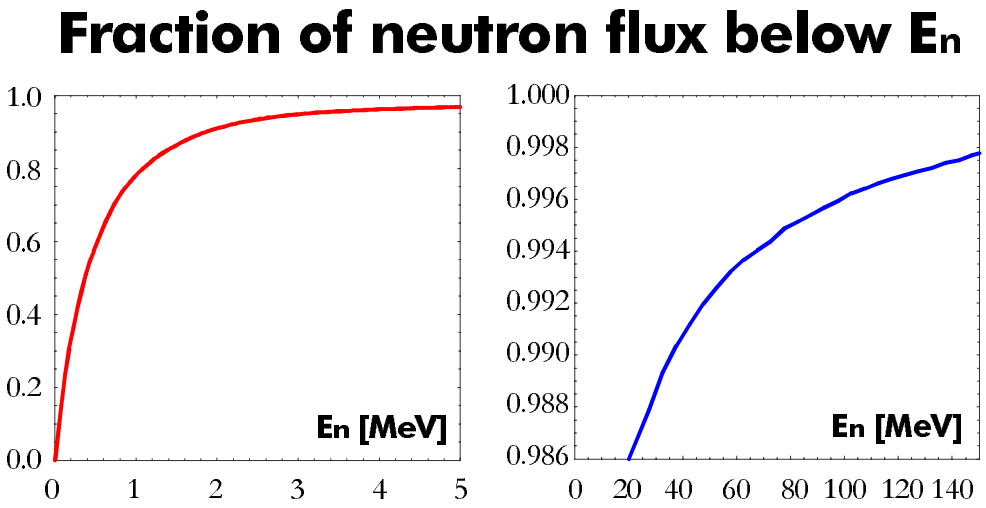

Figure 3: Fraction of spallation neutron flux in the target wall below energy E_n. Note that only 1.4% of the flux is above 20 MeV, even for a relatively small target such as the present.1.1% of the flux is found in the interval 20 - 150 MeV.

Considering that spallation neutrons account for less than 10% of the neutron flux in a typical waste transmutation system, one might think that the overall 1 promille fraction of high energy neutrons could be neglected also in detailed safety and neutronics analysis of the system. However, since material damage rates in form of lattice vacancy and helium gas production grow with neutron energy, it turns out that the high energy tail contributes with a significant fraction to these macroscopic observables. The effective lattice defect (interstitial-vacancy) production as function of primary recoil energy has recently been shown to follow a simple power law for recoil energies up to 40 keV in iron [Baco97] . Extrapolating this power law into the high energy recoil region, one may estimate that up to one third of the spallation neutron induced lattice damage in the target wall is due to the 1.5% fraction of high energy neutrons.

The cross section of the (n,α) reaction is practically equal to zero below a threshold energy of about 5 MeV in iron. Since the tail of the fission neutron spectrum declines to zero in the same region, helium gas production rates are much smaller in ferritic steels than in nickel-containing steels, where the threshold of the (n,α) reaction is about 3 MeV. Hence, the high energy tail of the spallation neutron spectrum will be the major contributor to helium gas production in ferritic steels used in accelerator driven systems. For the core

depicted in Figure 1, it is found that about 80% of the α production in the target wall is induced by spallation neutrons, in spite of the fact that they represent only 0.1% of the total neutron flux.

2.2 NUCLEAR DATA - EVALUATION AND PROCESSING

The reliability of simulation of accelerator driven transmutation depends both on quality of the simulation tools, i.e. computer codes and quality of nuclear data used on the input. It is therefore of a primary importance to review and re-evaluate the state-of-the art neutron cross-section data bases which have been developed during last 50 years mainly for nuclear reactor calculations. Moreover, due to spallation processes in accelerator-driven systems and an inadequate theory of particle interaction in the energy range between 20 and 150 MeV it is desirable to extend nuclear data-libraries well over the current upper neutron energy limit of 20 MeV. Studies of the accelerator-driven systems require also temperature dependent neutron cross section data (due to Doppler broadening of resonances).

There are two types of data libraries which are broadly used in simulations of nuclear systems:

a) transport data libraries,

b) activation (or transmutation) data libraries.

While transport data libraries contain all the partial cross-sections and angle dependencies necessary for simulation of neutron transport in matter, activation libraries contain data which can be used mainly for transmutation rates, radioactivity and burnup calculations. These activation libraries are a very important complement to transport libraries, hence they contain much more isotopes.

Several neutron transport data libraries available today which are of interest for ADS simulations:JEF2.2, ENDFB6.4 and JENDL3.2.

Enormous amount of work has been put into transport cross section data bases in the last 50 years for the energy range from meV to 20 MeV. However there are still significant uncertainties, discrepancies between different data bases and missing data important for transmutation research. Typical examples are shown on Figures 4 and 5. Figure 4 exhibits a large discrepancy between JEF2.2 and ENDFB6.4 data bases in high energy part of the capture cross section for ^{56}Fe. Both in the resonance part of the data and in the MeV region the discrepancies are very visible by as much as 2 orders of magnitude for some resonances and by factor of 2 in the high energy part. Figure 5 shows the quality of the data for fission cross-section of ^{238}Np for JEF2.2 and ENDFB6.4. Equally bad quality data exist for some higher actinides and new experiments are required (some of the experiments are under way) to improve this situation if very reliable transmutation simulations are to be performed.

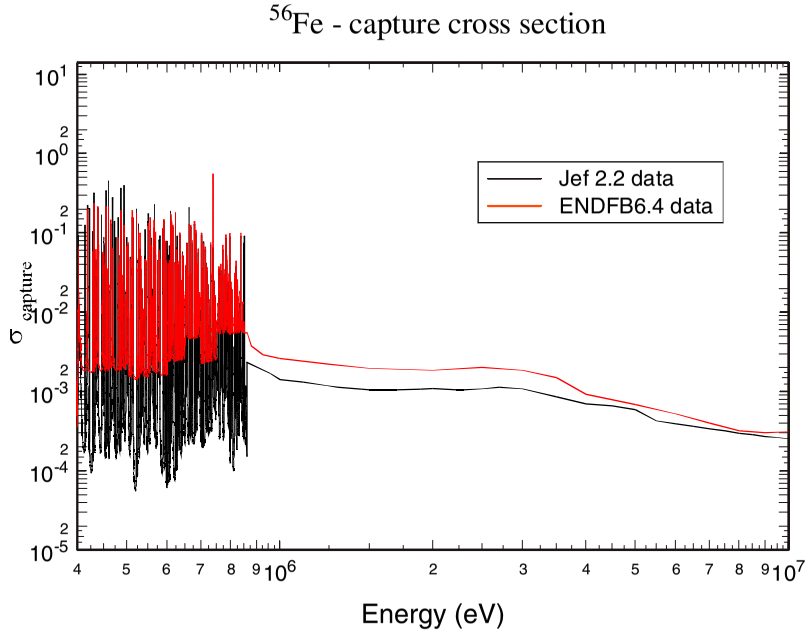

Figure4. Discrepancy between JEF2.2 and ENDFB6.4 data bases for the ^{56}Fe neutron capture cross-section.

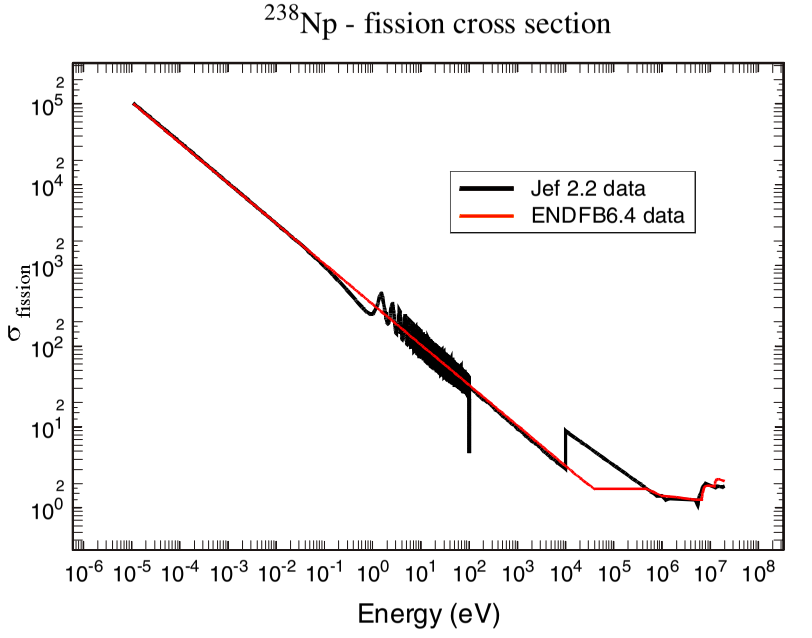

Figure5. The neutron fission cross-section of ^{238}Np. Quality of the data from JEF2.2 and ENDFB6.4 data libraries.

Transport cross-section libraries are represented in a commonly used ENDF6-format (evaluated nuclear data files) and the data must be reprocessed in a special way in order to be used for transport calculations. The reprocessing code is called NJOY97. The NJOY nuclear data processing system [MF92] is used to transform evaluated nuclear data in the ENDF format into forms useful for nuclear application calculations. Because of the favourable convergence of nuclear data formats all over the world, these evaluated data can come from the US ENDF/B libraries, the European JEF libraries, the Russian BROND libraries, the Japanese JENDL libraries, the Chinese CENDL libraries, the IAEA FENDL libraries, and others.

One of the most important capabilities of NJOY is to perform resonance Doppler-broadening calculations, crucial for creation of temperature dependent cross-sections. Some other important features include the gas-production capability, a DPA capability for MCNP, a radionuclide production capability, extensions for high-energy angular distributions and KERMA factors.

As mentioned before one of the major tasks done by NJOY is preparation of temperature dependent neutron (and/or proton) cross-section involving Doppler-broadening of resonances. A transport cross section data base prepared for our research consists of combined cross-section data from three libraries JEF2.2, ENDFB6.4 and JENDL3.2 at four temperatures (300K, 600K, 900K and 1200K). Data used in the calculation are picked-up in the following priority order: first JEF2.2 is searched, then ENDFB6.4 and finally JENDL3.2. A comprehensive list of isotopes in these different data bases can be found on our web site:

http://www.neutron.kth.se/publications/library.html

An activation (transmutation) cross-section data base has been prepared based on EAF3.2 (**E**uropean **A**ctivation **F**ile) and EAF97. This data-base contain continuous energy dependent capture (and other transmutation reactions) cross-section data for over 700 isotopes (over 400 isotopes more than in any transport library). A drawback of the EAF library, in its original form, is that it is not represented in the standard ENDF6-format. In order to be able to use this library in our calculations it had to be converted into ENDF6 format. It has been done using the PROCEAF code. (In collaboration with M. Embid, J. García-Sanz, R. Fernández and E. M. Gonzalez -FACET group, CIEMAT, Spain). Finally the data has been processed by NJOY97 for different temperatures.

Recognizing the importance of spallation neutrons (and spallation reactions) in accelerator-driven systems most effort of nuclear data evaluators in last few years has gone to the extension of the existing (neutron and proton) cross-section libraries to 150 MeV [Koni98]. In co-ordination with different international efforts and in collaboration with the European IABAT-project and a Russian group from Institute of Physics and Power Engineering in Obninsk we are developing the evaluation of neutron and proton cross-section transport libraries for the energy range up to 150 MeV for ^{232}Th and ^{238}U isotopes. The evaluation is based on nuclear model calculations that have been

benchmarked to experimental data. We used the GNASH code system [Yo92], which utilises Hauser-Feshbach statistical, preequilibrium and direct-reaction theories. Coupled-channel optical model calculations [Ra84] are used to obtain particle transmission coefficients for the Hauser-Feshbach calculations, as well as for the elastic neutron angular distributions. The energy-angle correlation for all outgoing particles are based on Kalbach systematics [Ka88]. Discrete level data from nuclear data sheets were matched to continuum level densities using the formulation of Ignatyuk [Ig75] and pairing and shell parameters from the Cook analysis [Co67]. Neutron and proton transmission coefficients were obtained from the optical potentials [Ra84]. Transmission coefficients for alpha, deuterons and tritons were calculated using the spherical optical model.

The total neutron cross section calculated with the parameters given above are shown in Figure 6 in comparison with available experimental data and with different previous evaluations. Figure 7 shows the neutron fission cross-section for Thorium up to 150 MeV. The evaluation for protons on ^{232}Th and for neutrons and protons on ^{238}U are under way.

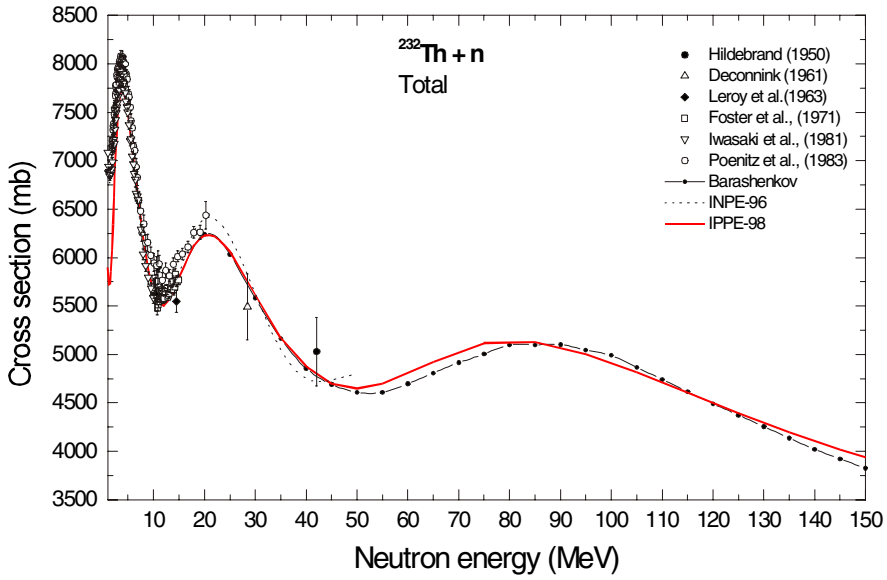

Figure 6. Comparison of the neutron total cross section for ^{232}Th with experimental data and previous evaluations.

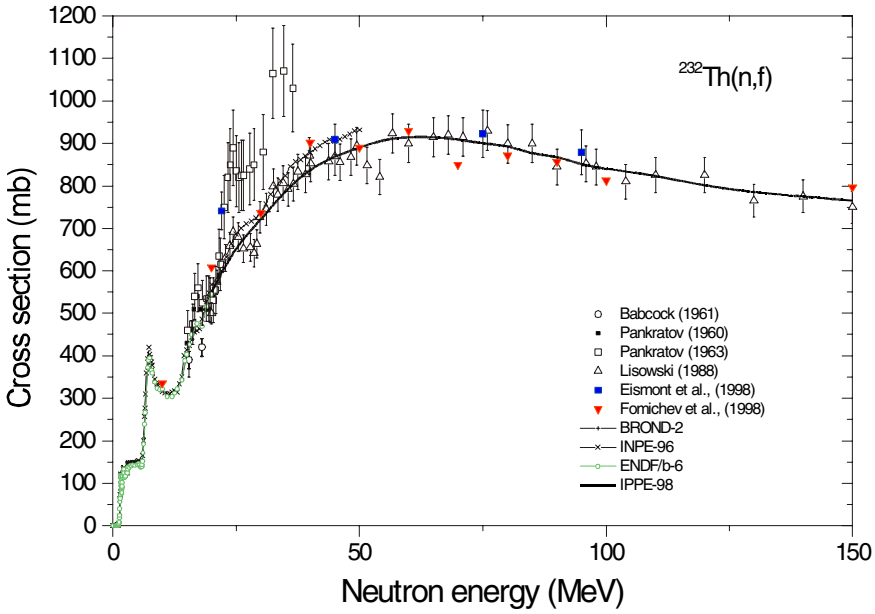

Figure 7. Comparison of the neutron fission cross section for ^{232}Th with experimental data and previous evaluations.

2.3 RADIATION DAMAGE

Construction materials in waste transmutation systems must be able to cope with large neutron fluences. The very hard neutron spectrum required for lowering curium accumulation is expected to cause high rates of lattice vacancy and helium gas production in claddings and ducts. In sub-critical systems, an additional burden is brought by significant flux peaking in the vicinity of the spallation target. Since experimental investigations of macroscopic radiation damage effects are time consuming, it is of importance to develop models that can predict the magnitude of swelling and embrittlement as function of neutron fluence and spectrum.

An evaluation of the recoil cascade simulation program MARLOWE [Robi92] was made at the department. Early versions of MARLOWE were used to fix a standard of lattice displacements yields known as "NRT DPA" [Norg75]. Even though it subsequently turned out that MARLOWE overestimates the number of surviving lattice displacements in fast neutron spectra by up to a factor of four, NRT DPA has remained a standard for characterization of radiation damage induced by a given fluence. Unfortunately, many estimations of radiation damage found in the literature still use the outdated Kinchin and Pease formula for lattice displacement rate calculations [Kinc55]. Even worse, some authors use values of displacement thresholds that are corrected for the errors of MARLOWE, but forget this fact when they compare their predicted damage yields with experimental NRT DPA limits of construction material resistance to irradiation. Therefore, it is important to arrive at a

consensus on how the actual displacement rates are to be characterized. Before such a consensus has been established, one should always state standard NRT DPA:s in conjunction with actual displacement rates, in order to avoid misinterpretation of simulation results.

As shown in both experimental investigations in pure copper, and more detailed modelling of displacement cascades in iron, recent versions of MARLOWE severely over-estimates lattice displacement rates for primary recoil energies above 1 keV [Zink93]. This is mainly due to the binary collision approximation implemented in MARLOWE being unable to account for collective lattice displacements. Since the major fraction of the recoil spectrum in waste transmutation systems will be present above this threshold, a better simulation tool was needed. The capability of molecular dynamics (MD) simulation codes have improved considerably during the last decade. These codes solve the full set of Newton's equations for a moving atom in a lattice, using a potential that is pre-calculated by quantum mechanical methods. Simulating displacement cascades in pure iron, Calder, Bacon and Gao showed that simple relations between the actual number of surviving defects and the NRT DPA value exist for a given material, at least within the recoil energy range investigated ($E_r < 40$ keV) [Baco97].

While MD simulations of displacement cascades in iron are very difficult to verify experimentally, predictions of lattice defect yields in copper agree fairly well with experimental findings [Zink93]. Hence Calder's formula was used for a first estimation of actual lattice defect production rates in the ferritic steels that are likely to be used as construction materials in heavy metal cooled reactors [Sand98]. It was found that the standard displacement rate in cladding and ducts of a Pb/Bi cooled sub-critical core did not exceed 20 NRT DPA per year, which should be within acceptable limits. This number corresponds to a much smaller actual displacement rate (< 5 defects produced per atom per year). However, since helium gas production in the spallation target wall will be about an order of magnitude larger than in critical reactor construction elements, the swelling threshold might be lower than the 100 - 200 NRT DPA that has been observed in ferritic steels irradiated with fission neutrons.

In order to improve the estimations presented in [Sand98] real recoil spectra should be used instead of average recoil energies. Further, a project to implement a displacement cascade potential for Fe-Cr alloys has been initiated and will be performed in cooperation with the University of Liverpool.

2.4 FISSION PRODUCT YIELD

Since experimental data on fission product yields of the minor actinides are scarce, and the energy dependence of mass and charge distributions are only known for three points (at best), there was a need for a theoretical model to create energy dependent fission product yield libraries. Three different models were investigated:

- The empirical Zp/Ap model of Wahl (Los Alamos National Laboratory) [Wahl85]
- The semi-empirical model of Koldobsky and co-workers at Moscow Engineering Physics Institute (MEPHI) [Kold95]
- The non-equilibrium thermodynamical model of Grashin and co-workers at MEPHI [Gras85].

Evaluation of the Zp/Ap model showed that the empirical curve-fitting of gaussians and exponentials applied lead to unacceptable uncertainties in predictions of fission product yields where experimental data are unavailable. The semi-empirical approach of Koldobsky turned out to give expectedly reliable predictions of low yield fission products in fission of uranium and plutonium. It appeared to be less reliable in the task of predicting minor actinide fission yields, however, since it was dependent on fitting of a about 20 free parameters for each nuclide .

The non-equilibrium thermodynamical model of Grashin is based on a new theoretical understanding of quantum mechanical processes in systems having too many free variables for non-statistical methods to be useful, while being too short-lived for standard equilibrium thermodynamics to be fully applicable [Gras85]. By introducing the concept of "free energy" of the excited compound nucleus, the model calculates the probability of finding final states of two (or three) fission products with concomitant release of a given number of neutrons within the manifold of the initial state. Thus the energy dependence of the fission product yield enters as a fundamental property in the model. Shell effects are taken into account , and most free parameters are fixed by fitting model predictions with experimental yields for a fission of a single nuclide at a single energy - in our case ^{235}U (see Figure 8). For other nuclides only one free parameter, the ground state temperature, remains. This can be determined from e.g. the ratio of peak to fission valley yields, which is better known for the minor actinides than individual yields. Since yield distributions for thermal fission of ^{235}U are comparatively well known, errors in the low yield predictions for arbitrary actinides should generally not be worse than the same errors for ^{235}U.

This is of great significance in transmutation simulations, as many system proposals are based on pure minor actinide fuels, which existing commercial codes never were intended to model accurately.

Accordingly, the non-equilibrium thermodynamical model of Grashin was chosen as a tool for producing energy dependent fission product yield libraries to the integrated burnup code. A collaboration with Grashin's group was initiated, which resulted in a updated Fortran version of their code. Figures 9 and 10 show the comparison of predicted fission product mass yields with experimental data at thermal and fast (0.5 and 1 MeV) incident neutron energies for ^{241}Pu and ^{245}Cm.

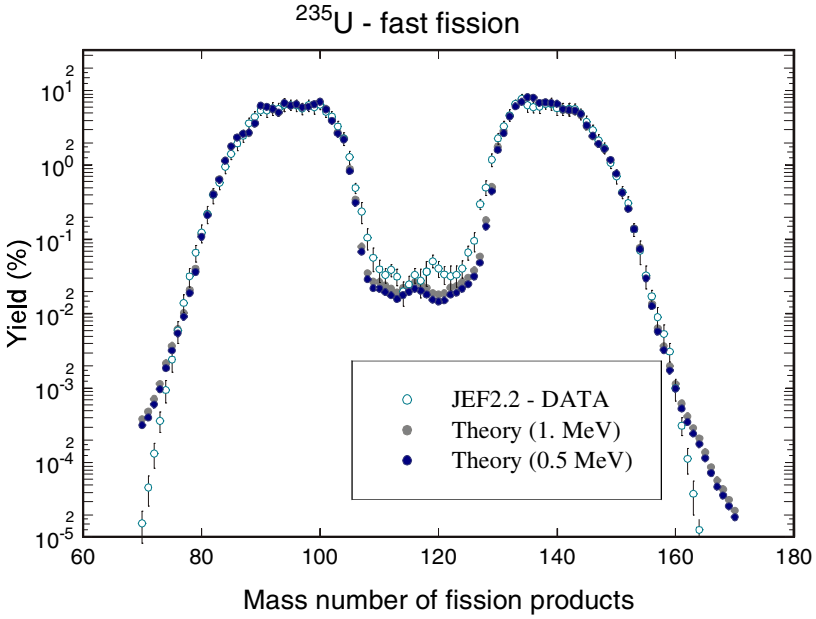

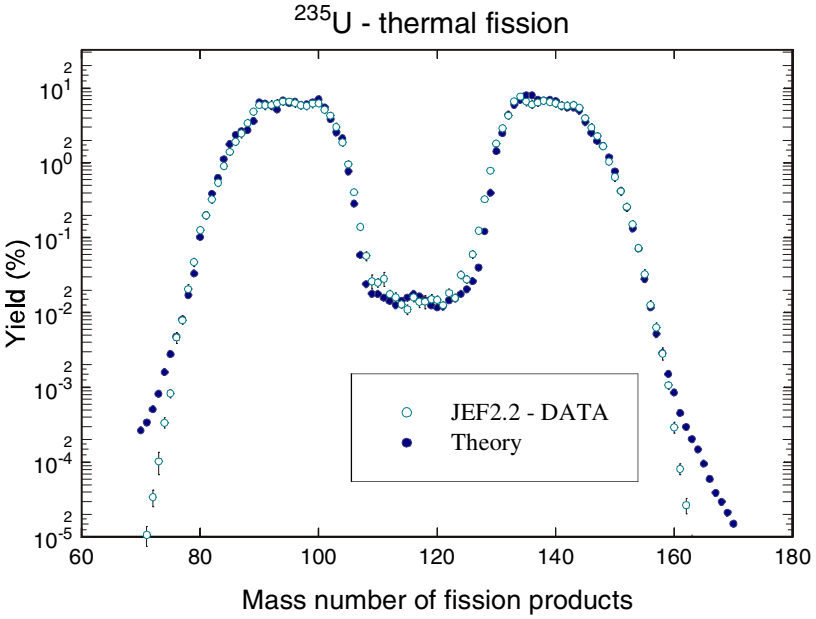

Figure 8. Fission product yields in neutron induced fission of ^{235}U. Open circles - evaluated data, solid circles - theory. Fast neutron induced fission for 1 and 0.5 MeV neutrons (upper), thermal neutron induced fission (lower). ^{235}U-data for thermal fission were used for fitting free parameters of the theoretical model.

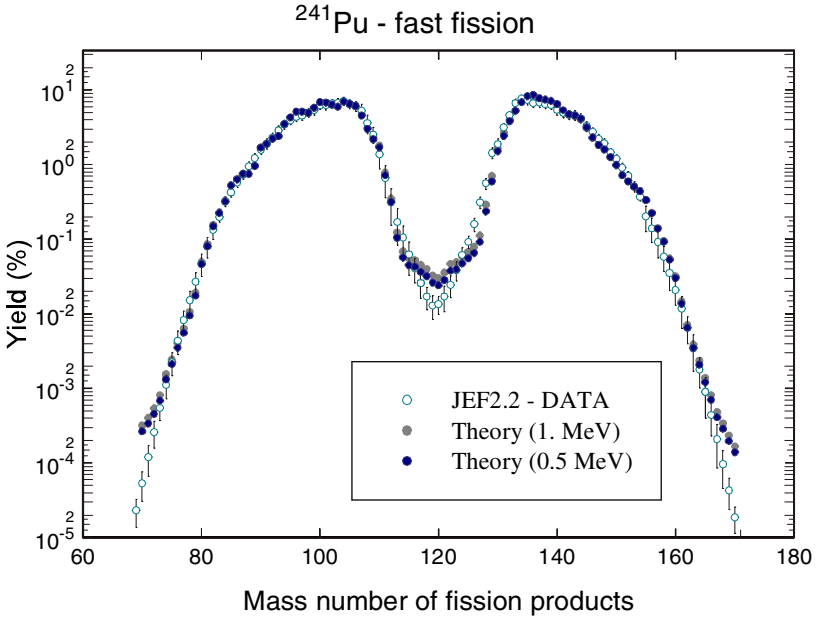

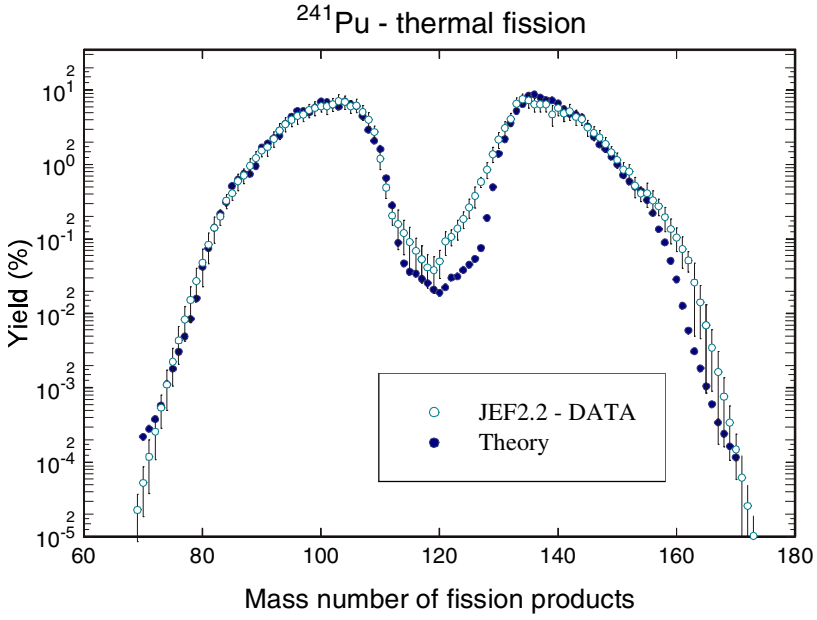

Figure 9. Comparison of theoretical prediction of fission yields for ^{241}Pu with JEF2.2 evaluated data. Fast neutron induced fission for 1 and 0.5 MeV neutrons (upper), thermal neutron induced fission (lower). Note difficulties of the theoretical model to reproduce right-hand fission-yield peak for thermal neutron induced fission.

As can be noticed from a comparison of Figures 9 and 10 significant differences in the yield of fission products with mass numbers around 90 and 110 appear. As the widely spread burnup simulation code ORIGEN2 approxi-

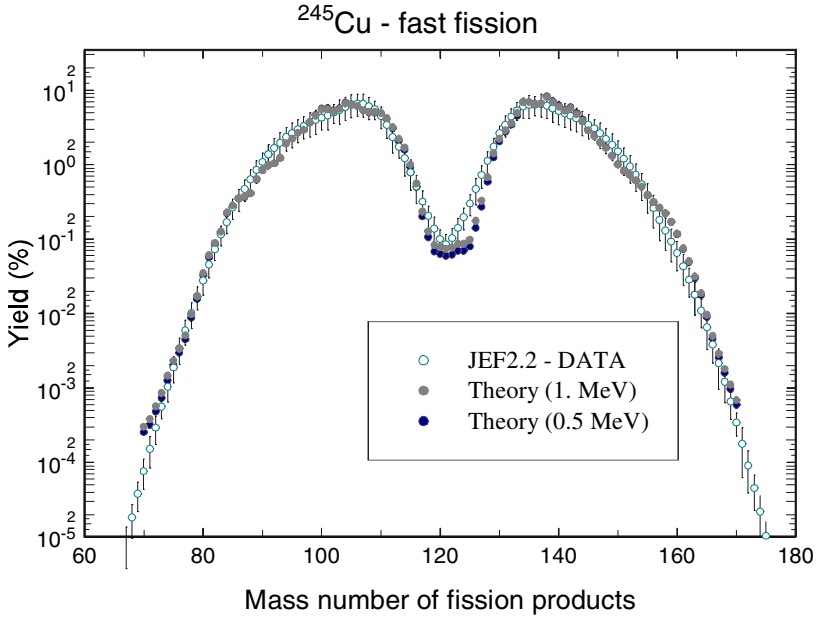

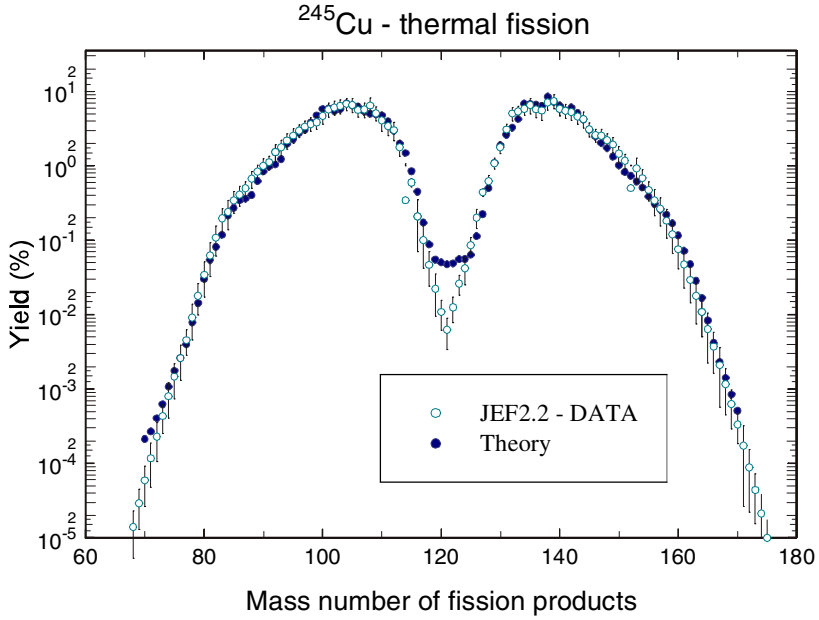

Figure 10. Fission product yields in neutron induced fission of ^{245}Cu. Open circles - evaluated data, solid circles - theory. Fast neutron induced fission for 1 and 0.5 MeV neutrons (upper), thermal neutron induced fission (lower).Note the discrepancy in the "fission valley" for thermal neutron induced fission, and surprisingly good reproduction of fast neutron induced fission.

mates any fission yield for Am and Cm with that of ^{241}Pu, one should take seri-

ous note of this discrepancy. Applying ORIGEN2 for modelling of burnup in the so called Minor Actinide burners proposed by JAERI and CEA/Cadarache may lead to errors in predictions of toxicity reduction. Especially, the yield of ^{90}Sr becomes over-estimated, as shown in Figure 11 below. Since ^{90}Sr dominates the ingestion radiotoxicity of high level nuclear waste during the first 100 years [Chop95], ORIGEN2 would over-estimate the short term radio-toxic inventory in Minor Actinide burner waste streams.

Further note the significant energy dependence in the yield of nuclides in the fission valley. In particular, the predicted yield of the long-lived radiotoxic nuclide ^{126}Sn in an accelerator driven system might be off by a factor of two or

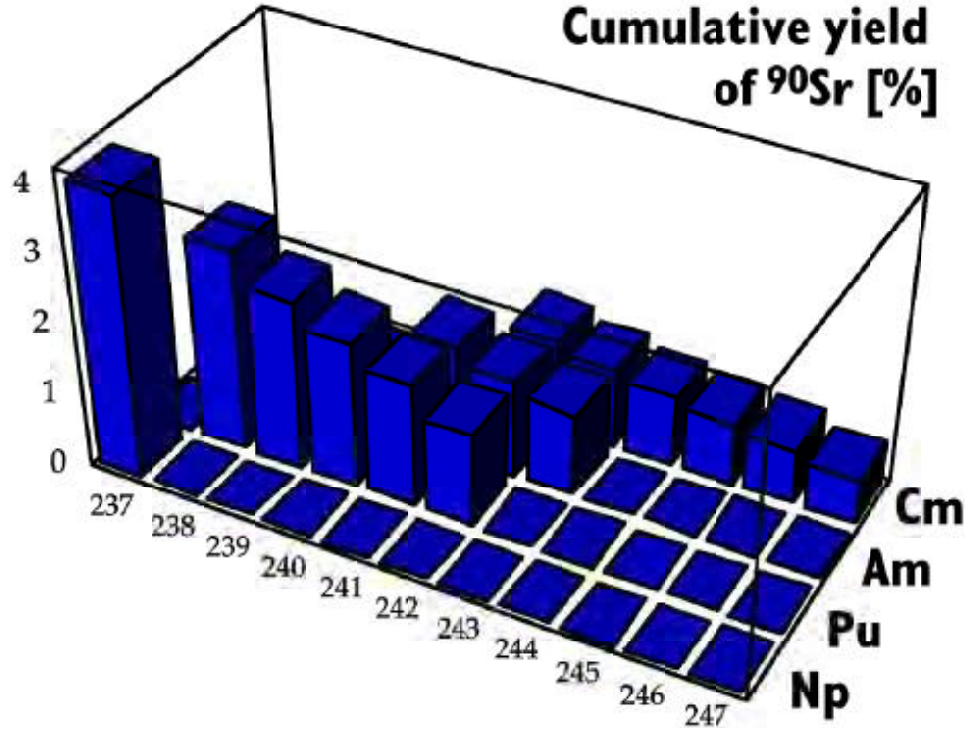

Figure 11. Cumulative yield of ^{90}Sr in 100 keV neutron induced fission of transuranic nuclides. Note the difference in yield between ^{239}Pu (main contributor in fast breeder reactors) and the minor actinides. Compare also with the 6 % yield in fission of ^{235}U! The cumulative yield includes ^{90}Sr nuclei appearing after β-decay of other fission products with the same mass number, but smaller Z. In the present case, all relevant precursors have decayed into ^{90}Sr within one hour.

so, when integrating over the spectrum of fission inducing neutron energies see Figure 12). However, since the bulk of fissions (> 75%) in fast breeder reactors are induced by < 100 keV neutrons, the thermal neutron yield is in this case a better approximation than the "reactor" fast neutron yield usually measured (E_n ~ 1 MeV).

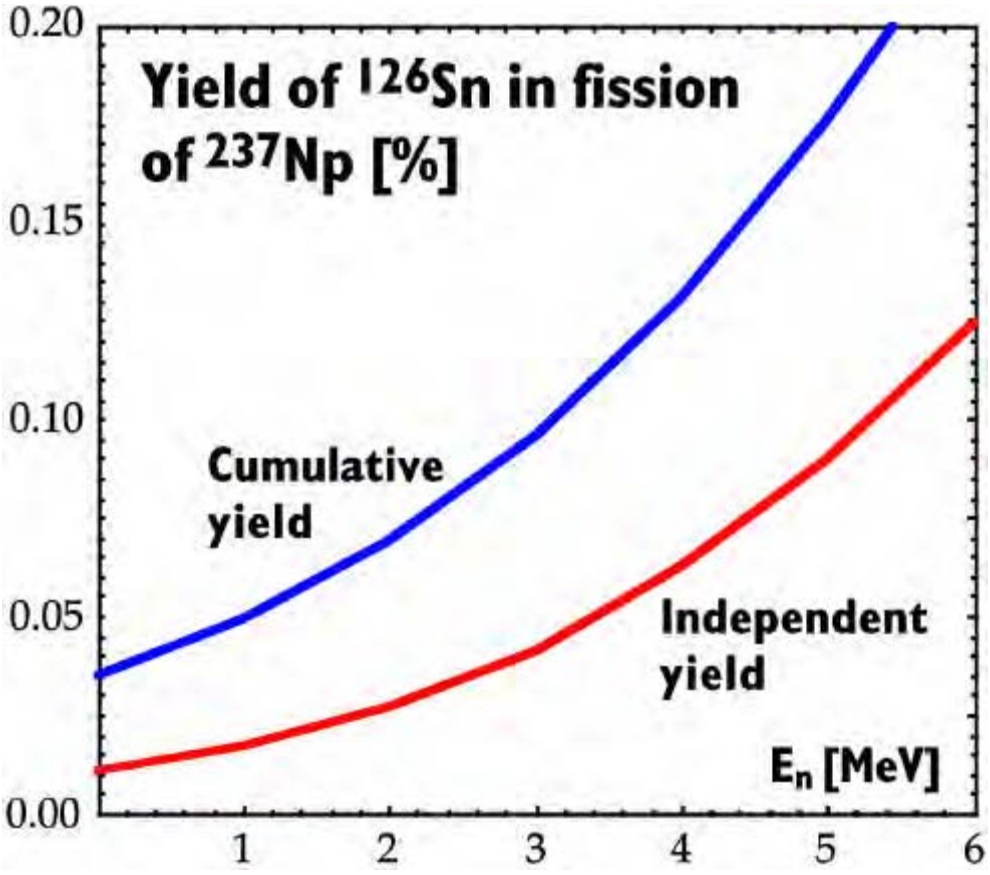

Figure 12. Independent and cumulative yield of the long-lived γ radiotoxic nuclide ^{126}Sn in fission of ^{237}Np, as function of incident neutron energy.

2.5 BURNUP

The requirements of the burnup code development are set by the demand of a correct modelling of sub-critical waste transmutation systems. These are supposed to transmute extraordinary large fractions of original materials present in the system. For instance, material compositions after 20% heavy atom burnup and up to 50% long lived fission product transmutation during a single irradiation cycle must be correctly predicted by the code, which means that significant spectrum changes and self shielding effects have to be treated by intelligent and self-adjusting time stepping procedures. Further, in order to optimize fuel and waste management, it is advantageous to apply the transmutation trajectory analysis method, which provides additional information of the transmutation process, as compared to the exponential matrix method of ORIGEN2.

The work on extending MCNP with advanced burnup capabilities required by the project was to a large extent completed during the year. Evaluation and validation of the integrated code MCB (Monte Carlo Burnup) is now underway.

The basic cross section and decay data used by MCB consist of:

- Decay data including decay constants and branching ratios for over 2400 nuclides. The decay data file was prepared on the basis of the Table of Isotopes (ToI) version 8E.
- Neutron transport cross section libraries for about 300 nuclides, prepared with NJOY at various temperatures on the basis of the room temperature evaluations ENDF/B-VI, JEF2.2 and JENDL3.2.
- Neutron reaction cross section libraries for about 400 additional nuclides (for which transport cross section evaluations do not exist), prepared with NJOY at various temperatures on the basis of the EAF evaluation.
- Continuous energy fission product yield libraries for 36 actinides, including yields of over 1000 fission products. The library was constructed using an updated version of the THERMO code, which calculates independent yields using the non-equilibrium thermo-dynamical model of Grashin [Grash85].
- Data for effective dose per unit intake for 738 nuclides, prepared on the basis of the Basic Safety Standards of IAEA.
- Meta-stable to ground state capture ratios for neutron capture on ^{241}Am and ^{243}Am according to the evaluation of Mann and Schenter [Mann77].

In addition to standard MCNP material specifications "burnup", "residual" and "mixed" materials are introduced in MCB. Burnup materials are not used in transport calculations unless their macroscopic cross section contribute to the total cross section with a fraction larger than a discrimination level supplied in the input file. Residual material have no defined density, and are used only for transmutation transition calculations. Finally materials may be mixed using the mixed material specification, which greatly simplifies initial system definitions. Materials for which burnup is to be calculated (not necessarily all materials) are specified with the "BURN" command.

The physical conditions of the irradiation (and decay) simulation are fixed by specifying time periods of constant conditions, and corresponding source strength or heat dissipation (power). If neither power nor source strength is specified, or both are set to zero, plain decay of unstable nuclides takes place.

The constraints of the automatized time-stepping routine are prescribed in the input file by specifying longest allowed time step (equal to the first trial time step), allowed variation of k-eigenvalue, neutron multiplication and/or reaction rate during a time step. Discrimination levels of macroscopic cross section contributions and nuclide to nuclide transmutation transitions may also be specified, as well as a half-life threshold for treatment of fast decaying nuclides.

At startup of the code, all unique cross section files pointed to in the XSDIR file are loaded. The program checks if nuclides with short half-life exist in the materials specified, and force them to decay before making a calculation of the k-eigenvalue of the system. If this is lower than a given threshold, a source particle transport run is made where system power and transmutation rates are

calculated "in flight". Otherwise, the particle flux is assumed to be sufficiently well described by the eigenflux and a new KCODE run is made, including sampling of heating and transmutation rates. Then, transmutation trajectories are selected, and the nuclide density evolution is calculated during the whole trial time step. The macroscopic cross sections of the appearing nuclides are calculated in order to check that they do not exceed the fraction of the total cross section set by the discrimination level. Similarly, a k-eigenvalue calculation is made to assure that changes in asymptotic neutron multiplication stays within the prescribed range. If either of these conditions are not fulfilled, a smaller time step is set for a renewed nuclide density prediction. Finally, new nuclide concentrations in the burnable materials are initialized and a new particle transport run is initiated.

3 INVESTIGATION OF SPALLATION TARGET PROPERTIES

The International Science and Technology Centre Project # 559 "Pilot flow lead-bismuth target of 1 MW_{th} for accelerator-based systems" is a collaborative project between Institute of Physics and Power Engineering (IPPE) in Obninsk, Los Alamos National Laboratory (LANL), Royal Institute of Technology and CEA-Cadarache. Funding parties of this project are USA, EU and Sweden.

The purpose of the project is to develop a heavy metal-Pb/Bi eutectic- flow target which possesses the best features for producing neutrons at a high power proton accelerator. Thus, the technical key problems of a flowing Lead-Bismuth 20 MW-power target should be investigated. Such a technical base will be established by the design of a pilot lead-bismuth 1 MW power target. It is decided that the pilot target will be tested at the LANSCE accelerator at LANL (LANSCE: 800 MeV, 1.5 mA linear proton accelerator) after extensive off-beam tests, first in Obninsk year 2000 and then in Los Alamos.

The project has started in January 1998, had its kick-off meeting in March 1998 and now it is at its half-way. The design work has been completed and presented to the collaborators.

Figure 13 shows the general sketch of the target system together with radiation shielding and all auxiliary equipment: pumps, drainage tank, plumbing etc.

Figure 14 presents the spallation target itself, i.e. the volume filled with liquid Pb/Bi-eutectic, into which the proton beam is dumped, producing an intense source of spallation neutrons. Spallation neutrons are produced through nuclear interactions with lead and bismuth nuclei. The window (1 on Fig. 13) is the most strained component of the target. Proton interaction with the window material generate a non-uniform volumetric energy deposition causing ther-

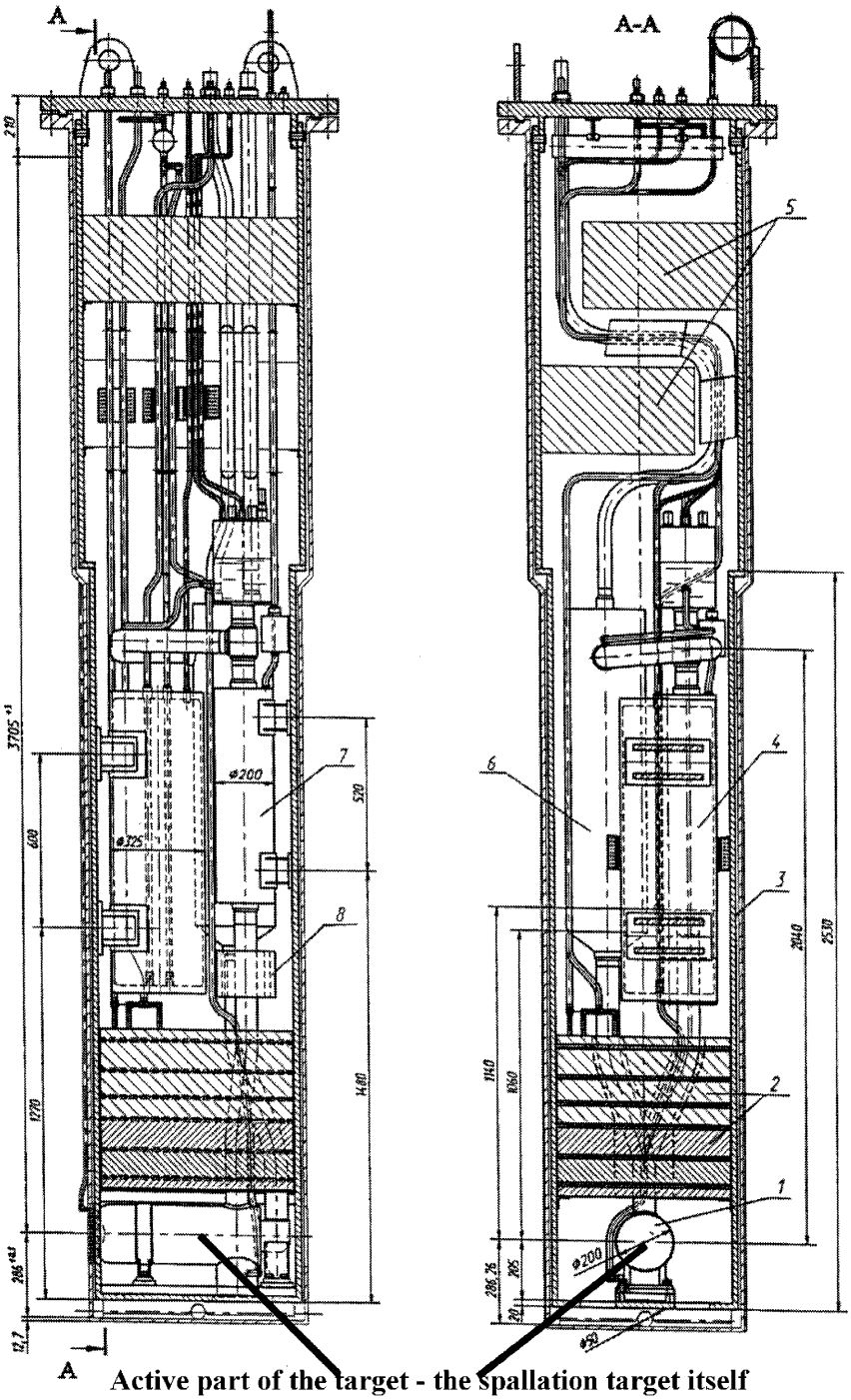

Figure 13. The layout of the 1 MW spallation target with all auxiliary equipment: 1 - spallation target itself, 2 - radiation shielding, 3 - steel containment, 4 - drainage tank, 5 -support structure, 6 - heat exchanger, 7 - MHD-pump, 8 - flow rate meter.

mal-mechanical loading on the window, large accumulation of displacements per atom and accumulation of helium. Moreover, frequent accelerator beam-trips (more than 1 per hour at the LANSCE accelerator) aggravate the window stress problem.

The unusual placement of the drainage tank (4 on Figure 13) - above the spallation target volume - is caused by geometrical constraints of the existing

experimental beam stop position at LANSCE where the target will be tested on-beam.

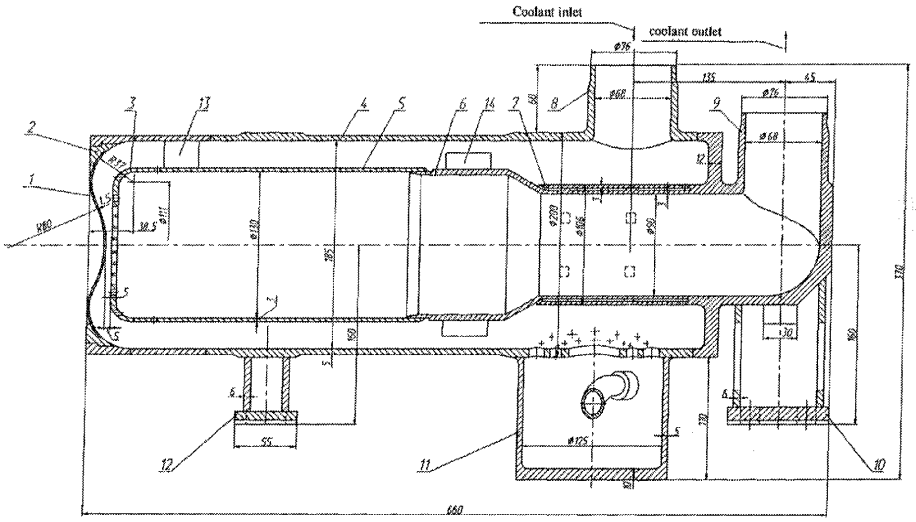

Figure 14. The spallation target. Main components of the target: 1 - window, 2 - window support, 3 - diffuser plate, 4 - target hull, 5 - inner channel.

The radiological safety problems have been studied for the target operation in the proton beam. A wide range of radionuclides is generated in the Pb/Bi eutectic (LBE) while irradiated by the proton beam of 0.8 GeV energy and consequently by high flux of spallation neutrons. The LBE total specific activity will be about 18.5 TeraBq after six months of irradiation with a proton beam of a nominal power 1MW. Figure 15 shows the decay of target specific radioactivity with cooling time.

The gaseous and volatile radionuclides which are partially collected in the cover helium gas in the compensator volume present the most distinct danger. The noble gases Krypton and Xenon, radioisotopes of Polonium, Mercury, Caesium, Iodine, Bromine and Rubidium are of the biggest concern. The calculations show [Grom98] that during normal operation the radioactive leakage into ventilation system is determined by ^{85}Kr, ^{131m}Xe, ^{129m}Xe and ^{127}Xe and so does not exceed the permissible value. In accidental conditions including the target window rupture the radiological contamination is determined by noble gases and will not exceed 0.1 TeraBq per day.

The benchmark calculations done at RIT - see Figure 16 confirm the thermal-hydraulic feasibility of the target design, from the point of view of cooling (temperature field) and flowing (velocity field) parameters. The limiting factor for the target performance seem to be a number of accelerator beam (power) trips which have to be accommodated in the target. The life-time number of trips has been estimated to about 3000.

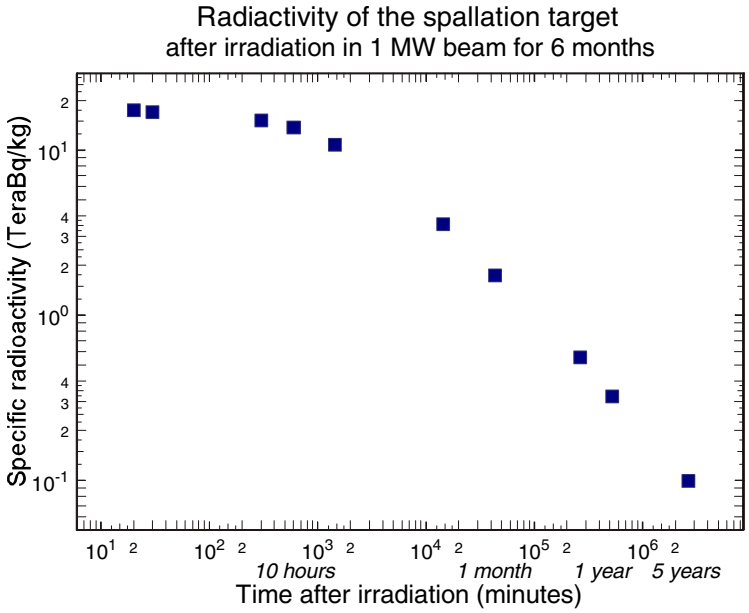

Figure 14. Specific radioactivity of the Pb/Bi eutectic as a function of cooling time after 6 months of irradiation in the 1 MW proton beam.

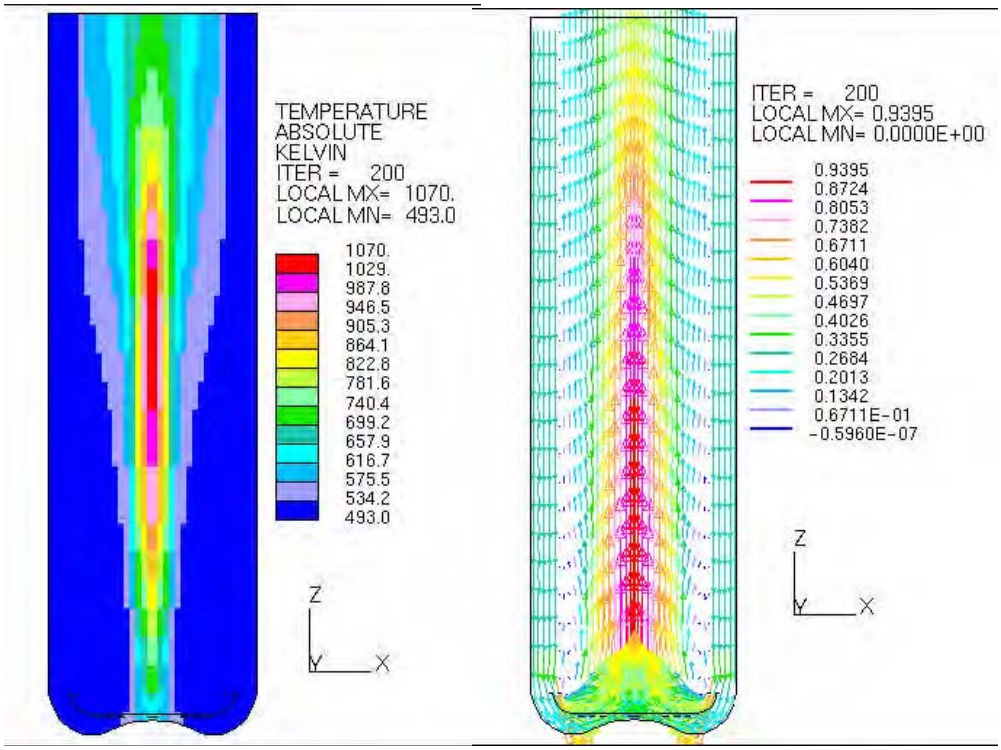

Figure 15. Benchmarking of spallation target calculations. Temperature field (left) and velocity field (right) for operational conditions of the target.

The target design is now under an intensive review and scrutiny process at Los Alamos, and in the smaller extent at CEA and RIT. A workshop will be organized in order to finally approve the target design for manufacturing.

4 SYSTEM STUDIES

4.1 NEUTRON ECONOMY

As shown by J-O Liljenzin et al in [Enar98], the success of a transmutation strategy is determined by the combination of high burnup fractions during irradiation of the waste, together with high separation degrees in the intermediate reprocessing that must take place. Radiation damage to solid fuel sets a general limit to the actinide burnup fraction at about 20%. Since reprocessing losses hardly can become smaller than 0.1% for any of the long lived actinides, a theoretical lower limit of the secondary waste stream necessary to put into geological repositories will be 0.5% of the initial TRU amount produced by commercial nuclear power plants. In order to achieve this goal in practice, however, it is necessary to design the transmutation system in such a way that neutron capture in fission products, construction material and fuel components can be accommodate for, within the number of neutrons produced in an average fission. Further, if one is to transmute long lived fission products like Technetium-99 and Iodine-129, the system must be able to provide an additional neutron surplus for this purpose. Hence, a complete design study of a nuclear waste transmutation system should include a neutron economy analysis. We define the neutron surplus G of a waste burning system as [Salv94]:

$$G = \sum_i [\eta_i D_i] - [L + CM] + S$$

Here, D_i is the average neutron gain due to neutron absorption in nuclide *i* and η_i is the cross section weighted atomic fraction of nuclide *i* in the waste:

$$D_i = \bar{\nu}_i \frac{\sigma_f^i}{\sigma_f^i + \sigma_c^i} - 1, \quad \eta_i = \frac{c_i\left(\sigma_f^i + \sigma_c^i\right)}{\sum_j c_j\left(\sigma_f^j + \sigma_c^j\right)}$$

L is the loss of neutrons due to leakage out of the core, CM is the loss of neutron due to absorption in construction materials, and S is the neutron surplus (per fission) due to sub-criticality of the system (if so configured). For most practically realizable reactors, L+CM is larger than 0.3.

If G is larger than zero, the surplus neutrons can be used for extending the burnup up to 20%, by allowing for increased absorption in generated fission products, and/or for transmutation of long-lived fission products. Hence, given an initial waste composition, the formulae above can be used for estimating the transmutation capabilities of a given system design. Table 1 shows the relative composition of transuranic nuclides in the waste of an average commercial PWR (burnup of 41 GWd/ton) and the resulting composition after having recycled the plutonium as MOX in a PWR once with moderate burnup (33 GWd/ton) [NEA98].

Table 1: Relative composition of transuranic nuclides in waste from an average PWR, with and without recycling of Plutonium as MOX. Four years of cooling is assumed.

Nuclide	PWR UOX-waste	PWR UOX + MOX-waste
^{237}Np	0.046	0.059
^{238}Pu	0.023	0.025
^{239}Pu	0.490	0.330
^{240}Pu	0.215	0.247
^{241}Pu	0.114	0.120
^{242}Pu	0.062	0.085
^{241}Am	0.028	0.072
^{243}Am	0.016	0.043
^{244}Cm	0.005	0.015
^{245}Cm	0.000	0.001

It is to be noted that the use of extended MOX burnup does not lead to a substantial decrease in TRU mass. Increasing the burnup from 33 GWd/ton to 43.5 GWd/ton only enlarges the effective TRU burnup from 20.9 to 22.7 % [NEA98]. At the same time curium content (and α–activity) is nearly doubled. Hence such MOX burnup levels may be considered contra productive in a waste transmutation scenario. In a previous report involving the present authors, larger figures for TRU reduction were claimed [Enar98]. Those numbers were however based on unverified ORIGEN2 calculations, which only with great difficulty can accommodate corrections due to decrease in self-shielding of ^{238}U capture as ^{239}Pu is fissioned away.

The individual nuclide neutron gain D for the minor actinides is displayed in Figure 17. It can be seen that ^{237}Np, ^{241}Am and ^{243}Am and Am all are neutron consumers, however less so in a Pb/Bi cooled ADS than in a fast breeder reactor. From these figures, one can conclude that a pure minor actinide fuelled system must contain exceedingly large ^{245}Cm fractions in order to become even close to critical (G>0). Accordingly, the JAERI design of their MA-fuelled ADS uses 40% Pu for "start-up".

The resulting neutron surplus G for different types of transmutation systems is shown in Figure 18. As seen, an arbitrary thermal spectrum system is hardly able to handle transmutation of MOX recycled waste at all. Only by continu-

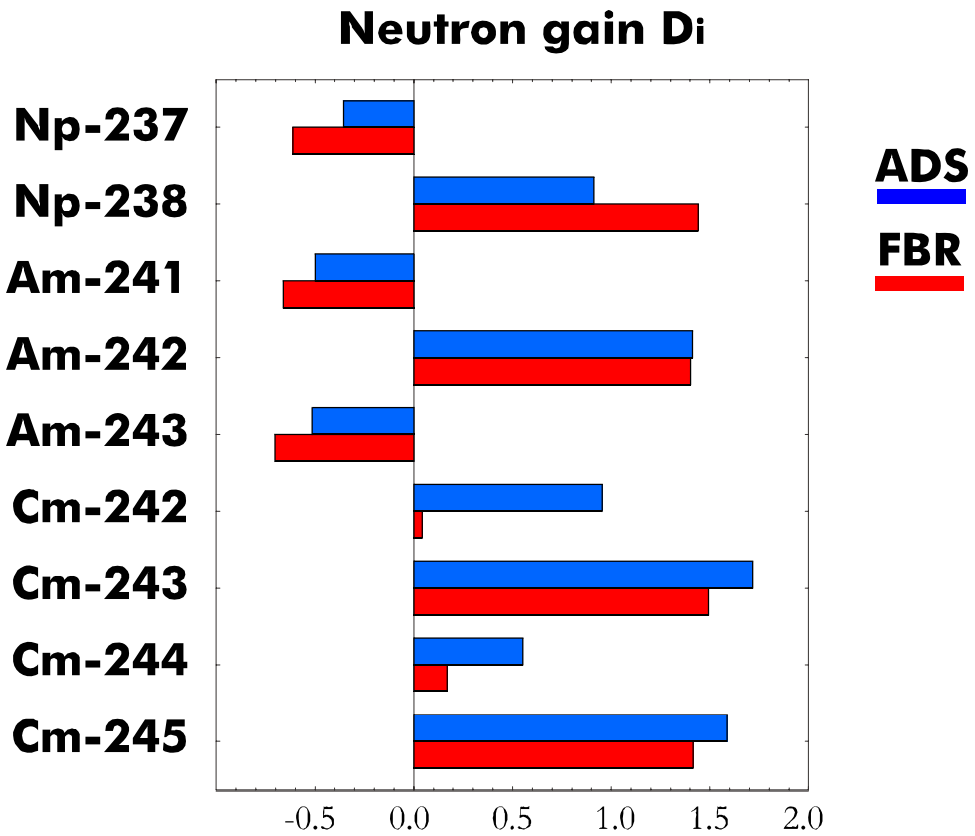

Figure 17: The neutron gain D_i in absorption of a neutron in minor actinide nuclides. Blue bars show values for a Pb/Bi cooled ADS spectrum, red bars for a sodium cooled fast breeder spectrum.

ous removal of fission products, as in the molten salt ADS, could a thermal spectrum be considered. The safety aspects of a liquid fuel approach are however quite cumbersome. In addition, there is very limited potential of long lived fission product transmutation in a thermal spectrum. The sodium cooled Fast Breeder Reactor can be used for transmutation of both transuranic waste, Technetium-99 (~0.2 surplus neutrons needed) and Iodine-129 (~0.05 neutrons needed), still allowing for close to 20% heavy atom burnup. The necessity of having large fractions of uranium in the fuel in order to obtain acceptable Doppler feedback makes the global TRU transmutation rate of the FBR significantly smaller than the corresponding rate in a purely TRU fuelled ADS, however. Further, the slower spectrum of the FBR leads to increased accumulation of curium in the waste during the transmutation process, which makes both reprocessing and fuel element manufacturing more difficult and expensive. Finally, the outstanding neutron surplus of the Pb/Bi cooled ADS would always allow for reaching highest possible burnup fractions, with close to complete transmutation of both technetium and iodine. There is even a theoretical potential for transmutation of Caesium-135 without isotope separation (~0.6 surplus neutrons needed), if this would be considered useful.

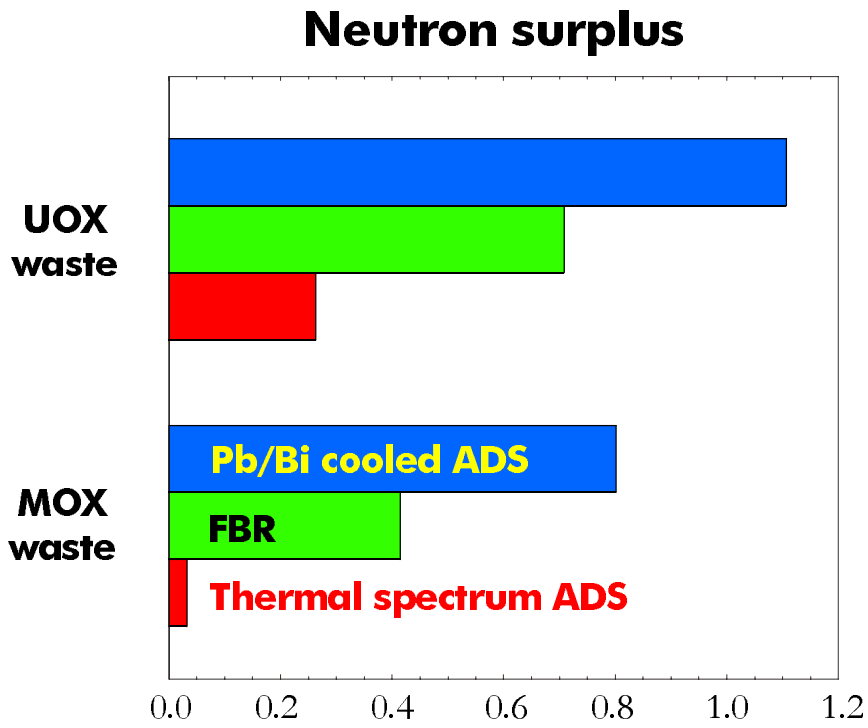

Figure 18. Neutron surplus G in a Pb/Bi-cooled ADS (blue bars), a sodium cooled FBR (green bars), and an arbitrary thermal spectrum ADS (red bars) loaded with UOX and UOX+MOX transuranic waste.

4.2 NEUTRONICS

The extraordinary neutron surplus of the Pb/Bi-cooled ADS would not be a decisive advantage with respect to the sodium cooled fast breeder, if it could not be utilized for transmutation purposes in practice. There are however several possible means of doing this, like:

- Transmutation of the long-lived fission products ^{99}Tc-,^{129} I and ^{135}Cs.
- Capture in burnable poisons for flattening of reactivity changes.
- Low-energy capture in absorbers in order to block capture in fuel nuclides and ^{209}Bi.
- Allow for fission product capture in fuel element in order to facilitate extended burnup (up to 20%).

The first three points can be implemented separately or in combination. The transmutation of ^{99}Tc and blocking of capture in ^{209}Bi was investigated using MCNP in a paper presented at the Heavy Liquid Metal Coolant (HLMC) conference held in Obninsk [Wall99]. It was shown that the comparatively fast neutrons leaking out of the periphery of a core analogue to the one depicted in Figure 1, easily are captured in ^{99}Tc rods placed in the direct vicinity of the core. The number of Technetium transmutations per fissioned TRU nucleus well exceeded the number of Tc-nuclides originally co-produced with the TRU nucleus. While capture cross sections are larger for moderated neutrons, the corresponding self-shielding effects severely lowers

the transmutation efficiency [Kon98]. Consequently, the wide-spread belief that moderation techniques are beneficial for FP-transmutation [Kloo95] appears to be wrong. In addition, the capture of fast leakage neutrons stops them from re-entering the core with a lower energy, and thus lowers curium accumulation in the outer fuel elements. Further, it was shown that a reduction of ^{210}Po accumulation in the coolant of up to 40% resulted as a side-effect of the Tc-rod introduction.

In a refined Monte Carlo study of the ^{99}Tc transmutation potential, a smaller amount (390 kg) of technetium was placed as 1.6 cm diameter rods surrounding the periphery of the core shown in Figure 1. This corresponds to about 1.4 Tc nuclei per TRU nucleus in the core, i.e. seven times the originally concomitant production. The amount could be relevant for a scenario where seven consecutive fuel loads are irradiated up to 15% burnup, without exchange of Tc-rods. The initial capture ratio (at k-eigenvalue ~ 0.965) was found to be 0.27 per TRU-fission. The neutron flux in the Tc-rods was only slightly deteriorated by self-shielding as shown in Figure 19. This should be compared to a self-shielding induced flux reduction of a factor of two found in Tc-rods irradiated in an epithermal spectrum [Kon98]!

An average neutron flux energy of 330 keV, an average capture energy of 130 keV and a mean free neutron path in the rods of 2.3 cm confirms the importance of applying a fast spectrum for efficient technetium transmutation. In all cases, mean free paths should not be much less that one cm for avoidance of self-shielding. Figure 20 shows the neutron spectrum at the instant of capture. Note that less than 2% of the captures take place below 1 keV.

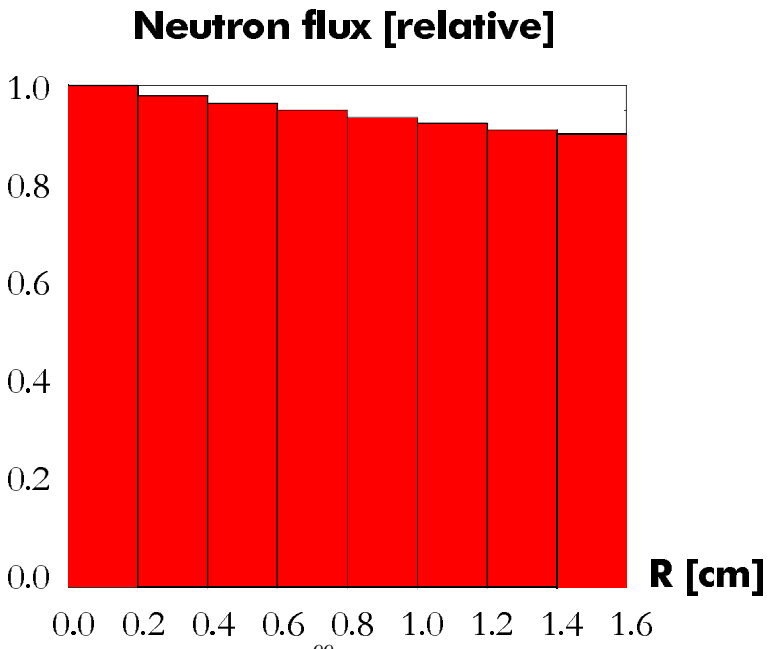

Figure 19. Neutron flux across ^{99}Tc rods placed at the periphery of a fast spectrum sub-critical core. The effect of self-shielding is visible, but does not deteriorate the transmutation rate across the rod significantly. R denotes radial distance from the point of the rod closest to the core. An epithermal irradiation would have led to a minimum in the flux (transmutation rate) in the center of the rod ® = 0.8 cm).

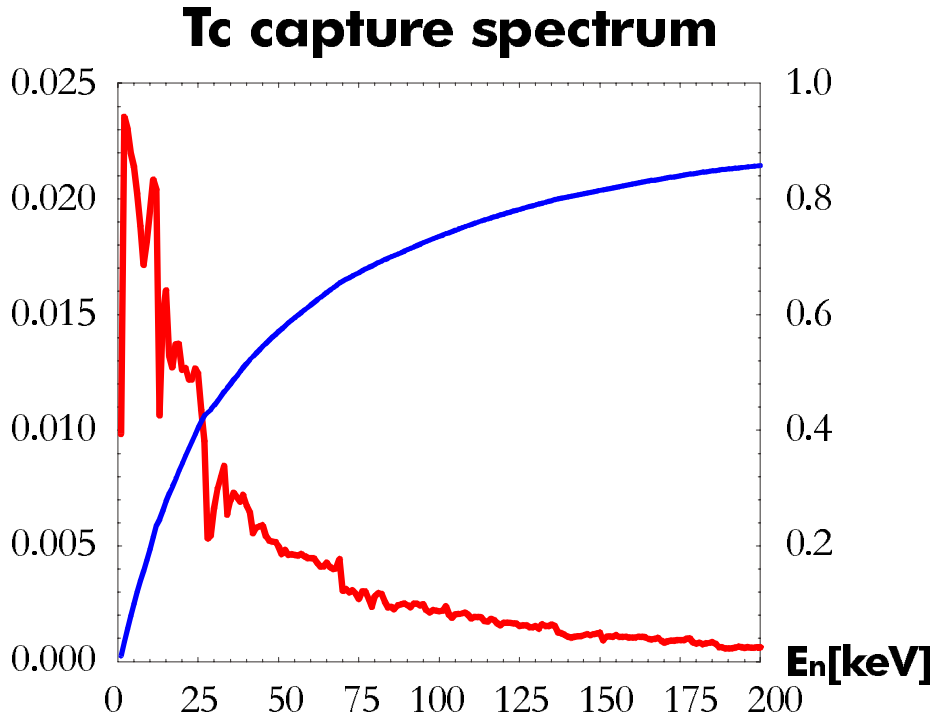

Figure 20. Neutron spectrum at instant of capture in ^{99}Tc, normalized to unity (red line). Fraction of captures below a given neutron energy (blue line).

4.3 FUEL TYPES

The choice of fuel type will be of certain importance for the performance of a transmutation facility. Early breeder reactors employed metallic fuels, having advantages of high breeding ratios and high thermal conductivities. However, the very fast neutron spectrum resulting, had the disadvantage of diminishing negative Doppler feedback to levels where safety margins became questionable. Further, swelling problems turned out to be severe even at moderate burnup levels. The comparatively well known di-oxides used extensively in Fast Breeder Reactors have the advantage of moderating the neutron flux enough for the overlap with the uranium resonance region to be significant. Hence, a large negative Doppler coefficient results, which has allowed for safe operation of sodium cooled prototype reactors like BN-600 and Phenix.

In the context of transmutation, where plutonium consumption is a priority, one would like to avoid large fractions of ^{238}U in the reactor. Thus the main technical advantage of the oxide fuel is lost. The considerable industrial experience of producing and reprocessing oxide fuels must then be re-evaluated in the light of disadvantages appearing in the specific context of transmutation like:

- Relatively high neutron moderation, yielding higher capture to fission ratios, in their turn leading to higher fractions of curium accumulation in

the fuel at given burnup levels. Curium isotopes are strong alpha emitters, which increase the cost of reprocessing and fuel manufacturing.

- Low thermal conductivity, which limits the maximal power per meter of fuel pin to 50 kW if fuel melting is to be safely avoided. Especially for non-recycled transuranic waste, which is highly reactive, this limits fuel pin diameters to extremely small values (<5 mm), even when introducing annular fuel pellet designs.

The requirement of a fuel type with small neutron moderation impact and high thermal conductivity therefore lead to reconsideration of metal fuels as well as nitride fuels, also developed and tested during the fifties and early sixties.

Metallic fuels undoubtedly yield the highest fission to capture ratios for most transuranic nuclides. However, the problems of swelling at high burnup fractions (minimum 10% burnup is required) can only be accommodate by means that lower the thermal conductivities of the TRU alloys down to levels where maximal linear power are in parity with the oxide fuels. Such means may be alloying with zirconium or lowering of fissile fuel density, and have been proposed by CERN and Los Alamos in their designs of waste transmutation systems.

Nitride fuels on the other hand, feature smaller moderation of neutrons than oxide fuel, due to one-third smaller fraction of light nuclides, moderate swelling and relatively high thermal conductivity. Irradiation tests also show that fission gas release is small [Arai97,Suzu99]. As shown in Figure 20, a maximal linear power of above 120 kW/m can be achieved without increasing the maximal temperature above 1400 K in annular nitride fuel pellets. This allows for a much smaller fraction of diluent material (uranium, thorium, zirconium, magnesium oxide), than required by oxide or metallic fuels. Further, fuel radiation damage and fission gas release that deteriorates thermal conductivity is minimized.

The main drawback of the nitride fuel is production of ^{14}C due to the (n,p) reaction in ^{14}N. Hence, ^{15}Nenriched nitrogen is envisaged for manufacturing of the fuel. A 99.9% enrichment would lead to a thousand fold reduction in ^{14}C accumulation while raising fuel assembly costs by an acceptable amount of 25% [Grup98].

Consequently, nitride fuels are considered as first choice for waste transmutation by JAERI and MINATOM, both having ongoing research programs on nitride fuels including fabrication and irradiation. In a Swedish perspective nitride fuels should also be considered as most interesting, taking the very high reactivity of un-recycled LWR waste into account.

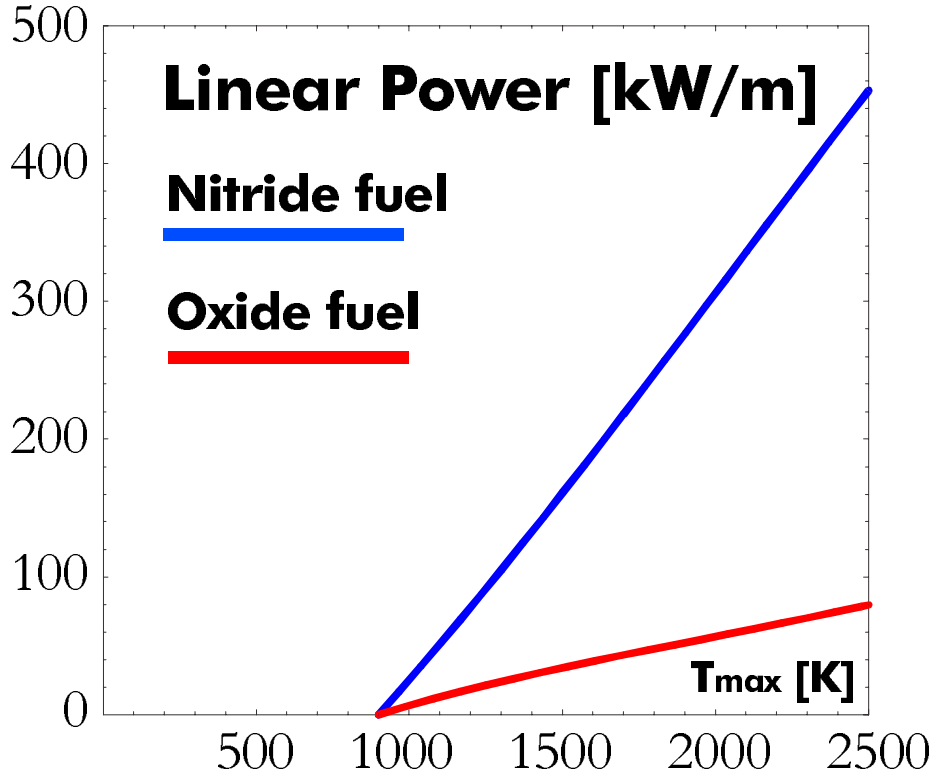

Figure 21. The linear power (power per length unit of fuel pin) produced in an annular fuel pellet of CAPRA dimensions, having a surface temperature of 900 K, as function of maximal temperature. Fuel melting occurs at about 2700 K for both oxide and nitride fuels, while fission gas release grows quickly at temperatures above 1400 K. Nitride fuel allows for at least four times higher linear power at any given maximal fuel temperature.

5 ACCELERATOR RELIABILITY STUDIES

In collaboration with Los Alamos National Laboratory a reliability study of the LANSCE accelerator have been performed [Eric98 and Appendices 3,4]. The reliability and availability of the accelerator in accelerator driven systems is an important issue. Taking into account the fact that proton beams from existing high power proton accelerators trip (suddenly stop) very frequently, it is indispensable to understand the effect of such beam trips on different subsystems, especially a subcritical reactor. Temperature fluctuation caused by power change in the accelerator beam enforces thermal transients to reactor structures and beam window, where thermal fatigue or creep-fatigue damage will be accumulated during life time. When large number of severe thermal stress cycles are enforced, there is a possibility of crack initiation and propagation at structural walls.

The first step towards a more reliable accelerator is to study the operational experiences of the existing high power proton accelerators, paying special attention to the beam trip records. The accelerator facility at Los Alamos Neutron Science Center (LANSCE) is the most powerful linear proton accelerator

in the world. The accelerator offers enough operating history to supply meaningful reliability data.

The LANSCE accelerator delivers two proton beams at 800 MeV: the H+ and the H- beam. The H+ beam may deliver 1.25 mA current (routine operation is at 1 mA) and the H- beam delivers 70 µA. Each injector system includes a 750 keV Cockcroft-Walton type generator. Both ions are accelerated simultaneously in one and the same structure. The low energy section of the accelerator is an Alvarez Drift Tube Linac (DTL). The drift tube linac accelerate the protons from 750 keV to 100 MeV. The high energy section is a Side Coupled Linac (SCL). The SCL may accelerate protons up to 800 MeV. After acceleration the H+ and H- beams are separated and diverted into different target areas.

The availability of an accelerator is expressed as the ratio of the achieved beam time to the scheduled beam time. However, in our case the reliability to beam trips and fluctuations becomes more important since sudden beam trips cause severe thermal shocks in the system. The accelerator reliability is typically determined by the mean time between failure and the mean down time of a trip.

The present work examines the data set of failure events for the LANSCE 800 MeV accelerator facility. The analysis considers scheduled accelerator operation of the H+ beam for 1997 and of the H- beam for 1996 and 1997. The H+ and the H- beams are investigated separately. A histogram of beam trips that occur in the H+ and the H- beam is presented in Figure 22.

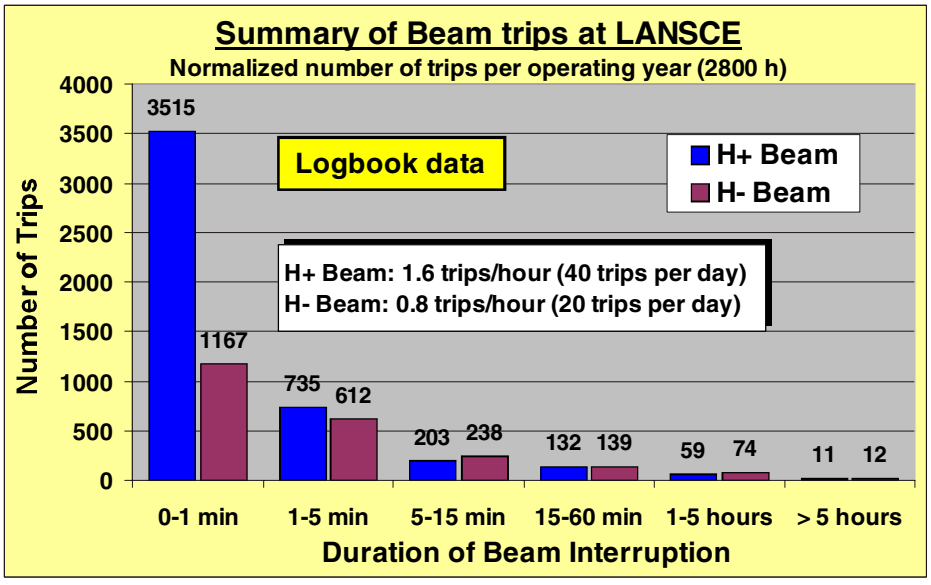

Figure 22. Beam failure statistics of the LANSCE accelerator facility.

From Figure 22 it is obvious that the H+ beam is exposed to many beam trips with short duration. 76% of all trips in the H+ beam are 0-1 minute long. On average, the H+ beam is exposed to 1.6 trips/hour and the H- beam 0.8 trips/hour. The data presented in figure 1 are based on operational data re-

corded in the accelerator logbook. Similar beam reliability analysis is also performed for data recorded by beam current monitors positioned near the targets. Approximately 2.4 trips/hour (60 trips per day) in the H+ beam are detected by the beam current monitors. The reason is that the current monitors are able to detect a larger number of short trips.

In Figure 23, the most frequent causes for beam trip and downtime are presented.

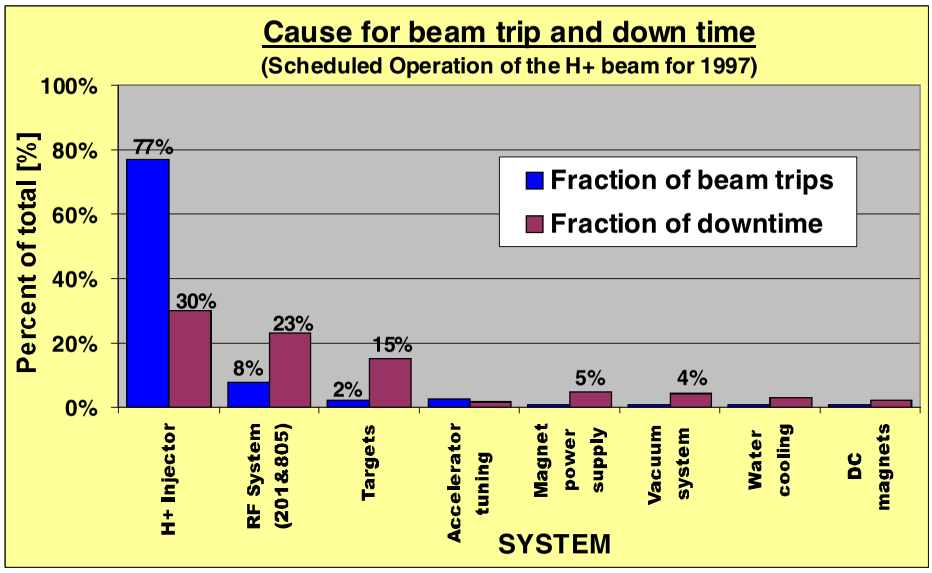

Figure 23. Systems responsible for trips and downtime in the H+ beam.

Figure 23 shows that 77% of all trips in the H+ beam are caused by a failure in the injector. The characteristic of the injector failure is the interruption length. It is usually shorter than 1 minute, often in the order of 15-20 seconds, the time it takes to reset the trip and re-energize the Cockcroft-Walton generator. An injector failure is usually caused by electric breakdown in the high voltage column. Since a typical injector failure is short, the injector is not as dominating when it comes to the generation of downtime. In other words, the injector is the main reason for beam current fluctuations but it has relatively smaller influence on the overall beam availability. The rf system, including the rf system for the DTL and the SCL, is responsible for 8% of the trips and is accountable for 23% of the downtime. Hence, a failure in the rf system usually results in a long downtime (> 5 minutes).

Some important conclusions of this study are:

- An actual beam trip rate of the LANSCE accelerator is typically 1.6-2.4 trips/hour or 40-60 trips/day. 75% of these trips are shorter than 1 minute.
- Approximately 10 trips/day with downtime longer than 1 minute occur in the LANSCE facility. Hence, if we assume an annual operation time

of 300 days/year the total number of trips in the LANSCE facility with down time longer than 1 minute is in the order of 3000 trips/year.

- The typical downtime of a short trip is 15-20 seconds and the main source of beam trip is sparking in high voltage components, for example the injector column.
- Upgrading the injector will result in a more stable beam with less interruptions, especially short ones. Upgrading the rf system will result in a better beam availability.
- Accelerator trips will be a strongly limiting constraint for a spallation target experiment ("'Obninsk target").

The results are useful in accelerator reliability modelling and identifying development issues in high power accelerators. One of the most important question is: **What beam trip rate is the maximum acceptable limit for a high power subcritical reactor?** The beam trip frequency should be compared with actual number of unscheduled shutdowns in existing nuclear plants (LWRs), which are in the region of 0.3-3.5 shutdowns/year. For instance, if a beam trip rate of the same level as the actual unscheduled reactor shutdown is required, the necessary improvement is tremendous and it seems to be very ambitious. On the other hand, if the maximum acceptable trip rate can be relaxed to 10-100 trips/year, the goal seems to be more realistic. Although, the beam trip rate for short beam trips (<1 min) is very high, one should keep in mind that short trips is not as serious as long trips in terms of thermal shock to structure material. The temperature swing in the reactor caused by a short beam trip is small due to the thermal inertia of the system, for example, it takes certain amount of time for the coolant to recycle the reactor.

6 SEMINARS AND INTERNATIONAL COLLABORATION: VISITS TO KTH AND PROJECT FOREIGN TRAVELS

The Swedish Spallator Network (SSN) is a network of Swedish scientists involved or interested in research on partitioning and transmutation, that was initiated by the department. Scientists from Chalmers University, Uppsala University (including the Studsvik division) and Lund University participate in the activities of the network. A series of SSN seminars on aspects of transmutation and partitioning was held in Uppsala, Stockholm and Göteborg during the spring of 1998. A general audience seminar with guest speakers Francesco Venneri and Hans Blix was arranged at the Royal Academy of Science in may 1999, attracting people from industry and educational institutions. SSN also participated in the energy technology exhibition held in Göteborg in April 1998.

Informational meeting at The Swedish Advisory Group on Spent Fuel Management "KASAM" : A review of the present status of transmutation research", presentation given by W. Gudowski and J. Wallenius (March 1998)

W. Gudowski gave a presentation on transmutation at Uppsala University for about 140 teachers of physics and technology from Swedish high schools (April 1998).

Between January and May Waclaw Gudowski represented Sweden and RIT on three meetings of the Nuclear Physics Group of OECD Mega Science Forum. The final meeting in Washington, May 1998, agreed on recommendation of transmutation research to the general meeting of OECD Research Ministers. This meeting will take place in the first half of 1999.

In July, 1998 W. Gudowski headed the IAEA consultancy meeting on review of ADS-activities in Russia, taking place in Moscow.

In August 1999 W. Gudowski presented the invited talk "The Importance of Nuclear Physics Research for Waste Transmutation" in the International Nuclear Physics Conference, INPC98 in Paris.

In September and December 1998 W. Gudowski participated in a meeting hosted by CEA in Paris on preparation of project proposals for V Framework Programme of European Community. The results of these meetings have been summarized and reported to SKB during last months.

J. Wallenius lectured at informational meetings arranged by The Swedish Advisory Group on Spent Fuel Management "KASAM" in Nyköping and Stockholm.

Marcus Eriksson was invited to present his paper on reliability of studies of the LANSCE accelerator [Erik98], OECD workshop on RELIABILITY of High Power Accelerators, Tokai (October 1999)

In October J. Wallenius participated in the conference on Heavy Metal Coolants (HLMC 98), held in Obninsk, Russia [Appendix 1]

J. Wallenius and K. Tucek took part in the 5th International Information Exchange Meeting on Actinide and Fission Product Partitioning and Transmutation in Mol, Belgium (November 1998) presenting paper on Monte-Carlo burnup code (see Appendix 2)

Kamil Tucek participated in the meeting of the IAEA Coordinated Research Project (CRP) - Use of Th-based Fuel Cycle in Accelerator Driven Systems (ADS) to Incinerate Pu and to Reduce Long-term Waste Toxicities NRG (formerly ECN) in Petten The Netherlands(December 1998). Results of our work in the third benchmark project were presented and discussed

RIT is coordinating an EC project IABAT - Impact of Accelerator-Based Technologies on Nuclear Fission Safety. Some of the projects and topics in the

IABAT activities are intimately connected and cross-linked with the work financed by SKB. A separate reports on IABAT progress are available and may be delivered to SKB.

Seminars organized in the frame of the project:

Swedish Spallator Network seminars: "Status of the transmutation research" took place:

- January 7, at Uppsala University
- March 3 at KTH
- April 24 at CTH, Göteborg

May 14, Seminar at the Royal Swedish Academy of Sciences: " Transmutation - a new view on nuclear energy", lectures of F. Venneri (LANL) and J. Wallenius

September 3, Seminar at KTH, Marcus Eriksson: Presentation of M.Sc. thesis: Reliability Assessment of the LANSCE Accelerator System

September 3, Prof. Yuri Shubin (IPPE, Obninsk): "Evaluation methods in the construction of high energy neutron cross section libraries"

September 4, Prof. Yuri Shubin (IPPE, Obninsk): "Properties of Heavy Liquid Metal Targets in Accelerator Driven Systems"

September 7, Prof. Yuri Shubin (IPPE, Obninsk): " A New Approach to Neutron Threshold Reaction Systematics (Physical grounds and creation of systematics for neutron induced reactions (n,p), (n,α),(n,np),(n,d), (n,t) at 14-15 MeV)".

November 5, Charlotta Sanders: Licentiate seminar: "Neutron induced material damage in subcritical systems"

November 1998, Prof. A.F.Grashin (MEPHI): "A nonconventional thermodynamical approach to subatomic phenomena (supernonequilibrium thermodynamics) - 2 seminars.

November 1998, Dr. Jerzy Cetnar (Technical University "Akademia Gorniczo-Hutnicza" in Krakow): Monte Carlo Continuous Energy Burn-up Code (MCB)

December 1998, Profs V.Barashenkov, A.Puzynin, A.Polanski (JINR, Dubna): "High Energy Transport Physics" and " A proposal of accelerator-driven experimental facility at JINR" - 2 seminars

December 1998, Kamil Tucek: The 5th International Information Exchange meeting on Actinide and Fission Product Partitioning and Transmutation, Mol, Belgium.

December 1998, Kamil Tucek: "The second stage of the IAEA CRP Benchmark - presentation of results"

Visits of foreign collaborators:

Dr. Francesco Venneri visited RIT in May 1998 giving seminars in Stockholm (RIT and Swedish Royal Academy of Sciences) and Uppsala University on progress of ADTT research at Los Alamos National Laboratory.

Prof. Y. Shubin (IPPE, Obninsk) visited RIT in September 1998 in the frame of our collaboration on nuclear data giving few lectures on nuclear data evaluation for the projectile energy region of 20 - 150 MeV.

Prof. A, Grashin (MEPHI, Moscow) visited RIT in November in the frame of the fission yield evaluation sub-project giving also 2 seminars on non-equilibrium thermodynamical model for fission processes.

Dr. J. Cetnar has been working at our department in November with a final version of MCB-code.

Profs V. Barashenkov and A. Puzynin (JINR, Dubna) together with Dr A. Polanski (INP, Swierk and JINR, Dubna) visited RIT in December 1998 giving 2 seminars on high energy transport modelling and presenting the activities of Joint Institute for Nuclear Research in accelerator-driven transmutation research.

7 GRADUATE COURSE IN TRANSMUTATION

A graduate course in transmutation was given at the department in December 1998. Lecturer is J. Wallenius, with guest appearances by J. Blomberg from Uppsala University and P. Ekström from Lund University. The course consists of 30 lectures and five laboratory exercises, and was attended by six students from Uppsala University, one from Lund University and four from KTH.

8 PROJECT MILESTONES

Milestone number two, for part one of the project was defined as "Integrated code package for system analysis completed". As accounted for in the present report, integration of burnup and neutron transport into a single code - MCB - has been accomplished by the participants of the project. Integration of the spallation simulation code LAHET and MCNP into MCNPX was made as a part of the APT project in Los Alamos, with contributions from participants of the present SKB-project. The final integration of MCB with MCNPX is not yet completed however, but is expected to be so during 1999.

Progress on system and safety analysis is on the other hand somewhat ahead of schedule. On the basis of MCNP and MCNPX calculations it could be established that liquid metal cooled reactors (fast neutron spectra) yield so much yield higher transmutation efficiencies (and lower curium accumulation) that such systems must be considered a mandatory part of a transmutation strategy. Regarding choice of fuel type it was also clarified that the high reactivity of un-recycled UOX-waste in conjunction with the requirement of low U-238 fractions in the fuel, makes the use of standard oxide fuel less advantageous. Mono-nitride fuel would, mainly due to its higher thermal conductivity, lead to a better transmutation efficiency and smaller problems with radiation induced fuel damage. Hence, nitride fuels should be considered as first option in a Swedish transmutation strategy.

9 REFERENCES

[Arai97]. Y. Arai et al, In Proc. Int. Conf. on future nuclear systems, Global 97, (1997) 664.

[Baco97]. D.J. Bacon, A.F. Calder and F. Gao, Radiation Effects and Defects in Solids 141 (1997) 283.

[Brie97]. MCNP - A general Monte Carlo N-particle transport code, version 4B. Ed. J.F. Briesmeister, LA-12625-M, Los Alamos National Laboratory (1997).

[Chop95]. G. Choppin, J.O. Liljenzin and J. Rydberg, Radiochemistry and nuclear chemistry, 2nd edition, Butterworth Heinemann (1995).

[Co67]. J.L. Cook, H. Ferguson, and A.R. Musgrove, "Nuclear Level Densities in Intermediateand Heavy Nuclei," Aust.J.Phys. 20, 477 (1967).

[Enar98]. Å. Enarsson et al, SKB-rapport R-98-06, SKB (1998).

[Erik98]. Marcus Eriksson and Christopher Piaszczyk, "RELIABILITY Assessment of the LANSCE Accelerator System", Proceedings of the OECD

Workshop on RELIABILITY of High Power Accelerators, Mito, Japan, October (1998)

[Gras85]. A. Grashin, A. Jefimenko and V. Kolobashkin, Izvestiya Akademii Nauk SSSR 49 (1985) 188 (in russian).

[Grup98]. H. Gruppelaar, J.L. Kloosterman and R.J.M Konings, ECN-R-98-008 (ECN) (1998).

[Hugh97]. H.G. Hughes, R.E. Prael and R.C. Little, XTM-RN (U) 97-012, Los Alamos National Laboratory (1997).

[Ig75]. A.V.Ignatyuk, G.N.Smirenkin, and A.S.Tishin, "Phenomenological Description of the Energy Dependence of the Level Density Parameter", Sov. J. Nucl. Phys. 21, 255(1975).

[Ka88]. C.Kalbach, "Systematics of Continuum Angular Distributions: Extensions to Higher Energies", Phys.Rev. C37, 2350 (1988); see also C.Kalbach and F.M.Mann, Phenomenology of Continuum Angular Distributions. I. Systematics and Parameterization", Phys.Rev.C 23, 112 (1981).

[Kinc55]. G.H. Kinchin and R.S. Pease, Rep. Prog. Phys. 18 (1955) 11.

[Kloo95]. J.L. Kloosterman and J.M. Li, ECN-R-95-002, ECN (1995).

[Kold95]. A. Koldobsky and V. Zhivun, Voprosi atomnoi nauki i tehniki (Yadernie konstanti) (1995) 74 (in russian).

[Kon98]. R.J.M. Konings et al, Nucl. Sci. Eng. 128 (1998) 70.

[Koni98]. A.J. Koning, M.B. Chadwick, R. E. MacFarlane, S. Mashnik and W.B. Wilson "Neutron and Proton Transmutation-Activation Cross Section Libraries to 150 MeV for Application", ECN, ECN-R—98-012, 1998

[Mann77]. F. M. Mann and R. E. Schenter, Nucl. Sci. Eng. 63 (1977) 242.

[MF92]. R. E. MacFarlane and D.W. Miur "The NJOY Nuclear Data Processing System", Los Alamos National Laboratory, LA-12740-M, 1992

[NEA98]. NEA/PTS/DOC(98)6 (final draft), OECD/NEA 1998.

[Norg75]. M.J. Norgett, M.T. Robinson and I.M. Torrens, Nuc. Eng. Des. B 33 (1975) 50.

[Prae89]. R.E. Prael and H. Lichtenstein, User guide to LCS: the LAHET Code System. Los Alamos National Laboratory (1989).

[Ra84]. J.Raynal, Mater. Of Workshop on Nuclear Model Computer Codes. 16 Jan - 3 Feb. 1984. Trieste.

[Robi92] M.T. Robinson, Nuc. Inst. Meth. B 67 (1992) 396.

[Sand98]. C. Sanders and J. Wallenius, Fission neutron induced defect production in heavy metal cooled reactors, submitted to Nucl. Sci. and Eng.

[Salv94]. M. Salvatores et al, Nucl. Sci. Eng. 116 (1994) 1.

[Suzu99]. Y. Suzuki et al, In Proceedings of the fifth international information exchange meeting on actinide and fission product partitioning and transmutation, to be published, OECD/NEA (1999).

[Wahl85]. A. Wahl, Phys. Rev. C 32 (1985) 184.

[Wall99]. J. Wallenius, K. Tucek and W. Gudowski, Technetium-99 neutron absorbers in the reflector of Pb/Bi cooled reactors, In Proceedings of Heavy Liquid Metal Coolants in Nuclear Technology (HLMC 98), to be published, IPPE (1999).

[Yo92]. P.G.Young, E.D.Arthur, and M.B.Chadwick, "Comprehensive Nuclear Model Calculations: Introduction to the Theory and Use of the GNASH Code," LA-12343-MS (1992).

[Zink93] S.J. Zinkle and B.N. Singh, J. Nucl. Mater. 199 (1993) 173.

APPENDIX 1

TECHNETIUM-99 NEUTRON ABSORBERS IN THE REFLECTOR OF PB/BI COOLED REACTORS

Jan Wallenius, Kamil Tucek and Waclaw Gudowski
Nuclear and Reactor Physics
Royal Institute of Technology
Stockholm, Sweden

Abstract

The transmutation rate of ^{99}Tc as function of position in the reflector of a Pb/Bi cooled sub critical reactor has been investigated. The reactor fuel was supposed to consist of depleted uranium and transuranic waste from a light water reactor in enriched mono nitride form. The TRU fraction was varied across the core in order to obtain a flat power distribution. Monte Carlo simulations show that a maximal transmutation rate for small ^{99}Tc concentrations is obtained at 25 cm distance from the periphery of the core. The maximal transmutation rate for large concentrations is about 0.5 ^{99}Tc nuclei per fissioned TRU nucleus, if the technetium rods are placed right at the periphery of the core. This rate is more than two times higher than the technetium production rate per TRU in spent light water reactor fuel, and corresponds to usage of about half the theoretical neutron surplus in a heavy metal cooled waste transmutation system. Further, the absorption of leakage neutrons in ^{99}Tc leads to a 40% reduction of ^{210}Po accumulation due to neutron capture in ^{209}Bi.

Introduction

While ideas of transmuting long-lived radiotoxic isotopes present in spent nuclear fuel appeared over 30 years ago [1], it was not until recently that consensus appeared regarding the necessity of applying fast spectrum neutron systems for achieving sufficient transmutation efficiency of both transuranics and fission products [2-6]. Especially, it seems that applying heavy liquid metal cooling of the core would yield a neutron surplus in principle allowing for transmutation of not only ^{99}Tc, but possibly also ^{129}I and ^{135}Cs [4]. In order to evaluate the actual potential for transmutation of these fission products, one should investigate the dependence of transmutation rates on neutron spectrum at various positions in the reflector of the waste transmutation system. The influence of self shielding also needs to be well understood. In the present paper, results of Monte Carlo simulations for transmutation rates of ^{99}Tc and ^{129}I as function of radial distance from the periphery of a TRU fueled sub critical core are presented. In the following section we describe the characteristics of the waste transmutation system we have chosen as a basis for our investigations. Then we discuss the advantages of the Monte Carlo method applied for calculating the transmutation rates. Finally we display the resulting rates in various forms and discuss their implications on further studies.

Core characteristics

Fission products contribute only with a minor share of the long term radio-toxicity of spent fuel. However, due to the higher mobility of certain isotopes, transmutation of long-lived fission products would lead to a significant reduction in potential radio-toxicity leakage from a geological repository to the biosphere. Hence we have chosen to investigate waste transmutation systems with high neutron surpluses, like heavy metal cooled, accelerator driven reactors fueled by TRU waste from light water reactors (without MOX recycling). Theoretically they may yield a surplus of 1.15 neutrons per TRU fission for the purpose of transmuting fission products [4]. In practice, one has to compromise with thermohydraulics-, corrosion- and material constraints, in order to design a realistic system. Hence we limit our investigations to lead/bismuth (Pb/Bi) cooled reactors using mono nitride fuels. Methods for managing liquid metal induced corrosion on cladding and construction material have been successfully applied in Russian Pb/Bi cooled submarine reactors, while it is doubtful whether the corresponding technology for pure lead will be applicable under reactor conditions. Mono nitride fuels have been manufactured and irradiated in the US, Russia and Japan, and feature higher linear ratings than oxide fuels while being less vulnerable to radiation damage than metallic fuels. The accelerator and spallation target of our system are yet unproven technologies, but are retained in order to maximize the fission product transmutation potential. The geometry of the sub critical core used in the present investigation was set up as follows: The spallation target was assumed to have a radius of 19.5 cm. A 0.5 cm thick target wall made out of 90% Fe and 10% Cr was adopted. Five cylindrical fuel zones with a height of one meter and 10 cm thickness contained 60% (volume) Pb/Bi coolant, 10% cladding and construction material of the same composition as the target wall, and 30% "fuel". The "fuel" consisted of ^{238}U and transuranics in mono nitride form (100% enriched ^{15}N). A TRU composition similar to that of 5% heavy atom burnup PWR spent fuel after 15 years of cooling

was adopted. The fraction on TRU versus U content was increased as function of radius for the threefold purpose of

- flattening the power density profile
- increasing the average neutron energy in the core for a better transmutation performance
- flattening the defect production profile in cladding and construction material.

Method of simulation

We used the continuous energy Monte Carlo code MCNP [7] for calculating multiplication eigenvalues, neutron fluxes and transmutation rates. Monte Carlo codes based on particle splitting techniques are especially useful for calculating neutron fluxes in materials with high neutron absorption cross sections, such as shielding blocks or, like in the present case, technetium rods. JEF 2.2 evaluated cross section data were processed with NJOY [8] to obtain pointwise cross section libraries suitable for MCNP at 900K (core materials) and 600K (target and reflector materials). The spallation neutron source was simulated as a volume source, with a spectrum calculated using HETC [9].

Results

First we made a reference calculation without any fission products in the reflector. The overall TRU enrichment was adjusted to obtain a neutron multiplication eigenvalue $k_\lambda = 0.96$. The fraction of TRU in the fuel zones was adjusted to obtain a flat power density profile with a ratio between maximal and minimal power density differing from unity by less than 15%. Folding the resulting neutron flux spectrum with the cross section of neutron capture in ^{99}Tc and ^{129}I, we obtained technetium and iodine transmutation rates as function of position in the reflector for concentrations small enough that self shielding effects would be negligible. Figure 1a) displays the results for technetium. As seen there is a clear maximum at 20 - 25 cm distance from the periphery of the core. This maximum is due to the combined effect of the magnitude of neutron flux declining with distance from the core, while the cross section increases as the neutron spectrum overlap with capture resonances becomes larger. In Figure 1b) the ratio of ^{129}I to ^{127}I capture rates is shown for equal concentrations of the isotopes. In the direct neighborhood of the core the probability of capture in ^{129}I is about half of that in ^{127}I. As the spectrum slows down the ratio declines to 0.3. Since isotope separation of iodine from spent fuel is hardly conceivable, we conclude that iodine should be place as close to the core as possible for efficient transmutation.

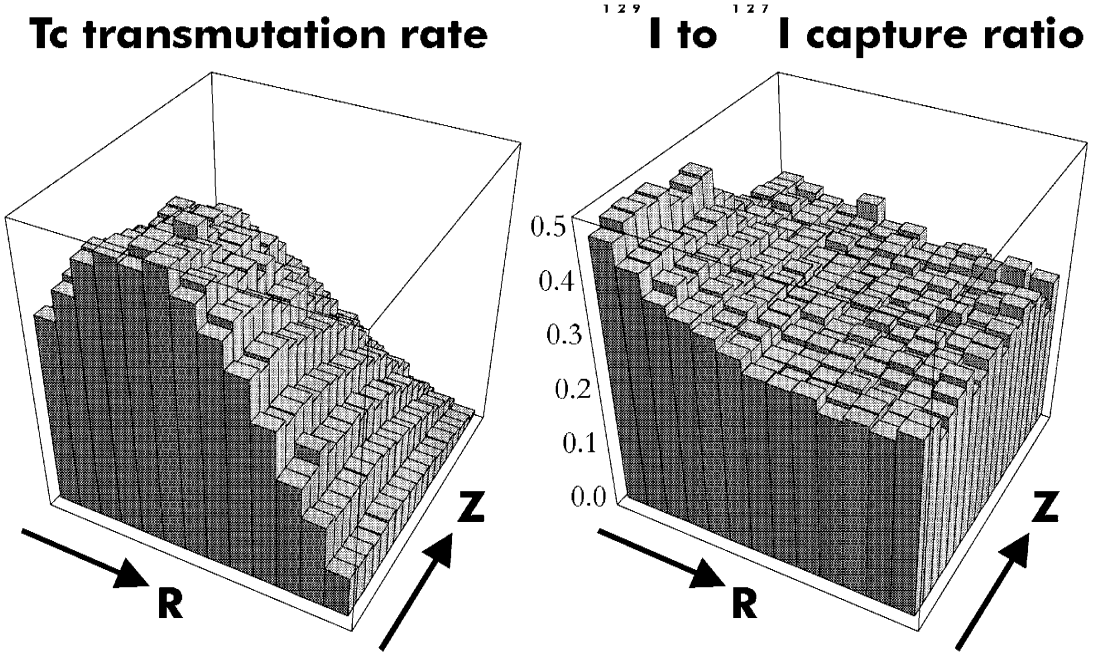

Figure 1: *The rate of ^{99}Tc neutron captures (in arbitrary units) in the reflector of the sub critical core here investigated (a). In (b) the ratio of ^{129}I to ^{127}I capture probabilities is shown. It is assumed that the concentration of the fission products is small enough for self shielding effects to be negligible. R ranges from 0 to 65 cm.*

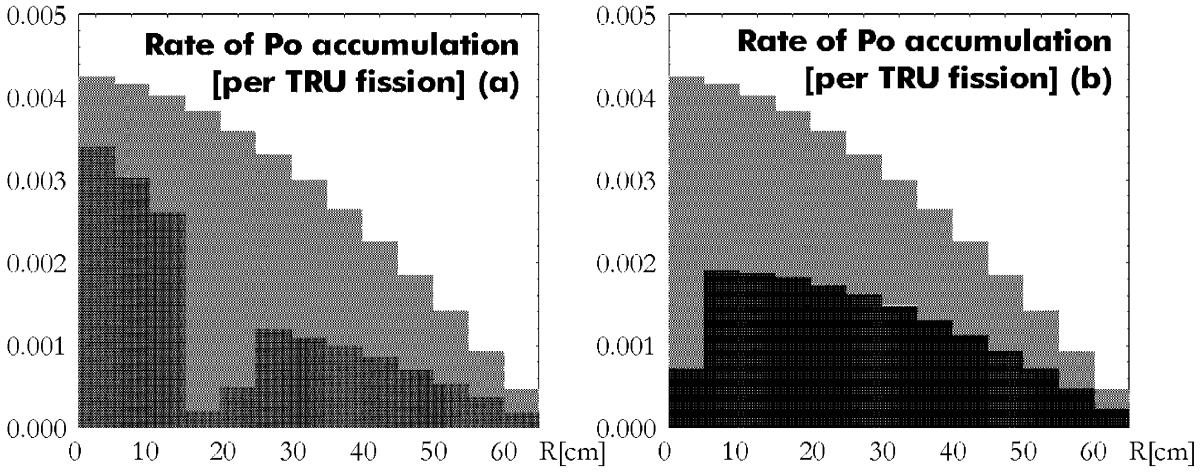

Figure 2: *The rate of polonium accumulation (per TRU fission) in the reflector of the sub critical core. In (a) 4000 kg ^{99}Tc was placed at a distance of 20 - 25 cm from the periphery of the core. In (b) 3100 kg was placed right at the periphery of the core. The rate of Po accumulation without any neutron absorber in the reflector is shown in the background.*

We also calculated the number of neutron captures in ^{209}Bi leading to the creation of ^{210}Po in the spallation target, the coolant and the reflector, in order to evaluate the impact of putting neutron absorbers in the reflector on global polonium accumulation.

Two calculations with ^{99}Tc added into the reflector were made. First we put 4000 kg of the substance in between 20 to 25 cm distance from the periphery of the core, corresponding to 60% of the volume in this region. The TRU content and distribution in the core was again adjusted to obtain $k_\lambda = 0.96$ and a flat power density profile. The number of fissions per source neutron increased slightly due to the higher concentration of TRU accompanied by the longer time needed to establish the eigenmode. It was found that 0.36 technetium nuclei were transmuted into ^{100}Ru, per fission taking place in the core. The number of polonium nuclei created in neutron captures on bismuth decreased from 0.067 to 0.047 globally, while the bismuth captures in the reflector were reduced from 0.036 to 0.016.

The bismuth capture rate as function of radius is depicted in Figure 2a) with a comparison of the rate for the technetium free reflector.

A less obvious effect was an increase in the neutron flux average energy in the periphery of the core, which can be ascribed to the fewer number of neutrons re-entering the core after slowing down in the reflector. This leads to a better transmutation efficiency of transuranic elements in the core, as the ratio between fission and capture increases with neutron energy for most of these nuclides.

Then we put 3100 kg of technetium right at the periphery of the core (0 - 5 cm distance), corresponding to 60% of the volume in this region. The number of transmuted technetium nuclei now became 0.48 per core fission, mainly due to the higher neutron flux available in the vicinity of the core. The bismuth capture rate as function of radius is depicted in Figure 2b). Polonium accumulation was not affected by moving the technetium closer to the core, but the average neutron flux energy in the core periphery was increased even further.

We also calculated the neutron energy at the point of absorption in technetium. The "capture energy" spectrum is displayed in Figure 3. Note that 98% of the captures take place at energies above 1 keV. This can to a large extent be ascribed to the effects of self shielding.

Finally, we evaluated the potential for transmuting ^{129}I by putting 230 kg of the isotope in direct connection to the core. Three tons of technetium was placed in the adjacent reflector zone. We assumed an iodine composition corresponding to a fission yield of 32% ^{127}I and 68% ^{129}I. Further, we assumed that the iodine was chemically confined as cesium iodide (natural Cs), having a comparatively high melting point (920 K). The total number of

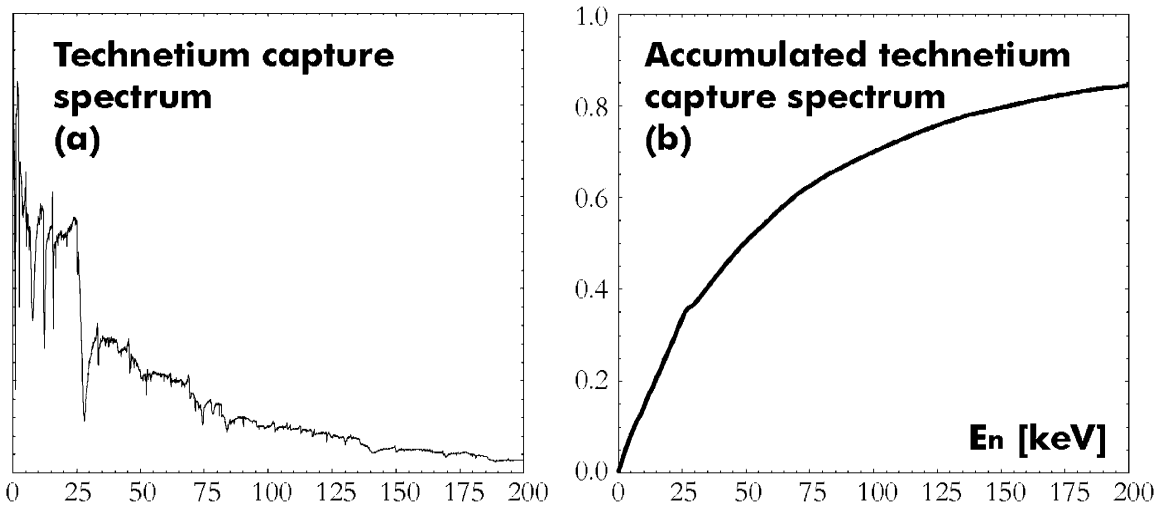

Figure 3: *Spectrum of neutron energies at the instant of technetium capture in the reflector, when having placed 4100 kg ^{99}Tc at R = 20 – 25 cm distance from the periphery of the core (a). In (b) the accumulated fraction of captures below a given threshold energy is given.*

transmuted fission products did not increase by much (from 0.48 to 0.50 per fission), including merely 0.024 ^{129}I nuclei. 0.060 neutrons per fissions were consumed by absorption in non toxic ^{127}I and ^{133}Cs, while the fraction of neutron captures in bismuth went down to 0.041 per fission. The transmutation efficiency of iodine appears to me much lower than that of technetium. Therefore, one should investigate if other chemical compounds of iodine may be better suited for a solid form at temperatures around 600 K. Possibly lead iodide (PbI_2) could be a candidate, if it may be produced from separated iodine at a sufficiently low cost.

Table 1 summarizes the characteristics of the four cases presented above. Note that k_s denotes the source neutron multiplication constant. For sub critical systems k_s may deviate significantly from the neutron multiplication eigenvalue k_λ, which was set to be the same ($k_\lambda = 0.96$) for all configurations.

Table 1: Summary of the characteristics of the sub critical cores investigated, assuming a total fission power of 800 MWth. All configurations had a multiplication eigenvalue equal to 0.96. The transmutation rate of ^{99}Tc (per core fission) is denoted by λ_{tr}(Tc), the ^{210}Po accumulation rate (per core fission) by λ_{tr}(Bi).

Case 1: No fission products in the reflector, $k_s = 0.953$, $\lambda_{tr}(Bi) = 0.67$

Core Zone	TRU fraction	E_n [keV]	E_{flux}[keV]	Neutron Flux [10^{15}/(cm^2 s)]	PowerDensity [W/cm^3]
1	0.100	124	390	9.69	516
2	0.115	134	407	8.70	522
3	0.135	145	436	7.97	557
4	0.160	155	466	7.12	584
5	0.200	138	465	5.88	599

Case 2: Tc at R = 20 – 25 cm, k_s = 0.954, λ_{tr}(Bi) = 0.47, λ_{tr}(Tc) = 0.36

Core Zone	TRU fraction	E_n [keV]	E_{flux}[keV]	Neutron Flux [10^{15}/(cm^2 s)]	Power Density [W/cm^3]
1	0.105	128	396	10.2	544
2	0.120	138	415	9.14	550
3	0.140	150	443	8.26	575
4	0.165	163	476	7.20	582
5	0.210	163	482	5.61	562

Case 3: Tc at R = 0 – 5 cm, k_s = 0.962, λ_{tr}(Bi) = 0.42, λ_{tr}(Tc) = 0.48

Core Zone	TRU fraction	E_n [keV]	E_{flux}[keV]	Neutron Flux [10^{15}/(cm^2 s)]	Power Density [W/cm^3]
1	0.115	132	406	12.2	583
2	0.130	145	429	11.0	588
3	0.150	159	460	9.80	598
4	0.175	175	494	8.11	573
5	0.235	188	510	5.73	519

Case 4: CsI at R = 0–5 cm, k_s = 0.957, λ_{tr}(Bi) = 0.41, λ_{tr}(Tc) = 0.41, λ_{tr}(^{129}I) = 0.41

Core Zone	TRU fraction	E_n [keV]	E_{flux}[keV]	Neutron Flux [10^{15}/(cm^2 s)]	Power Density [W/cm^3]
1	0.115	134	409	11.1	603
2	0.130	146	431	9.88	603
3	0.150	158	460	8.67	603
4	0.170	173	491	7.12	558
5	0.235	187	511	4.99	514

Conclusions

In the present investigation, we showed that for small concentrations of ^{99}Tc in the reflector of a Pb/Bi cooled sub-critical core fueled with TRU waste from a LWR, the maximal transmutation rate is obtained at a distance of 25 cm from the periphery of the core. For large concentrations (60% volume) the maximal transmutation rate is about 0.5 technetium nuclei per core fission, if the neutron absorber is placed right at the periphery of the core. As a beneficial side effect, the overall polonium accumulation is decreased by 40%. Further, the average neutron flux energy in the periphery of the core is increased by 10%, which yields a better transmutation efficiency of the TRU:s in that region.

As the relative fraction of technetium in spent light water reactor fuel is about 0.2 Tc nuclei per TRU nucleus (~6% per fission), all configurations here investigated are able to transmute LWR technetium at higher rates than that of their concomitant TRU destruction rates. The transmutation efficiency of iodine here found is slightly too small for keeping up with its production rate. However, as the present system utilizes less than half of the theoretical neutron surplus in a heavy metal cooled sub critical reactor, there will be room for improvements in the design, especially so with respect to choice of iodine compound.

Acknowledgments

Financial support from the Swedish Nuclear Fuel and Waste Management company (SKB), the Swedish Institute (SI) and the Center for Nuclear Technology (KTC) is gratefully acknowledged.

References

[1] M. Steinberg, G. Watsak and B. Manowitz, Neutron burning of Long Lived Fission Products for Waste Disposal, BNL-8558, Brookhaven National Laboratory (1964).

[2] T. Sasa et al, in Proceedings of the international conference on future nuclear systems, Global 97, 425 (1997).

[3] M. Salvatores et al, in Proceedings of the international conference on future nuclear systems, Global 97, 428 (1997).

[4] M. Salvatores et al, in Proceedings of the international conference on future nuclear systems, Global 97, 561 (1997).

[5] F. Venneri et al, Disposition of Nuclear Waste using Sub Critical Accelerator Driven Systems, LA-UR 98-985, Los Alamos National Laboratory (1998).

[6] C. Rubbia et al, Fast neutron incineration in the Energy Amplifier as alternative to geologic storage, CERN/LHC/97-01, CERN (1997).

[7] MCNP - A general Monte Carlo N-Particle transport code, version 4B, LA-12625-M. Editor J.F. Briesmeister, Los Alamos National Laboratory (1997).

[8] R.E. MacFarlane and D.W. Muir: The NJOY nuclear data processing system, versions 97-99, Los Alamos National Laboratory (1998).

[9] IAEA study on the neutronic potential of a modular fast spectrum for radiotoxic waste transmutation, editor I. Slessarev, CEA/Cadarache (1998).

APPENDIX 2

Neutronic Potential of a Modular Fast Spectrum ADS for Radiotoxic Waste Transmutation ADS-Benchmark (stage 2)

Kamil Tucek, Jan Wallenius & Waclaw Gudowski
Department of Nuclear & Reactor Physics
Royal Institute of Technology
100 44 Stockholm, Sweden

November 2, 1998

1. Introduction

Investigation of the transmutation potential of accelerator-driven systems is an essential part in the assessments of their capabilities to reduce the environmental and safety threats arising from long-term radiotoxicity of spent nuclear fuel as well as possible proliferation of nuclear materials.

In the present paper, a study of a fast spectrum sub-critical system with a nitride based fuel matrix is made. The investigations are performed for two types of fuel compositions: transuranics and minor actinides.

2. Calculation methodology

The Monte Carlo code MCNP (version 4b) [1] is used as the tool for neutronic transport simulations. Energy continuous cross-section files for individual nuclei were taken from the JEF2.2 data evaluation except for ^{56}Fe, ^{58}Fe and Pb nuclei retrieved from the ENDF/B-VI library and data for ground and isomeric states of ^{244}Am which were taken from the JENDL3.2 evaluation. The averaged fission product cross-section for ^{239}Pu was obtained from the FOSTER library. The cross-section data were processed by the NJOY code [2] in order to adjust for temperature dependencies, which were assumed to be 1200 K in the core region and 900 K in remaining parts of the reactor. The multiplication eigenvalue k_{eff} was found by running MCNP in KCODE mode where multiplication values yielded in consecutive neutron generations are averaged when asymptotic state is attained.

Effective one-group cross-sections and power distribution within the reactor core were obtained in MCNP fixed source calculation. These data were processed by an intermediate code to format the cross-section and input data for ORIGEN2 [3,4] which simulates burn-up. The emerging of actinides and fission products is modeled quasi-two-dimensionally with the core divided vertically into several slices where individual cross-section sets are calculated at BOL. The one-group cross-sections were supposed to remain virtually unchanged during the burn-up.

The source energy distribution for the neutronic and burn-up calculations was set up as given in the first stage of benchmark (HETC calculation of the spallation process), while for the sensitivity study of the external source neutron importance a quasi-mono-energetic neutron spectrum at 10 MeV (the first group of HETC spectrum), 2 MeV (the third group of HETC spectrum) as well as ^{239}Pu fission spectrum were used. Additionally, the spatial distribution of neutron velocities was assumed to be isotropic.

3. Results

3.1 Neutronic calculations

The first task in the benchmark was to adjust the core radius of the system in order to obtain multiplication eigenvalue k_{eff} at the level of 0.96. The calculation procedure consists of determination of multiplication eigenvalues for individual core radii, in the case of transuranic system varying from 38 *cm* up to 47 *cm* and in the interval $R_{core} \in < 50;130 > cm$ for the MA-fueled ADS.

For both systems – fueled by transuranics and minor actinides, calculated values of k_{eff} were fitted using the least-square method by polynomials of the third, respectively the fourth order in the later case. According to our calculations, the TRU-fueled system fulfils the condition $k_{eff} = 0.96$ at the radius of 43.59 *cm* while MA-fueled reactor at the radius of 92.42 *cm*.

3.2 Calculation of ADS power, critical masses and specific fuel inventories

The power of the system was calculated assuming average specific fission power density for nitride fuel as being equal to 600 MW/m^3. For the transuranic core with a volume of 0.4737 m^3 at BOL we obtain a fission power of the reactor equal to 284.2 MW_{th}. For the MA-fueled system, the core volume was determined to 2.3512 m^3 at BOL, which yields the total fission power 1410.7 MW_{th}, see Tables 1, 2.

As described in the benchmark propositions, the TRU fuel composition corresponds to equilibrium state while concentrations of nuclei in MA fuel are only near-equilibrium. Thus, the *critical mass* of the fuel could be determined at BOL as being 616.1 *kg* for TRU system and 3065 *kg* for MA-ADS. As for Specific Fuel Inventory (SFI) calculations, the value of $SFI = 2.168 \times 10^6$ kg/TW_{th} was obtained for TRU-fueled and $SFI = 2.172 \times 10^6$ kg/TW_{th} for MA-fueled systems when using recommended values of (TRU/MA)N+ZrN mixture density (9.2 g/cm^3) and average power density.

3.3 Calculations of burn-up and ^{99}Tc transmutation rates

As a further step, the burn-up calculations were performed for a burn-up interval of 100 days with a time step of 20 days. The transmutation rate of ^{99}Tc in the system was calculated by subtracting the amount of Tc in the LLFP blankets at EOL from that at BOL and normalizing per TW_{th} and *day*. For TRU-fueled system, we obtained $R_{Tc} = 695.1$ $kg/TW_{th}\,day$ while for MA-fueled reactor the value of R_{Tc} appeared to be somewhat lower (383.6 $kg/TW_{th}\,day$). On the other hand – regarding ^{99}Tc transmutation rates per reactor unit – a total amount of Tc transmuted in the MA-ADS is approximately 2.5 times higher than in transuranic system.

3.4 Neutron balance

The neutron balance was calculated for the whole ADS as well as the core region only. The *production* term describes the normalized production of neutrons by the external neutron source, fission and (n,2n) reactions while the *loss* term shows the normalized losses of neutrons in capture, fission, (n,xn) reactions, and in leakage. Thus, the expression *production by fission* points to the total number of neutrons released in fission rather than to the excess of such neutrons over the number absorbed in a fission as it is understood in classical reactor theory.

Table 1: Summary of the results for TRU-fueled ADS

R_{core}	P	M	SFI	R_{Tc}	*Neutron balance*							
[cm]	*[TW]*	*[kg]*	*[kg/TW]*	*[kg/TWday]*	*loss*				*production*			*Region*
TRU-fueled ADS					*capture*	*(n,xn)*	*fission*	*leakage*	*fission*	*(n,xn)*	*source*	
43.59	2.842E-4	616.1	2.168E+6	695.1	0.6661	0.0053	0.3175	0.0111	0.9582	0.0109	0.0309	*ADS*
					0.2105	0.0022	0.3299	0.4574	0.9956	0.0044	0	*Core*

Table 2: Summary of the results for MA-fueled ADS

R_{core}	P	M	SFI	R_{Tc}	*Neutron balance*							
[cm]	*[TW]*	*[kg]*	*[kg/TW]*	*[kg/TWday]*	*loss*				*production*			*Region*
MA-fueled ADS					*capture*	*(n,xn)*	*fission*	*leakage*	*fission*	*(n,xn)*	*source*	
92.42	1.411E-3	3065	2.172E+6	383.6	0.6897	0.0051	0.2945	0.0107	0.9578	0.0104	0.0318	*ADS*
					0.4674	0.0022	0.3060	0.2244	0.9956	0.0044	0	*Core*

3.5 Sensitivity study of the external source importance

Once the sub-critical reactor system relaxes to the asymptotic state, the criticality source in MCNP KCODE calculation well approximates the spatial and energetic distribution of neutron sources within the core as obtained from the solution of the eigenvalue problem of the Boltzmann neutron transport equation. Hence, the differences observed in our calculations of the core radii, and consequently total thermal powers and *critical masses* for different types of external neutron source spectra C1-C4 are only of statistical character, see Table 3.

The source multiplication coefficient k_{source} was obtained from the following formula:

$$k_{source} = 1 - \frac{k_0}{\nu_0}\frac{\bar{\nu}-1}{G_f}$$

where k_0 is the number of neutrons emerged from fissions induced by one external source neutron, ν_0 is the average neutron yield in such fissions, G_f is the overall gain of neutrons in the fission reactions normalized to one source neutron and $\bar{\nu}$ has customary sense of the averaged number of neutrons emitted per one fission. The calculated multiplication coefficients k_{source} for individual source types showed to be quite the same when considering their 99% confidence intervals.

The external source importance was according to the proposal from CEA defined as:

$$\phi^* = \bar{\nu}\frac{1-k_{eff}}{k_{eff}}\frac{P}{S_0}$$

where P is the fission power of the reactor (fissions/s) and S_0 is the external neutron source strength (neutrons/s). Since values of $\bar{\nu}$ appeared to be virtually independent on the neutron spectrum type and system's multiplication eigenvalue k_{eff} is maintained constant ($k_{eff} = 0.96$), the external source importance depends only on the fission density in the core (i.e. number of fissions per source particle).

In the case of source type C2, which corresponds to the quasi-mono-energetic neutron spectrum at 10MeV, a single source neutron appears to induce significantly higher number of fissions than in the other cases. This can be ascribed to the enhanced production of secondary neutrons from (n,xn) reactions in the lead of the target (approx. 0.3 neutrons per source particle). It decreases the external source strength necessary to maintain a constant total thermal power.

Table 3: Results for sensitivity study of the external source neutron importance, TRU-fueled ADS

Type of external spectrum	R_{core} [cm]	P [TW]	M [kg]	SFI [kg/TW]	k_{source}	*Source Neutron Importance*
C1	43.593	2.8422E-4	616.15	2.168E+6	0.96327	1.351
C2	43.592	2.8420E-4	616.11	2.168E+6	0.96366	1.939
C3	43.573	2.8391E-4	615.48	2.168E+6	0.96395	1.296
C4	43.581	2.8404E-4	615.75	2.168E+6	0.96403	1.242

4. Conclusions

Performing the eigenvalue calculation for TRU- and MA-fueled sub-critical ADSs with different core radii, we determined the values of R_{core} corresponding to the multiplication eigenvalue $k_{eff} = 0.96$. Consequently, the fission powers of the systems, *critical masses*, and Specific Fuel Inventories were calculated using proposed value of the average specific power density. The ^{99}Tc transmutation rates in the transuranic and minor actinide systems were assessed at the burn-up calculations within the interval of 100 days. In the TRU-fueled system roughly twice as much ^{99}Tc transmutations per power and time unit occur in comparison to the MA-fueled ADS. Nevertheless, the total amount of transmuted ^{99}Tc per time unit is about 270% higher in minor actinide system than in TRU-ADS. The sensitivity of the external neutron source was evaluated only for the transuranic system. A higher value of the source importance corresponds to a higher number of fissions caused by each individual source neutron, leading to a lower strength of the external neutron source necessary for maintaining a constant fission power.

Bibliography

[1] Editor: Judith F. Briesmeister. *MCNP - A General Monte Carlo N-Particle Transport Code, Version 4B, LA-12625-M*. Los Alamos National Laboratory, New Mexico, USA, March 1997.

[2] Editors: R.E.MacFarlane and D.W.Muir. *The NJOY Nuclear Data Processing System, Version 91, LA-12740-M*. Los Alamos National Laboratory, New Mexico, USA, 1994.

[3] A.G.Croff. *A User's Manual for the ORIGEN2 Computer Code*. Chemical Technology Division, Oak Ridge National Laboratory, Oak Ridge, Tennessee, USA, July 1980.

[4] A.G.Croff. ORIGEN2: A Versatile Computer Code for Calculating the Nuclide Compositions and Characterictics of Nuclear Material. *Nuclear Technology*, 62:335-352, September 1983.

APPENDIX 3

RELIABILITY ASSESSMENT OF THE LANSCE ACCELERATOR SYSTEM

Marcus Eriksson
Royal Institute of Technology, Sweden

Christopher Piaszczyk
Northrop Grumman Corporation, USA

Abstract

This paper describes the reliability analysis of the accelerator facility at Los Alamos Neutron Science Center (LANSCE)[1]. The goal of the analysis is to present beam failure statistics of LANSCE and identify the root cause of a beam failure. Beam trips and failure causes are assembled using operational data records, accelerator logbook and beam monitor data. Mean Time Between Failure and Mean Down Time estimates are obtained for typical accelerator components. The results are useful in accelerator reliability modelling and identifying development issues in high power accelerators.

Introduction

The reliability and availability of the accelerator in an accelerator driven system is an important issue. New applications for high power proton accelerators such as the production and destruction of radioactive elements demand high availability, reliability and maintainability. Persistant beam power fluctuations have a negative influence on a hybrid system. In order to estimate and improve the availability and reliability of future accelerator designs, data from existing accelerators are being analyzed. The accelerator facility at Los Alamos Neutron Science Center (LANSCE) is the most powerful linear proton accelerator in the world. The accelerator offers enough operating history to supply meaningful reliability data.

The objective of the present data collection and analysis effort is to understand the behavior of existing operating accelerator facilities so that better, more reliable systems can be designed and built in the future. Previous work has identified the current state of the art lacking in the area of reliability database information for components typically used in rf accelerator systems, such as rf stations, rf drives, rf transport, cooling, vacuum systems, magnets, and magnet power supplies. Thus, while it is possible to use the reliability theory to model accelerator systems, the input data currently available for such analyses lacks credibility. This led to the initiation of an effort of data collection and analysis of which this study is one of the tasks. The present work examines the data set of failure events for the LANSCE 800 MeV accelerator facility.

The LANSCE Accelerator Facility

The LANSCE accelerator delivers two proton beams at 800 MeV: the H+ and the H- beam. The H+ beam may deliver 1.25 mA current (routine operation is at 1 mA) and the H- beam delivers 70 μA. Each injector system includes a 750 keV Cockcroft-Walton type generator. Both ions are accelerated simultaneously in one and the same structure. After acceleration the H+ and H- beams are separated. The H- beam is injected into a Proton Storage Ring for accumulation and delivery to the neutron scattering center or weapons neutron reseach.

Beamline	Energy	Current	Injector (High Voltage Generator)	Proton Storage Ring
H+ beam	800 MeV	1.25 mA	Cockcroft-Walton	No
H- beam	800 MeV	70 μA	Cockcroft-Walton	Yes

Table 1. The LANSCE accelerator delivers two ion beams

The low energy section of the accelerator is an Alvarez Drift Tube Linac (DTL). The drift tube linac accelerate the protons from 750 keV to 100 MeV. The high energy section is a Side Coupled Linac (SCL). The SCL may accelerate protons up to 800 MeV. Different rf systems are used for the drift tube linac and for the side coupled linac. In the DTL, triode power tubes are used for the generation of rf power while in the side coupled linac klystrons are used. The rf system for the DTL is sometimes referred to as the 201 system since the rf frequency in the drift tube linac is 201.25 MHz. The rf system for the SCL is called the 805 rf system since the rf frequency is 805 MHz.

Linac Section	Energy region	RF Power	RF Frequency
Drift Tube Linac	750 keV-100 MeV	Triode power tubes	201.25 MHz
Side Coupled Linac	100 MeV-800 MeV	Klystrons	805 MHz

Table 2. Different rf systems are used in the DTL and the SCL

Ahead of time a beam schedule has been organized with respect to time-sharing between experiments, beam intensity, and beam energy. An overall schedule of commissioned beam time for each beamline is set out. Scheduled operation at LANSCE is divided into run cycles. During scheduled operation, the accelerator is operated almost 24 hours per day for an entire run cycle with only a few scheduled breaks. A run cycle is maintained for approximately 5-6 weeks (800-1000 hours). A large fraction of the year the accelerator is not scheduled due to maintenance activities. Scheduled operation is usually in the region of 2000-3000 hours per year, which is about 30 % of the year. In reliability assessment of LANSCE the total scheduled beam time is an important factor **-beam trips are only analyzed if they occur within scheduled accelerator operation.**

Input Data

Beam delivery is measured by current monitors near the targets. If the beam current for some reason is below half the scheduled current the beam is considered as interrupted. This event/trip generates loss of scheduled beam time, commonly called down time. The operator assigns a failure cause, or down time assignment, to each trip. The down time assignment is recorded in the logbook. The failures and down time assignments are also entered into operational data records. Separate data records are maintained for each beam line or target area. In this investigation beam trips associated with the H+ beam and the H- beam are analyzed. The records obtained cover run cycles 71 through 76, over the period 1996-97.

The first, and most time intensive task of this effort was collecting the input data. Thanks to the cooperation of the LANSCE Operations Group, a large amount of data was collected. This included the:

1) Operational data records
2) Central Control Room Logbook
3) Operations Shift Supervisor's Summary Reports
4) Beam Monitor data for 1997

Overall LANSCE Reliability

In this section, the distribution of beam trips and down time for the entire LANSCE accelerator facility is presented. The analysis considers scheduled accelerator operation of the H+ beam for 1997 and of the H- beam for 1996 and 1997. The H+ and the H- beams are investigated separately. All

calculations are based on operational data records or indirectly accelerator logbook data. A histogram of beam trips that occur in the H+ and the H- beam is presented in figure 1.

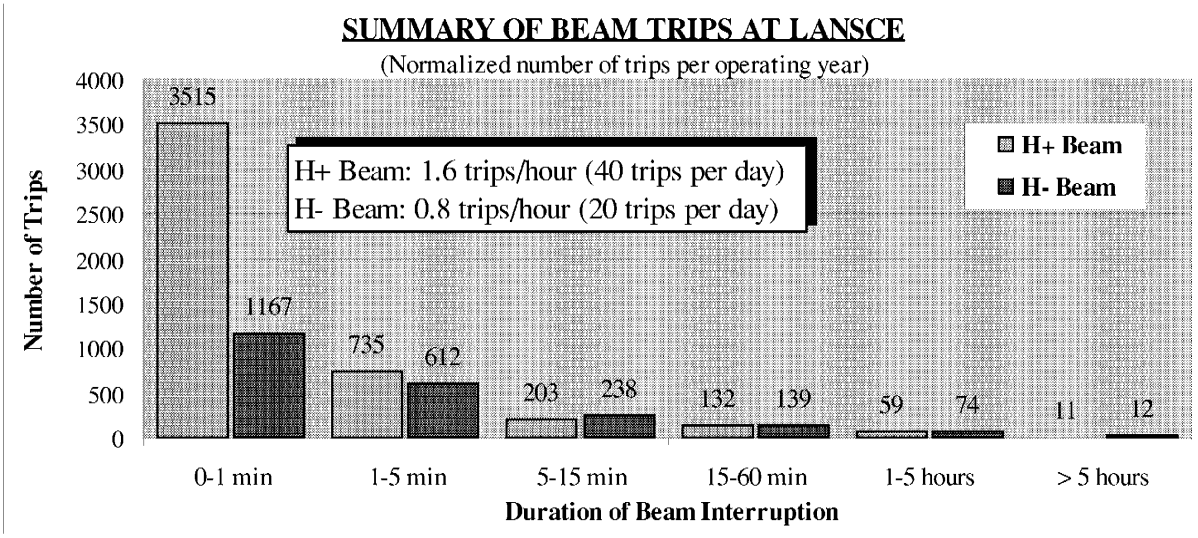

Figure 1. Beam failure statistics of the LANSCE accelerator facility

From figure 1 it is obvious that the H+ beam is exposed to many beam trips with short duration. 76% of all trips in the H+ beam are 0-1 minute long. When comparing the total number of trips in the H+ and H- beams, the conclusion is that twice as many trips occur in H+ beam. When operating, the H+ beam is exposed to 1.6 trips/hour and the H- beam 0.8 trips/hour. The main reason is the larger number of short trips in the H+ beam. For long down times (> 5 minutes), almost the same number of trips occur in the H+ and the H- beams. This makes sense since both beamlines utilize, for most of their length, the same accelerating structure. At a closer look, a slightly larger number of long trips occur in the H- beam. The reason is that the H- beamline is more complex. It includes the Proton Storage Ring and hence more components are subject to failure.

In figure 2, the most frequent causes for beam failure and beam downtime in the H+ beam are presented. Two columns are displayed for each individual system. The leftmost column in each system shows the fraction of total number of H+ trips the system is responsible for. The rightmost column shows the equivalent fraction of total downtime. It is a good thing to separate trips and downtime. Trips affect beam stability and produce power fluctuations. Downtime has a negative influence on the overall beam availability.

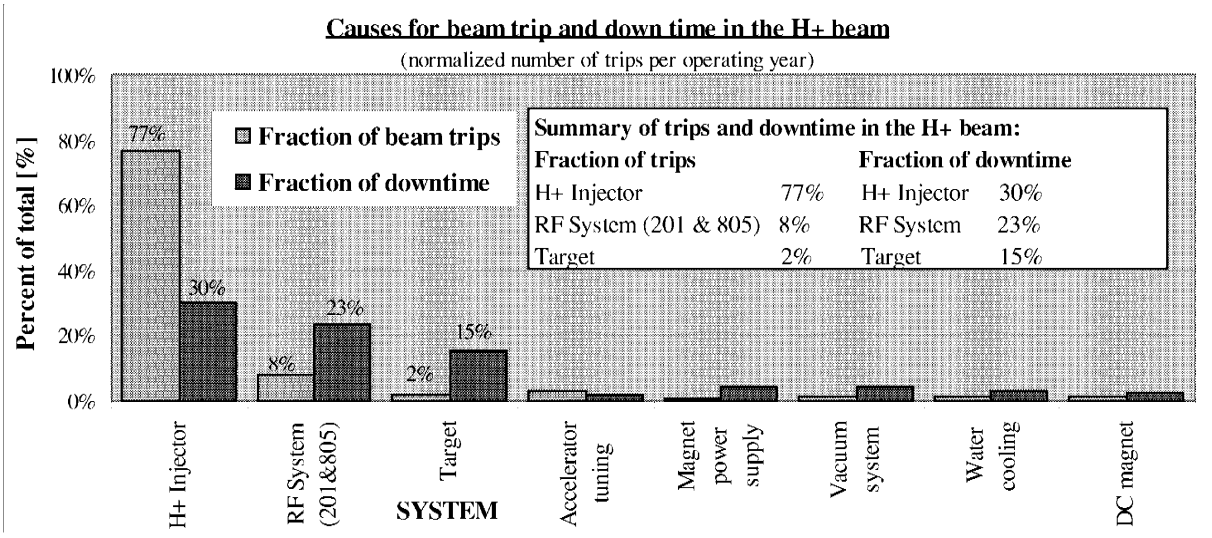

Figure 2. Systems responsible for trips and downtime in the H+ beam

From figure 2, it is obvious that an injector failure is the most frequent cause for beam trip. In the H+ beam 77% of all trips are caused by a failure in the H+ injector. The characteristic of the injector failure is the interruption length. It is usually shorter than 1 minute,often in the order of 15-20 seconds, the time it takes to reset the trip and re-energize the Cockcroft-Walton generator. An injector failure is usually caused by electric breakdown in the high voltage column. Since a typical injector failure is short, the injector is not as dominating when it comes to the generation of downtime. While the H+ injector is responsible for 77% of the trips it is "only" responsible for 30% of the downtime. In other words, the injector is the main reason for beam current fluctuations but it has a significantly smaller influence on the overall beam availability. The rf system, including the rf system for the DTL and the SCL, is generating 8% of the trips but is accountable for 23% of the downtime. Hence, a failure in the rf system usually results in a long downtime (> 5 minutes).

In figure 3, historical data on overall beam availability and beam schedule for the years 1979-97 is presented [2]. The line graph represents beam availability and the column bars represent the scheduled beamtime. It is important to remember that the availability only measures the availability of the accelerator during scheduled operation. A common misunderstanding is that the availability of the machine gives the year round availability.

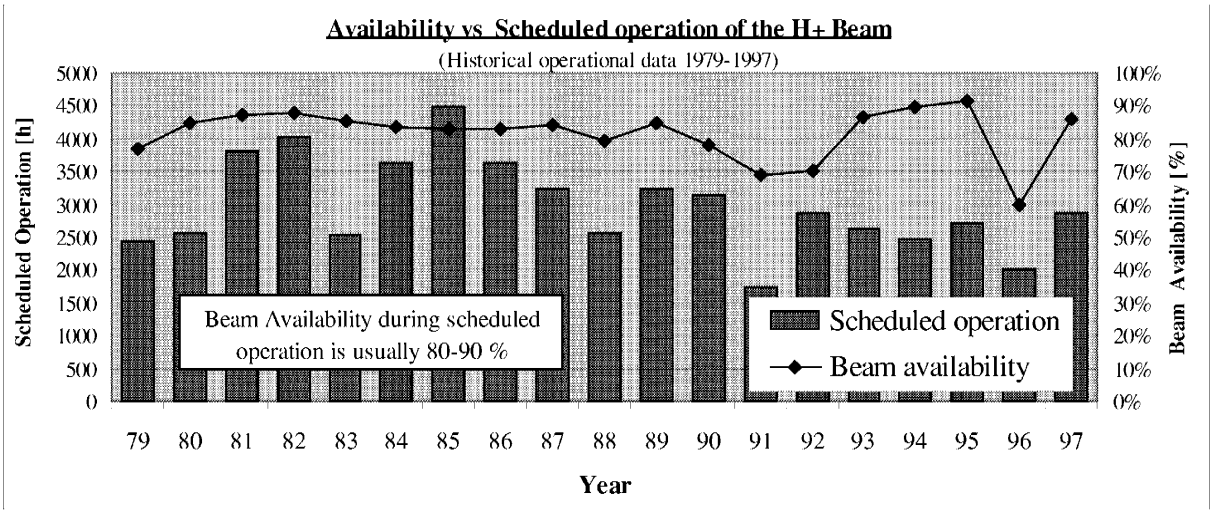

Figure 3. Historical availability and scheduled beamtime of the H+ beam [2]

Figure 3 is interesting in that sense it shows the relation between beam availability and the length of the operating period. Since a short scheduling period is usually followed by a longer maintenance period figure 3 also gives information on the affect of accelerator maintence on overall availability. When examining figure 3, the conclusion is that **the scheduled beamtime seems to have little influence on the availability**. It means that a long schedule does not have to imply lower beam availability. This is not all true but one obvious example occured in 1985. In 1985, the longest schedule ever was practiced. The accelerator was commissioned for 4500 hours (50% of the year) and it operated with normal availability (83%). In some years the availability actually drops when the accelerator is operated for less time! In 1996, the availability experienced a decline due to a single water leak in one of the targets, otherwise the standard availability of LANSCE is in the region of 80-90%. This level of availability is similar to the availability experienced in other accelerator facilities.

Analysis of beam current

Previous calculations and diagrams presented in this paper were all based on data originating from the accelerator logbook. Similar beam reliability analysis is performed for data orginating from beam current monitors. The H+ beam current has been analyzed during scheduled operation of 1997. The beam current at the end of the H+ beamline is inspected and interruptions are registered. A total of 163.000 beam current recordings are included in the analysis. The current analysis will verify previous results and it will present the "true" beam performance. When analyzing beam current data it is not possible to investigate the failure cause. Results of the beam current analysis are presented in figure 4. The histogram includes the total number of beam trips detected in the beam current and the corresponding down time. For comparison, the total number of trips registered in the logbook during the same time period are also included in the histogram.

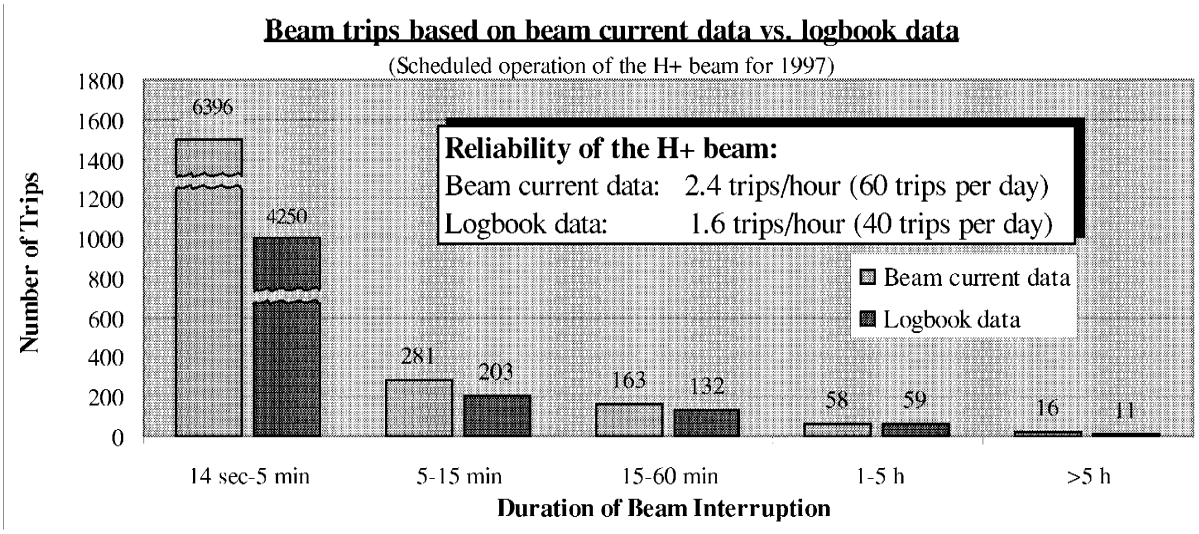

Figure 4. Reliability of the H+ beam at LANSCE

The trips occured during scheduled operation of the H+ beam for 1997. When analyzing the beam current a total of 6914 beam trips are detected. This number is larger than the number of trips recorded in the logbook (4655 trips) under the same period of time. From figure 4 it is clear that the main reason is that a large number of short interruptions (15-20 seconds) are detected in the beam current which are not included in the logbook. This is also confirmed by operating personnel. For example, in difficult periods when the injector is tripping frequently all short beam trips are not recorded in the logbook, instead comments like "continous arcing in the injector column" are used.

For trips with long downtime (>5 minutes) it is remarkable how well the results agree even though the underlying data origins from two completely different sources. That is a strong evidence for the correctness of the results from both analyses. When analyzing the beam current it is also evident that practically no interruptions with downtime shorter than 10 seconds occur. In other words, if an interruption occurs it is likely it will last for at least 10 seconds.

Reliability of subsystems & components

In this section the reliability of major LANSCE subsystems and components are investigated. A first cut analysis of the available LANSCE data is performed. Mean Time Between Failure (MTBF) and Mean Down Time (MDT) for individual subsystems are studied to obtain input data for accelerator reliability modelling (RAMI). Individual failures are thoroughly investigated with the help of logbooks, operational reports, operators, maintenance personnel. In case the cause of a trips is uncertain, experts in particular field are consulted to correctly classify the event. The aim is to detect the root cause, down to components level, of each failure. For this purpose, the raw data is divided into categories corresponding to individual subsystems and subsequently estimates of failure and repair rates are obtained. These categories are listed in table 2.

MAIN SYSTEM	SUBSYSTEMS		
805 RF	Klystron assembly High Voltage system 805 Tank	Phase and Amplitude Control Resonance Control Module Control	Other Unknown
DC Magnets	Magnet Hardware Interlocks	Water cooling	Vacuum
Magnet Power Supplies	Electronics Capacitors	Transformers Water cooling	Interlocks Unknown
Pulsed Power	Harmonic Buncher Deflector	Chopper	Kicker
Water System	Water Pump Other	Piping	Unknown
Vacuum System	Ion Pump	Piping	Unknown

Table 2. Classification of subsystems

Failures corresponding to each subsystem are merged and classified into individual databases. In table 3, an illustration of the database format for failures in the Klystron Assembly of the 805 RF System is presented. Similar databases are compiled for each subsystem. The database contain trips that affect both the H+ and the H- beams. Failures are only recorded if they occur within scheduled operation.

DURATION OF BEAM INTERRUPTION			LOCATION OF FAILURE			CAUSE OF FAILURE	
Date & Time of Outage	Date & Time of restoration	Down Time [h:min]	Area	System	Subsystem	Component failure or other reason	Comment
Klystron Assembly							
11/01/96 02:09	11/01/96 02:29	0:20	LINAC	805	Klystron	Flow switch	Module 21 Klystron water not okay. Mechanically agitated flow switch and it made up.
11/23/96 09:43	11/23/96 09:56	0:13	LINAC	805	Klystron	Water flow	Sector D off. Module 21 klystron water flow trip. The klystron magnet supply valve has been opened 1/8 of a turn.
11/23/96 23:17	11/23/96 23:32	0:15	LINAC	805	Klystron	Water flow	Module 21 klystron water flow trip
03/17/97 07:25	03/17/97 07:40	0:15	LINAC	805	Klystron	Ion Pump	Module 46 (Sector H) Klystron ion pump supply failed. It was replaced.
05/24/97 07:24	05/24/97 13:14	5:50	LINAC	805	Klystron	Klystron	Module 36 Main Amplitude crowbar. Sector F tripped a second time and the fire alarm went off. Acrid smell from the capacitor room. Module 36 klystron was replaced.

Table 3. Illustration of final database format

The database is for practical reasons divided into three major sections: One section deals with the Duration of the Interruption. It contains the date and time of the beam outage and restoration. It also includes the Down Time of each interruption. The second section considers the Location of the Failure. The Area defines the geographical location of the failure [3]. The System and Subsystem columns specify in what System and Subsystem the failure is located. The third section gives detailed information on the Cause of the Failure. The cause may be a component failure that needs replacement, a bad condition such as a water flow problem or an adjustment failure that needs to be tuned. In the comment column, extra text has been added to explain the failure.

The main objective of the analyses is to obtain estimates for the MTBF and MDT for typical accelerator components, such as RF amplifiers, HV power supplies, magnets, magnet power supplies, vacuum system components, or water cooling components. For illustration the mean down time estimate as a function of time for the magnet power supplies is presented in figure 5. Each dot marks a failure in the magnet power supply. Spaces in between dots is the time between failure. The diagram shows the Mean Down Time estimate at a certain number of failures. The final Mean Down Time estimate for the magnet power supplies is obtained at the last failure in the diagram.

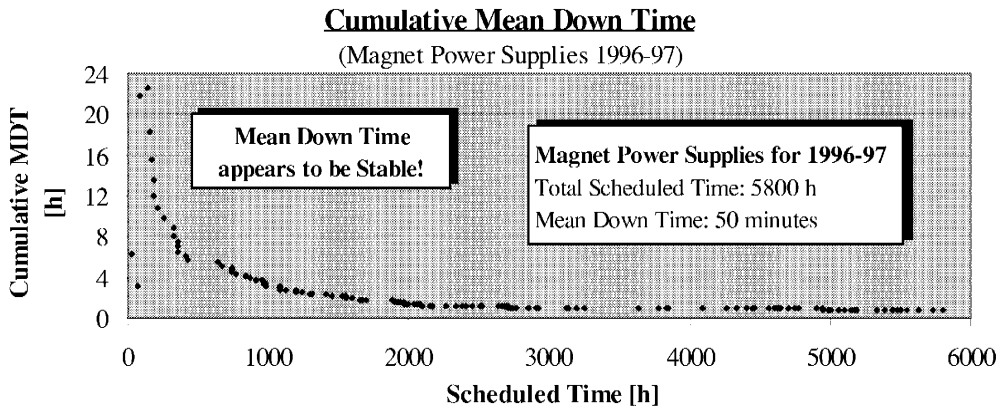

Figure 5. Cumulative Mean Down Time for Magnet Power Supplies

One indication of sufficient number of entries in the data set is the asymptotic behavior of the statistical estimators for the desired quantities, such as the Cumulative Mean Downtime which is calculated as the ratio of the cumulative downtime to the cumulative number of events as shown in figure 5. The conclusion in this case is that further data collection is not necessary, Mean Down Time estimate appears to be stable at approximately 50 minutes. A similar plot is made for the cumulative Mean Time Between Failure in figure 6.

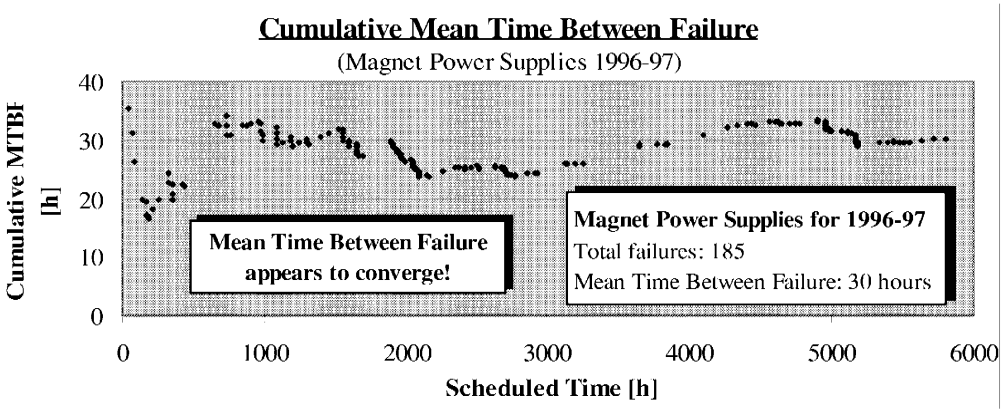

Figure 6. Cumulative Mean Time Between Failure for a single Magnet Power Supply

Cumulative Mean Time Between Failure is calculated as the ratio of the cumulative number of failures to the cumulative up time (scheduled time - downtime). As illustrated in figure 6, the MTBF behavior for the magnet power supplies is not as smooth as for the cumulative downtime but it appears to converge somewhere in the region of 30 h. With 278 magnet power supplies total in the system, the MTBF estimate for an individual magnet power supply is 8445 hours, assuming that all supplies have the same failure rate and can be treated as a series system of independent power supplies.

The results obtained via similar analyses for the other subsystems at LANSCE are summarized in table 4.

RESULTS OF RELIABILITY STUDY AT LANSCE				
Main System	**Subsystem**	**MDT** [h:mm]	**MTBF for all devices** [h]	**MTBF for a single device** [h]
805 RF	Klystron Assembly	0:44	262	11560
	High Voltage System	0:18	137	960
DC Magnets		0:53	290	232280
Magnet Power Supplies		0:50	30	8445
Pulsed Power	Harmonic Buncher	0:09	44	44
	Chopper magnet	0:08	291	291
	Deflector magnet	0:10	342	684
	Kicker magnet	1:58	185	557
Water System		1:20	120	
	Water pump	0:29	245	29506
Vacuum System		0:48	77	
	Ion pump	0:29	101	25308

Table 4. Some results of the reliability investigation of subsystems and components

The MTBF for the klystron assembly calculated from the raw data corresponds to the entire 805 RF system consisting of 44 klystron assemblies. An estimate of the MTBF for an individual klystron assembly was obtained by multiplying this value by 44 as 11560 hours. This value is not unreasonable when compared with the 20-50,000 hours commonly quoted for the typical klystron tube by itself. A total of 800 dc magnets exist in the LANSCE facility. MTBF for a single magnet is 232280 hours (≈26 years). The dc magnets at LANSCE are very reliable. This is also confirmed by maintenance personnel at LANSCE. 50% of the magnet failures are water cooling problems inside the magnet. The most frequent failure cause in a magnet power supply is malfunctioning electronic equipment. Most of the power supplies at LANSCE are controlled by manual electronics. Modern power supplies are computer controlled and proves to be much more reliable. MDT for a water pump is 29 minutes and MTBF is 29500 hours (≈3 years). MDT for an ion pump is 29 minutes and MTBF is 25300 hours (≈3 years).

Failure analysis

Analysis of failure causes is performed for all major systems. In this section the failure analysis of the rf system is illustrated. In figure 7, the distribution of trips in the rf system is presented. In figure 8, on a deeper level, the distribution of trips in the klystron assembly is presented.

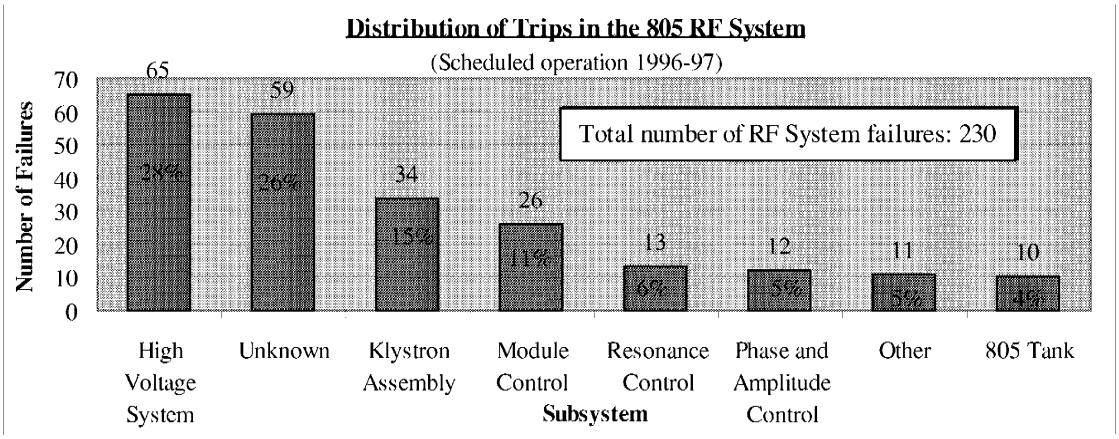

Figure 7. Distribution of trips in the 805 rf system

All subsystems of the 805 rf system are represented in figure 7. The High Voltage System causes many short interruptions. Usually the High Voltage system causes phase or amplitude disturbances to the beam. 26% of the failures in the rf system are unknown. Sometimes when a failure occurs in the rf system it is not possible to point out any specific subsystem (but it is known that the failure occured in the rf system!). 15% of the failures in the rf system are caused by the klystron assembly. In figure 8, typical failure causes in the klystron assembly are presented.

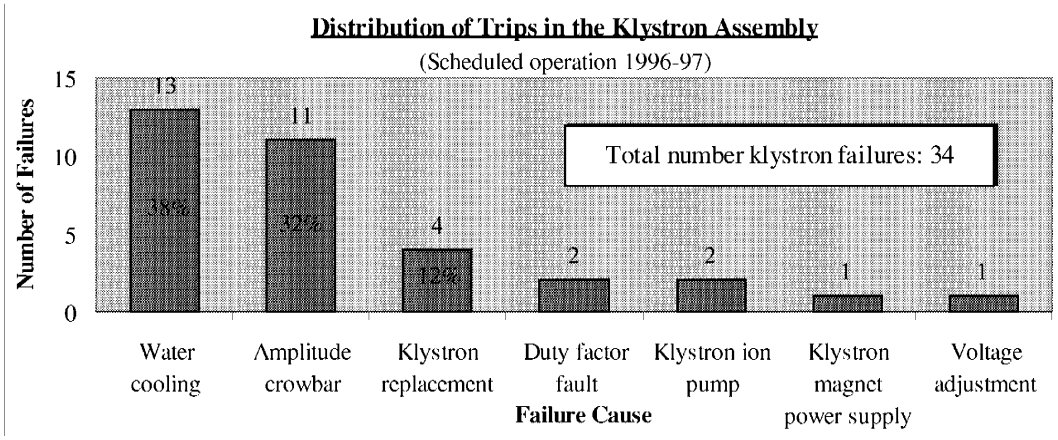

Figure 8. Failure causes in the Klystron Assembly

The klystron assembly includes some other components beside the klystron tube, for example an ion pump, a klystron magnet etc. 38% of all failures in the klystron assembly are water cooling problems and 32% are amplitude crowbars. Amplitude crowbars are usually electric sparking in the klystron tube or switchtube (and this may be due to an old switchtube). Most of the downtime occurs when klystron replacement is necessary. During scheduled operation of 1996-97, four klystron replacements occurred.

Conclusions

Operational statistics of the powerful 1.25 mA H+ beam at LANSCE has been obtained using the accelerator logbook and beam monitor data. When the beam current is inspected over a long period of time (2800 hours), on average 2.4 trips/hour or 60 trips per day are registered. Approximately 75% of all trips are 0-1 minute long. The typical down time of a beam trip is 15-20 seconds.

In the overall reliability balance of the entire LANSCE accelerator, the injector is responsible for most of the trip events. The injector is accountable for 77 % of all trips in the H+ beam. The injector is primarily generating short trips. For long down times (>5 min) the rf system is the largest producer of trips. Upgrading the injector will result in a more stable beam with less interruptions, especially short ones. Upgrading the rf system will result in a better beam availability.

In summary, as a result of the investigation of individual systems, estimates for both MTBF and MDT were obtained for several typical accelerator components: DC magnet power supplies, DC magnets, klystron assemblies, HV power supplies, vacuum system, and water system. The results will be useful in developing preliminary estimates for reliability, availability, and maintainability of high power accelerator systems planned in the future. However, before we can fully trust them, they have to be corroborated through comparison with statistics obtained from other facilities. The impact of maintenance activities outside of the scheduled production time needs to be tracked down and included in the estimates as well.

Aknowledgement

The generous assistance of many LANSCE Operations Personnel in performing this work is greatly appreciated. Special thanks are due to Michael Oothoudt and Tim Callaway of LANSCE-6. Also, special thanks are due to Stan Cohen of LANSCE-6 for valuable help with magnet power supplies and John Lyles of LANSCE-5 for help with RF Technology.

References

[1] Marcus Eriksson, "Reliability Assessment of the LANSCE Accelerator System", M.Sc. thesis at the Royal Institute of Technology, Stockholm, 1998.

[2] Olin van Dyck, "LAMPF Reliability History and Program", International Conference on Accelerator-driven Transmutation Technologies and Applications, Las Vegas, 1994.

[3] Michael Oothoudt, "Availability for cycle 75", LANSCE-6 Technical Report LANSCE-6-97-51-TR, 1997

APPENDIX 4

RELIABILITY ASSESSMENT OF THE LANSCE ACCELERATOR SYSTEM

BY

MARCUS ERIKSSON

STOCKHOLM 1998

THE ROYAL INSTITUTE OF TECHNOLOGY

NUCLEAR & REACTOR PHYSICS

RELIABILITY ASSESSMENT OF THE LANSCE ACCELERATOR SYSTEM

BY

MARCUS ERIKSSON

M.SC. THESIS AT THE
ROYAL INSTITUTE OF TECHNOLOGY

Examiner: Waclaw Gudowski
Supervisor: Christopher Piaszczyk, Northrop Grumman Corp.

The thesis is availabile at the Dep. of Nuclear & Reactor Physics and the University Library of the Royal Institute of Technology

DEP. NUCLEAR & REACTOR PHYSICS
ROYAL INSTITUTE OF TECHNOLOGY
S-100 44 Stockholm, Sweden

Preface

This report is a M.Sc Thesis prepared at the Department of Nuclear and Reactor Physics at the Royal Institute of Technology, Stockholm. For the most time the analyses were conducted at Los Alamos National Laboratory, USA.

The objective is to present the reliability and availability of the high current linear proton accelerator at LANSCE (Los Alamos Neutron Science Center). The reliability and the underlying cause of failure in major accelerator systems and components are investigated. The distribution of beam failures and down time for 6 consecutive run cycles (1996-97 accelerator operation) are analyzed. The investigation offers the opportunity to evaluate power fluctuations and long-term reliability and availability of high power linear accelerators.

The analysis was initiated with the intention to examine the reliability and availability of an accelerator for the purpose of transmutation of nuclear waste. It may as well be valuable in availability assessment of similar accelerators for use in other applications. Results may also be helpful in development of a reliability and availability model of high power accelerator systems.

Abstract

High availability is of vital importance for future high power proton accelerator applications such as the Accelerator driven Transmutation of Waste (ATW). The ATW accelerator demand excellent year round availability in order to match the desired transmutation performance. In order to estimate the availability and reliability of accelerator designs, data from existing accelerators are analyzed. The Los Alamos Neutron Science Center (LANSCE) is an accelerator facility with enough operating history to supply meaningful reliability data. The report describes the data collection and analysis effort of the LANSCE accelerator operational data which was initiated to supply the accelerator reliability models with credible input data. A preliminary database of beam trips was assembled using operational data records, Central Control Room Logbook, and Operations Shift Supervisors' Summary Reports covering 1996-97. The events were classified according to the underlying cause into categories corresponding to typical accelerator subsystems. The ambition has been to identify the root cause of the down times. Mean Time Between Failures (MTBF) and Mean Down Time (MDT) estimates were obtained for magnets, RF stations, power supplies, etc. The results are useful for identifying development issues in high power accelerators.

Persistent power fluctuations in the accelerator may effect beam window characteristics and have a negative influence on a hybrid system. At LANSCE, beam delivery is frequently measured by current monitors near the target. The thesis investigates the beam current history and a better insight into power fluctuations of the LANSCE accelerator is achieved.

Table of Contents

1 Introduction

One of the most important specifications on an ion accelerator for transmutation of waste is the overall beam availability and reliability. Such large accelerators are major capital investments and the availability determines the return of investment. A year round availability of 90% is necessary to match the desired transmutation performance. High component reliability is also essential to minimize power fluctuations, radiation hazards, and activation of structure material. Power fluctuations are particularly important in applications for transmutation since the accelerator is coupled with a subcritical reactor. In a hybrid system, short beam trips creates a loss of heat generation and causes thermal shock to the structure material and fuel rods.

The LANSCE accelerator is the world's most powerful linear proton accelerator. It delivers 800 MeV protons at 1 mA of beam current. It has been in operation for many years and offers considerable quantities of operational data.

In chapter 2, the option for transmutation of nuclear waste will be briefly reviewed.

For the general reader, an introduction to particle accelerators will be made in chapter 3, "Introduction to Accelerators". The principle of particle acceleration, accelerator development, different types of accelerators and some basic definitions are discussed. In this chapter, formulas will not be described but rather focus on different technical realizations of particle acceleration.

Chapter 4 presents the current Los Alamos National Lab concept for linear accelerator design for transmutation of waste. Also, the circular accelerator design proposed by the CERN group is presented. At the end of this chapter advantages and disadvantages of both accelerators are discussed.

In chapter 5, the LANSCE accelerator complex is outlined. A general description of different beam lines and important areas is made. Major parts of the accelerator are explained.

Information on LANSCE accelerator operations are discussed in Chapter 6. The method for classification, organization, and recording of beam interruptions are shown. Run cycles and beam schedules are explained.

Chapter 7 investigates the overall reliability of the LANSCE accelerator. Statistics of beam interruptions and down time for the H+ and H- beams are analyzed. For the most part operational statistics for 1996-97 is presented but some previous historical reliability data is also shown. Mean Time Between Failure and Mean Down Time for the entire accelerator are calculated. Conclusions and proposals for reliability improvements are summarized.

In Chapter 8, a more detailed reliability assessment of major systems and subsystems is carried out. Particular emphasis is made for systems which are used in modern rf accelerator systems such as rf stations, rf drives, rf transport, magnets, magnet power supplies, cooling and vacuum.

In Chapter 9, statistics of beam monitor data during 1997 for the H+ beam is shown. Analysis of 163,000 beam current recordings is performed. The analysis verifies the true beam performance. It does not investigate the cause of the beam failure. These results are compared with results from Chapter 7 "Overall LANSCE Reliability". Important conclusions with respect to both analyses are summarized.

2 Nuclear Waste

If one assumes the same level of global nuclear power generation for the future as it exists today there will be more than 250.000 tons of spent reactor fuel in the world by the year 2015. The spent fuel contains large quantities of long lived transuranics and fission products. This amount of long lived radiotoxic waste presents a major threat to all living organisms if released to the environment.

Due to different geological conditions, national views on nuclear energy, reprocessing, and proliferation concerns various programs have evolved for dealing with nuclear waste. One option is storing unprocessed spent fuel in geological repositories. Other options involves utilization of the fissile material contained in the spent fuel before storage in waste repositories. Long term uncertainties, the possibility for dilution of radiotoxic elements and extraction of weapon grade plutonium are the main concerns for the geological repository.

2.1 Transmutation of Waste

Nuclear waste may be eliminated in a nuclear way. One option for dealing with nuclear waste and weapon plutonium is transmutation. Transmutation is the conversion of one element into another. A nuclear transmutation entails a change in the structure of atomic nuclei. The transmutation reaction (see examples below) may be induced by a nuclear reaction such as neutron capture, or occur spontaneously by radioactive decay, such as alpha decay and beta decay. Chemical reactions are not capable of effecting the nuclear changes required for transmutation.

Examples of transmutation reactions in nuclear waste:

Transuranics: $n + {}^{239}Pu \rightarrow fissionproducts + energy$ *or*

$n + {}^{240}Pu \rightarrow {}^{241}Pu \rightarrow$

$n + {}^{241}Pu \rightarrow fissionproducts + energy$

Fissionproducts: $n + {}^{99}Tc \rightarrow {}^{100}Tc \rightarrow {}^{99}Ru + e^{-}$ *(*${}^{99}Ru$ *is stable!)*

Transmutation of waste aims to enhance the viability of the geological repository. By transmuting the long lived transuranics by fission and the long lived fission products by neutron absorption the waste repository would have substantially reduced inventories of the long term radioactivity and heat sources. This will transform the time scale of repository performance requirements from a geological scale (tens of thousands years) to an engineering scale (hundreds of years). Transmutation of waste has the potential to provide added flexibility to the design of the waste repository and reduce the uncertainties about its performance.

2.2 Spallation

Large neutron availability is essential for transmutation of waste. Lack of neutrons make transmutation of waste in normal reactors less effective. A high intensity neutron source may be achieved in a process called spallation. Spallation occurs when high energy particles strike a target of heavy elements. The target material is usually tungsten, lead or an lead-bismuth alloy. In the collision, the incoming particle may tear

out protons, neutrons and nuclear fragments. Protons knocked out in the initial collision may strike a second tungsten nucleus, causing a "cascade" of nuclear fragments. The remaining nucleus is left in an excited state. In the deexcitation process the nucleus emits additional nuclei. Most of these nuclei are neutrons which are emitted isotropically.

2.3 Accelerator driven Transmutation of Waste

Several options of transmutation methods have been proposed. Up today the most reasonable suggestions utilize high power proton accelerators. In Accelerator driven Transmutation of Waste (ATW) protons are accelerated to high energy ($\approx$1 GeV) and then hit a heavy metal target. The result is an intense spallation neutron source.

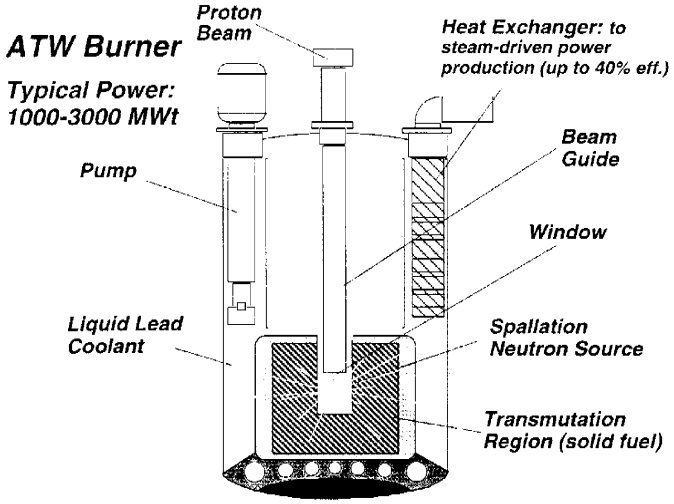

Figure 2.1 Illustration of the ATW burner, the Los Alamos National Lab concept [1]

In the ATW burner (see Figure 2.1), the target is surrounded by a subcritical transmutation region containing the fuel, "transmutation assemblies". The fuel consists of spent fuel and recycled ATW fuel. Since considerable neutron multiplication and heat production arises from fissioning of waste actinides, adequate heat removal must be present. The ATW burner may use an alloy of liquid lead-bismuth both as coolant and spallation target material. Because of its subcritical mode of operation the ATW system do not rely on delayed neutrons for control and power change, it is only driven by the externally generated neutron source. Control rods and reactivity changes have very low importance. Subcriticality allows the ATW burner to work with any composition of fuel. The neutron poor thorium-uranium fuel cycle may for example be used rather straightforwardly in the ATW burner. Extended burnup is achieved with appropriate accelerator operation. If desirable, significant electric power may be generated in a steam-cycle connected to the ATW burner.

3 Introduction to Accelerators

A particle accelerator is a device that produces a beam of fast-moving, electrically charged atomic or subatomic particles [2]. Physicists use accelerators in fundamental research on the structure of nuclei, the nature of nuclear forces, and the properties of nuclei not found in nature, such as the transuranic elements and other unstable elements. Their application as research tools in nuclear and high energy particle physics require the biggest and most energetic facilities. One of the ironies of modern physics is that the study of tiny nuclear particles and interactions often requires an extremely large apparatus, such as an accelerator. The world's longest electron linac is the 3.2-kilometre (2-mile) machine at the Stanford (University) Linear Accelerator Center, California (see Figure 3.1). SLC can accelerate electrons to 50 billion electron volts (50 GeV).

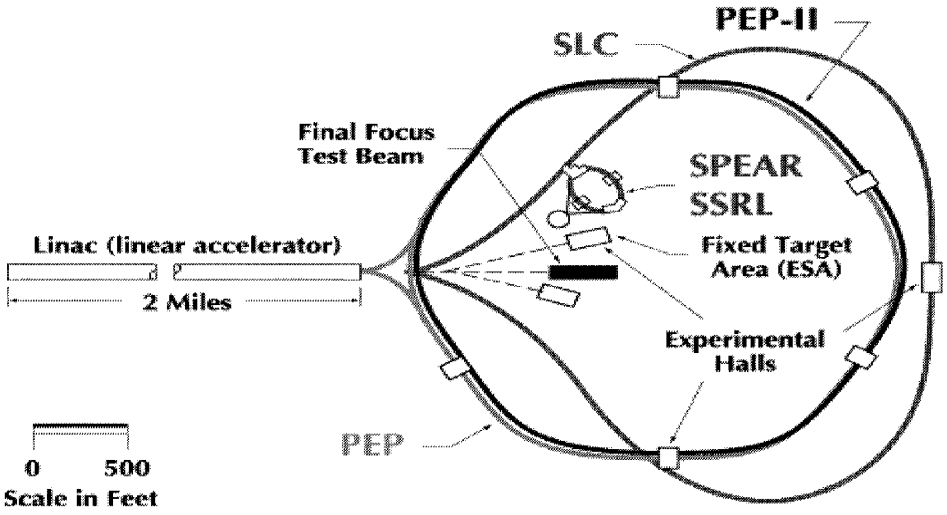

Figure 3.1 The Stanford Linear Accelerator
The Stanford Linear Accelerator Center has a 3.2-kilometre linear accelerator that produces one of the highest-energy electron beams in the world. At the far end of the accelerator, the electrons and positrons can be directed into the Stanford Linear Collider (SLC), which consists of two separate arcs of magnets forming a loop to bring the two beams into head-on collision at a total energy of about 100 GeV.

Much smaller accelerators, however, have found broad applications in a wide variety of basic research and technology, as well as medicine. Examples of such applications are radioisotope production, industrial radiography, cancer therapy, sterilization of biological materials and polymerization of plastics. Today, large particle accelerators are proposed for new applications, such as transmutation of waste, energy production, and production of tritium for use in nuclear weapons.

The particles that are accelerated most often are electrons or protons, and their antiparticles, or heavier ionized atoms. All electric charged particles may be accelerated, but for neutron production in a spallation target high energy protons are generally used.

Sometimes the primary beam is used, in other cases, the primary beam is directed onto a fixed target to produce a beam of secondary particles, such as X rays, neutrons, mesons, hyperons, or neutrinos. Such fixed target experimentation dominated nuclear and high energy particle experimentation from the first applications of artificially accelerated

particle beams far into the seventies and is still a valuable means of basic research. Obviously, it is also this method in conjunction with a heavy metal target which is used to produce secondary particles like neutrons for use in a ATW burner.

To increase the energy available for interaction the particles are sometimes aimed not at fixed targets but to collide head on with other particles. By this, almost all kinetic energy come to use in the collision. This is the main goal for the construction of colliding beam facilities (see figure 3.1).

A few circular accelerators are operated as sources of the intense radiation, called synchrotron radiation, emitted by electrons moving at almost the speed of light along curved paths. This radiation is highly collimated in the forward direction, of high brightness and therefore of great interest for basic research, technology, and medicine.

3.1 Accelerator technology

Particle accelerators come in many forms applying a variety of technical principles. All are based on the interaction of the electric charge with static and dynamic electromagnetic fields and it is the technical realization of this interaction that leads to different types of particle accelerators.

The development of charged-particle accelerators has progressed along double paths which by the appearance of particle trajectories are distinguished as linear accelerators and circular accelerators. Particles travel in linear accelerators only once through the accelerator structure while in a circular accelerator they follow a closed orbit periodically for many revolutions accumulating energy at every traversal of the accelerating gaps. No fundamental advantage or disadvantage can be claimed for one or the other class of accelerators. It is mostly the particular application and sometimes the available technology that determines the choice between both classes. Both types have been invented and developed early in this century, and continue to be improved and optimized as associated technologies advance.

Since the late 1920's, when the first accelerators were built, the highest energies accessible have risen from around 1 MeV to 1 TeV. Several specific developments have allowed this progress to successively higher energies, but the basic principles of particle acceleration have remained essentially the same. For example, superconductivity has been employed to extend the reach of the highest-energy machines, but the machines themselves are still direct descendants of the first accelerators.

The effectiveness of an accelerator is usually characterized by the kinetic energy, rather than the speed, of the particles. The unit of energy commonly used is the electron volt (eV), which is the energy acquired by a particle that has a charge of the same magnitude as that of the electron when it passes between electrodes that differ in potential by one volt; it is equivalent to $1.602*10^{-19}$ J. The protons in the proposed ATW accelerator reaches an energy of 1 GeV and travel about 87 percent of the speed of light.

The particle beam current is measured generally in Amperes, no matter what general system of units is used but occasionally in terms of the total charge or number of particles. In a simple case, if the particles come by in a continuous stream the beam current is proportional to the particle flux. This case, however, occurs very rarely since particle beams are generally accelerated by rf fields. As a consequence there is no continuos flux of particles. The particle flux is better described as series of bunches separated by a number of wavelengths of the accelerating rf field. In these cases the

current is distinguished between different definitions. The peak current is the peak instantaneous beam current for a single bunch, while the average current is defined as the particle flux averaged over the duration of the beam pulse.

Particle accelerators consist of two basic units, the particle source or injector and the main accelerator structure. The region in which the particles are accelerated must be highly evacuated to keep the particles from being scattered out of the beam, or even stopped, by collisions with molecules of air.

The most successful acceleration of particles is based on the use of radio frequency alternating electromagnetic waves (rf fields). Acceleration occurs in resonant cavities (see figure 3.2) which are fed by rf power. Very high accelerating voltages can be achieved in resonant rf cavities, far exceeding those obtainable in electrostatic accelerators of similar dimensions. Particle acceleration in linear accelerators as well as in circular accelerators are based on the use of rf fields.

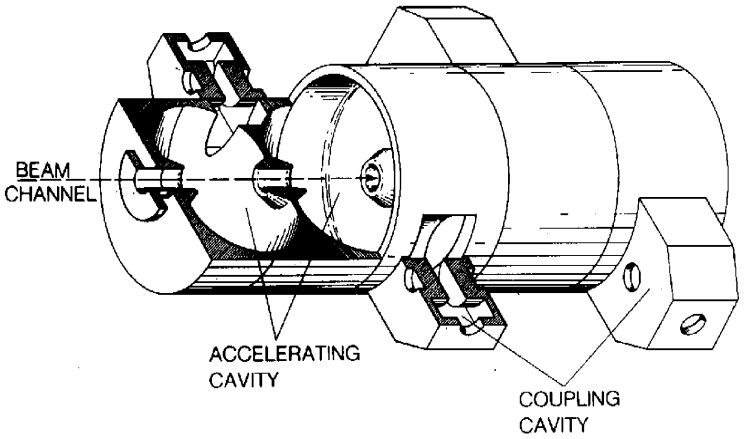

Figure 3.2 Illustration of the Side Coupled Cavity at LANSCE

RF accelerators require very powerful sources of electromagnetic fields. RF fields are produced by large klystrons (high-frequency vacuum-tube amplifiers) with power outputs of 20-30 megawatts.

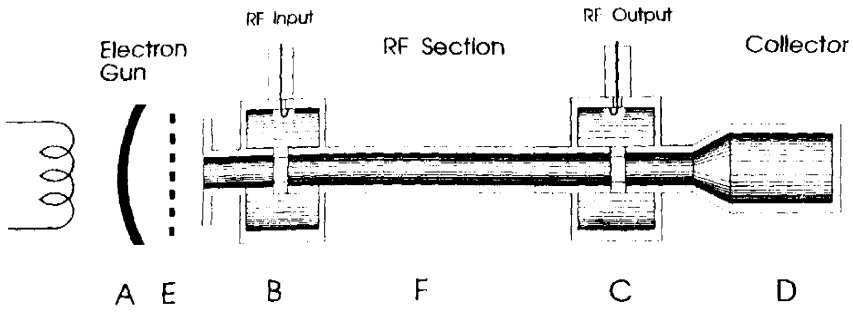

Figure 3.3 Picture of the 2-cavity Klystron Amplifier [3]

The principle of the two-cavity klystron amplifier can be understood from figure 3.3. A is an electron emitter and D is a collector for the beam. E is a modulating element, often used when pulses of power are required. Power is coupled into cavity B (input

cavity) and the rf voltage developed across the gap of the cavity modulates electrons in the beam. The tunnel between cavities B and C is called the drift tube (F) and its length is designed to provide optimum bunching of the beam at the gap of cavity C (output cavity). The electron bunches induce an rf current in the output cavity which can be coupled out as rf power. Depending on the resonant frequency of the second cavity (C) compared with the frequency of the input signal, an rf voltage will be excited in the second cavity which will be larger than that in the first cavity. Thus an amplified signal can be coupled out from the second cavity. In a multi-stage klystron (for example the LANSCE klystron) several cavities are connected in series and the rf energy grows in successive cavities as the beam flows from cathode to collector.

3.2 Linear Accelerators

In linear accelerators the particles are accelerated by definition along a straight path by either electrostatic fields or oscillating rf fields. When rf fields are used the linear accelerator is commonly called a linac [2].

The final energy of the particles is proportional to the sum of the voltages produced by the accelerating devices along that line. The linac consists of a linear sequence of many units where accelerating rf fields are generated and timed such that particles absorb and accumulate energy from each acceleration unit.

The principle of the linear accelerator based on alternating fields and drift tubes was proposed by Ising in 1925 and demonstrated by Widerö in 1928. In this method particles are accelerated by repeated application of rf fields (see figure 3.4).

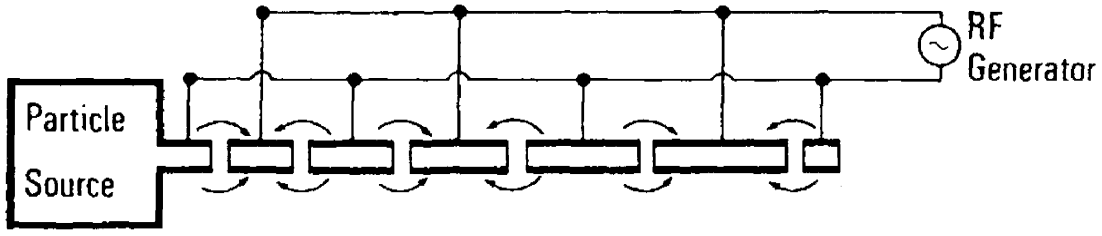

Figure 3.4 Principle of the Widerö accelerator [4]

While the principle of the linear accelerator is simple, the realization requires specific conditions to ensure that the particles are exposed to only accelerating rf fields. For efficient acceleration the motion of the particles must be synchronized with the rf fields in the accelerating sections. During the half period when the fields reverse sign the particles must be shielded from the fields in order not to be decelerated again. Technically this requirement is realized by surrounding the beam path with metallic drift tubes as shown in figure 3.5. The electric field is zero inside the drift tubes, and the length of the tube segments are chosen such that the particles reach the gap between two successive tubes at the moment the rf field is accelerating. The length of the tubes are therefore almost as long as it takes the particles to travel for half an rf period.

In the twenties when this principle was developed it was difficult to build high frequency generators at significant power. In 1928 rf generators were available only up to about 7 MHz and this principle was useful only for rather slow particles like low energy protons and ions. The drift tubes can become very long for low rf frequencies. At higher

frequencies, however, the capacitive nature of the Widerö structure becomes very lossy due to electromagnetic radiation. To overcome this difficulty, Alvarez proposed to enclose the drift tubes in a long cylindrical metal tank, or cavity. The Alvarez linac is based on the formation of standing electromagnetic waves inside the tank. The electric field is parallel to the axis of the tank. Most of these accelerators operate at frequencies of about 200 MHz. Focusing is usually provided by magnetic quadrupoles placed inside the drift tubes. The Alvarez linac is suitable for acceleration of protons and ions from a few hundred keV to a few hundred MeV. That energy range makes the Alvarez structure useful in the first accelerating stage in a linear accelerator or as a preaccelerator into a synchrotron.

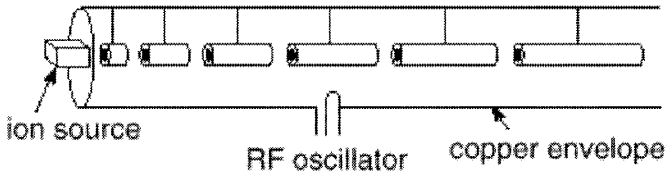

Figure 3.5 The Alvarez linac
The acceleration chamber is an evacuated cylindrical pipe that serves as a waveguide for the accelerating field.

Linear accelerators fall into two distinct types: standing-wave linear accelerators (used for heavy particles) and traveling-wave linear accelerators (used to accelerate electrons). The reason for the difference is that after electrons have been accelerated to a few MeV in the first few metres of a typical accelerator, they have speeds very close to that of light. Therefore, if the accelerating wave also moves at the speed of light, the particles do not get out of phase, their speeds do not change. Protons, on the other hand, must reach much higher energies before their speeds can be taken as constant, so that the accelerator design must allow for the prolonged increase in speed.

In most new linac designs RFQs (radio frequency quadrupole accelerators) are included. The RFQ is a low velocity, high current linear accelerator. Many laboratories have adopted the RFQ as a "front end" accelerator. The Alvarez linac is most efficient in a higher energy range (0.5-100 MeV). Below that range, RFQs are more appropriate. Separate bunching devices are not necessary in the RFQ. The RFQ receives a continuos stream of ions from the injector, forms it into bunches, and accelerates nearly 100 % of the beam. In other linacs the bunching process usually discards 30 to 50 % of the beam. The RFQ has eliminated the historic requirement of operating the ion source at several hundred kilovolts above ground before injection into a drift tube linac. Increased accelerator reliability is gained due to a lower probability of high voltage sparking in the injector column.

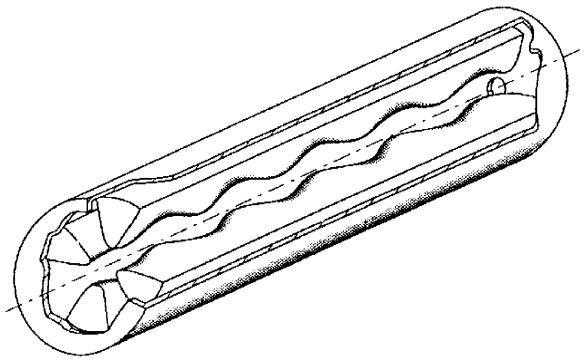

Figure 3.6 Illustration of a Radio Frequency Quadrupole [5]

The RFQ, as shown in figure 3.6, is a focusing structure to which acceleration is added as a perturbation. Other linac designs impose focusing onto an accelerating structure. This fundamental focusing attribute of the RFQ gives rise to very good beam stability in all three dimensions.

3.3 Circular Accelerators

In a circular accelerator, the path of the particles is bent by the action of a magnetic field into a spiral or a closed curve that is approximately circular. In this case, the particles pass many times through the same accelerating devices. This simplifies the rf system compared to the large number of energy sources and accelerating sections required in a linear accelerator. While this approach seemed at first like the perfect solution to produce high energy particle beams, its progress soon became limited for the acceleration of electrons by the generation of synchrotron radiation.

The simplicity of circular accelerators and the absence of significant synchrotron radiation for protons and heavier particles like ions has made circular accelerators the most successful and affordable principle to reach the highest possible proton energies for fundamental research in high energy physics.

In circular accelerators, the final energy depends on the magnitude of the voltages multiplied by the number of times the particles pass through the accelerating gaps. Because the total distance traveled by the particles in a cyclic accelerator may be more than a million kilometres, cumulative effect of small deviations from the desired trajectory would be dissipation of the beam. Therefore, the beam must be continually focused by the magnetic fields, which are precisely shaped by powerful magnets.

The magnetic resonance accelerator, or cyclotron, was the first cyclic accelerator and the first resonance accelerator that produced particles energetic enough to be useful for nuclear research. For many years the highest particle energies were those imparted by cyclotrons modeled upon Lawrence's archetype. In these devices, commonly called classical cyclotrons, the accelerating electric field oscillates at a fixed frequency and the bending magnetic field has a fixed intensity (see figure 3.7). The principle of the cyclotron is basically the application of the Widerö linac in a coiled up version to save space and rf equipment.

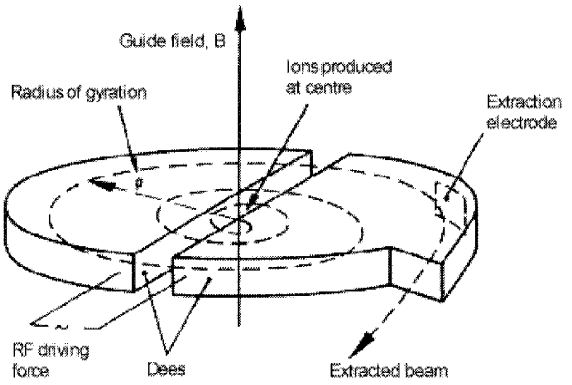

Figure 3.7 Classical cyclotron
The magnetic resonance accelerator, or cyclotron, conceived by Lawrence as a modification of Widerö's linear resonance accelerator.

The accelerating cavity has basically the form of a circular pillbox cut in two halves, where the accelerating fields are generated between those halves and are placed between the poles of the magnet. Because of the form of the half pillbox, these cavities are often called the Dees of a cyclotron. The particle orbits occur mostly in the field free interior of the Dees and traverse the accelerating gaps between the two Dees twice per revolution. Due to the increasing energy, the particle trajectories spiral to larger and larger radii.

The bending magnet field serves only as a beam guidance system to allow the repeated passage of the particle beam through the cavity. Since the cavity fields are oscillating, acceleration is not possible at all times and for multiple accelerations we must meet specific conditions of synchronization between the motion of particles and the field oscillation. The time it takes the particles to travel along the orbital path must be an integer multiple of the oscillation period for the rf field.

The energy gained by a particle in a classical cyclotron is limited by the relativistic increase in the mass of particle, a phenomenon that causes the orbital frequency to decrease and the particles to get out phase with the alternating voltage. This effect can be reduced by applying higher accelerating voltages and shorten the overall acceleration time. The highest energy imparted to protons in a classical cyclotron is less than 25 MeV, and this achievement requires the imposition of hundreds of kilovolts to the Dees.

Cyclotrons in which the frequency of the accelerating voltage is changed as the particles are accelerated are called synchro cyclotrons, frequency-modulated (FM) cyclotrons. Because of the frequency modulation, the particles do not get out of phase with the accelerating voltage, so that the relativistic mass increase does not impose a limit on the energy. The particles reach the maximum energy in bunches, one for each time the accelerating frequency goes through its program. In other words, the particle flux has a pulsed macro structure equal to the cycling time of the rf modulation. The average intensity of the beam is much lower than that of a classical cyclotron.

The isochronous cyclotron is another modification of the classical cyclotron that also evades relativistic constraint on its maximum energy. The isochron cyclotron is the solution to obtain high intensity (classical cyclotron) at high energy (synchrocyclotron). Its advantage over the synchrocyclotron is that the beam is not pulsed and therefore more

intense. The frequency of the accelerating voltage is constant, and the orbital frequency of the particles is kept constant as they are accelerated by causing the average magnetic field on the orbit to increase with orbit radius. This ordinarily would cause the beam to defocus axially. Hence, the magnetic field in an isochronous cyclotron would not be axially symmetric. But, if the magnetic poles are constructed from sectors, the particles in the cyclotron would experience azimuthal variation of the magnetic field. This in turn introduces an axially restoring force on the particles at the edges of the sectors.

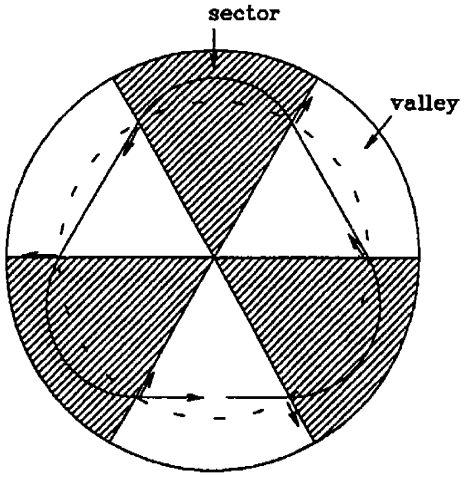

Figure 3.8 Isochronous cyclotron

If the sectors are twisted to a spiral form we get some additional axial focusing since the particles enter and leave the magnet edges with a larger spiral angle.

The development of circular accelerators has finally made a full circle. Starting from the use of a constant rf field, in classical cyclotrons, the need for frequency modulation was obvious to meet the synchronicity condition for particles through the relativistic transition region. Application of technically complicated focusing schemes allowed to revert back to the most efficient way of particle acceleration with constant fixed frequency fields.

Accelerating protons with isochronous cyclotrons is usually limited by the focusing limit of the magnet. The ultimate focusing limit for this is a separated sector cyclotron. In the separated sector cyclotron (or ring cyclotron) the magnets consist of sectors only (see figure 3.9). In the valley between the sectors there is no iron and practically no magnetic field. RF cavities, extraction and other beam diagnostic equipment may be installed in the space between the sectors. This type of cyclotron is a possible candidate for transmutation of waste purposes (see section 4.2).

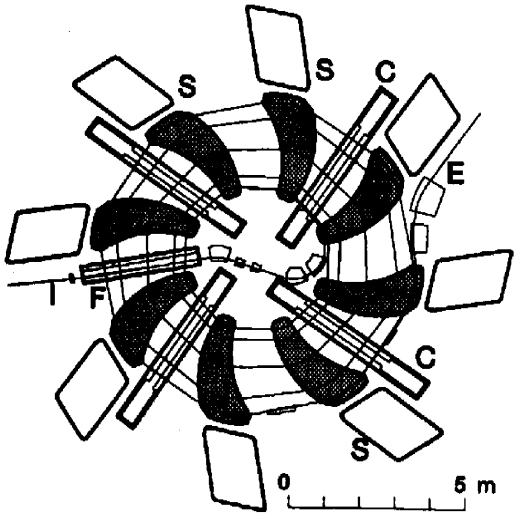

Figure 3.9 Sector Separated Cyclotron at PSI
The Ring Cyclotron at Paul Scherrer Institute (PSI). The cyclotron accelerates protons to 590 MeV at 1.5 mA.

4 The ATW Accelerator

To produce enough neutrons in a spallation target the accelerator must deliver energetic protons at high current (see figure 4.1). Since the neutron yield increases almost linearly (in the range 0.8-4 GeV) with proton energy the energy and current may be exchanged. For example, if the proton energy is doubled and the beam current is divided by two the neutron yield stays approximately the same. Typical specifications of an ATW linac are 30-40 mA at 1 GeV. Such high power accelerators do not exist today, but considering recent progress in accelerator technology there is a good confidence in realization of these accelerators.

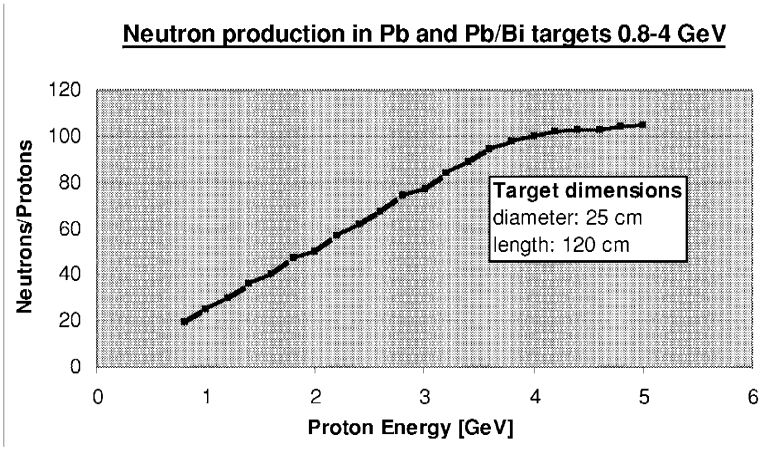

Figure 4.1 Illustration of neutron yield in a spallation target [6]

The ATW accelerator must be designed to deliver large beam currents to a target facility with very little beam losses along the accelerator. Several types of difficulties arise when one tries to increase the beam intensity. One effect is the mutual repulsion of particles due to their electric charge. This repulsion affects phase stability as well as focusing. In the case of beam loss, relative losses increase with intensity and there is a risk for contamination, local heating and damage of the accelerator structure. Light ions, such as protons, have long stopping ranges, penetrate deeply, and have nuclear reactions that cause radioactivity buildup in the structure [7]. This activation is the main problem with beam losses in light ion accelerators. It is desirable to be able to perform maintenance activities without using remote manipulators (hands-on maintenance) over the lifetime of the facility.

4.1 The ATW Linac

In this section the linear accelerator design for transmutation of waste purpose is outlined. The proposed accelerator is the Los Alamos National Lab concept for accelerator design. Most of the text is based on the ATW accelerator design by George Lawrence of Los Alamos National Lab [8].

A linac for an ATW facility should be designed:

- To have high availability and operational flexibility
- To have high reliability and minimal power fluctuations
- To have very high electrical efficiency (ac to beam power)
- For minimum capital and operating costs
- To have short length
- To vary the power on target over a wide range

The ATW linac design is based on the APT (Accelerator Production of Tritium) linac design and technology. Extensive Research and Development on the APT linac has been in progress for several years. The baseline accelerator design for the ATW linac is a normalconducting-superconducting proton linac that produces a continuos wave beam power of 40 MW at 1 GeV. The ATW linac is illustrated in figure 4.2.

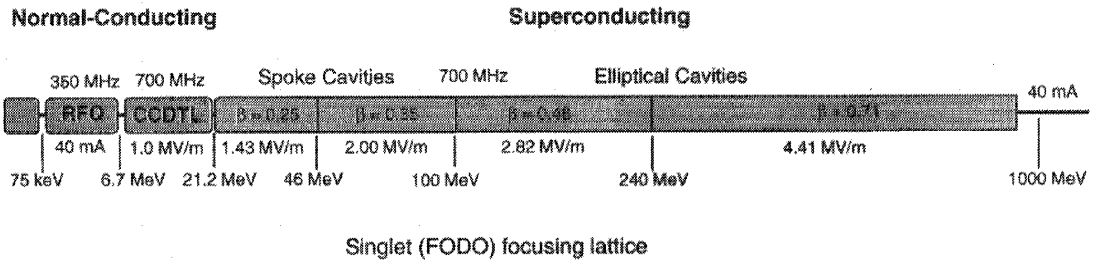

Figure 4.2 The ATW linac proposal [8]

Normalconducting (nc) linac is used for low energies. This facilitates a high-density magnetic focusing lattice and smoothly varying accelerating and focusing parameters. It also allows for excellent emittance control of the high-current beam and minimal generation of halo. Halo is the formation of an outer ring of particles surrounding the inner core of the beam. The beam halo affects particle losses in an accelerator. This of great concern for the next generation of high power proton linacs.

At high energies superconducting cavities and quadrupoles are used. This eliminates RF cavity losses and provides very high power efficiency. Large aperture dramatically reduces beam loss threat. Short cavities provide wide velocity acceptance bandwidth.

The ATW linac design is more advanced than APT. Some of the most important aspects an the linac proposal for ATW are:

- **High accelerating gradients in the superconducting section**
  - gradients of 15MV/m in superconducting section. These gradients have been achieved in cavity tests (TESLA).
  - short linac (only 345 m) ⇒ reduces size as well as costs

- **Cryomodules contain superconducting quadrupoles**
  - stronger focusing ⇒ larger aperture/beam-size ratio ⇒ less contamination
  - higher electrical efficiency ⇒ minimizes quadrupole power

- **Superconduction starts at lower energy (20 MeV)**
  - reduces RF losses in low energy linac ⇒ increases efficiency
  - increases aperture size at low energies
  - makes use of 1/2-wave (spoke-type) superconducting resonators

Table 4.1 Global ATW accelerator parameters

Parameter	**Value**
Output proton current	40 mA
Duty factor	100%
Final energy of nc linac	21.2 MeV
Final energy of sc linac	1000 MeV
Length	345 m
RF power	44.6 mA
Number of klystrons	3 at 350 MHz; 53 at 700 MHz
Number of cryomodules	31
Number of nc accelerating cavities	106*2
Number of sc accelerating cavities	134
Number of nc quadrupoles	105*2
Number of sc quadrupoles	165

At Los Alamos a 110 mA, 75 keV proton injector is being developed for the APT project. The new injector is based on a microwave proton source which operates at 2.45 GHz. The ion source is coupled with a two-solenoid, LEBT system for matching into a RFQ [9].

A low-energy demonstration accelerator (LEDA) has been developed. LEDA is virtually identical to the first 20 MeV of the APT accelerator. It is used to confirm beam parameters, system availability, component reliability, provide experimental determination of the beam halo distribution, develop a commissioning plan for a continuous wave system, and prototype the low-energy portion of the APT plant accelerator. As far as now the LEDA injector has demonstrated APT beam performance requirements and reliability. In 1997, the injector was operated for 168 hours. In this time, the injector operated at 75 keV, > 120 mA with an availability of 96-98 % [9]. The ion source accounted for 3.4 hours of down time (see definition in section 8.5.1) because of recovery from high voltage sparks.

4.2 The ATW Cyclotron

In the section the solution based on circular machines for accelerator driven transmutation projects is presented. The proposal is made by the transmutation group at CERN (European Organization for Nuclear Research). The text is a summary of the proposition in the IAEA Status report on Accelerator driven systems [10]. The accelerator complex is based on a three-stage cyclotron accelerator (figure 4.1)

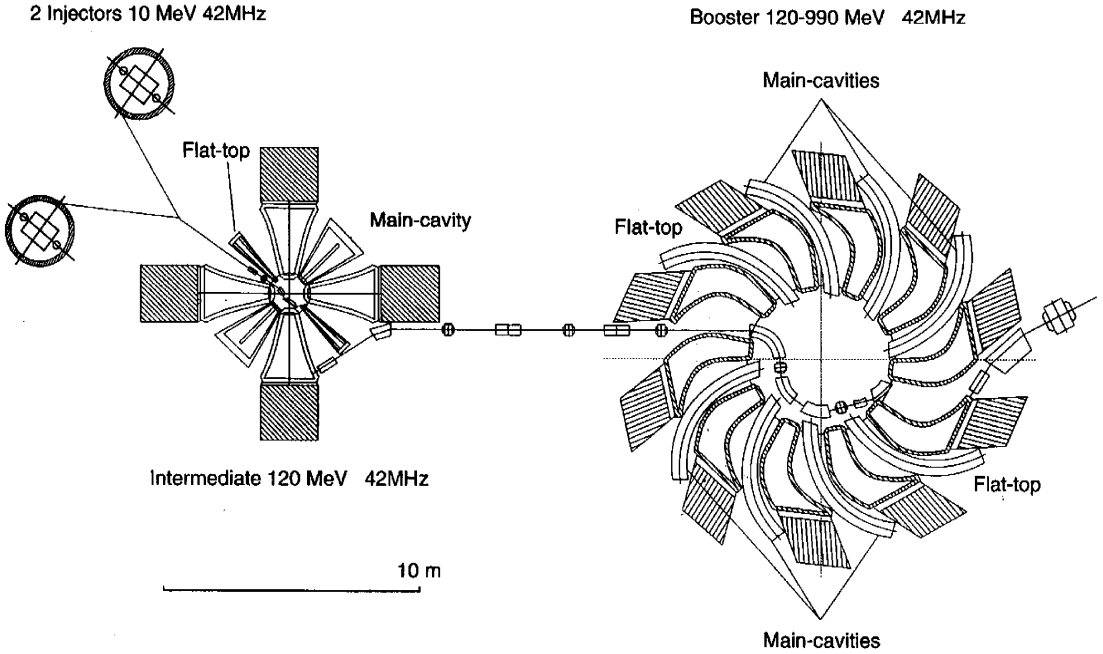

Figure 4.1 General layout of the CERN group accelerator complex [10]

The injector is made of two 10 MeV, Compact Isochronous Cyclotrons (CIC). Beams are merged with the help of negative ion stripping to the intermediate stage, a cyclotron with four separated sectors (ISSC) bringing the beam up to 120 MeV. In the final booster, a ten separated and six cavities cyclotron (BSSC), the kinetic energy is raised up to 1 GeV. The main parameters of the cyclotrons are presented in table 4.2.

Table 4.2 Main parameters of the cyclotrons

Parameter	Injector	Intermediate	Booster
Injection energy	100 keV	10 MeV	120 MeV
Extraction energy	10 MeV	120 MeV	990 MeV
Frequency	42 MHz	42 MHz	42 MHz
Harmonic	4	6	6
Magnet gap	6 cm	5 cm	5 cm
Niobium sectors	4	4	10
Sector angle (injection/extraction)	15°/34°	26°/31°	10°/20°
Sector spiral extraction	0°	0°	12°
Niobium cavities	2	2	6
Type of cavity	delta	delta	single gap
Gap peak voltage	110 kV	170 kV	550 kV
Gap peak voltage extraction	110 kV	340 kV	1100 kV
Radial gain per turn extraction	16 mm	12 mm	10 mm

4.2.1 The Injector Cyclotron

The injector cyclotron consists of a four sector isochronous cyclotron capable of delivering 5 mA. The beams of two such injectors working at the same frequency are then merged before injecting them into the intermediate stage (ISSC) and the final booster. Since high current is required the injection energy must be about 100 keV in order to avoid space charge effects. A stripper is installed at the end of the injection line, before beams enters the ISSC to convert the H- beam into a H+ beam. As a result the particle density in the phase space is doubled at no increase of the single beam emittance.

4.2.2 Intermediate cyclotron

A four-separated-sector cyclotron has been chosen as the intermediate stage. Acceleration of the beam is provided by two main resonators located in opposite valleys giving an energy gain per turn of 0.6 MeV at injection and 1.2 MeV at extraction, increasing the beam energy from 10 MeV to 120 MeV. The RF frequency of the accelerating cavities has been chosen equal to 42 MHz. The choice of the injection energy into the ISSC is certainly one of the most important parameters which influences the overall performances of the cyclotron complex. The space charge effects are strong at low energy. They are present in both transversal and longitudinal directions of the beam. Results of simulations show that a nominal 10 mA beam can be handled at an injection energy of the order of 10 MeV.

Double gap cavities have been selected because their radial extension is much smaller leaving more space in the centre of the machine for the bending and injection magnets and the beam diagnostics.

4.2.3 Booster cyclotron

The magnet of the final booster consists of 10 identical C-shaped sector magnets with a strong spiral in order to obtain sufficient vertical focusing at high energies. Acceleration of the beam is provided by 6 main resonators located in the valleys. They should provide an energy gain per turn of 3 MeV at injection and 6 MeV at extraction, increasing the beam energy from 120 MeV to 990 MeV. In order to compensate the effects of the space charge forces, two flat-topping cavities are needed (flat-topping is a technique to achieve a constant accelerating voltage at a phase width of 30°). The RF frequency is equal to 42 MHz. A voltage ratio of 2.0 is used between injection and extraction in order to reduce the number of turns in the cyclotron and to have sufficient turn separation at extraction.

4.3 Linacs Vs Cyclotrons

As mentioned before, both linear and circular accelerator designs are proposed for transmutation of waste and energy production. Both accelerators use radio frequency (rf) electromagnetic waves for acceleration. The main advantage for the linac is the possibility to produce high currents. For the cyclotron, the main advantages are low cost and compact size.

Due to longitudinal space charge effects and extraction losses the maximum beam current is limited for the cyclotron. For the current state of the art at about 10-20 mA. Since the space charge influence is strong at high current and low energy it is suitable to inject protons at high energy. To achieve high intensities in a circular accelerator one may utilize a multistage sector separated cyclotron, consisting of several low energy, low current cyclotrons feeding into one high energy, high current cyclotron.

The cyclotron can be made very compact in size due to repeated use of the same accelerating cavities and not requiring a long beam transport system. The beam is held on a circular path by magnetic fields in bending magnets. The cyclotron is cheaper, but to deliver a beam current comparable to a linac one must use two or three cyclotron facilities. To increase particle energy is less costly. Since the neutron yield per incident proton is proportional to beam power in the region 1-4 GeV, beam current and beam energy may be exchanged.

One problem in cyclotrons is beam extraction. In order to get a high extraction efficiency, it is necessary to achieve a large radial separation of the last turns. This may be accomplished by a low average magnetic field and a high energy gain per turn.

For very high beam energies linear accelerators become very long, often several hundred meters long, and more expensive than cyclotrons. The linac length determines the total cost and the maximum energy hence the cost is proportional to the particle energy. Increase of particle energy in a linac is much more costly than for the cyclotron. New superconducting linac structures offers high accelerating gradients this reduces the size of the linac. Superconduction also reduces operational costs as rf losses in cavities are negligible. Most of the existing cyclotrons utilize room temperature magnets (conventional magnets) where the maximum magnetic field is limited to 2 T due to iron saturation. Superconducting cyclotrons offer higher energies as compared with conventional cyclotrons. Also, superconductivity offers a way to build small magnets to give relatively high energies However, superconduction in cyclotrons is complicated since presence of a strong magnetic field destroys the superconducting state.

Linear electron accelerators constructed of superconducting materials have been developed. Such structures dissipate far less energy than conventional metal structures, allowing a continuous electron beam, rather than a pulsed beam, to be accelerated.

5 The LANSCE Accelerator

5.1 Short History

Operated by the Los Alamos National Laboratory of the University of California for the United States Department of Energy, Los Alamos Neutron Science Center (LANSCE) is a national research facility for nuclear physics.

The initial name of the facility was LAMPF, Los Alamos Meson Physics Facility. Later, the complex was renamed as the Clinton P. Anderson Meson Physics Facility because of the late senator's long-time interest in and support of Los Alamos National Laboratory. In the 1990´s, Los Alamos National Laboratory decided to focus on neutron research and applications. In October 1995, the accelerator complex was renamed to the present Los Alamos Neutron Science Center (LANSCE).

LANSCE is a pulsed spallation neutron source facility that includes the world's most powerful proton linear accelerator. LANSCE is ideal for research in neutron scattering, neutron physics, and transmutation technologies. The linac was brought into initial operation at 800 MeV with a low intensity beam on June 9, 1972, within the time schedule and the revised cost estimate of $57 000 000. By January 1983 the accelerator produced a beam current of 1.2 mA. Routine operation now is at 1 mA and 800 MeV.

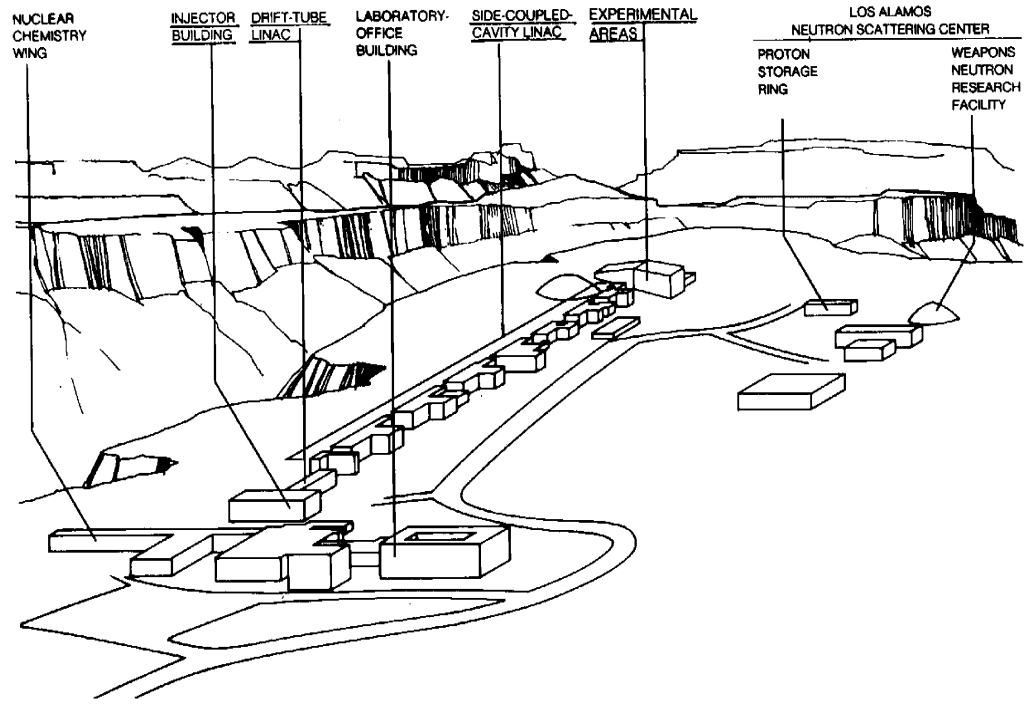

Figure 5.1 Overview of LANSCE

5.2 General

Two particle beams are available at LANSCE: H+ and H- (the third polarized H- beam is not in use). Both ions are accelerated simultaneously by alternating electric fields in the accelerator cavities. The first stage of the accelerator contains the injector systems, one for each kind of particle (see figure 5.2). The beams are passed through Low Energy Beam Transport (LEBT) systems before injection into the second stage of the accelerator which is an Alvarez Drift Tube Linac (DTL). The DTL accelerate protons from an energy of 750 keV to 100 MeV. The beams are then transported through a transition region for matched injection into the third section, the Side Coupled Linac (SCL). The SCL is the main section of the linac, it can accelerate protons to energies varying from 113 MeV to 800 MeV.

At the end of the linac the beams enter a switchyard in which the beams are separated, focused and diverted into their final beam lines.

The high intensity proton beam (H+) is directed through Line A (LA) to experimental area A, passing through secondary beam production targets as desired, and culminating at the isotope production, radiation effects, and beam stop area.

The negative hydrogen ion beam (H-) may be directed to Line D. Selected pulses are then delivered to the Proton Storage Ring (PSR) for accumulation and delivery to the Manuel Lujan Jr. Neutron Scattering Center (Lujan or LANSCE) target or to the Weapons Neutron Research area (WNR, Target 2 and 4).

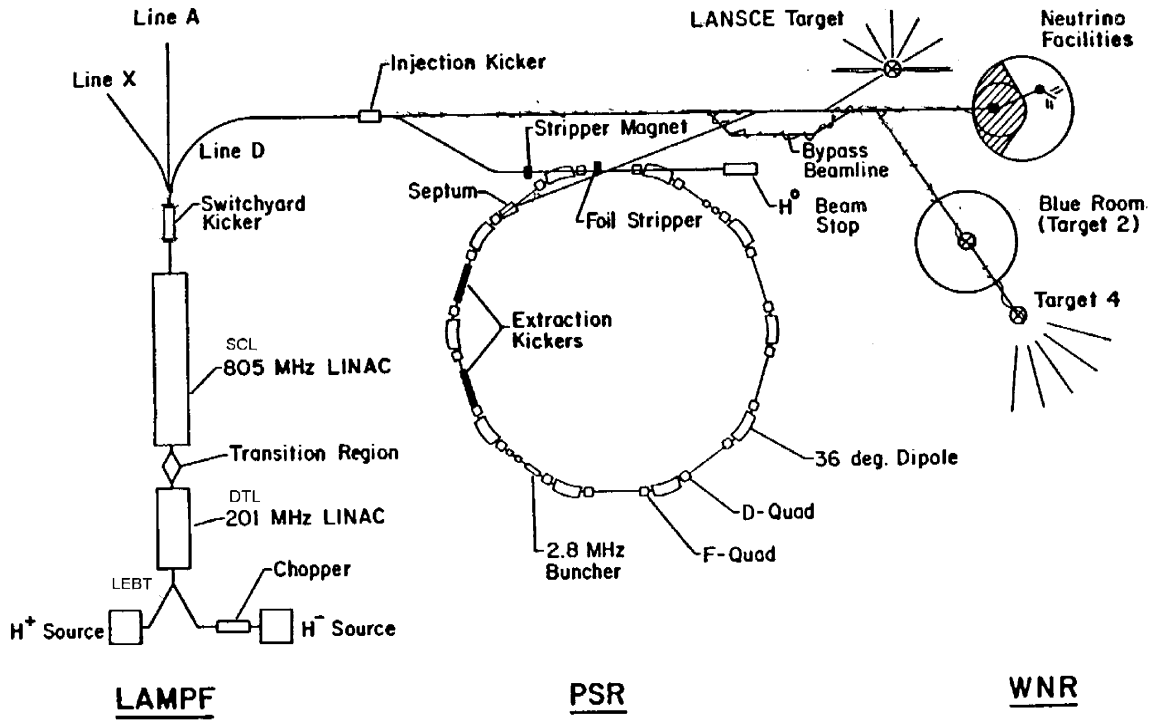

Figure 5.1 Major Accelerator Sections and beam lines at LANSCE

The accelerator is divided into different sectors. Beam transport systems and experimental facilities are designated as beam lines and target areas.

Table 5.1 Description of sectors of the accelerator

Sector	Sector Description	Detailed Sector Description
Sector J	Injector Building	The injector building houses the injectors and Low Energy Beam Transport (LEBT) Systems.
Sector A	Drift Tube Linac (DTL)	Sector A houses the DTL and the Transition Region (TR) which permits matching of the different beams from the DTL to the SCL.
Sectors B-H	Side Coupled Linac (SCL)	These sectors includes the SCL structure. Six or seven klystrons and a high voltage capacitor room are associated to each sector.
Sector S	Switchyard (SY)	The Switchyard (SY) provides magnetic separation of the beams at the end of the SCL.

Table 5.2 Description of beam lines and target areas

Beam line	Target Area Description	Detailed Line and Area Description
Line A	Area A	Line A delivers the H+ beam to a number of targets in Area A.
Line D	Lujan and Weapons Neutron Research	Line D provides H- beam to the Proton Storage Ring (PSR), Lujan Neutron Scattering Center, and the Weapons Neutron Research (WNR) area.
Line X	Area B and C	Line X provides H- beam to experiments in Area B or C.

5.3 Injector Building

Each injector system has a 750 keV Cockcroft-Walton type generator and an duoplasmatron type ion source (see figure 5.4) to produce positive and negative charged protons. The ion source is positioned within the high voltage terminal of the Cockcroft-Walton generator. These units are located within large electrically shielded bays in the injector building. Created inside the high voltage dome, the ions are accelerated by the electrostatic field as they travel in the injector column connecting the dome to a grounded plane. Beams from the two ion sources enter a beam transport (LEBT) area which directs each one into the entry of the DTL without interference with the other.

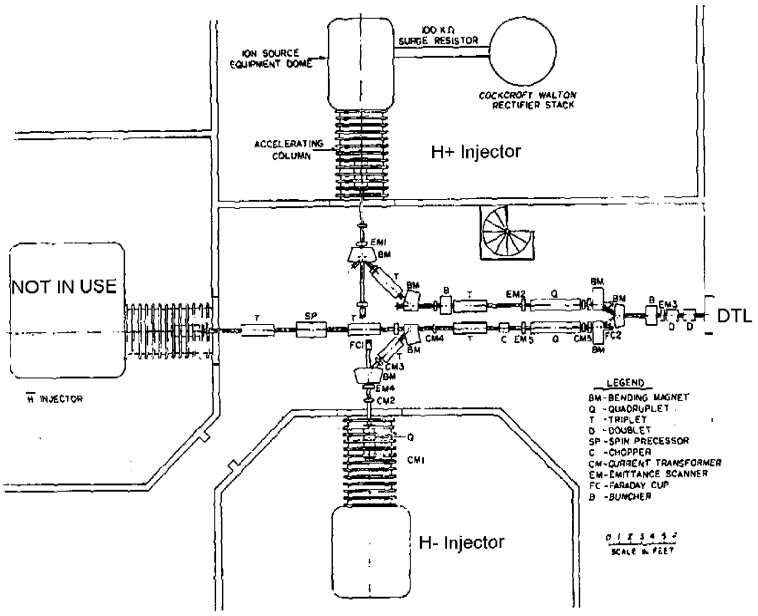

Figure 5.3 The Injector Building and LEBT system at LANSCE [11]

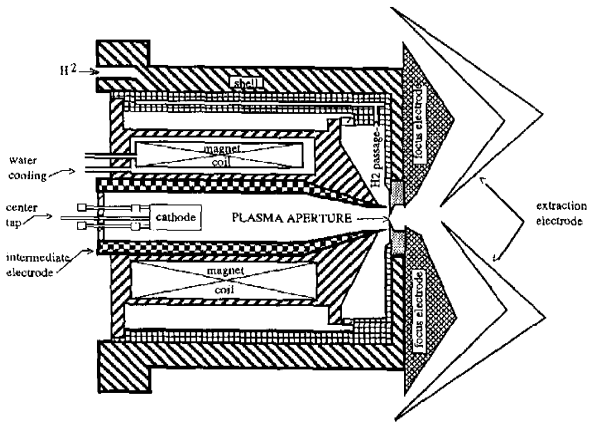

Figure 5.4 The H+ ion source at LANSCE (Duoplasmatron)

5.4 Low Energy Beam Transport System

Before the protons enter the DTL the beams must pass through a Low Energy Beam Transport system (LEBT) where the protons are steered, focused and bunched (see figure 5.3). Timing when these bunches are injected into the drift tube linac is crucial to ensure their acceleration by the rf field.

Particles from the ion source enter the beam line in what appears to be a constant stream. This stream could be injected into the accelerator structure and a small percentage of the particles which entered the accelerator at the correct phase angle would be accelerated, the rest would be lost. For high beam densities it is desirable to compress the continuous stream of particles from the source into short pulses with the help of a prebuncher, figure 5.5.

Efficient acceleration by rf fields occurs only during a very short period per oscillation cycle and most particles would be lost without proper preparation. It is the purpose of the buncher to collect the particles into bunches and to time the progress of

these bunches so that they enter the accelerator at the most favorable phase angle. Early particles within a bunch are decelerated and late particles are accelerated. This process may be imitated to the bunching of vehicles that occurs as they go through a traffic light: protons are accelerated or slowed, as required, to group them into bunches. By this technique the percentage of the particles in the initial ion stream that are successfully accelerated is substantially increased.

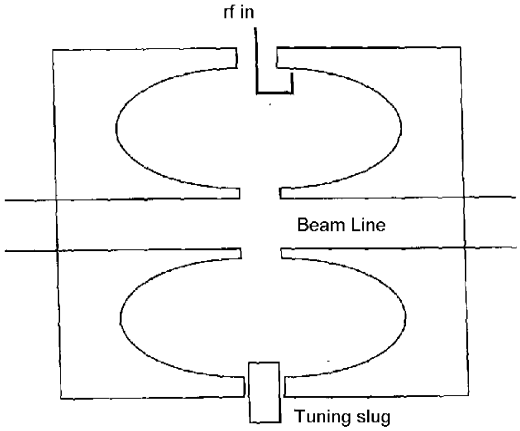

Figure 5.5 The prebuncher at LANSCE

The buncher itself is simply a resonant cavity that establishes an alternating potential across a gap in the beam line. In the LANSCE accelerator there are two bunchers between the ion generator and the drift tube linac. Both are driven at 201 MHz. The rf power for the two bunchers are in phase coherence with the rest of the 201 MHz rf system (DTL rf system). The first buncher is excited with relatively low power of 10-20 Watts, the second is excited with several hundred Watts.

5.5 Drift Tube Linac

The first section of the linac is of drift tube type developed from the original Alvarez design (figure 3.5). It uses four successive copper-lined tanks with drift tubes mounted along their axes to accelerate the beams from 750 keV to 100 MeV. An alternating electric field is set up in the tanks at a frequency of 201.25 MHz. The basic problem is to arrange for the particle bunches to reach each cavity at the exact time at which the rf fields is of the right sign and proper amplitude. This is done in the Alvarez linac by letting the particle bunches "drift" inside the tubes while the rf field goes through the decelerating part of its cycle (figure 5.6).

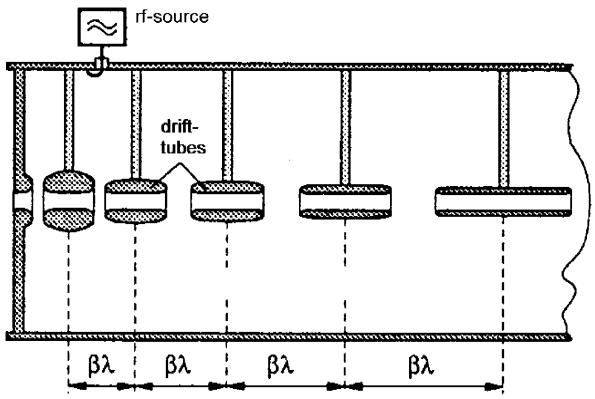

Figure 5.6 Illustration of drift tubes [12]
Electric field accelerates particles while they are in gap between drift tubes. Drift tubes shield particles while the field reverses direction.

In practice the cavities or cells at LANSCE are grouped together into four separate series known as a tank. There are a number of modes in which the particles can be accelerated in these tanks. In the 2pi mode (figure 5.7a), which is normally employed in Alvarez accelerators, the field is in the same direction in each cell at any given moment (standing wave). In the pi mode, the fields are oppositely directed in adjacent cells (figure 5.7b). In the pi/2 mode the field also alternates in direction but in addition every other cell contains no field.

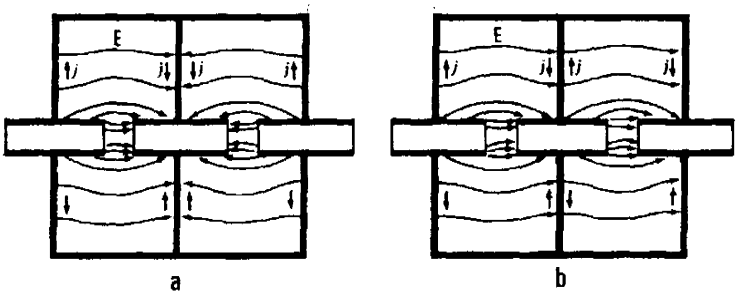

Figure 5.7 a)pi mode and b) 2pi mode

At LANSCE resonant posts are placed facing the drift tubes, they will transform the mode of operation of the drift tube linac from the conventional 2pi mode to something which approximates a pi/2 mode. By this, a way has been found to stabilize the beam, by a factor of 100. However, although it works very well for low energy protons, the drift tubes must become ever longer as the particle velocity increases, and correspondingly more of the rf power is then dissipated in the copper walls of the tanks and drift tubes. Another accelerating structure is necessary if one is to go much beyond 100 MeV at high duty factor.

5.6 Transition Region

The beam transport section between the Drift Tube Linac and the Side Coupled Linac is called the Transition Region (TR). The main functions of the Transition Region is to:

1) Transversely match the output H+ and H- beams from the DTL to the acceptance of the SCL.
2) To increase the flight path of the H- beam by 8 cm compared with the H+ beam so that the H- particles enter the SCL at an instant one-half 805 MHz rf cycle later than the H+ particles [13].

The TR have three beam lines. These lines are called (from top to bottom in Figure 5.8) the short track (H+), the straight through section, and the long track (H-). Each line includes four quadrupole magnets. During normal operation, one 20° bending magnet in the beginning of the TR separates the H+ and H- beam, another 20° bending magnet at the end recombine the beams. The short track includes two bending magnets and the long track includes four bending magnets. All the bending magnets are of the same design.

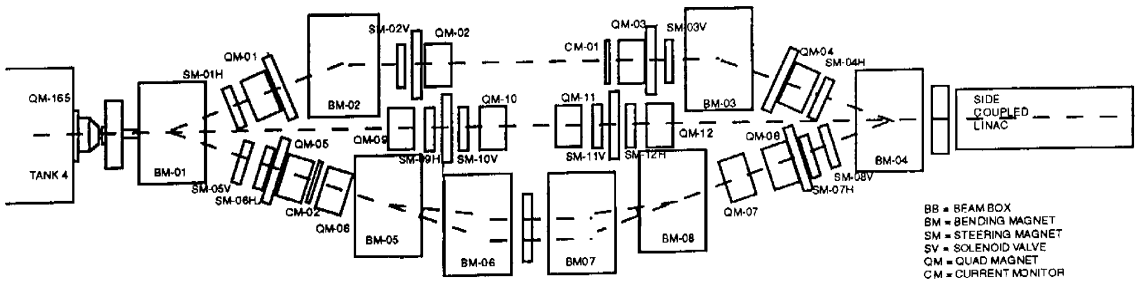

Figure 5.8 Transition Region at LANSCE [13]

5.7 Side Coupled Linac

The main section of the linac is a side coupled cavity system operated in the pi/2 mode at a rf frequency of 800 MHz. The side coupled linac (SCL) was developed at LANSCE over the years 1963 to 1970. The SCL allows the particles to be accelerated to high energy in much shorter distances than in the drift tube linac. With cells that are nearly enclosed instead of suspended drift tubes, the SCL is designed for maximum efficiency in space and power. Conversion of rf power to beam power is about four times more efficient in this section than in the DTL.

The unique field distribution in the pi/2 mode of operation provides a high degree of stability of the electromagnetic wave against effects due to heavy beam loading and manufacturing imperfections. The combination of efficiency and field stability allow high duty factor. The problem with the pi/2 mode, is that every other cavity carries no field and the accelerator is likely to be twice as long as a conventional one reaching the same energy.

From the mathematical model [14], it is realized that the pi/2 mode of operation allows a multitude of possible cavity configurations to be considered, all with the same excellent "mode" characteristics (see figure 5.9).

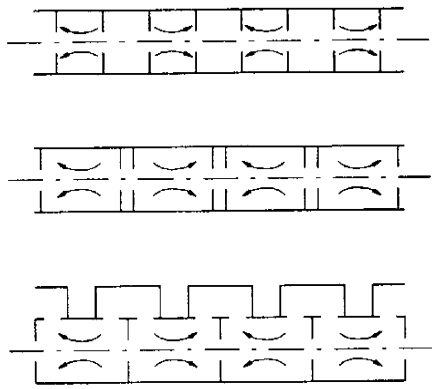

Figure 5.9 Illustration of different pi/2 mode structures [12]
All structures are excited in the pi/2 mode. Obviously the field free cavity may be completely moved off beam line.

In fact, the odd (empty) cavity may be completely moved off beam line. Of course, they still remain coupled via slots to the field carrying cavities.

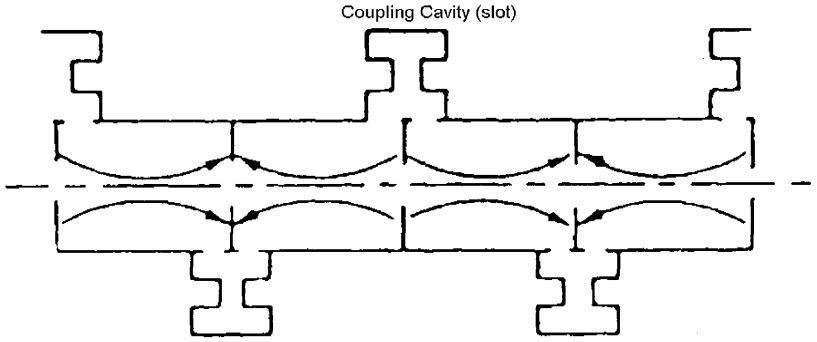

Figure 5.10 Side Coupled structure in pi/2 mode

This scheme has substantial advantages, namely (a) the a maximum length along the beam line is available for accelerating fields, (b) only small slots at the outer wall are required for coupling, allowing large amounts of freedom to design the online cavity for maximum efficiency, (c) the coupled cavity stores very little energy and thus little attention need to be paid to its geometry.

At LANSCE, the beam is accelerated in a series of 4962 resonant cavities, powered through coupling cavities on the side of the structure. The physical spacing between centers of resonant cavities increases steadily with increasing velocity of the particles, so each of the cavities has a different length. From a cell length of about 10 cm at 100 MeV to 20 cm at 800 MeV. A group of individual cells (12-18) are brazed into a section ranging from 1.5-2.5 m, including the side cavities, which forms a single vacuum-tight unit. A total of 352 such multi cell sections are spaced along the main linac. Various beam handling devices are mounted in the space between sections, such as quadrupole focusing magnets, beam monitors, and other control systems.

5.8 Switchyard

At the end of the linac the beams enter a beam switchyard in which a variety of focusing and deflecting magnets and other beam handling equipments are located. The beams are separated, focused, and diverted into the final beam lines and experimental areas. Deflection magnets provide simultaneous but separated H+ and H- beams. A large switchyard kicker magnet deflects the H- beam by 1.2° to the Proton Storage Ring or Line X. The H+ beam is deflected upwards and then into Line A.

5.9 Proton Storage Ring

The 30 m in diameter storage ring is located under ground and it became operable in April 1985. The Proton Storage Ring (PSR) acts as a bunch compressor, it converts the long beam pulses into short, intense proton pulses that provide the capability for precise neutron time-of-flight measurements. The Proton Storage Ring does not accelerate the particles. It compresses the 750 μs H- proton pulses from the accelerator into pulses about three thousand times shorter. These protons are used to produce neutrons in a target by spallation in either Manuel Jr. Lujan Neutron Scattering Center or the Weapons Neutron Research Center.

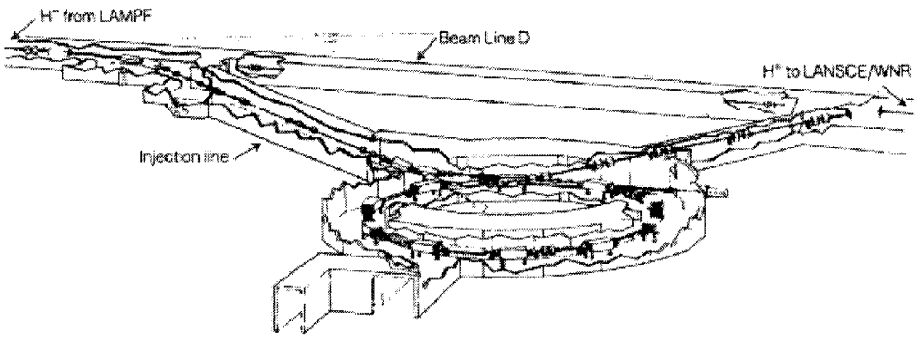

Figure 5.11 The Proton Storage Ring at LANSCE

5.10 Manuel Jr. Neutron Scattering Center

The Manuel Jr. Neutron Scattering Center (Lujan) is a high power, pulsed source of spallation neutrons that is used in condensed matter science, nuclear physics, and nuclear applications. Neutrons are produced when the proton beam impinges on a tungsten target. Moderators adjacent to the target is used to slow down neutrons. Lujan includes 16 neutron flight paths [15].

5.11 Weapons Neutron Research Center

In the Weapons Neutron Research Center (WNR) two target areas (target 2 and 4) are available, each with several flight paths aimed at bare target locations. Neutron beams with energies ranging from about 0.1 MeV to 600 MeV are produced in Target 4 (an unmoderated tungsten spallation source). In the Target-2 area (Blue Room) samples can be exposed to the direct 800 MeV proton beam. A H- chopper is installed to allow isolated micropulses of beam to be delivered to these targets. The WNR complex is used for national security research and basic nuclear physics research.

6 LANSCE Accelerator operations

6.1 Introduction

During operation beam delivery is measured by current monitors near the target. If the beam current for some reason is below a threshold current the beam is considered as interrupted. The event/trip generates a loss in scheduled beam time, commonly called down time. The underlying cause of the event is appointed a down time assignment, this is done by the operator (Beam Delivery Team) situated in the Central Control Room. The down time assignment is recorded in the logbook. An automated system extracts the down time assignments from the logbook and enter them along with current monitor data in a database (Excel spreadsheet). One database exists for each beam line or target area. From the database further down time statistics are obtained.

6.2 Down time assignment

The operator or the Beam Delivery Team is situated in Central Control Room (CCR). Whenever a beam loss occurs the operator appoints the trip a down time assignment. The computer presents a menu to the operator that requires entries of down time assignments. The computer also prompts the operator for comments on the cause of the beam trip.

Every down time assignment includes an Area assignment and a System assignment. A single set of Area and System categories are available to choose from. A list of System categories is presented in table 6.1.

The Area assignment indicates the geographical location in the accelerator complex where the failure occurred. The System assignment defines the kind of equipment responsible for the down time [16].

Table 6.1 System Definitions Used for Down Time Assignment [16]

SYSTEM	DEFINITION
201	201 MHz Radio Frequency System: pad power supplies, capacitor rooms, amplifier systems, interlocks (flow, temp, etc.), resonance controllers and valves.
805	805 MHz Radio Frequency System: pad power supplies, capacitor rooms, amplifier systems, klystron systems, interlocks (flow, temp, etc.), resonance controllers and valves. Includes prebunchers (but excludes Proton Storage Ring buncher.)
CTRL-HW	Control HardWare: Computer, control system and network hardware. Includes hardware on VAXes, Suns, remotes, CAMAC, VME, Remote Instrument and Control Electronic (RICE), Analog Digital System (ADS), networks, console equipment, printers, knobs, etc. Excludes Master Timer.
CTRL-SW	Control Software: Computer, control system and network software. Includes software on VAXes, Suns and remotes.
DIAG	Diagnostics: Problems with harps, wire scanners, current monitors, Delta T hardware, strippers, scrapers, emittance systems, and Beam Position Monitors.
DC-MAG	DC Magnets: Magnets, winding, DC cabling, flow and temperature switches, vacuum and water leaks, magnet water strainers. Does not include power supplies.
DC-MAG-PS	DC Magnet Power Supplies: electronics, trips, interlocks (flow, ripple, etc.), water leaks.
EXPT	Experimenter: Flight paths, shutters and secondary beam lines, experimenter requested beam-off. *Further clarification TBS by M. Zumbro.*
FACILITY	Facility problems not elsewhere on the list (water main leaks, compressed air, natural gas, etc.)

HVAC	Heating, Ventilation and Air Conditioning system problems.
INJECTOR	Ion sources, ion source support equipment, Cockcroft-Walton generator. Includes ion source power supplies, 80KV/670KV/750KV columns and power supplies.
INTLKS	Interlocks: Fast Protect, Run Permit, Hard Ware Transmission Monitor, Loss Monitors and Area Protect problems. Weekly Radiation Security System (RSS) checks. Interlock checks during scheduled production that are not required by an RSS trip. Failures of interlock hardware. If an RSS trip report is required, see RSS-TRIP.
OTHER	Cause is known but does not fit in above categories. Use comments to identify.
POWER	Site power, the AC electrical distribution system for 110V and above. Includes outlets, breaker failures, power line surges, etc.
PULS-PWR	Pulsed Power System: Kickers, Ring buncher, deflectors, inflector, choppers and their related power supplies, local controls and modulators.
RSS-TRIP	Radiation Security System (RSS) trips: RSS and Personal Security System (PSS) trips. E.g. SCRAM switch actuation, doors rattled, high spill on gamma detectors, current detector sees too high current, etc. Anything requiring an RSS trip report. RSS-TRIP is not part of INTLKS because an RSS trip is an important safety issue.
TARGETS	All production targets, target boxes, beam stops, proton inserts, degraders, isotope stringers and foils. Includes flow and temperature interlocks and water and vacuum leaks.
TIMING	Problems with Master Timer and timing signal distribution.
TUNE-RECOVERY	Tuning other than TUNE-UP. Spill. High losses. Off-energy beam, micropulse contamination, off-center beam at Lujan target, etc.
TUNING	Intentional tuning to bring beam to production status. Does not include tuning time require to recover from an equipment problem. Typically used for recovery from inter-cycle breaks and scheduled maintenance periods. *(This system assignment was abandoned in 1996, hence only assignments made before 1997 may include "tuning".)*
TUNE-UP	Tuning to bring beam to production status after scheduled down-time periods such as inter-cycle breaks and maintenance days. Tuning to recover after down-time caused by equipment failure is attributed to the failed system.
UNKNOWN	Cause of down-time cannot be identified.
VACUUM	Vacuum system: Vacuum pumps, pump power supplies, roughing packages, valves, instrumentation, controls, pipes, flanges. Does not include leaks in individual components or loads such as magnets, targets, etc.
WATER	Cooling water systems: pumps, pump controls, makeup water, valves, pipes, heat exchanges. Does not include leaks and flow problems in individual cooled components such as magnets, amplifiers, cavities, etc. unless problem is caused by variations or limits in water system.

Usually the System assignment identifies the personnel responsible for attending the failure, although the same crew may be responsible for several Systems. In general, the assignment should point to the System to "cost effectively make the problem go away", not to the first-out system. This may in some cases result in misleading down time assignment. For example, if the prebuncher malfunctions the System assignment in the logbook is 805 since the 805 rf personnel is responsible for the prebuncher, but the prebuncher is actually driven by the 201 rf system and the correct assignment should be 201.

6.3 Databases

Beam trips that occur within the frame of scheduled production are recorded in the databases. Events affecting the beam that take place outside scheduled production may be available in the logbook but this information is not included in the databases.

Depending on which beam line or target the trip affects beam trips are sorted into different databases (Excel spreadsheets). Subsequently, beam trips are classified into five databases, namely:

Table 6.2 Description of Databases

Database	Description
Area A	Includes all beam trips affecting the H+ beam line from the H+ injector to target Area A.
Lujan	Includes beam trips affecting the H- beam when delivered to Manuel Jr. Neutron Scattering Center.
WNR T2	Includes beam trips affecting the H- beam when delivered to Weapons Neutron Research Center Target 2.
WNR T4	Includes beam trips affecting the H- beam when delivered to Weapons Neutron Research Center Target 4.
Line X	Includes beam trips affecting the H- beam when delivered to Line X.

A schematic overview in table 6.3 presents which accelerator section is an integral part of each database.

Table 6.3 Schematic overview of equipment and beam lines corresponding to each database
LEBT - Low Energy Beam Transport located after the injector, before the Drift Tube Linac (DTL). In this table the Linac embraces all equipment associated with the Drift Tube Linac, Transition Region, and the Side Coupled Linac.

Database	Accelerator Section								
	H+ Injector	**H- Injector**	**H+ LEBT**	**H- LEBT**	**Linac**	**Line A**	**Line D**	**Line X**	**PSR**
Area A	X		X		X	X			
Lujan		X		X	X		X		X
WNR T2		X		X	X		X		X
WNR T4		X		X	X		X		X
Line X		X		X	X			X	

Table 6.3 gives information in which database (or databases) a particular failure is recorded. For example, a failure in the H+ injector will only be recorded in the Area A database. Where a failure in the Linac will be recorded in all databases since all beam lines utilize the Linac section. **This allows for overlapping of beam trips in the databases.** Identical trips may be recorded in several databases. This must be taken in consideration when merging of databases is in question.

6.4 Beam Schedule

Ahead of time a beam schedule has been organized with respect to time-sharing between experiments, beam intensity, and beam energy. An overall schedule of commissioned beam time between different beam lines is set out.

Scheduled operation at LANSCE is divided into run cycles. During scheduled operation, the accelerator is operated almost 24 hours per day for an entire run cycle with only a few scheduled breaks. A run cycle is maintained for approximately 5-6 weeks

(800-1000 hours). In table 6.4 run cycles and beam schedules for the H- beam are presented.

Table 6.4 Run cycles and scheduled H- beam time

Year	Cycle	Scheduled Time [hours]
1993	63	648
	64	636
	65	549
1994	66	Not Scheduled
	67	Not Scheduled
	68	Not Scheduled
1995	69	1366
	70	998
1996	71	964
	72	1062
	73	654
1997	74	755
	75	956
	76	752

Between run cycles two or three maintenance days are scheduled. Usually there are three run cycles per year. An extended maintenance period is initiated at the end of the last run cycle each year. In figure 6.1 an illustration of the scheduled H- production for 1996 is displayed.

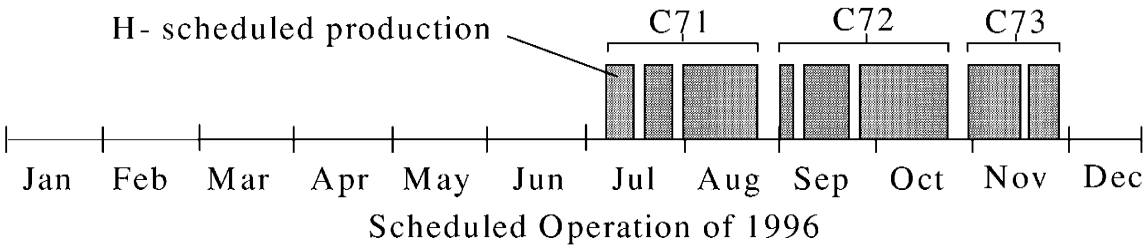

Figure 6.1 Illustration of Scheduled H- Production at LANSCE
Gray boxes are scheduled operation, white spaces in between represent maintenance period.

The LANSCE accelerator delivers two beams (H+ and H-) to different target areas and each target area has a separate schedule. In other words, Area A, which receives the intense H+ beam from Line A has a different schedule compared to the Lujan or WNR target facility which receives the H- beam via Line D.

7 Overall LANSCE Reliability

7.1 Introduction

In this chapter operational statistics of the entire LANSCE accelerator facility is presented. The overall reliability/availability of the accelerator is analyzed, all systems are included. For the most part, the reliability for cycles 71-76 is discussed, but some early reliability history will also be presented. A more penetrating reliability analysis for individual subsystems and components is performed in chapter 8.

The Area A and the Lujan databases for Cycles 71-76 (1996-97 operations) are used for all statistics.

Main reasons for utilization of Area A and Lujan databases are:

- At a rough estimate, Area A and Lujan covers >95% of all beam trips and scheduled beam time for 1996-97 operation.
- Area A includes all beam trips common to the powerful H+ beam line.
- Lujan includes trips common to the H- beam line and the Proton Storage Ring.
- During 1996-97, commissioned beam time was longest for Area A and Lujan
- Most beam trips common to Lujan and WNR are overlapping. On comparison, only a small fraction of beam trips are unique for each beam line. Therefore it is little gain in processing the WNR database as well.
- Line X was hardly ever in operation during 1996-97.

Trips that arise in the Linac (DTL and SCL) structure will overlap in both databases. But, results are treated separately and comparison of beam trips is not necessary.

7.2 Definitions

down time - any unscheduled time recorded in the logbook when beam current is below a threshold current. For 1997 the threshold current was one-half the scheduled current.

availability - time beam was delivered at or above a threshold current divided by the scheduled time.

7.3 Operational statistics

7.3.1 H+ Beam line (Area A)

In this section, the distribution of beam trips and down time of the H+ beam line are presented. The analysis considers accelerator operation during scheduled H+ production for 1997 (Cycles 74-76).

7.3.1.1 H+ Beam schedule

The total scheduled beam time is an important factor **-beam trips are only recorded if they occur within scheduled production**. To obtain the total scheduled beam time it is necessary to investigate the beam schedule closely. In Appendix 1, a detailed beam schedule is available for the H+ beam.

For 1997, the total scheduled beam time of the H+ beam was 2870 hours. The accelerator was operated in three run cycles (cycles 74-76), scheduled production started in 18th of March and ended the 27th of July. In general, one or two scheduled interruptions took place inside each run cycle. Each of these interruptions lasted for 1-2 days. At the end of each run cycle a two-day maintenance activity was performed. In figure 7.1, a perspective on the historical operation of the H+ beam is presented.

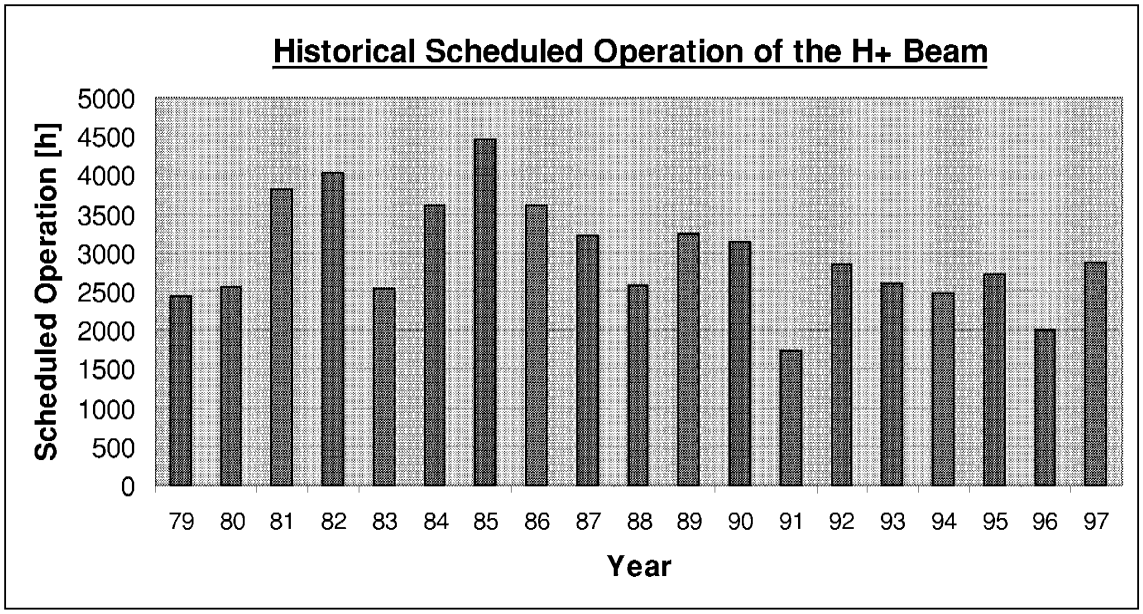

Figure 7.1 Scheduled Operation of the H+ Beam at LANSCE (1979-97) [17]

Scheduled operation is usually in the region of 2000-3000 hours per year, about 30 % of the year. In 1985, the longest schedule ever was practiced. The accelerator was commissioned for 4500 hours and it operated with normal availability (83 % in figure 7.5).

7.3.1.2 H+ Beam statistics

Beam trips and the distribution of down time of the H+ beam are shown and discussed.

From the Area A database, statistics of beam trips and the distribution of down time is obtained for the H+ beam. In figure 7.2 beam trips are sorted into down time intervals. In order to explicitly show the influence of the injector an extra column has been added which does not include any trips caused by the H+ injector.

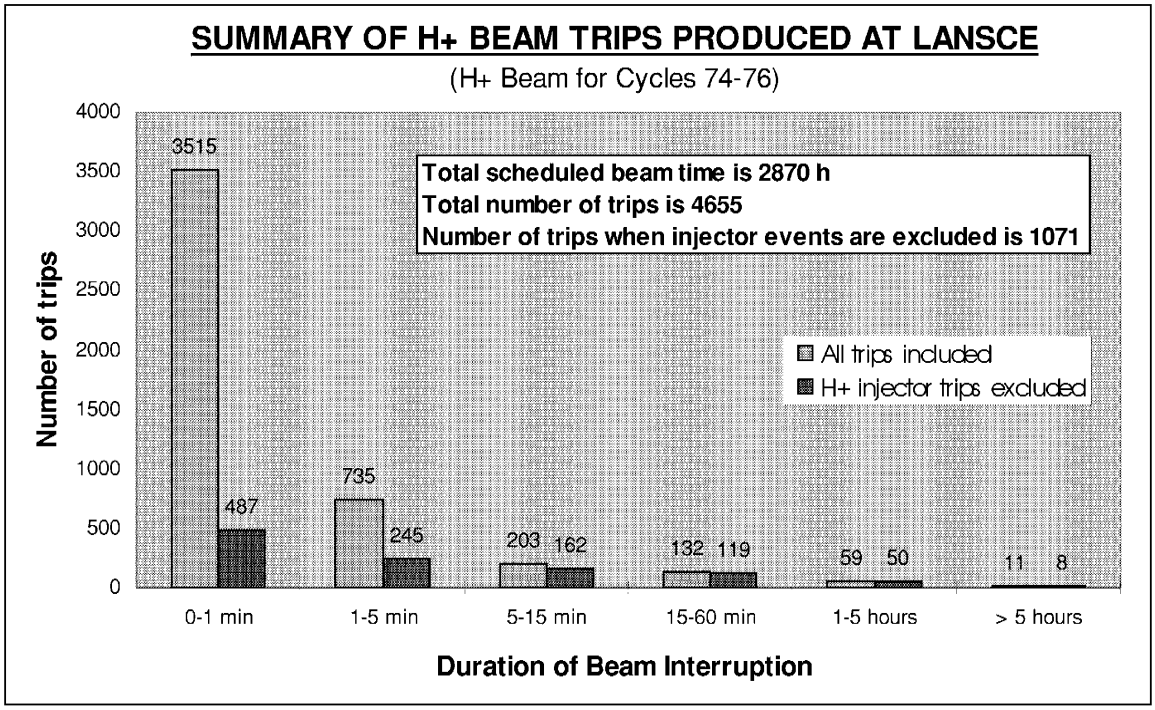

Figure 7.2 Summary of H+ Beam trips produced at LANSCE for Cycles 74-76

From figure 7.2 it is obvious that the H+ injector is causing many short beam interruptions. Using the numbers from figure 7.2 the average number of H+ trips per hour may be calculated:

Average number of H+ trips per hour:
4655/2870 = 1.62 trips/h

The most common injector failure is arcing in the high voltage column. This may be due to a contaminated column, bad vacuum, dust on the column surface etc. The characteristic of the injector trip is the interruption length. It is shorter than 1 min, usually in the order of 10-20 seconds, the time it takes to reset the trip and re-energize the generator. In each down time interval the three most dominating failures are presented in table 7.1. The Systems are ordered in the fraction of total number of trips the system is responsible for in each downtime interval (for System references see table 6.1).

	H+ Beam Interruption length					
	Short		**Medium**		**Long**	
No	**0-1 min**	**2-5 min**	**5-15 min**	**15-60 min**	**1-5 h**	**>5 h**
1	Injector (86%)	Injector (67%)	Injector (20%)	805 RF (37%)	Injector (15%)	Targets (36%)
2	Unknown (3%)	201 RF (11%)	201 RF (18%)	201 RF (11%)	Targets (14%)	Injector (27%)
3	Tune-Recovery (3%)	Interlocks (4%)	805 RF (16%)	Injector (10%)	805 RF (12%)	805 RF (18%)

Table 7.1 Predominant H+ failures in each down time interval
The Systems are ordered after the fraction of trips the system is responsible for. For example, in the down time interval 15-60 min the 805 RF System is responsible for 37% of all trips.

In the interval of 0-1 min the injector is responsible for almost 90% of all H+ beam interruptions. For medium down times, the fraction of trips produced by the injector is much smaller. Some short trips were unknown, since they were short they were, at the time of occurrence, not investigated thoroughly. On the other hand, it was possible to assign a known system for all other trips with down time longer than 5 minutes. At medium down times (>5 min) the RF System contributes more to the total number of trips. In fact, the 805 RF System (includes the klystron system) dominates the failure cause in the interval of 15-60 minutes. For long down times the Targets and the Injector are responsible for a large portion of the trips. The injector was shutdown in order to investigate the reason for the short injector trips. Only a few trips with long down time occurs and a system causing only a small number of long trips is rather dominating.

In figure 7.3 all trips are classified into systems. The systems are presented in order of importance, starting at left-hand side with the System responsible for most of the trips.

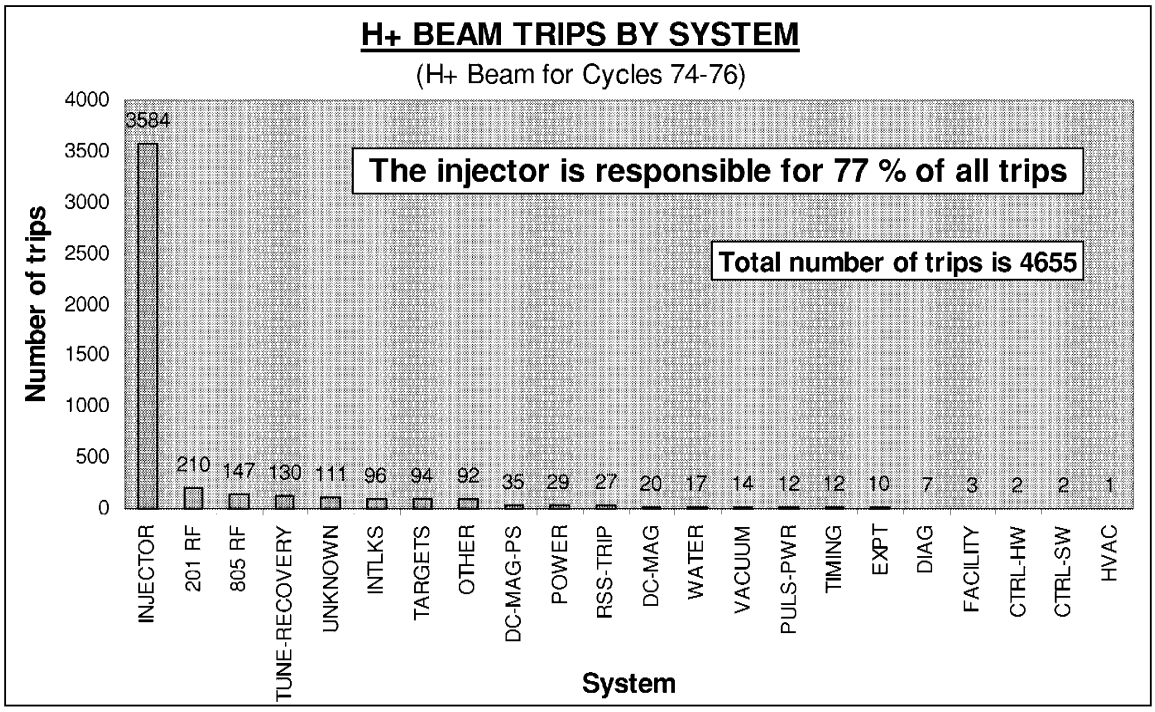

Figure 7.3 H+ Beam trips produced by each System

Again, it is obvious that the injector is the origin for most of the trips.

Predominant failure causes of the H+ beam are:

1) H+ Injector (77 % of all trips)
2) 201 RF System (5 % of all trips)
3) 805 RF System (3 % of all trips)

As far as now we have only looked at the number of **trips** (interruptions) each system is responsible for, another important point is the **down time**. In figure 7.4, the total down time produced by each system is presented.

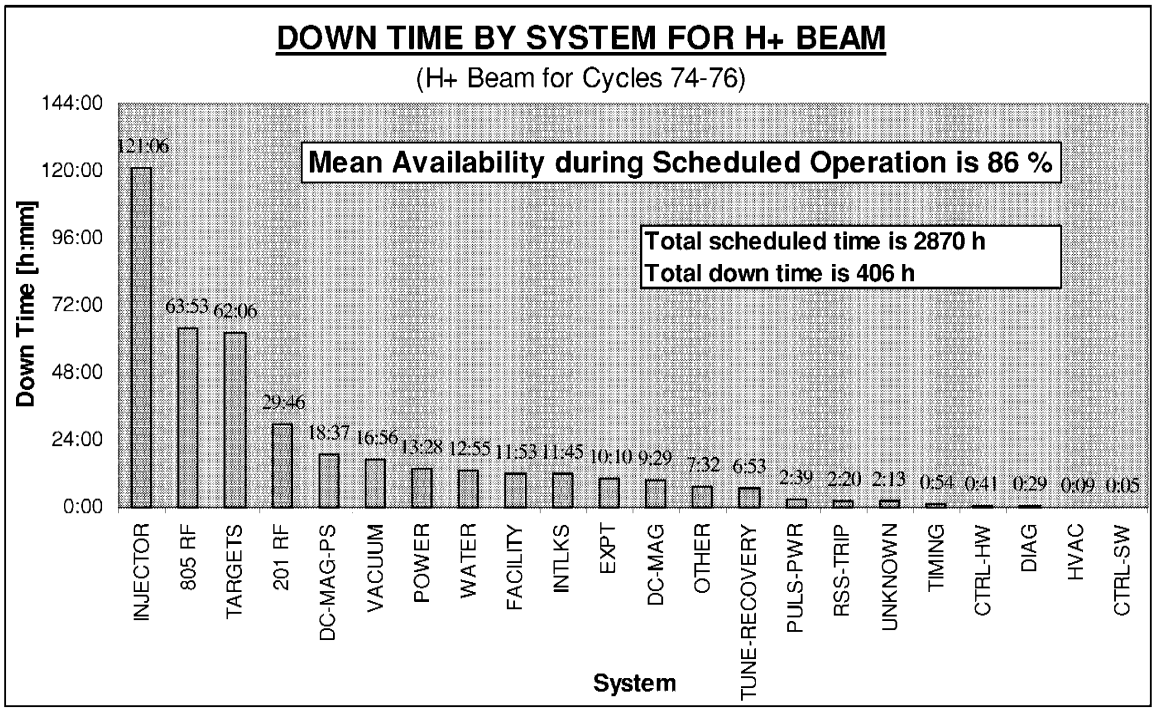

Figure 7.4 H+ down time produced by each System

Now the result looks a little bit different. While the injector is responsible for 77% of all trips it is "only" producing 30% of the down time. The 805 RF System is generating 3 % of the trips but is accountable for 16 % of the down time. This is a direct consequence of the fact that the injector is producing mainly short interruptions while the 805 RF System generates trips with long down time (15-60 min). Most of the H+ down time is concentrated to a few Systems, namely:

The three largest contributers of H+ down time are:
1) H+ Injector (30 % of all down time)
2) 805 RF System (16 %)
3) Targets (15 %)

The availability of the accelerator is defined as:
Availability = Total Up Time [h] / Scheduled Beam Time [h]

The availability is a measure of how large fraction of the scheduled beam time the accelerator is actually operating. Another interpretation would be what the probability is for a functioning accelerator at a given instant of time.

For 1997, the availability of the H+ Beam at LANSCE was:
H+ Availability = (2870-406)/2870 = 86 %

It must be noted that the availability only measures the availability of the accelerator during **scheduled operation**. A common misunderstanding is that the availability of the machine is the availability over the whole year. If that was the case, the availability of LANSCE for 1997 would be (2870-406)/8760 = 28 %. A large fraction of the year the accelerator is not scheduled due to maintenance activities. In figure 7.5 historical H+ availability data for 1979-97 is presented [17].

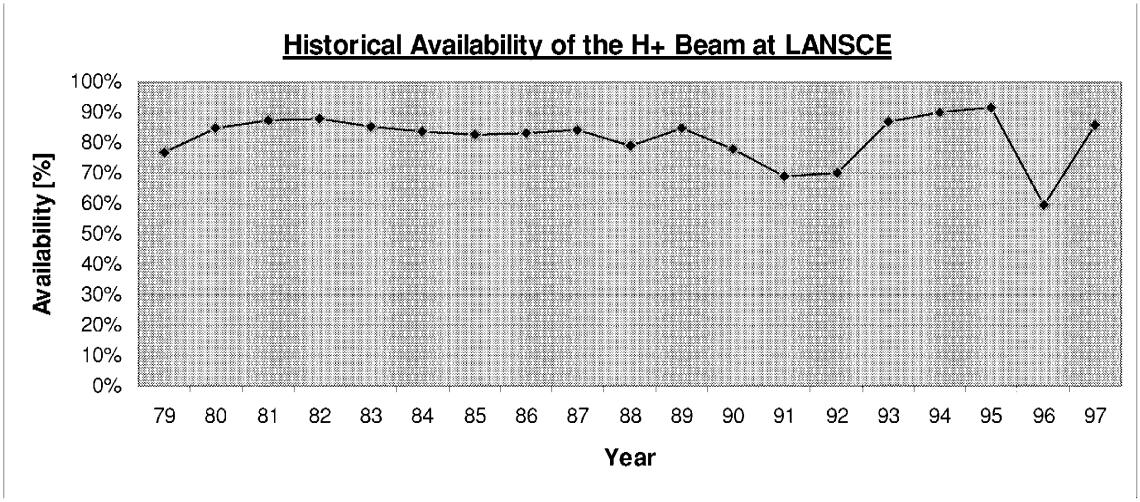

Figure 7.5 Perspective on the historical Availability of the H+ Beam at LANSCE (1979-97) [17]

In 1996, the availability experienced a decline due to a single water leak in one of the targets, otherwise the availability of LANSCE is usually in the region of 80-90 %. This level of availability is also in good agreement with other accelerators, for example at SLAC:

Accelerator	Year	Availability
SLC	1993	82.8 %
SLC	1994	80.7 %
SLC	1996	79.0 %

Table 7.2 Availability of the Stanford Linear Collider (SLC) ref SLAC Accelerator operations report.

7.3.2 H- Beam line (Lujan)

Similar analysis of beam trips and down time has been done for the H- beam. Operational statistics of the H- beam line to Lujan Neutron Scattering Center are investigated. The H- beam is analyzed during scheduled production for 1996-97 (Cycles 71-76).

7.3.2.1 H- Beam schedule

During 1996 the H- beam was operated in three run cycles (Cycles 71-73). Cycle 71 started at the 10th of July and Cycle 73 ended at the 28th of November. Between each

run cycle the beam was off schedule for 4-8 days due to maintenance periods. Within each run cycle the beam was also off for shorter maintenance activities. The total scheduled H- beam time for 1996 was 2681 h.

In 1997 the H- beam was also operated in three run cycles (Cycles 74-76). Cycle 74 was initiated at the 7th of March and Cycle 76 ended at the 24th of July. During 1997 the H- beam was scheduled for 2463 h.

Since this section investigates the reliability for both 1996 and 1997 the important beam time is the total scheduled time. For 1996 and 1997 the total scheduled time was 5144 h. In Appendix 1 a detailed schedule of the H- beam during 1996-97 is available.

In figure 7.7 some historical scheduling information of the H- beam line at LANSCE is presented.

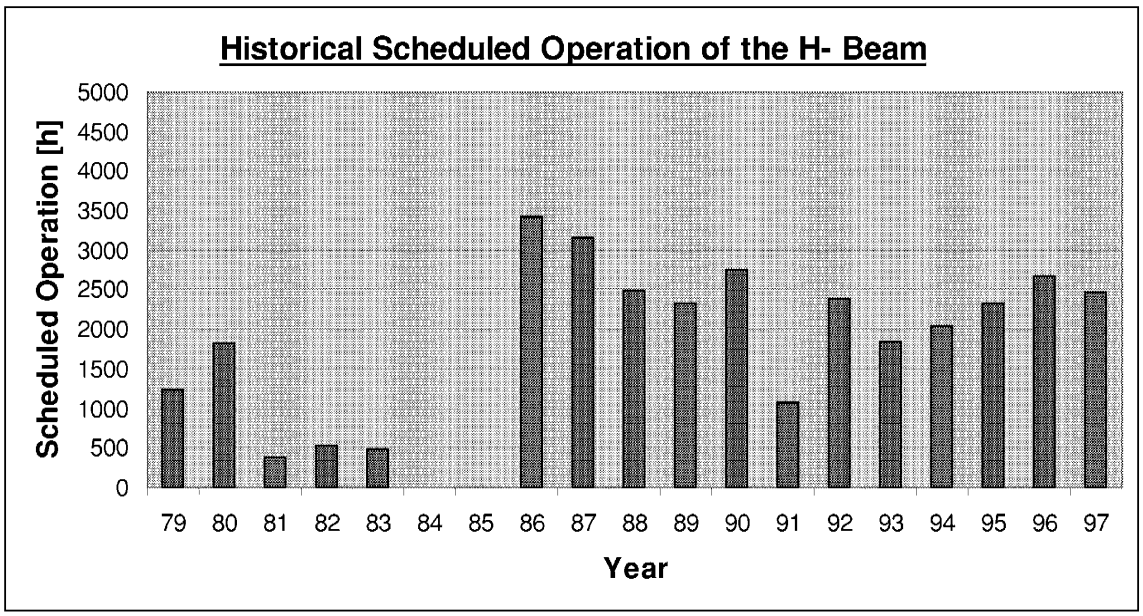

Figure 7.7 Scheduled Operation of the H- Beam at LANSCE (1979-97) [17]

Historically the H- beam has been scheduled less time than the H+ beam (compare with figure 7.1). During 1984-85 the Proton Storage Ring was under construction and hence the H- beam was not scheduled at all.

7.3.2.2 H- Beam statistics

The overall statistics of beam trips and down time produced by the H- beam are presented.

In fig 7.8 a summary of all beam trips is shown. An extra column has been added in order to point out the influence of the injector.

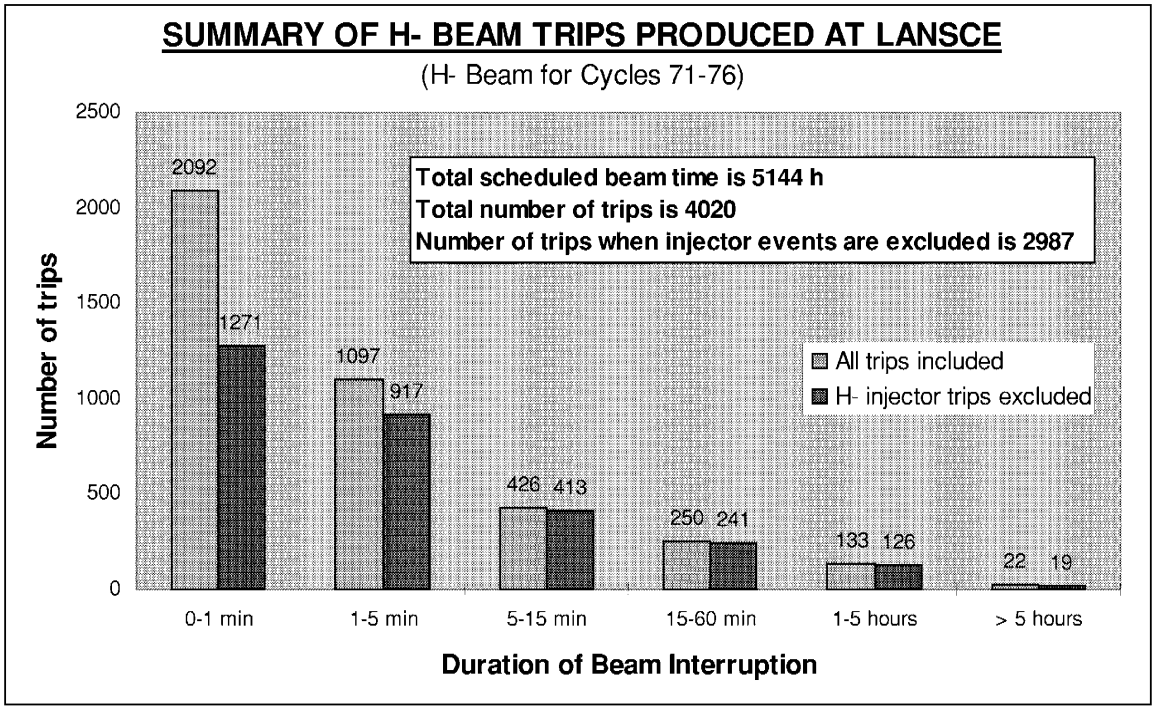

Figure 7.8 Summary of H- Beam Trips produced at LANSCE during 1996-97

The H- beam is more reliable than the H+ beam (compare with figure 7.2). This is mainly due to a more stable H- injector.

Average number of H- trips per hour:
4020/5144 = 0.78 trips/h

In table 7.3 the predominant failures in each down time interval are presented.

	H- Beam Interruption length					
	Short		Medium		Long	
No	**0-1 min**	**2-5 min**	**5-15 min**	**15-60 min**	**1-5 h**	**>5 h**
1	Injector (40%)	Other (21%)	805 RF (19%)	Targets (17%)	Targets (16%)	Mag PS(18%)
2	Interlocks (12%)	Injector (16%)	Other (13%)	805 RF (13%)	Water (11%)	Vacuum(18%)
3	Unknown (10%)	201 RF (11%)	Rss-trip(12%)	Rss-trip (9%)	Mag PS (9%)	Injector (14%)

Table 7.3 Predominant H- failures in each down time interval
The Systems are ordered after the fraction of trips the system is responsible for in each interval. For example, in the down time interval 5-15 min the 805 RF System is responsible for 19% of all interruptions.

In the interval 0-1 min the H- injector is "only" responsible for 40% of the trips. The H- injector produces only a few long down times. Again, as in the case with the H+ beam, the 805 RF System is responsible for many trips in the medium down time interval (5-60 min). It is natural these trips occur to both beams since both beam lines utilize the same RF System. In the medium and long down time interval the targets are troublesome. Many long H- trips occurred due to problems with the target moderator. A single Magnet

Power Supply in the Proton Storage Ring was causing very long interruptions during 1996.

In figure 7.9 all trips are classified into systems. The systems are presented in order of importance, starting at the leftmost with the system responsible for most of the trips. The diagram does not consider the duration of the interruption.

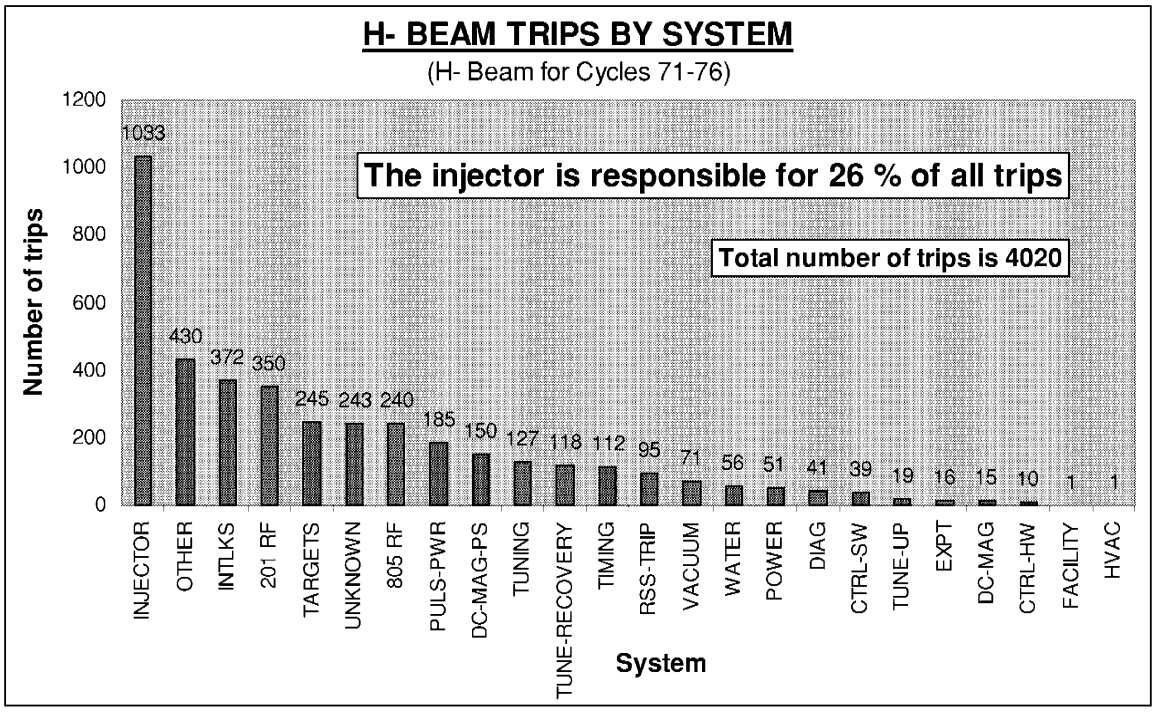

Figure 7.9 H- Beam trips produced by each System

Predominant failure causes of the H- beam are:

1) H- Injector (26% of all trips)
2) Other (11%)
3) Interlocks (9%)

Even though the H- injector is still the largest producer of trips (26% of all trips) it is obviously much more reliable than the H+ injector (77% of all trips). The assignment "Other" is responsible for 11 % of the trips. In most of these trips the accelerator is not subject to any actual component failure. Sometimes beam measurements are performed which prevents the beam from reaching the target. 9% of all H- beam trips are assigned "Interlocks". The underlying cause of these interruptions are sometimes unknown. For example, a loss monitor detects a high beam spill in the Proton Storage Ring and subsequently the Fast Protect System shuts the accelerator off, but the underlying cause of the beam spill is unknown.

In figure 7.10 the total down time produced by each system is displayed. The systems are presented in order of importance, starting with the largest contributor of down time on the left-hand side.

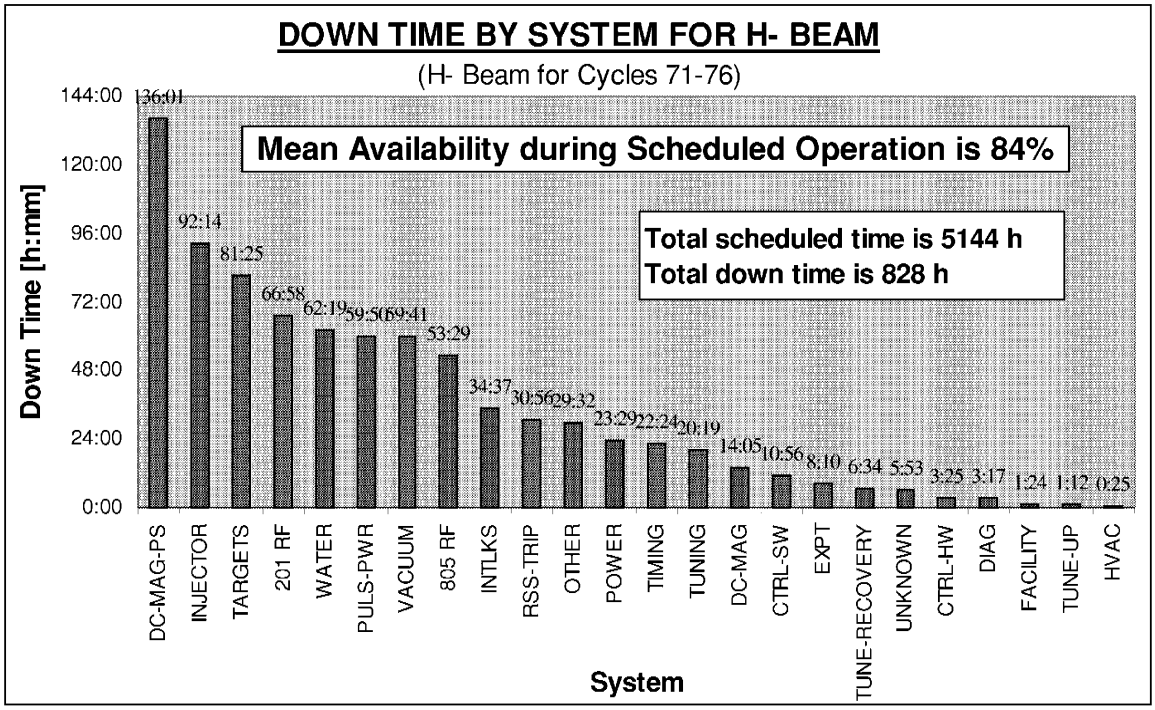

Figure 7.10 H- down time produced by each System

The H- down time is more evenly distributed among several systems in comparison with the H+ beam (see figure 7.4). It is interesting to note that the H- injector is not causing as much down time even though it is without doubt the largest producer of trips (see figure 7.9). Instead the Magnet Power Supply system is clearly the largest contributor of down time. During 1996 a single power supply in the Proton Storage Ring was causing very long interruptions (days). For that reason, the event may be regarded as extraordinary, it is not likely that the Magnet Power Supply System will cause a similar failure the following year. On the other hand, it is not unusual that one or a few extraordinary failures are responsible for a large portion of the total down time. For example, during 1996 the H+ beam was off for several days due to a single water leak in the target. Therefore, it is not justified to exclude the extraordinary down time, since they do occur, but the Magnet Power Supply System will not always be predominant. Almost any System may be responsible for a failure which causes long down time.

For 1996 and 1997, the largest contributors of H- down time were:

1) Magnet Power Supplies (16 % of all down time)
2) H- Injector (11%)
3) Targets (10%)

The Availability of the H- Beam was:

Availability 1996 = (2680-449)/2680 = 83 %
Availability 1997 = (2463-379)/2463 = 85 %

In figure 7.11 a perspective on the historical availability of the H- beam is presented.

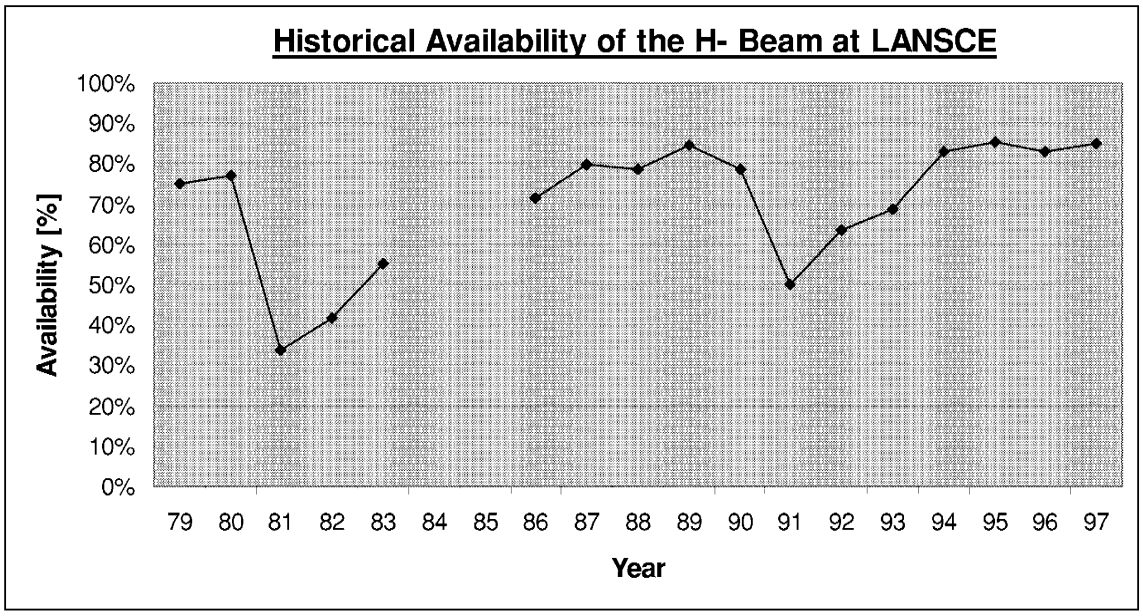

Figure 7.11 Perspective on the historical Availability of the H- Beam at LANSCE (1979-97) [17]
1984-85 the Proton Storage Ring was under construction, hence no H- beam was delivered.

Obviously the historical availability of the H- beam has changed significantly from year to year, but the last 4 years (1994-97) the availability has been in the region of 80-90 %.

7.3.3 Conclusions

In the overall reliability balance of the entire LANSCE accelerator, the injector is responsible for most of the trip events. For short interruptions (<1 min) the H+ injector is accountable for 90 % of all trips of the H+ beam. In other words, a more reliable injector in combination with, for example, an RFQ could substantially reduce the number of beam interruptions. For long down times (>5 min) the injector is no longer the main source of trips, but instead the RF System is the primary generator of trips. A short summary of all beam trips produced by the H+ and H- beam is presented in table 7.4.

SUMMARY OF THE LANSCE ACCELERTOR					
Beamline	**Period**	**Cycles**	**Scheduled Beam Time [h]**	**Total number of trips**	**Average number of trips per hour [trips/h]**
H+ Beam	1997	74-76	2870	4655	1.62
H- Beam	1996-97	71-76	5144	4020	0.78

Table 7.4 Summary of Beam Trips produced at LANSCE

One may conclude that the H+ beam experiences twice as many trips per hour than the H- beam. When operating, the H+ beam experiences almost 40 trips/day. That is mainly due to problems with the H+ injector. One should keep in mind that the injector

used at LANSCE is an electrostatic Cockcroft-Walton type injector. It is therefore justified to exclude many of its trips when using these numbers for future accelerators. Modern microwave ion sources present a significant increase in reliability. For example, the new microwave proton injector developed for the APT project proves to be very reliable. In figure results from the LEDA Injector Availability Test [9] is presented.

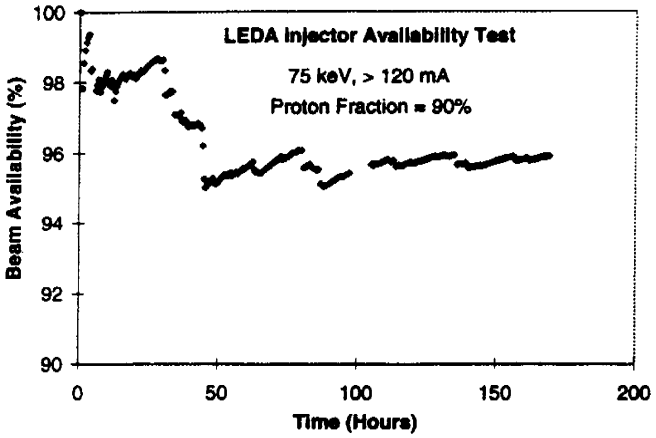

Figure 7.12 LEDA injector beam availability test
LEDA is the Low Energy Demonstration Accelerator developed to demonstrate the LEBT system for the APT accelerator [9]

Two important means when measuring reliability is the Mean Time Between Failure (MTBF) and the Mean Down Time (MDT). In Table 7.5, the Availability, MDT and MTBF for the entire accelerator are shown.

OVERALL RELIABILITY OF LANSCE				
Beamline	**Classification**	**Availability** [%]	**MDT** [h:mm]	**MTBF** [h:mm]
H+ Beam	All trips included	86 %	0:05	0:31
	Injector trips excluded	90 %	0:15	2:22
H- Beam	All trips included	84 %	0:12	1:05
	Injector trips excluded	87 %	0:14	1:35

Table 7.5 Overall Reliability of LANSCE

The overall availability of the machine is in the region of 80-90 % for both the H+ beam and the H-. This level of availability is in the same range as that observed in other accelerators. MDT for the H+ and H- are both found shorter when the injector trips are included compared to the case when the injector trips are excluded. This is obvious since the injector produces mainly short interruptions (see figure 7.2 and 7.7). MTBF for the H+ beam is significantly shorter due to the large amount of injector trips produced.

In the case where the injector trips are excluded, it is interesting to note that the MDT is almost the same for H+ and H- even though these numbers originate from two different data sets. This makes sense since both beam lines utilize, for most of their length, the same accelerating structure. Where the beam lines are separate, the components are very similar. MTBF for the H+ beam when the injector trips are excluded is longer in comparison to the MTBF for the H- beam. The reason is that the H- beam

line is more complex, since it includes the Proton Storage Ring, and hence more components are subject to failure.

The conclusion is that upgrading the injector would result in a more stable beam with less interruptions, especially short ones. This would significantly increase the MTBF. The RF System and the Magnet Power Supplies are next in order important. Upgrading the RF System would reduce the total down time and the accelerator would gain a better availability. A shorter MDT would be also be achieved since the RF System is responsible for many long interruptions.

8 Subsystem and Component Reliability

8.1 Introduction

In this chapter the reliability of major LANSCE accelerator systems are investigated. For this purpose, the raw data is divided into categories corresponding to individual subsystems and subsequently estimates of failure and repair rates are obtained. With the progression towards individual components, the available statistics become more and more scarce. To address this issue, the analysis combines the data from the H+ and the H- beam for six run cycles to enlarge the size of the samples.

The objective of the present data collection and analysis effort is to understand the behavior of existing operating accelerator facilities so that better, more reliable systems can be designed and built in the future. Previous work has identified the current state of the art lacking in the area of reliability database information for components typically used in rf accelerator systems, such as rf stations, rf drives, rf transport, cooling, vacuum systems, magnets, and magnet power supplies. Thus, while it is possible to use the reliability theory to model accelerator systems, the input data currently available for such analyses lacks credibility. This led to the initiation of an effort of data collection and analysis of which this study is one of the tasks. The present work examines the data set of failure events for the LANSCE accelerator facility.

8.2 Method

From the input data (section 8.2.1) failures associated with the following main systems were extracted and analyzed.

Main Systems for which reliability analysis has been performed:

1) 805 RF System
2) DC Magnets
3) Magnet Power Supplies
4) Pulsed Power
5) Water System
6) Vacuum System

Individual failures corresponding to these systems were thoroughly investigated with the help of logbooks, operational reports, operators, maintenance personnel and other experts in particular fields. The aim was to detect the root cause (down to component level) of each failure. Each failure was classified into subsystems (see table 8.1). Trips were then entered along with their failure causes into different databases (see table 8.2) depending on which system and subsystem the trip affected. Trips affecting the H+ and the H- beam line were merged into the same records. From the databases further reliability statistics were obtained.

8.2.1 Input data

In this investigation beam trips associated with the H+ beam to Area A and the H- beam to Lujan Neutron Scattering Center are analyzed. The records obtained cover run cycles 71 through 76, over the period of 1996-97.

The first, and most time intensive task of this effort was collecting the input data. Thanks to the cooperation of the LANSCE Operations Group, a large amount of data was collected. This included the:

1) Operational data records from LANSCE-6
2) Central Control Room Logbook (CCR Logbook)
3) Operations Shift Supervisor's Summary Reports (OSS Reports)

The data includes all beam delivery trips during cycles 71-76 ordered by time of occurrence for H+ and H- beams. The Operational data records are the same records that were used for reliability calculations in Chapter 7 (Overall LANSCE Reliability). The Central Control Room logbook contains operational information such as trips, down time assignments (section 6.2), repairments and other maintenance activities in progress etc. The logbook is used to determine the underlying cause of each event down to the level of subsystem and component. At the end of each shift the shift supervisor summarizes a report. The OSS Report contains information concerning significant events during the shift. The report may include additional information that was not included in the logbook. In case the cause of the trip is uncertain, experts in particular fields are consulted to correctly classify each event

Due to the extra knowledge that was added, a few failure assignments were changed from the original assignment. Sometimes the real cause of a failure is realized several days or weeks after the failure incident. This may initially lead to an incorrect classification of the failure at the time of occurrence.

8.2.2 Subsystems

In order to categorize the trips, each system to be studied was broken down to subsystems. These subsystems are listed in table 8.1

Table 8.1 Classification of Subsystems

MAIN SYSTEMS	SUBSYSTEMS		
805 RF	Klystron assembly	Phase and Amplitude Control	Other
	High Voltage system	Resonance Control	Unknown
	805 Tank	Module Control	
DC Magnets	Magnet Hardware	Water	Vacuum
	Interlocks		
Magnet Power Supplies	Electronics	Transformers	Interlocks
	Capacitors	Water cooling	Unknown
Pulsed Power	Harmonic Buncher	Chopper	Kicker
	Deflector		
Water System	Water Pump	Piping	Unknown
	Other		
Vacuum System	Ion Pump	Piping	Unknown

A detailed description of the subsystems is outlined in section 8.4, "LANSCE Subsystems".

8.2.3 Database

Trips associated with the H+ and H- beam lines were merged and classified into different databases depending on what System the trip affected. Since merging of two databases "Area A" and "Lujan" occurred, trips that affected both beam lines were originally present in both databases. In other words, some trips overlapped in both databases. Therefore identical trips were recognized and only one trip was finally recorded in the merged database. Within each database trips were classified into subsystems. In table 8.2 an illustration of the final database format is presented. In this case, the 805 RF System database and trips corresponding to the Klystron Assembly are shown.

Table 8.2 Illustration of final database
In this case, the database for failures in the Klystron Assembly of the 805 RF System is presented. Similar databases are compiled for each subsystem. The database contains trips that affect both the H+ and the H- beam line.

DURATION OF BEAM INTERRUPTION			LOCATION OF FAILURE			CAUSE OF FAILURE	
Date & Time of Outage	Date & Time of restoration	Down Time [h:min]	Area	System	Subsystem	Component failure or other reason	Comment
Klystron Assembly							
10/29/96 22:19	10/29/96 22:37	0:18	LINAC	805	Klystron	Water flow	Sector D tripped on Module 21 Klystron water flow
11/01/96 02:09	11/01/96 02:29	0:20	LINAC	805	Klystron	Flow switch	Module 21 Klystron water not okay. Mechanically agitated flow switch and it made up.
11/23/96 09:43	11/23/96 09:56	0:13	LINAC	805	Klystron	Water flow	Sector D off. Module 21 klystron water flow trip. The klystron magnet supply valve has been opened 1/8 of a turn.
11/23/96 23:17	11/23/96 23:32	0:15	LINAC	805	Klystron	Water flow	Module 21 klystron water flow trip
03/17/97 07:25	03/17/97 07:40	0:15	LINAC	805	Klystron	Ion Pump	Module 46 (Sector H) Klystron ion pump supply failed. It was replaced.
03/26/97 07:22	03/26/97 07:33	0:11	LINAC	805	Klystron	Klystron	Sector B trip on Main Amplitude Overcurrent. RFON aborted. Locally recovered. Loud hum from klystron/switchtube
04/18/97 23:23	04/18/97 23:24	0:01	LINAC	805	Klystron	Voltage adjustment	Linac excursion. Adjustment of voltage in Klystron 1 in Sector D recovered linac.
05/24/97 07:24	05/24/97 13:14	5:50	LINAC	805	Klystron	Klystron	Module 36 Main Amplitude crowbar. Sector F tripped a second time and the fire alarm went off. Acrid smell from the capacitor room. Module 36 klystron was replaced.

The database is for practical reasons divided into three major sections: One section deals with the Duration of the Interruption. It contains the date and time of the beam outage and restoration. It also includes the Down Time of each interruption. The second section considers the Location of the Failure. The Area defines the geographical location of the failure. The System and Subsystem columns specify in what System and Subsystem the failure is located. The third section gives detailed information on the Cause of the Failure. The cause may be a component failure that needs repairment, a bad condition such as a water flow problem or a bad adjustment failure. In the comment column, extra text has been added to explain the failure.

8.3 Scheduled Beam Time

In the analysis scheduled beam time of the H- beam for 1996-97 and the H+ beam for 1997 is considered. This means that the total scheduled beam time embraces the scheduled H- beam time for 1996 plus the merged scheduled beam time of the H+ and H- beams for 1997. The analysis investigates accelerator operation during scheduled operation only. In Appendix 1, a detailed beam schedule of the H- and the H+ beams are available. In table 8.3 the merged beam schedule of the H+ and H- beams for 1997 is presented.

Table 8.3 Merged Beam Schedule for 1997 of the H+ and H- Beams at LANSCE

LANSCE: 1997 SCHEDULED DELIVERY OF H+ AND H-			
Active Beam Line	**Beam On**	**Beam Off**	**Beam Time [h:mm]**
CYCLE 74			
H- On	03/06/93 08:00	03/17/93 17:00	273:00
H+ and H- On	03/17/93 17:00	03/21/93 08:00	87:00
H+ On	03/21/93 08:00	03/22/93 17:27	33:27
Both Off	03/22/93 17:27	03/24/93 19:28	
H+ On	03/24/93 19:28	03/25/93 21:50	26:22
Both Off	03/25/93 21:50	03/27/93 08:00	
H+ and H- On	03/27/93 08:00	04/12/93 20:00	396:00
H+ On	04/12/93 20:00	04/20/93 08:00	180:00
Scheduled Beam Time for Cycle 74:			**995:49**
Minus 1 hour daylight savings time			-01:00
		Adjusted Time:	**994:49**
CYCLE 75			
H+ and H- On	04/22/93 08:00	05/13/93 08:00	504:00
H+ On	05/13/93 08:00	05/18/93 08:00	120:00
Both Off	05/18/93 08:00	05/19/93 22:50	
H+ On	05/19/93 22:50	05/20/93 07:30	8:40
H+ and H- On	05/20/93 07:30	06/08/93 04:00	452:30
H+ On	06/08/93 04:00	06/15/93 08:00	172:00
Scheduled Beam Time for Cycle 75:			**1257:10**
CYCLE 76			
H+ and H- On	06/17/93 08:00	07/11/93 08:00	576:00
H+ On	07/11/93 08:00	07/13/93 08:00	48:00
Both Off	07/13/93 08:00	07/15/93 04:41	
H+ On	07/15/93 04:41	07/16/93 08:00	27:19
H+ and H- On	07/16/93 08:00	07/23/93 10:00	170:00
H+ On	07/23/93 10:00	07/26/93 08:00	70:00
Scheduled Beam Time for Cycle 76:			**891:19**
Total Scheduled Beam Time for H+ and H-, 1997			**3143:18**

By merging the statistics of two beams the total scheduled beam time increases and thereby more trips are included in the analysis. For 1997, the H+ beam alone, was scheduled for 2870 hours and the H- beam was scheduled for 2463 hours. The merged beam time was 3143 hours. Sometimes the H- beam is scheduled while the H+ beam is not and the other way around. For 1996, the H- beam was scheduled for 2681 hours and hence the total scheduled beam time used in the analysis is 5824 hours

8.4 LANSCE Subsystems

8.4.1 805 RF System

The rf system is the most complicated and also the most expensive system of an linear accelerator. The rf system supplies the necessary power to the accelerator and controls this power within specified limitations. There are different rf systems for the DTL and the SCL. The DTL operates at 201.25 MHz and is powered by triode power tubes. The SCL operates at 805 MHz and rf power is produced by klystrons, this system is sometimes referred to as the 805 RF System. The RF System for the envisioned ATW accelerator is more similar to the 805 RF System than the 201 RF System. Therefore, reliability analysis has been performed for the 805 RF System and not the 201 RF System. No further explanation of the 201 RF System will be made.

The 805 RF system is divided, basically, into two parts:
1) RF Reference System - which provides a stable phase and amplitude reference for each accelerator section.
2) The Klystron System - which provides rf power for the beam. This system also includes phase and amplitude control circuits.

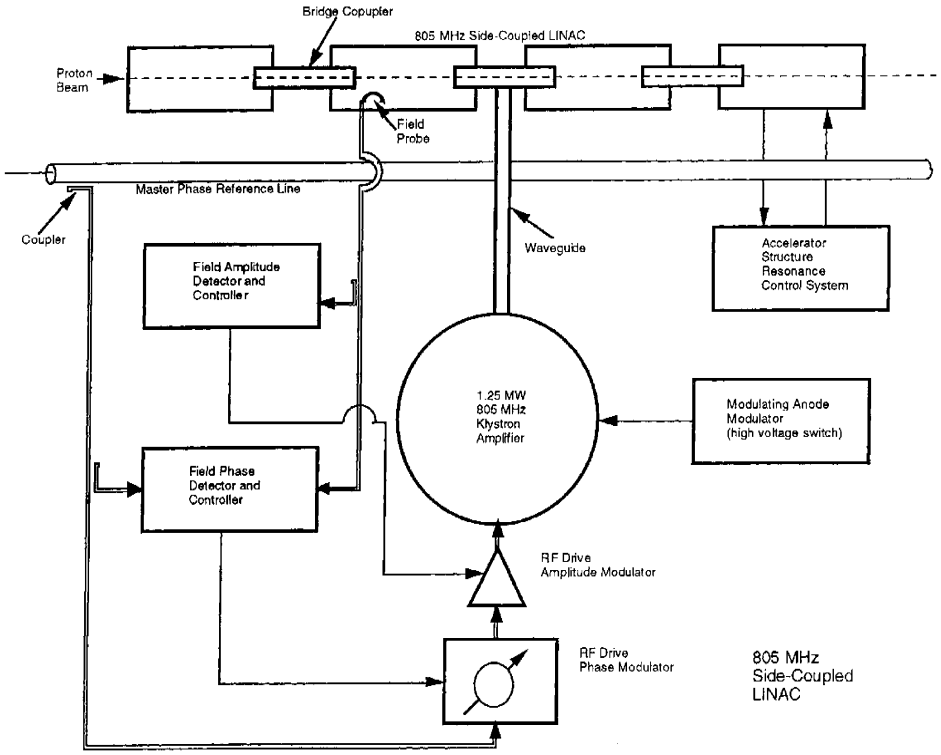

Figure 8.1 805 MHz Side Coupled Linac (805 RF System)

8.4.2 RF Reference System

The rf reference system provides precisely controlled power at 201.25 MHz and 805 MHz for distribution throughout the accelerator. This power is also used to drive all rf equipment other than the more power demanding modules and bunchers. It is used as a standard of comparison in all systems for phase relationships, power levels, and timing. The rf reference system consists of a low frequency oscillator, multipliers to derive the two operating frequencies, power amplifiers, distribution system, distribution system temperature control, and the source phase and amplitude control equipment.

The basic reference is a sophisticated crystal oscillator operating at the relatively low frequency of 6.289 MHz. It is followed by multipliers which derive 201.25 MHz and 805 MHz. Since the power output of the multipliers is only 1 W and because of transmission line losses, power amplifiers are required at each frequency. This power is then distributed along the accelerator and when a reference or drive power is required, roughly 6 W is coupled out of the transmission line.

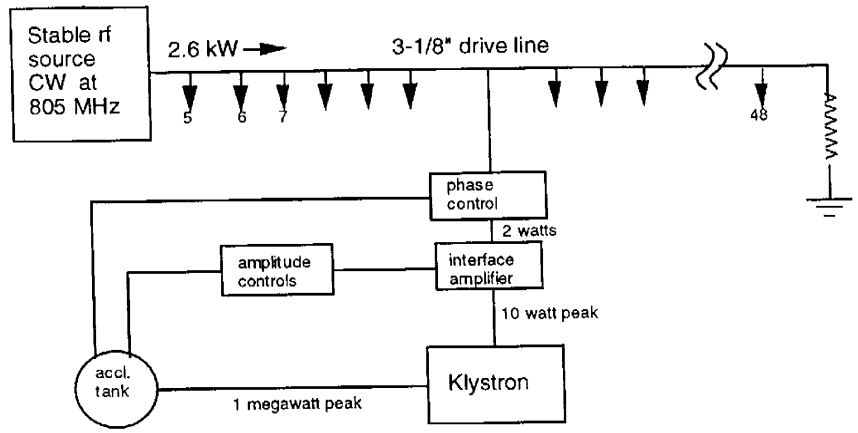

Figure 8.2 The RF reference system for the Side Coupled Linac

Since almost every operation connected with the accelerator is dependent upon the rf reference system, there are two identical units of the oscillator, multiplier and amplifier system. These are designated the A and B chains. One is in service 24 hours a day, while the other is in standby mode but pretuned and ready for service.

8.4.3 The Klystron System

The heart of the 805 MHz rf system is the klystron system. The klystron system provides rf power at 805 MHz to the side coupled linac. The SCL is divided into 44 modules. Each module contains its own klystron system. Modules are clustered into groups of six or seven, each group is fitted into a cluster building (sectors B to H):

Table 8.4 Count of Klystron Systems and High Voltage System

Sector or cluster building	Modules	No of Klystron Systems	No of High Voltage Systems
B	5-10	6	1
C	11-17	7	1
D	18-24	7	1
E	25-30	6	1
F	31-36	6	1
G	37-42	6	1
H	43-48	6	1
Total		44	7

The number of klystron systems used for the SCL is 44.

8.4.3.1 The Klystron

Two types of klystrons are used at LANSCE; the Varian (VA-862) and the Litton (L-5120), both klystrons produces 1.25 MW pulses of rf power with a time duty factor of up to 12% (duty factor during normal operation is 6%). The klystron provides a power gain of more than 100,000. An input rf drive of about 10 Watts results in an output of 1.25 MW.

The LANSCE klystron is comprised of three parts:

1) The electron gun, where the beam is formed and focused. The gun end is under oil in the modulator tank. In this end are the filament, cathode, beam focus electrode and the modulating tank.
2) The rf interaction region, where the actual amplification of the rf signals take place. The rf interaction region contains five cavities and four drift spaces.
3) The collector, where the electron beam is intercepted. The collector is water cooled as considerable beam power is dissipated their, especially when low levels of rf drive are used.

These components are shown in greater detail in figure 8.3.

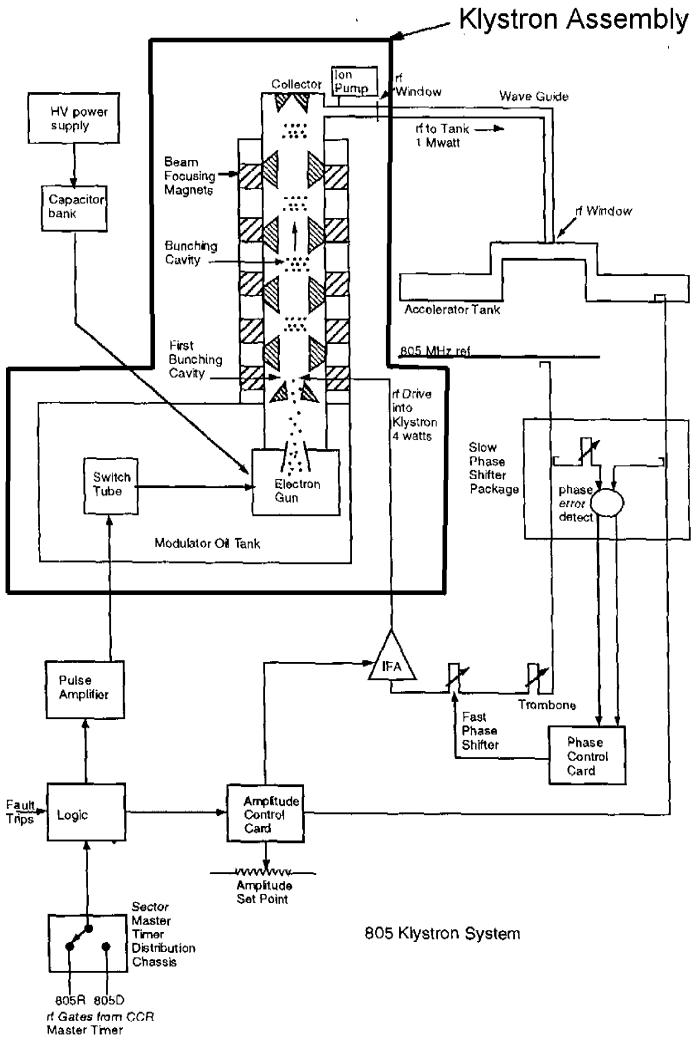

Figure 8.3 The Klystron System and the Klystron Assembly subsystem

The High Voltage System, the Phase and Amplitude Control System, and the accelerator tank are not included in the Klystron Assembly.

Some other equipment associated with the Klystron Assembly are:

- a focusing klystron magnet
- a klystron magnet power supply provides DC power for the focusing magnet
- a klystron ion pump is used to maintain the vacuum within the klystron
- an ion pump power supply provides high voltage power for the ion pump
- a klystron water system including a flow switch and a bypass flow switch

8.4.3.2 The Klystron Modulator

The main purpose of the modulator is to switch the electron beam in the klystron on and off. The Pulse Amplifier turns the modulator switchtube on and off. The switchtube turns the klystron beam on and off. Another important function of the modulator is to prevent arcing and corona discharge from the cables which is connected

to the electrodes of the klystron. Thus, the large modulator tank is filled with transformer oil to provide good high voltage insulation. The oil is circulated within the modulator tank by an oil pump. The oil pump circulates oil through a heat exchanger in the modulator tank and supplies cooling oil to the high voltage switchtube and other heat sources in the tank.

8.4.3.3 Phase and Amplitude Control System

When the beam is turned on, energy is transferred from the cavity fields to the beam. Beam loading up to 40% is anticipated in the LANSCE accelerator. That is, up to 40% of the total rf power supplied will be transferred to the beam, with the remaining 60% lost in the cavities. Beam loading in a cavity in which the rf phase and amplitude are not controlled results in a decrease in the amplitude of the accelerating gradient and a shift in the apparent synchronous phase angle. The result is reduced acceleration and loss of particles. Since the beam is somewhat "sucking" power from the cavity fields correction signals must be applied to both amplitude and phase to keep them within tolerance at all times when there is beam in the cavities.

The phase and amplitude control systems are designed to maintain the rf field in the cavities within the specified limits of 1° in phase and 1% in amplitude during the entire rf pulse. One system controls amplitude another controls phase. A magnetic pickup loop located inside the tank is used to obtain a "sample" of the rf cavity field. The control system operates by comparing the actual tank amplitude or phase to a reference value and then applying a correction signal to the rf amplifier chain to produce the desired result.

This phase and amplitude loop is sometimes referred to as the servo loop and a fault in this chain is called a servo fault.

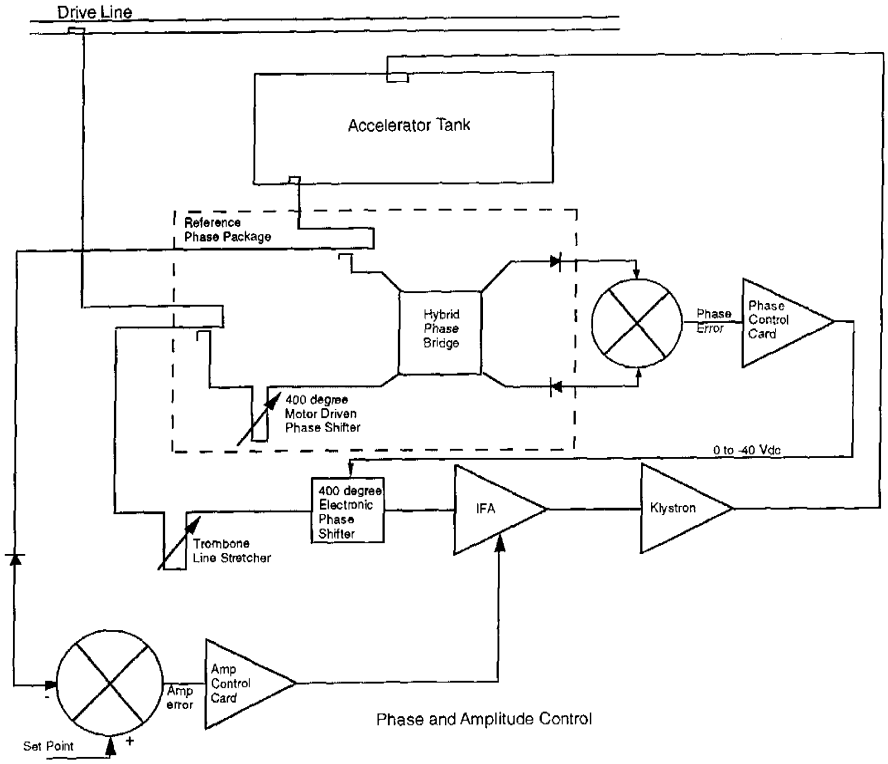

Figure 8.4 Phase and Amplitude Control System

8.4.4 High Voltage System

The High Voltage (HV) system provides HV power to the 6 or 7 klystrons in each sector. The capacitor room is a large metal enclosed structure which contains the HV distribution system and the crowbar system. Each HV distribution system consists of:

- HV switch
- capacitor bank, including 50 capacitors
- 84 Amp fuse + air cooling blower
- two crowbar resistor banks
- shorting bar switch
- voltage divider
- current meter shunt
- cable fault detection system
- klystron duty factor detector

8.4.5 DC Magnets

Most magnets constructed for beam transport lines are electromagnets rather than permanent magnets. Such magnets are excited by electrical current carrying coils around magnet poles. Iron magnets are the most commonly used magnets for particle beam transport systems. Quadrupole Magnets together with bending magnets are the basic building blocks for focusing devices to keep the particle beam close to the desired beam path.

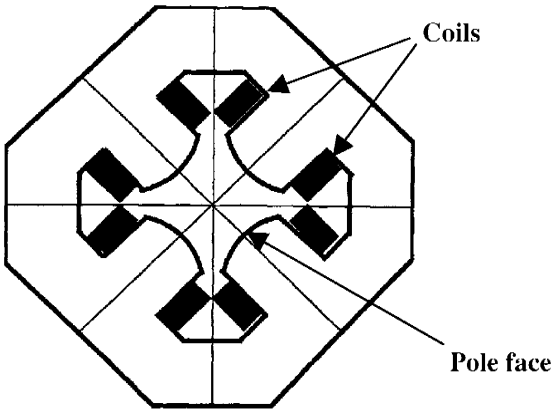

Figure 8.5 Standard Quadrupole Magnet geometry
The figure shows a standard design for the quadrupole magnet geometry. The core is symmetric around the four poles, with coils mounted on the pole sides [18].

In the LANSCE accelerator complex most magnets are supplied with DC (Direct Current) power. A table of summary of all magnets located at LANSCE is available in Appendix 2. DC magnets are used for focusing, steering, and bending actions on the beam. The most suitable device for producing a focusing effect is the quadrupole magnet. The quadrupole magnet reduces the transverse dimensions of the beam and confines it to the vicinity of the accelerator axis.

In the SCL there is a quadrupole doublet between each tank of the structure, for a total of 103 quadrupole doublets. The quadrupole magnets have a center-to-center

spacing of 20 cm. Each quadrupole doublet is protected by two interlocks, namely a thermal switch and a flow switch. The thermal switch senses that the quadrupole doublet temperature is less than 93°C (200 F), and the flow switch senses that the flow of coolant is normal. Both of these interlocks must be satisfied in order for the quadrupole doublet power supply to operate.

In the DTL, the quadrupole magnets are located inside the drift tubes. There are quadrupole magnets in every drift tube of tanks 1 and 2 and in every other drift tube of tanks 3 and 4. Totally, this system includes 132 quadrupole magnets. The quadrupole magnets of each tank are cooled by water that comes from a supply line, passes through a high pressure pump and is distributed to each magnet by a supply header. The magnet windings are cooled in parallel by water that flows from the supply header through a throttling valve. The flow is throttled so that the temperature rise in each magnet is about the same for all magnets in the tank.

8.4.6 Magnet Power Supplies

In an electromagnet, the strength of the magnetic field is proportional to the current flowing in the magnet windings. Therefore, magnet power supplies are designed to deliver relatively high currents to the magnets.

The magnets used in LANSCE requires DC power for operation. In the power supplies, AC power from the building power distribution system is converted to DC power. A typical power supply generates 50 Amps of output DC current. Sometimes, for reason of economy, one power supply is providing several magnets with power. Generally, each power supply is set to deliver the maximum current required by any magnet in the group (usually the first or second magnet). The required currents for the quadrupole magnets in each group generally decrease with magnet number.

The power supplies are protected by a number of interlocks. These interlocks are power supply temperature, ground current, door interlock, transformer primary overload protection, and shunt control power.

8.4.7 Pulsed Power System

The pulsed Power System includes:

Table 8.5 The Pulsed Power System

Count	Subsystem	Specification
1	Harmonic Buncher	The harmonic buncher is located in the Proton Storage Ring.
1	Chopper	The beam chopper is located in H- Low Energy Beam Transport.
2	Deflectors	One deflector each for the H+ and H- Low Energy Beam Transport.
3 (5)	Kickers	One Injection Kicker in Line D. Two Extraction Kickers in the Proton Storage Ring. *The Switchyard Kicker (includes two ferrite kicker magnets) was not in operation during 1996-97.*

A detailed list of components for the Pulsed Power System is available in Appendix 3 [19].

8.4.7.1 Harmonic Buncher

The Harmonic Buncher is located in the Proton Storage Ring. The buncher itself is simply a resonant cavity that establishes an alternating potential across a gap in the

beam line. It is the purpose of the buncher to collect the stream of particles into clusters and time this process in a proper manner. The resonant cavity is excited with 2.8 MHz rf power.

The Harmonic Buncher includes:

- RF Cavity
- Low Level Electronics
- RF Preamplifier
- RF Drive Amplifier
- Output Transmission Line
- Controls/Interlocks
- Computer Interface

8.4.7.2 Chopper

The chopper is a deflecting magnetic moving the continuous beam across the opening of a slit. The chopper produces macropulses of H- ions, called bunches. These bunches are further processed by the 201 prebuncher. The Chopper system also includes a DC power supply, a slow wave structure and a distributed amplifier.

8.4.7.3 Kicker Systems

Altogether there are five kicker magnets at LANSCE, namely:

Kicker Magnets

- 1 Switchyard Kicker (comprised of two ferrite kicker magnets in series)
- 1 Injection Kicker
- 2 Extraction Kickers

During 1996-97 three kickers were in use, the Switchyard Kicker was not in operation.

Injection Kicker

The Injection Kicker is located in Line D. The Kicker injects protons into the Proton Storage Ring.

The Injection Kicker includes:

- Kicker Magnet
- Charging System
- Modulator
- Controls/Interlocks
- Computer Interface

Extraction Kickers

Two extraction kickers are used for single-turn fast extraction of the accumulated proton beam. The horizontally kicked beam is captured by a pair of septum magnets for transfer to the extraction line and then to the WNR target.

The Extraction Kickers include:

- 2 kicker magnets (vacuum vessels, electrodes etc.)
- Charging System
- Switching System
- Cables
- Controls/Interlocks
- Computer Interface

8.4.8 Summary of Subsystems

Table 8.6 Summary of Subsystems

System	Subsystem	Count	Definition
805 RF System			805 MHz Radio Frequency System (section 8.4.1): pad power supplies, capacitor rooms, amplifier systems, klystron systems, interlocks (flow, temp, etc.), resonance controllers and valves. Does not include prebunchers.
	Klystron Assembly	44	The klystron (section 8.4.3.1) and the klystron modulator (section 8.4.3.2). Klystron ion pump and magnet and their associated power supplies. Any water or vacuum failure inside the klystron system. The Phase and Amplitude, Resonance and Module Control System is NOT included in the Klystron Assembly.
	High Voltage System	7	The High Voltage System (section 8.4.4). The HV switch, capacitors, cabling, fuses etc.
	805 Tank	44	Any failure in the tank module vacuum leaks, valves etc.
	Phase and Amplitude Control	44	Phase and Amplitude Control System (section 8.4.3.3)
	Resonance Control	44	Resonance Control System
	Module Control	44	Module Control System
	Other		Extraordinary failure that is not classified into any other subsystem.
	Unknown		Unknown failure within the 805 RF System.
DC Magnets		800	Magnets, winding, DC cabling, flow and temperature switches, vacuum and water leaks, magnet water strainers. Does not include power supplies.
	Magnet Hardware		Any failure to the hardware (wiring, cabling)
	Water		Water cooling problems (leaks, valves, flow switches, flow problems)
	Interlocks		Magnet interlocks (flow interlocks)
	Vacuum		Vacuum leaks
Magnet Power Supplies		278	DC Magnet Power Supplies: electronics, trips, interlocks (flow, ripple, etc.), water leaks.
	Electronics		Power supply electronics (computer control system, SCR, regulation, filtering, shunts, overcurrent problems, magnet drifting problems)
	Capacitors		Capacitors inside the power supply (usually dry out)
	Transformers		Transformer for power supply (insulation aging)
	Water cooling		Water cooling problems within the power supply (flow switches, valves, hoses)
	Interlocks		Power supply interlocks (door interlock)
	Unknown		Unknown failure within the power supply.

Pulsed Power			Pulsed Power System: Kickers, Ring buncher, deflectors, inflector, choppers and their related power supplies, local controls and modulators.
	Harmonic Buncher	1	Failures connected to the buncher and power supply (water flow, arcs, crowbars, adjustments etc.)
	Deflectors	2	Failures connected to the deflectors and power supplies
	Chopper	1	Failures connected to the chopper and power supplies (water flow, adjustments, FET)
	Kickers	3	Injection kickers, extraction kickers and their associated power supplies (timing problems, Blumlein, arcs)
Water System			Cooling water systems: pumps, pump controls, makeup water, valves, pipes, heat exchanges. Does not include leaks and flow problems in individual cooled components such as magnets, amplifiers, cavities, etc. unless problem is caused by variations or limits in water system.
	Water pump	120	Water pumps and their associated power supplies
	Piping		Water lines, valves, hoses etc. which do not belong to any other System.
	Other		Other failures that occur in the Water System
	Unknown		Unknown failure in the Water System
Vacuum System			Vacuum system: Vacuum pumps, pump power supplies, roughing packages, valves, instrumentation, controls, pipes, flanges. Does not include leaks in individual components or loads such as magnets, targets, etc.
	Ion pump	250	Ion pumps and their associated power supplies.
	Piping		Vacuum lines, tanks, valves etc. which do not belong to any other System.
	Unknown		Unknown failure within the Vacuum System

8.5 Operational Statistics

All trips are divided into different databases depending on which system is responsible for the failure. The total number of trips corresponding to each system is presented in table 8.7.

Table 8.7 Summary of Trips produced by the Systems Analyzed

TRIPS PRODUCED BY INDIVIDUAL SYSTEMS			
Main System	**No. of trips 1996**	**No. of trips 1997**	**Total**
805 RF	68	162	230
Pulsed Power	127	72	199
Magnet Power Supplies	102	83	185
Vacuum System	27	47	74
Water System	30	18	48
DC Magnets	3	17	20
Total	**357**	**399**	**756**

The systems are presented in order of importance, starting with the system responsible for most of the trips. It must be noted that not all accelerator systems are included in the summary, only the systems which being are analyzed. The total number of trips included in this analysis (756 trips) are significantly less than the actual number of trips that occurred in the entire accelerator (≈8000 trips). In other words, one may not

conclude that, for example, the 805 RF System is the most "troublesome" system at LANSCE. Reliability estimates of the entire accelerator and other systems are outlined in chapter 6.

In the systems analyzed, the 805 RF System is causing most of the interruptions. Next in order is the Pulsed Power System followed closely by the Magnet Power Supply system. The DC Magnets are causing the smallest number of interruptions, only 20 trips. The DC Magnets are in fact one of the most reliable systems of the entire accelerator.

During 1996, 357 trips occurred and for 1997 the number was 399. It is understandable, the accelerator was scheduled for more time in 1997 (3143 hours) than in 1996 (2681 hours).

8.5.1 Reliability Calculations

For all systems and subsystems identical reliability calculations have been performed. The Magnet Power Supply System is selected for the purpose of illustrating some reliability calculations. In table 8.8 the first cut of some of the calculations are presented.

Table 8.8 Illustration of Reliability Calculations

1	2	3	4	5	6	7	8	9	10
No	**Date & Time of Outage**	**Date & Time of Restoration**	**Time Between Failures [h:min]**	**Cum Failure Rate [1/d]**	**Cum MTBF [h:min]**	**Down Time [h:min]**	**Cum Down Time [h:min]**	**Cum MDT [h:min]**	**Cumulative Availability**
68	10/17/96 17:59	10/17/96 18:02	3:41	0.87	27:38	0:03	102:49	1:30	0.948139
69	10/18/96 15:51	10/18/96 15:52	21:49	0.87	27:33	0:01	102:50	1:29	0.948695
70	10/18/96 16:15	10/18/96 16:16	0:23	0.88	27:10	0:01	102:51	1:28	0.948697
71	10/18/96 20:04	10/18/96 20:05	3:48	0.89	26:50	0:01	102:52	1:26	0.948786
72	10/19/96 08:41	10/19/96 08:48	12:36	0.90	26:38	0:07	102:59	1:25	0.949051
73	10/20/96 00:53	10/20/96 00:58	16:05	0.91	26:29	0:05	103:04	1:24	0.949414

Each row represents an event or a failure that resulted in a beam interruption. In this case, event numbers 68-73 are displayed. In columns 2-3 the date and time when the beam was interrupted and restored is shown.

Time Between Failures - time between the end of one trip to the beginning of the next. For example, Time Between Failure = Date & Time of Outage 69 - Date & Time of Restoration 68.

Cumulative Failure Rate - this number reflects what the failure rate would be based on the events up to that point. In other words, if the Magnet Power Supply system only included 70 trips then the mean failure rate would be 0.88 failures per day. Cumulative Failure Rate = Event number/cumulative time between failures

Cumulative MTBF - Mean Time Between Failure up to that event. For example, if the Magnet Power Supply system only included 70 trips then the MTBF would be 27 hours and 10 minutes. Cumulative MTBF = Cumulative Time Between Failures/Number of failures.

Down Time - duration of individual trips. Down Time = Date & Time of Restoration - Date & Time of Outage.

Cumulative Down Time = down time 1 + down time 2 + ...

Cumulative MDT - Mean Down Time up to this event. For example, if the Magnet Power Supply system only included 70 trips then the MDT would be 1 hour and 28 minutes. Cumulative MDT = Cumulative Down Time/Event number.

Cumulative Availability = Cumulative MTBF/(Cumulative MTBF+Cumulative MDT). The probability that the magnet power supply system is functioning.

To visualize the reliability behavior of the Magnet Power Supplies the calculations have been plotted. The most important plots are presented in figures 8.6 - 8.11. All these plots apply to the Magnet Power Supply System only. Similar plots have been made for the other Systems as well.

For illustration the cumulative number of trip events as a function of time is presented for the magnet power supply system in figure 8.6.

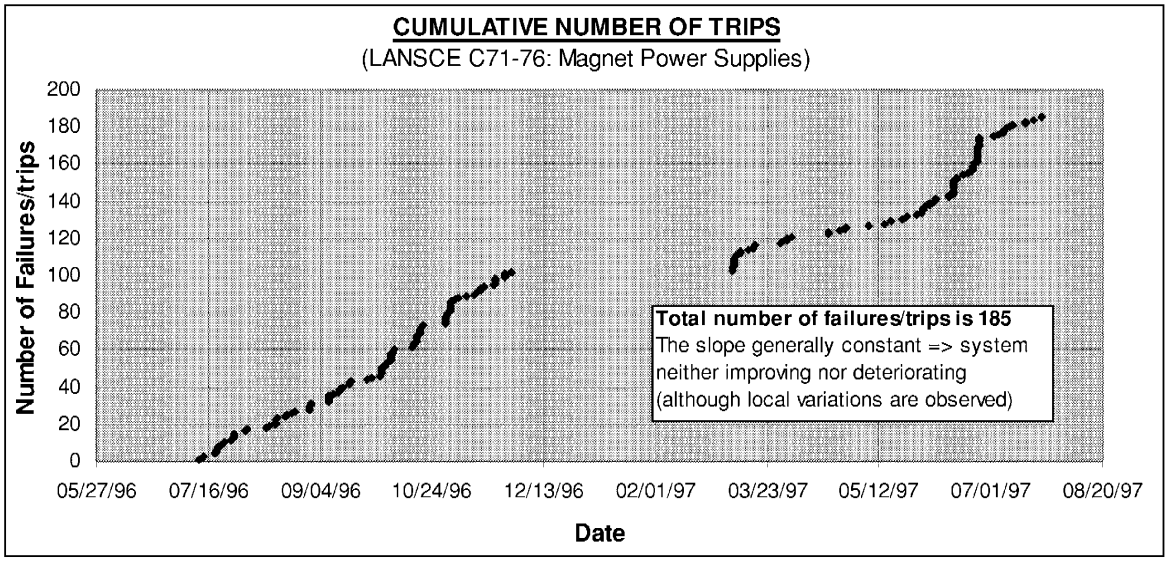

Figure 8.6 Magnet Power Supplies: Cumulative Number of Trips

This plot is remarkably straight, despite the fact that it is the sum of many different types of activities by many different people and equipment. One can see neither significant improvement nor deterioration of the system, although local variations are visible. At some instances, several trips occur in a short period of time. That is an indication of the real failure was never attended at the first time. The trip was reset but the failure was probably never investigated until numerous trips had occurred. The wide gap in the middle of the plot shows the duration of the extended maintenance period between 1996 and 1997. Some other short maintenance periods or periods when the accelerator was not scheduled are visible as well.

In figure 8.7 the cumulative down time is illustrated.

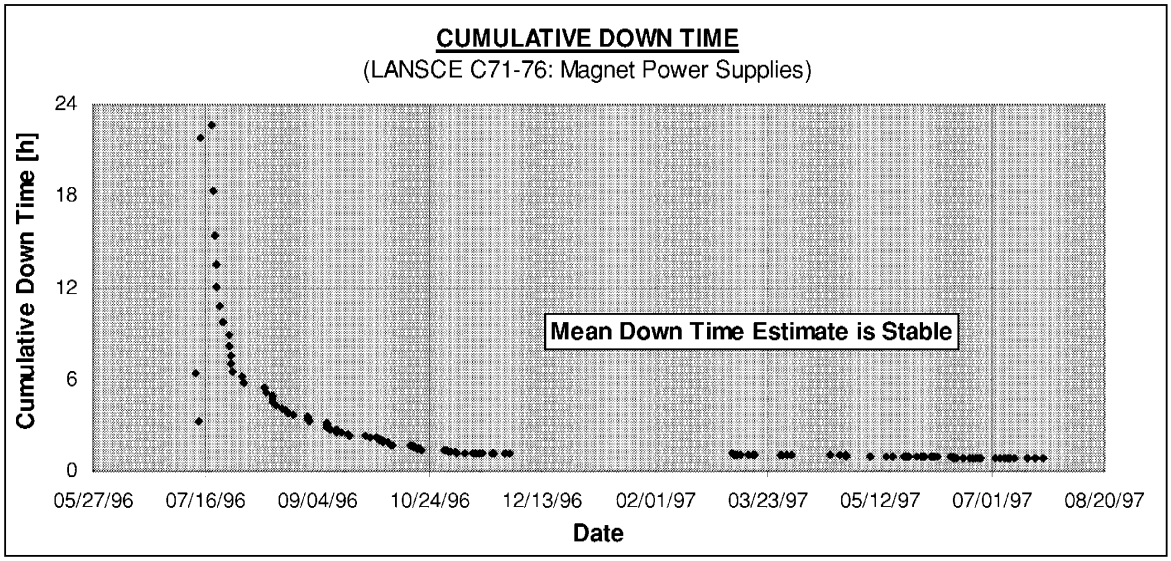

Figure 8.7 Magnet Power Supplies: Cumulative Down Time

Mean Downtime is calculated as the ratio of the cumulative downtime to the cumulative number of events as shown in figure 8.7. One indication of sufficient number of entries in the data set is the asymptotic behavior of the statistical estimators for the desired quantities, such as Cumulative Mean Down Time. The conclusion is that further data collection is not necessary, the MDT estimate appears

A histogram of magnet power supplies down times is presented in figure 8.8

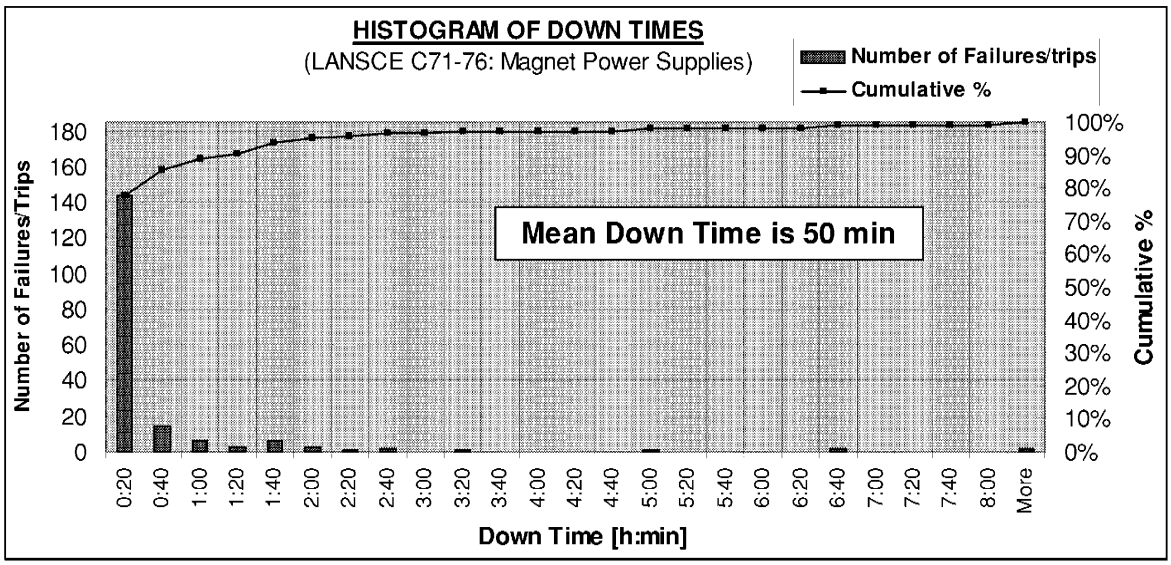

Figure 8.8 Magnet Power Supplies: Histogram of Down Times

On the x-axis different down time intervals are displayed. The y-axis displays on one side, the number of trips within each down time interval, and on the other the fraction these trips represent. The majority (80%) of the trips have down times <20 minutes. Two

trips which resulted in very long down times occurred. The Mean Down Time for the magnet power supplies is 50 min.

Cumulative Failure Rate is calculated as the ratio of the cumulative number of events to the cumulative up time. As shown in figure 8.9 the behavior is not as smooth as for the cumulative downtime but appears to converge.

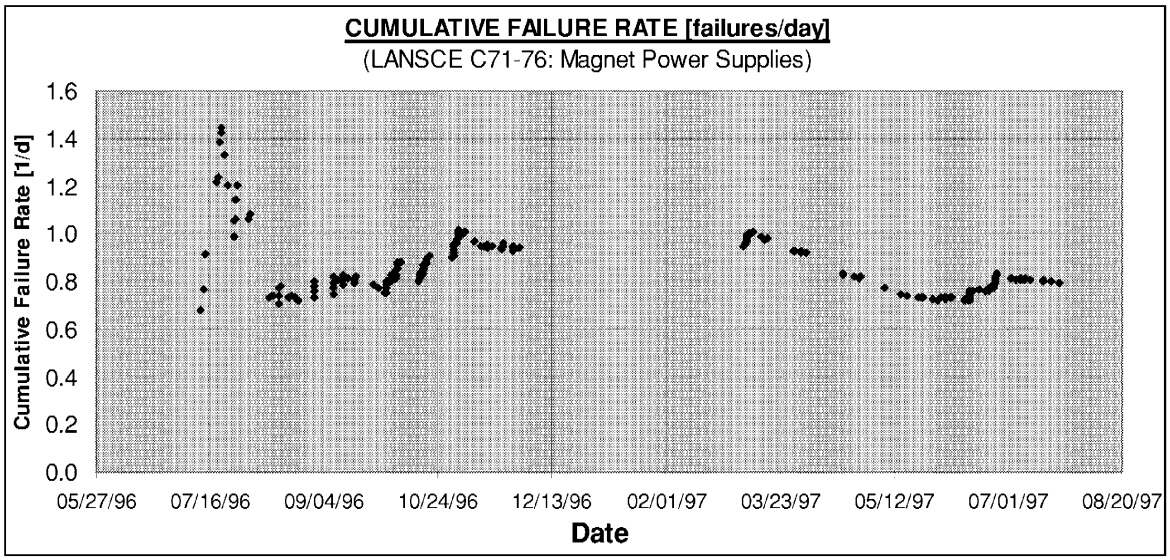

Figure 8.9 Magnet Power Supplies: Cumulative Failure Rate

Figure 8.10 shows the histogram of Times Between Failures.

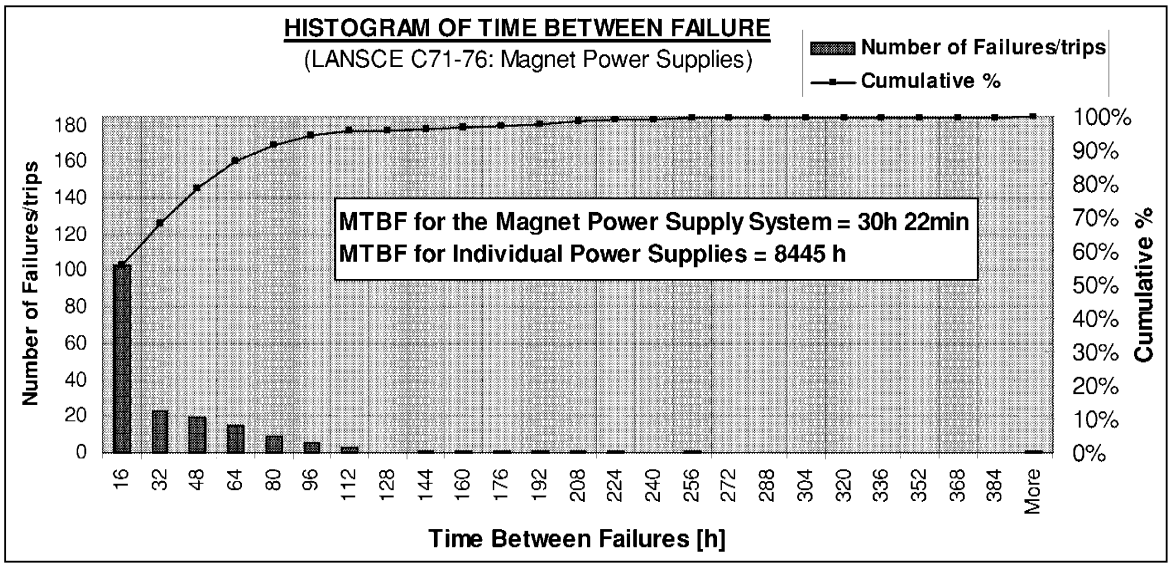

Figure 8.10 Magnet Power Supply: Histogram of Times Between Failures

The Mean Time Between Failures is 30 h 22 min. With 278 magnets power supplies total in the system, we can estimate the MTBF for an individual magnet power

supply as 8445 hours, assuming that all the supplies have the same failure rate and can be treated as a series system of independent power supplies.

8.5.2 Results

The results obtained via similar analyses for the other components of the LANSCE accelerator are summarized in table 8.8. Information on failure causes in the individual systems are presented in Appendix 4.

RESULTS OF RELIABILITY STUDY AT LANSCE				
Main System	**Subsystem**	**MDT** [h:mm]	**MTBF for all devices** [h]	**MTBF for a single device** [h]
805 RF	Klystron Assembly	0:44	262	11560
	High Voltage System	0:18	137	960
DC Magnets		0:53	290	232280
Magnet Power Supplies		0:50	30	8445
Pulsed Power	Harmonic Buncher	0:09	44	44
	Chopper magnet	0:08	291	291
	Deflector magnet	0:10	342	684
	Kicker magnet	1:58	185	557
Water System		1:20	120	
	Water pump	0:29	245	29506
Vacuum System		0:48	77	
	Ion pump	0:29	101	25308

Figure 8.8 Results of Reliability Investigation of Systems and Subsystems

The MTBF calculated from the raw data corresponds to the entire 805 RF system consisting of 44 klystron assemblies. An estimate of the MTBF for an individual klystron assembly was obtained by multiplying this value by 44 as 11560 hours. This value is not unreasonable when compared with the 20-50,000 hours commonly quoted for the typical klystron tube by itself. 38% of all failures in the klystron assembly are water cooling problems and 32% are amplitude crowbars (which is usually due to an old switchtube). Most of the downtime occurs when klystron replacement is necessary. During 1996-97, four klystron replacements occurred, these replacements were responsible for 54% of the downtime in the klystron system.

The High Voltage System is exposed to many short interruptions. Sometimes when a failure occurs in the High Voltage System it is not possible to point out any specific component. Usually the High Voltage system causes phase or amplitude disturbances (85% of all trips), commonly called servo faults. In this analysis, all servo-faults are classified as high voltage failures, but in some cases these failures are caused by the phase and amplitude control system. Even though many servos occur the total downtime caused by these failures is small. Sometimes the capacitors dry out and needs to be replaced, this causes long downtimes. Capacitor failures are responsible for 68% of the downtime in the high voltage system.

A total of 800 dc magnets exist in the LANSCE facility. MTBF for a single magnet is 232280 hours (≈26 years). The dc magnets at LANSCE are very reliable. This is also confirmed by maintenance personnel at LANSCE. When a magnet failure occurs it

is usually a water cooling problem inside the magnet. 50% of the magnet failures are related to the water cooling system. Water cooling failure is also responsible for 52% of the downtime. 5 failures in the magnet hardware occurred. Hardware failures accounted for 32% of the total downtime in dc magnets.

The Magnet Power Supply System includes 278 power supplies. For a single power supply the MDT is 50 minutes and the MTBF is 8445 hours (≈1 year). A single capacitor failure inside a power supply was responsible for 80 hours, or 54% of the downtime. The most common failure cause is problems with the electronics (31% of all trips). Most of the power supplies at LANSCE are controlled by manual electronics. Modern power supplies are computer controlled and proves to be much more reliable. Many unknown trips occur in the power supplies (58%), according to expertise at LANSCE most of these trips are caused by malfunctioning electronic equipment as well.

48 trips occurred in the water system. A water system failure is usually connected to the piping subsystem (42%) or water pumps (35%). Most of the downtime is also caused by the piping (68%). Failures with hoses, valves, water lines etc are included in the piping system. MDT for a water pump is 29 minutes and MTBF is 29500 hours (≈3 years).

In the vacuum system, 76% of the trips were caused by ion pump failures and 18% were caused by piping failures. On the other hand, piping failures were responsible for 54% of the downtime and ion pumps accounted for 45%. MDT for an ion pump is 29 minutes and MTBF is 25300 hours (≈3 years).

8.6 Conclusions

In summary, as a result of the investigation of individual systems, estimates for both MTBF and MDT were obtained for several typical accelerator components: DC magnet power supplies, DC magnets, klystron assemblies, HV power supplies, vacuum system, and water system. Both MTBF and MDT values are shorter than expected, driven by short beam trips, rather than major replacement jobs. The results will be useful in developing preliminary estimates for reliability, availability, and maintainability of high power accelerator systems planned in the future. However, before we can fully trust them, they have to be corroborated through comparison with statistics obtained from other facilities. The impact of maintenance activities outside of the scheduled production time needs to be tracked down and included in the estimates as well.

9 Beam Current Analysis

9.1 Introduction

In this chapter statistics of beam interruptions originating from current monitor data are presented. The analysis verifies the true beam performance. It does not investigate the cause of the beam failure. Mean Time Between Failure and Mean Down Time estimates of the H+ beam are obtained. The analysis considers scheduled production of the H+ beam for 1997 (Cycle 74-76).

9.2 Input data

Near the targets of Line A (H+ beam) current detectors are positioned. These detectors monitor the beam continuously. Every change in beam current is registered. From the detectors the current level is read at a steady rate, about once per second. Software running on the main control computer of the LANSCE accelerator facility collects the current monitor data and automatically calculates the average current integrated over the last minute. This average value is the final input data used in the Beam Current Analysis. In figure 9.1 an illustration of this procedure is presented.

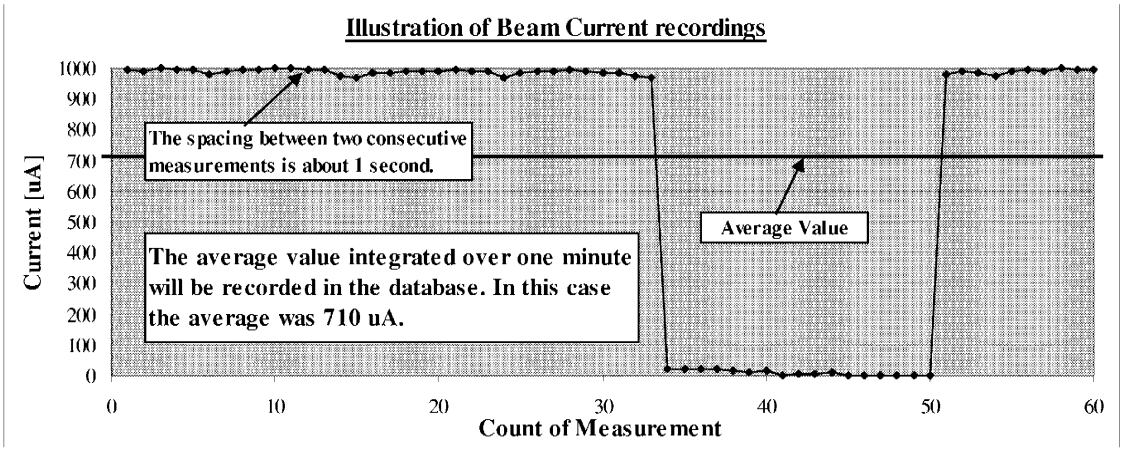

Figure 9.1 Illustration of Beam Current recordings

On average, a new current value is recorded to the database every 1.10 min. The analysis extends over the period 20th of March to 27th of July 1997 (Cycle 74-76) and the input data contains 163,000 current recordings.

9.3 Method

From the original database the current data is extracted and compiled into Excel spreadsheets. Due to the large amount of data the final input data is divided into several data files. In table 9.1 the final database format is illustrated. Beam recordings which occur outside scheduled production are not included in the analysis. The scheduled current is entered along with the beam current data to the final database. This is done because the beam is considered as interrupted only if the current is below a threshold current. For 1997, the threshold current was one half the scheduled current. For most of

the time the scheduled current is 1000 μA, but sometimes other current levels are scheduled.

Table 9.1 Illustration of final database

Date	Time	Average Delivered Current	Scheduled Current	Time between measurement	Classification of event	Event Down Time	0-2 min	2-5 min	5-15 min	15-60 min	1-5 h	>5 h
		[μA]	[μA]	[mm:ss]	0=below threshold 1=above threshold	[h:mm:ss]	0=No 1=Yes	0=No 1=Yes	0=No 1=Yes	0=No 1=Yes	0=No 1=Yes	0=No 1=Yes
Schedule On, threshold level = 0.5*Scheduled Current												
97-06-11	0:00:30	996.70	1000.00	01:07	1	0:00:00	0	0	0	0	0	0
97-06-11	0:01:37	997.20	1000.00	01:07	1	0:00:00	0	0	0	0	0	0
97-06-11	0:02:43	996.90	1000.00	01:06	1	0:00:00	0	0	0	0	0	0
97-06-11	0:03:49	734.30	1000.00	01:06	1	0:00:00	0	0	0	0	0	0
97-06-11	0:04:56	387.10	1000.00	01:07	0	0:00:00	0	0	0	0	0	0
97-06-11	0:06:02	465.30	1000.00	01:06	0	0:02:13	0	1	0	0	0	0
97-06-11	0:07:09	993.30	1000.00	01:07	1	0:00:00	0	0	0	0	0	0

In the database, each current value is checked and determined whether or not the current was above or below the threshold value. Consecutive events below the threshold current are interpreted as one interruption. Interruptions are classified into down time intervals. Six down time intervals exist: 0-2, 2-5, 5-15, 15-60 minutes and 1-5 hours and >5 hours. As we shall see later, the intervals 0-2 and 2-5 minutes are combined into one interval which is denoted 0.5-5 minutes for reasons which will be explained later.

9.3.1 Beam Schedule

In this analysis, beam current data are only processed if they occur within scheduled production. Therefore, the beam schedule is important. The scheduled beam time used in this analysis is most similar to the beam schedule used for the H+ beam in chapter 7, "Overall LANSCE Reliability" (or Appendix 1). After all, both analyses investigates the same beam during the same period of time, but small divergences exist. These are:

- Current recordings starts in the 20th of March
- Small differences in time following maintenance periods when the beam is switched on and off.

First of all, the current recordings used in the Beam Current Analysis started in the 20th of March at 07:47, where in the Overall Reliability Analysis the scheduled production started at the 18th of March at 17:00. Meaning that 38 hours of beam time is not included in the Beam Current Analysis compared to the Overall Reliability Analysis. Also, when the current data is more closely investigated it is obvious in some cases that the beam was not switched on exactly at 08:00 rather at 08:45. In order to be able to compare the two analyses this difference in time should not be considered as down time which would be the case if the schedule had started at 08:00.

In table 9.2 the final schedule used in the Beam Current Analysis is presented.

H+ BEAM SCHEDULE USED FOR THE BEAM CURRENT ANALYSIS		
Beam On	**Beam Off**	**Beamtime [h:mm]**
CYCLE 74		
03/20/97 07:47	03/23/97 17:27	81:40
03/25/97 19:30	03/26/97 21:49	26:19
03/28/97 09:56	04/21/97 06:09	572:13
Scheduled beam time for Cycle 74:		**680:12**
Minus 1 hour daylight savings time		-1:00
	Adjusted Time:	**679:12**
CYCLE 75		
04/23/97 08:45	05/19/97 04:04	619:19
05/20/97 22:51	06/16/97 06:00	631:09
Scheduled beam time for Cycle 75:		**1250:28**
CYCLE 76		
06/18/97 08:00	07/14/97 08:00	624:00
07/16/97 04:42	07/27/97 08:00	267:18
Scheduled beam time for Cycle 76:		**891:18**
Total Scheduled H+ Beam Time for 1997		**2820:58**

Table 9.2 Final Beam Schedule used in the Beam Current Analysis

The total scheduled beam time is 2821 hours. Interruptions that occur during this time are included in the analysis. In the Overall Reliability Analysis the total scheduled H+ beam time for 1997 was 2870 h. In other words, the accelerator in the Beam Current Analysis is scheduled for 50 hours less beam. The difference in scheduled beam time have a very little effect on the total number of interruptions. On average

50 hours / 2821 hours = 1.8%

Meaning that if the number of interruptions would be extrapolated for an extra 50 hours the Beam Current Analysis should include 1.8 % more interruptions (which is negligible).

9.4 Results of Beam Current Analysis

Beam current statistics originating from beam monitor data are presented. Statistics of two data runs are shown and discussed. The first computation uses a threshold factor of 0.5. The threshold factor determines at what beam current the beam should be regarded as interrupted. Threshold factor 0.5, or half the scheduled current, is the definition for an interruption used in the Overall LANSCE Reliability Analysis in Chapter 7. By comparing these two investigations a verification of the correctness and reliability of both analyses is achieved. The second computation is performed at a threshold factor of 0.8 for reasons which will be explained later.

9.4.1 Threshold Factor 0.5

It is interesting to compare the results of the Beam Current Analysis with the results in the Overall Reliability Analysis. In order to easily discuss and compare results from both analyses similar diagrams have been assembled. The results are presented in figures 9.2 and 9.3

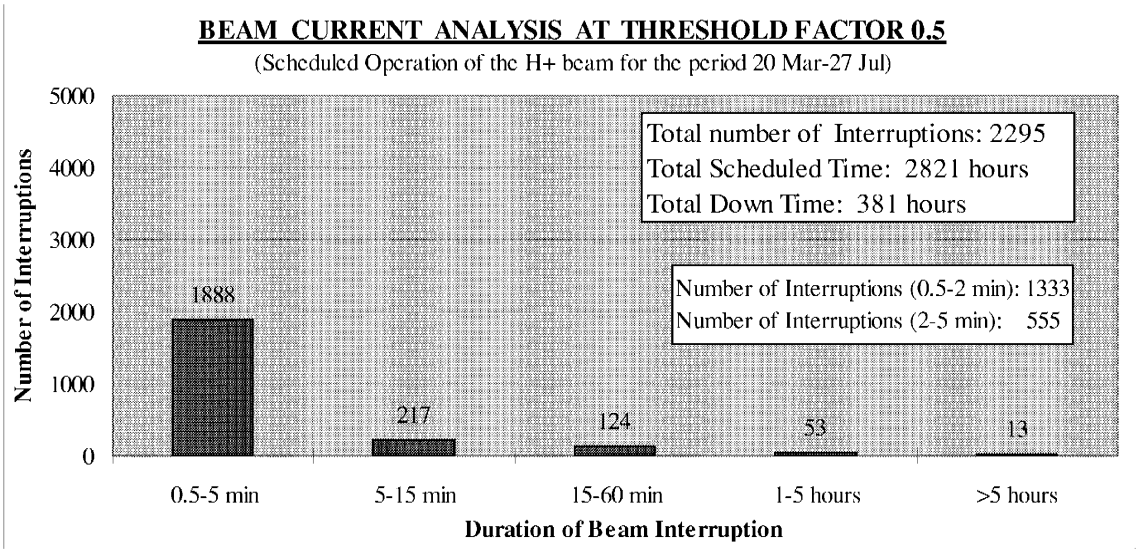

Figure 9.2 Summarize of Interruptions from the Beam Current Analysis at threshold factor 0.5

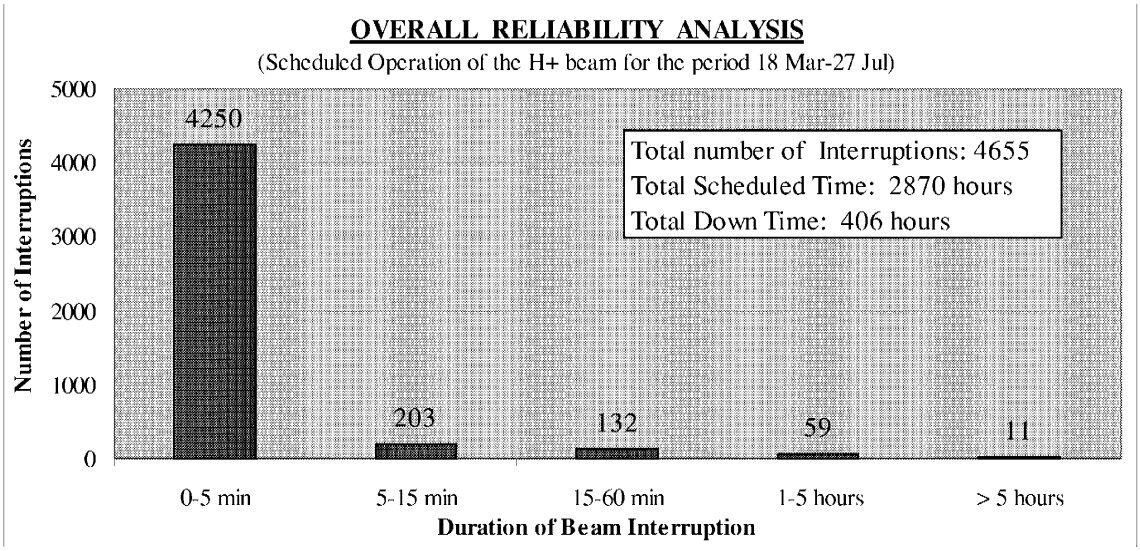

Figure 9.3 Summarize of Interruptions from the Overall Reliability Analysis

In the Beam Current Analysis, events which fall below 0.5*Scheduled Current are interpreted as interruptions. This is the same definition for interruptions used in the Overall Reliability Analysis. Lets start by comparing the rightmost columns in both

figures. It is remarkable how well the two analyses agree even though the underlying data origins from two completely different records. The Overall Reliability Analysis is based on comments in the logbook while the Beam Current Analysis is based on current recordings from a beam monitor. In table 9.3 the number of interruptions are summarized for both analyses.

Table 9.3 Comparison of Interruptions which occur in the Beam Current Analysis and the Overall Reliability Analysis

	NUMBER OF INTERRUPTIONS	
Down Time Interval	**Beam Current Analysis** (Current Monitor data)	**Overall Reliability Analysis** (Logbook data)
0-5 min*	1888	4250
5-15 min	217	203
15-60 min	124	132
1-5 hours	53	59
> 5 hours	13	11
Total	**2295**	**4655**

**The interval 0.5-5 min is used for the Beam Current Analysis since interruptions shorter than 0.5 minutes are not included.*

For interruptions longer than 5 minutes both analyses agree very well. 407 interruptions with down time >5 minutes occur in the Beam Current Analysis compared to 405 interruptions in the Overall Reliability Analysis. But, in the interval 0-5 minutes significant differences occur. The reason is due to the existence of a large number of short interruptions of the H+ beam. As observed in table 7.1, 86 % of all short interruptions (0-1 min) are caused by the injector, and a typical injector failure lasts for 10-20 seconds (sparking in the high voltage column). Interruptions which last for only 20 seconds will not affect the average current sufficiently enough in order for it to fall below the threshold current. Subsequently, short interruptions will not be interpreted as a "real" interruptions in the Beam Current Analysis and therefore they will not be included in the statistics. In the Overall Analysis any interruption is included. If the beam current is below half the scheduled current an interruptions is registered no matter how short the interruption is.

During steady state operation (without any interruptions) the beam is usually delivered at the scheduled current level. Of course, this is not all true. Sometimes the operator deliberately delivers the beam with less current, for example at tuning, but this is exceptional. For most of the time the operator tries to deliver the beam at the scheduled current level. When a failure or a beam disturbance occurs it is usually the Fast Protect System or the Run Permit System which activates and shuts the beam off. The result is that the beam current drops to zero immediately. This means that during continuous operation the accelerator delivers either the scheduled current or zero current (see Appendix 5). On the other hand, the average current which is recorded in the database and used as input data may be anywhere in between, it depends on the duration of the interruption. As mentioned the input data is based on the average current during one minute (usually 70 seconds). This means that:

At threshold factor 0.5, most Interruptions shorter than 35 seconds are not included in the Beam Current Analysis

9.4.2 Threshold Factor 0.8

A similar investigation as in section 8.4.1 has been performed at a threshold factor of 0.8.

If we say that the accelerator during scheduled operation delivers either the scheduled current or zero current (during a failure) then if we raise the threshold factor from 0.5 to 0.8 we actually increase the ability to detect short interruptions. The reason is due to the nature of the input data. Each input value represents the average current delivered during 70 seconds. Since the delivered current is either full scheduled current or zero the interruption length will determine the average current. This is illustrated in figure 9.4a and 9.4b.

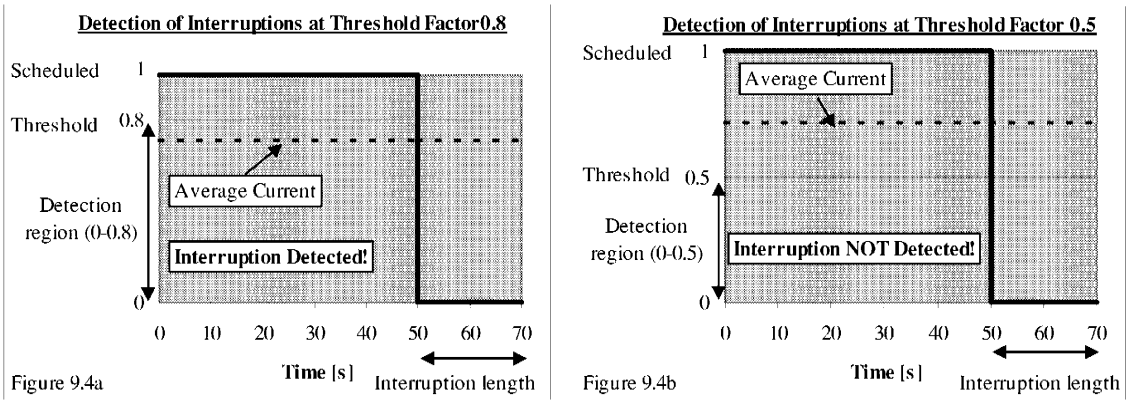

Figure 9.4a and 9.4b. Detection of Interruptions at Threshold factor 0.8 and 0.5

If the average current is below the threshold current the event will be detected and subsequently an interruption will be recorded. For example, if the threshold current is set to 0.8*(Scheduled Current) and an interruption with a duration of 20 seconds occur, the average current will be 0.71*(Scheduled Current) and the interruption will be detected (see figure 9.4a). But, if the threshold is set to 0.5*(Scheduled Current), the average current will exceed the threshold current and the interruption will not be detected (see figure 9.4b). In summary,

At threshold factor 0.8, interruptions > 14 seconds are detected.
At threshold factor 0.5, interruptions > 35 seconds are detected.

The risk of having a too high threshold factor (>0.9) is that you start detecting events that are actually no interruptions. For example, if the scheduled current is set to 1000 μA but the beam is deliberately delivered at 900 μA then the software would start to detect many false interruptions since small current fluctuations always occur.

In figure 9.5 the total number of detected interruptions at threshold factor 0.8 is presented. The analysis considers scheduled operation of the H+ beam for the period 18th of March - 27th of July, 1997.

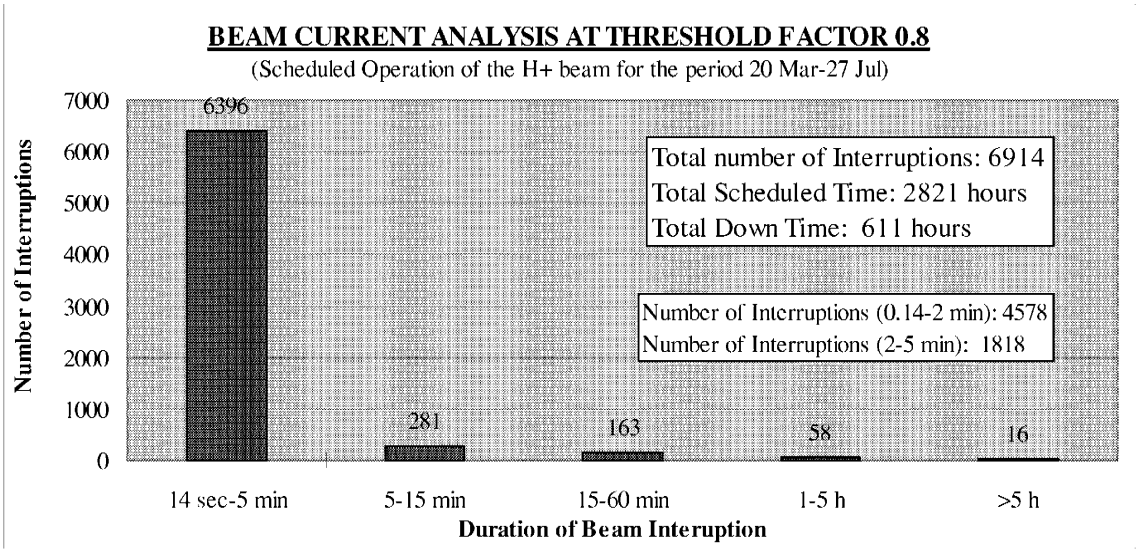

Figure 9.5 Summarize of Interruptions from the Beam Current Analysis at Threshold factor 0.8

A total of 6914 interruptions were detected. Significantly more than at threshold factor 0.5. In table 9.4 all three analyses are compared.

Table 9.4 Comparison of Interruptions which occur below threshold factor 0.5 and 0.8 and the Overall Reliability Analysis

	NUMBER OF INTERRUPTIONS		
Down Time Interval	**Threshold Factor 0.8** (current monitor data)	**Overall Reliability Analysis** (Logbook data)	**Threshold Factor 0.5** (current monitor data)
0-5 min*	6396	4250	1888
5-15 min	281	203	217
15-60 min	163	132	124
1-5 hours	53	59	53
> 5 hours	16	11	13
Total	**6914**	**4655**	**2295**

**The interval 0.5-5 min is used at threshold factor 0.5 and the interval 14 sec-5 min is used at threshold 0.8*

The increase in number of interruptions at threshold 0.8 is mainly due to the fact that a large number of short interruptions is detected. This is natural since the most common failure is high voltage sparking in the H+ injector column and this failure causes a down time of 10-20 seconds. At threshold factor 0.8, interruptions longer than 14 seconds are detected and hence most of the injector failures are recorded. Another important conclusion is that more interruptions are detected in the Beam Current Analysis at threshold factor 0.8 than in the Overall Reliability Analysis. This means that all short beam interruptions are not recorded in the logbook. This is also confirmed by operating personnel. For example, in periods when the injector is tripping very frequently the exact number of interruptions is not recorded, instead comments like "continuous arcing in the injector" are used.

In table 9.5 the growth of detected interruptions as a function of the threshold factor is presented.

Table 9.5 Threshold Factor as a function of Total number of Interruptions

Threshold Factor	Total Number of Interruptions
0.1	825
0.5	2295
0.7	4636
0.75	6558
0.8	6914
0.85	7030
0.9	6845

Obviously, the number of detected interruptions begin to grow less for threshold factors larger than 0.75, reaching a maximum around 0.85. This means that most interruptions are found at that point, and it also implies there are actually not many interruptions with down time less than 10 seconds. The reason why less interruptions are detected at threshold factor 0.9 is that individual interruptions which occur closely in time starts to "melt" together and form single interruptions with longer down time. For example, at threshold factor 0.9 22 interruptions with down time >5 hours are registered, while at threshold factor 0.8 16 interruptions are detected.

In figure 9.6 a representative plot of the average beam current is presented. A similar plot that reflects the instantaneous beam current every minute is presented in Appendix 5.

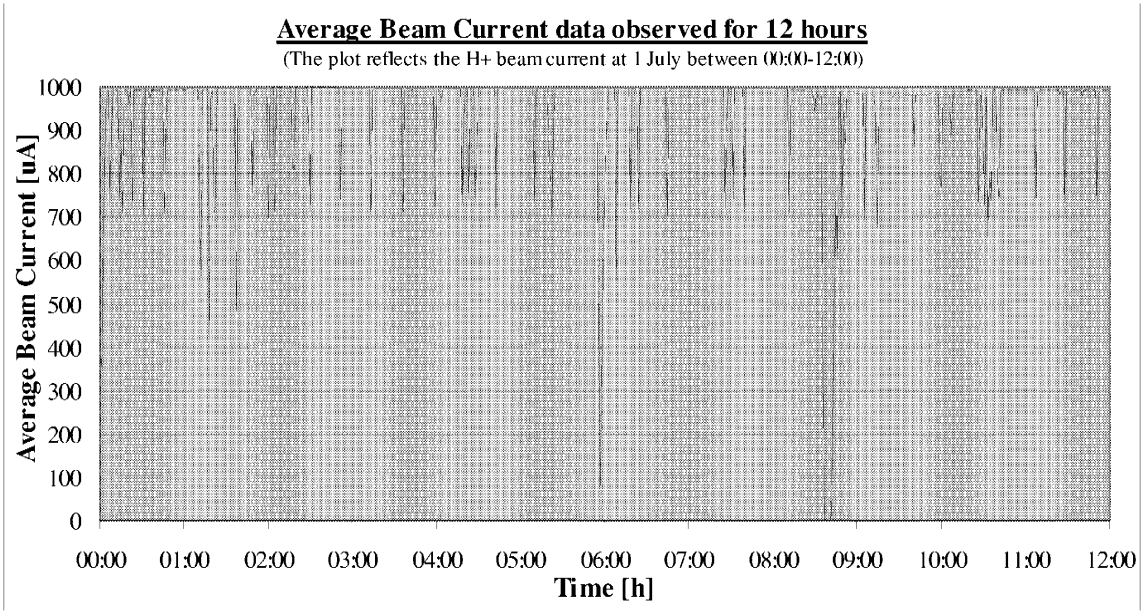

Figure 9.6 Plot of Average Beam Current as a function of time

The scheduled current is 1000 μA and most of the vertical spikes reach down to the region of 700-750 μA. This is no coincidence, the majority of the spikes represent injector failures with a duration of 15-20 seconds. As observed, very few spikes ends

above 800-900 μA. This means that there don't occur many interruptions with down time shorter than 10 seconds. In other words, if an interruption occurs it is likely it will last for at least 10 seconds.

9.5 Reliability Estimates

From the beam current data estimates of the Availability, Mean Time Between Failure (MTBF) and Mean Down Time (MDT) may also be obtained. In table 9.6 these numbers are summarized for all three analyses.

Table 9.6 Summary of the Availability, MTBF and MDT

Analysis	Availability	MTBF [h:mm]	MDT [h:mm]
Overall Reliability Analysis (Logbook data of H+ Beam, 1997)	86 %	0:31	0:05
Threshold Factor 0.5 (Current data of H+ Beam, 1997)	86 %	1:04	0:10
Threshold Factor 0.8 (Current data of H+ Beam, 1997)	78 %	0:19	0:05

The Availability for both the Overall Reliability Analysis and the Beam Current Analysis at threshold factor 0.5 is 86 % while it is 78 % at threshold factor 0.8. Since the availability is determined by the total down time, it means a substantial amount of additional down time is included in the Beam Current Analysis at threshold factor 0.8 in comparison with the other two analyses. We know for a fact that many more interruptions are detected at threshold 0.8, but most of these interruptions are short and the contribution to the total down time should not be that much. Due to the nature of the input data any short interruption (< 70 seconds) will be assigned a down time of 70 seconds even if the interruption only lasted for 20 seconds. In other words, the calculated availability at threshold factor 0.8 does not reflect the real availability. Of course this applies at threshold factor 0.5 as well but the effect is not as pronounced. Actually, a somewhat similar problem occurs in the Overall Reliability Analysis where only discrete numbers of down time are recorded 1,2,3... minutes (every short interruption will be assigned a down time of 1 minute). The conclusion is that the overall availability of the H+ beam is most likely in the region of 85%.

MTBF in the Overall Reliability Analysis is 31 minutes which is half the value compared to the MTBF in the Beam Current Analysis at threshold 0.5. This is natural since the Overall Reliability Analysis includes twice as many interruptions. At threshold factor 0.8 even more interruptions are included and subsequently the MTBF is lower (19 minutes). The correct MTBF estimate of the H+ beam should probably be in the region of 20-25 minutes.

MDT is 5 minutes for both the Overall Reliability Analysis and the Beam Current Analysis at threshold 0.8. At threshold factor 0.5 the MDT is 10 minutes, but this number reflects more what the MDT would be if the injector interruptions were not included in the analysis. Naturally, the injector interruptions have a big influence on the MDT. Since the total down time observed at threshold factor 0.8 is too large the actual MDT is in fact shorter than 5 minutes, more likely in the region of 4 minutes.

9.6 Conclusions

When comparing the Overall Reliability Analysis of the LANSCE Accelerator facility with the Beam Current Analysis it is remarkable how well the results agree even though the underlying data origins from two completely different records. The Overall Reliability Analysis is based on comments in the logbook while the Beam Current Analysis is based on current recordings from a beam monitor. For down times >5 minutes a total of 407 interruptions are detected in the Beam Current Analysis compared to 405 interruptions in the Overall Reliability Analysis. That is a strong evidence for the correctness of both analyses. For down times <5 minutes, especially <1 minute, significant differences in reliability results occur. This is due to the nature of the input data in the Beam Current Analysis. When analyzing interruptions where the average delivered current should fall below half the scheduled current, interruptions with down time shorter than 35 seconds are not detected. By raising the threshold current to 0.8*(Scheduled Current) interruptions with down time >14 seconds are detected. At this interruption length most of the short interruptions are detected. When taking in consideration the results from all three Analyses, the conclusions are:

Conclusions concerning the reliability of the H+ beam at LANSCE:

- Many short interruptions with down time in the region of 10-20 seconds occur.
- The occurrence of short interruptions is larger than recorded in the logbook.
- Practically no interruptions with down time <10 seconds occur.
- The Availability is ≈85%
- Mean Time Between Failure is about 20-25 minutes.
- Mean Down Time is about 4-5 minutes.

10 Acknowledgement

First of all I would like to thank Christopher Piaszczyk of Northrop Grumman Corporation for all his expert advice and help. The generous assistance of many LANSCE Operations Personnel in performing this work is greatly appreciated. Special thanks are due to Michael Oothoudt and Tim Callaway of LANSCE-6. Also, special thanks are due to Stan Cohen of LANSCE-6 for valuable help with magnet power supplies and John Lyles of LANSCE-5 for help with RF Technology.

Finally I would like to express my appreciation to Waclaw Gudowski of the Royal Institute of Technology and Francesco Venneri of the Los Alamos National Laboratory for providing the opportunity to carry out this work.

11 References

[1] Francesco Venneri, "Accelerator-driven Transmutation of Waste", Technical Review MIT, 1998.

[2] Helmut Wiedemann, "Particle Accelerator Physics", Springer-Verlag, 1993.

[3] M. J. Smith and G. Phillips, "Power Klystrons Today", Research Studies Press LTD, 1995.

[4] J. Le Duff, "Dynamics and Acceleration in Linear Structures", Laboratoire de l'Accélérateur Linéaire.

[5] John W. Staples, "RFQ's- An Introduction", Lawrence Berkeley Laboratory, University of California, 1990.

[6] Johan Carlsson, "Optimization of the neutron production in a spallation target", Royal Institute of Technology, 1996.

[7] R.A. Jameson, "Beam Losses and Beam Halo in Accelerators for New Energy Sources", International Symposium on Heavy Ion Fusion, 1995.

[8] George Lawrence, "Accelerator Design for ATW", Technical Review MIT, 1998.

[9] J. Sherman, A. Arvin, L. Hansborough, D. Hodgkins, E. Meyer, J.D Schneider, H.V. Smith, Jr., M Stettler, R.R. Stevens, Jr., M. Thuot, T. Zaugg, and Robinm Ferdinand, "Status Report on a dc 130 mA, 75 keV Proton Injector", 7th International Conference of Ion Sources, 1997.

[10] C. Rubbia, "The Accelerator Complex", IAEA Status Report on Accelerator driven systems (1997)

[11] M. Stanley Livingstone, "A Nuclear Research Facility", LA-6878-MS, 1977.

[12] Staffan Rosander, "Acceleratorteknik", Alfvénlaboratoriet, Royal Institute of Technology, 1997.

[13] Oscar R. Sander, "LAMPF Transition Region", LA-9315-MS, 1982

[14] E. A. Knapp, B. C. Knapp, and J. M. Potter, "Standing Wave High Energy Linear Accelerator Structures", Los Alamos National Laboratory, 1968

[15] Manuel Jr. Neutron Scattering Center, Los Alamos National Laboratory, LP-95-219, 1995.

[16] Michael Oothoudt, "Availability for cycle 75", LANSCE-6 Technical Report LANSCE-6-97-51-TR, 1997.

[17] Olin van Dyck, "LAMPF Reliability History and Program", International Conference on Accelerator-driven Transmutation Technologies and Applications, Las Vegas, 1994

[18] Neil Marks, "Conventional Magnets - 1", Daresbury Laboratory, Warrington, 1992.

[19] R. Macek, "LANSCE PSR Technical Note #17", PSR-94-017, Los Alamos National Laboratory, 1994.

Appendix 1

A1 Beam Schedules

1997 H+ BEAM SCHEDULE TO AREA A		
Beam On*	**Beam Off***	**Beamtime [h:mm]**
CYCLE 74		
03/18/97 17:00	03/23/97 17:27	120:27
03/25/97 19:28	03/26/97 21:50	26:22
03/28/97 08:00	04/21/97 08:00	576:00
Scheduled beam time for Cycle 74:		**722:49**
Minus 1 hour daylight savings time		-1:00
	Adjusted Time:	**721:49**
CYCLE 75		
04/23/97 08:00	05/19/97 08:00	624:00
05/20/97 22:50	06/16/97 08:00	633:10
Scheduled beam time for Cycle 75:		**1257:10**
CYCLE 76		
06/18/97 08:00	07/14/97 08:00	624:00
07/16/97 04:41	07/27/97 08:00	267:19
Scheduled beam time for Cycle 76:		**891:19**
Total scheduled H+ beam time for 1997		**2870:18**

Table A1.1 Summarize of 1997 scheduled beam time for H+ beam (Cycles 74, 75 and 76)
**Times and dates based on Area A database.*

1997 H- BEAM SCHEDULE TO LUJAN		
Beam On*	**Beam Off***	**Beamtime [h:mm]**
CYCLE 74		
03/06/93 08:00	03/21/93 08:00	360:00
03/27/93 08:00	04/12/93 20:00	396:00
Scheduled beam time for Cycle 74:		**756:00**
Minus 1 hour daylight savings time		-1:00
	Adjusted Time:	**755:00**
CYCLE 75		
04/22/93 08:00	05/13/93 08:00	504:00
05/20/93 07:30	06/08/93 04:00	452:30
Scheduled beam time for Cycle 75:		**956:30**
CYCLE 76		
06/17/93 02:00	07/11/93 08:00	582:00
07/16/93 08:00	07/23/93 10:00	170:00
Scheduled beam time for Cycle 76:		**752:00**
Total scheduled H- beam time for 1997		**2463:30**

Table A1.2 Summary of 1997 H- Beam Schedule

1996 H- BEAM SCHEDULE TO LUJAN		
Beam On*	**Beam Off***	**Beamtime [h:mm]**
CYCLE 71		
07/09/92 08:00	07/15/92 08:00	144:00
07/17/92 21:30	07/27/92 08:23	226:53
07/29/92 14:00	08/23/92 08:00	594:00
Scheduled beam time for Cycle 71:		**964:53**
CYCLE 72		
08/29/92 02:10	09/02/92 08:00	101:50
09/06/92 08:00	09/20/92 08:00	336:00
09/24/92 07:00	10/20/92 07:00	624:00
Scheduled beam time for Cycle 72:		**1061:50**
CYCLE 73		
10/28/92 20:00	11/17/92 07:00	467:00
11/19/92 07:00	11/26/92 00:00	161:00
11/26/92 18:00	11/27/92 20:00	26:00
Scheduled beam time for Cycle 73:		**654:00**
Total scheduled H- beam time for 1996		**2680:43**

Table A1.3 Summary of 1996 H- Beam Schedule

Appendix 2

A.2 Summary of DC Magnets and Power Supplies at LANSCE

By Marcus Eriksson, RIT

LOCATION	Device Area	Quadrupole Lenses QL	Quadrupole Magnets QM	Quadrupole Doublets QD	Quadrupole Triplets QT	Focussing Quadrupoles QF	Defocussing Quadrupoles QU	Bending Magnets BM	Steering Magnets SM	Vertical Magnets VM	Horizontal Magnets HM	Total Magnets	Power Supplies MP
Injector Building													
Transport A	TA	18						1	5			**24**	**24**
Transport B	TB	18						1	7			**26**	**26**
Transport D	TD	4						1	1			**6**	**6**
Accelerator													
201	M1-M4		132						10			**142**	**16**
805	M5-M48			103								**103**	**54**
Transition Region	TR		8					8	12			**28**	**11**
Switchyard													
Line A	LA		2	4				4	6			**16**	**11**
Line XD	XD		2					3				**5**	**4**
Line D (LD Kicker to RI Kicker)	LD			12	10			18		6	6	**52**	**33**
Proton Storage Ring													
Line D (RI Kicker to Line E)	LD			22						11	9	**42**	18
Ring Injection Line	RI					5	5	5		10	6	**31**	21
PSR	SR					10	10	10		10		**40**	4
Ring Extraction Line	RO					6	6	2		3	3	**20**	10
Bypass Beamline	BY							4		1	3	**8**	4
Line to Target Station 1 in Lujan	1L			6				4			3	**13**	8
Line to Target Station 2 and 4 in WNR	1R			6				2		3	3	**14**	11
Area-A													
Target Station 1	1A				3				3			**6**	3
Target Station 2	2A				6				3			**9**	5
Target Station 3	3A			2					3			**5**	3
Mass Separator	4A			2					2			**4**	3
Bio-Medical Target Station	5A				3				2			**5**	3
TOTAL		**40**	**144**	**157**	**22**	**21**	**21**	**63**	**54**	**44**	**33**	**599**	**278**
Number of Dipoles								63				**63**	
Equivalent number of Quadrupole Magnets. (Quadrupole Doublets and Triplets have been converted into single Magnets)		40	144	314	66	21	21		54	44	33	737	
TOTAL NUMBER OF DC MAGNETS												**800**	

Appendix 3

A3 Summary of Components in the Pulsed Power System

Subsystem	Assembly	Component
Switchyard Kicker		
	Kicker Magnet	
		Vacuum Vessel
		Current Connections
		Current Buses
		Compensation Capacitor
	Charging System	
		HVPS, EMHP
		External Capacitor Bank
		Charge SCR
		Resonate Inductor
		Do-Q SCR
		DE-Q Shunt Resistor
	Modulator	
		PFN Capacitors
		Output SCR
		Shunt Resistor
		Load
		Regulator Transistors
		PS, Sorensen DCR40-250A
	Output Transmission Line	
		Transmission Line
		Cooling Blower
	Controls/Interlocks	
		PS, PD Model 6050A
		LDK101 Run Permit Interface Panel
		LDK102 Run Panel Permit Interface Panel
		SCR fire Module
		Switchyard Kicker Interlock/Control Chassi
		Regulator Amplifier Module
		Current Regulator Drive Module
		Fast Protect Module
		DAC Do-Q Module
		Gate Generator Module
		PS, PSR Low Voltage Group
	Computer Interface	
		CAMAC
Injection Kicker		
	Kicker Magnet	
		Current Connections
		Coils
	Charging System	
		PS, Sorensen SCR
		Zener Diode Assembly
		Charge Recover SCR
		Freewheel SCR
		Transfer Chassis
	Controls/Interlocks	
		RIK101 Run ? Interface Channels
		NIM Crate w/6 Modules
		Short NIM Crate w/8 Modules
	Computer Interface	
		CAMAC

Harmonic Buncher		
	Cavity	
		Ceramic Gap
		Gap Shunt Capacitors
		Ferrite
		RF Connector
		Cooling Hoses
		Bias PS. RF Choke
		Bias PS, PEI SR 1064
	Low Level Electronics	
		Dual TTL Fanout 63Y182451
		2.8 Mhz Harmonic Buncher
		CW Leveling Amplifier
		Hex Analog Fanout 63Y182290
		Harmonic Buncher Fast Protect
		Buncher Wide Band Amplifier
	RF Preamplifier	
		ENI A-300
	RF Drive Amplifiers	
		HVPS UVC 15 kV/3 A
		UVC Capacitor Bank
		UVC Crowbar Unit
		HVPS UVC 15 kV/6 A
		Tube 4CW25000
		Tube 8919
		Driver Filament PS Chassis
		Final Filament PS Chassis
		Final Filament Transformer
		PS, UVC 1 kV/1 A
		Pulsed Bias PS Chassis
		Screen Grid PS Chassis
		Balun Transformer
		Driver Coupling Transformer
		Final Coupling Transformer No. 1
		Final Coupling Transformer No. 2
	Output Transmission Line	
		Output Transmission Line
	Controls/Interlocks	
		UVC Monitor/Control/Interlock Chassis
		Harmonic Buncher Control/Interlock Chassis
		Buncher Cavity Bias Remote Control Chassis
		PSR Buncher Interface Chassis
		Cap Voltage Distribution/Monitor/Filter Chassis
		Master Sync System 2.8 MHz Chassis
	Computer Interface	
		CAMAC
Extraction Kickers		
	Kicker Magnets	
		Vacuum Vessel 71
		Vacuum Vessel 81
		Electrodes 71
		Electrodes 81
		HV Vacuum Feedthroughs
		HV Cable Connectors
	Charging System	
		UVC HVPS 1.6 kV/6 A
		Charge Thyatron
		Bias PS, HP 6207B
		Bias PS, Bertan Model 210-00R

		Driver, IE TD-25
		Do-Q Thyratron, HY 3002
		Do-Q Thyratron Driver
		Storage Capacitors
		Pulse Transformer
		Pulse Charging Diode Stack
		Inverse Diodes
		Rec-Htr PS
	Switching System	
		Switch Thyratron, CX1725
		Switch Driver
		PS, Bertan Model 210-00R
		Ree/Htr PS
		Blumlein Cables
		Heat Exchanger System
		Hydraulic Lift
	Cables	
		Output Cables
		Output Connectors
		Output Cables ? Modulators
		Load Cables
	Loads	
		Loads
	Controls/Interlocks (NIM Modules)	
		ESI PS-90-N
		ESI LDM-2N
		Voltage Comparator, Dual
		Fast Kicker Audio Arc Monitor
		Arc Threshold Detector
		Local/Remote Timing
		Fine Pulse Booster
		SRFK71 Fast Protect
		SRFK81 Fast Protect
		Extraction Kicker Control/Interlocks Chassis
	Computer Interface	
		CAMAC

Table A3.1 List of Components for the Kickers and Buncher [19]

Appendix 4

A4 Statistics of failure causes in individual Systems

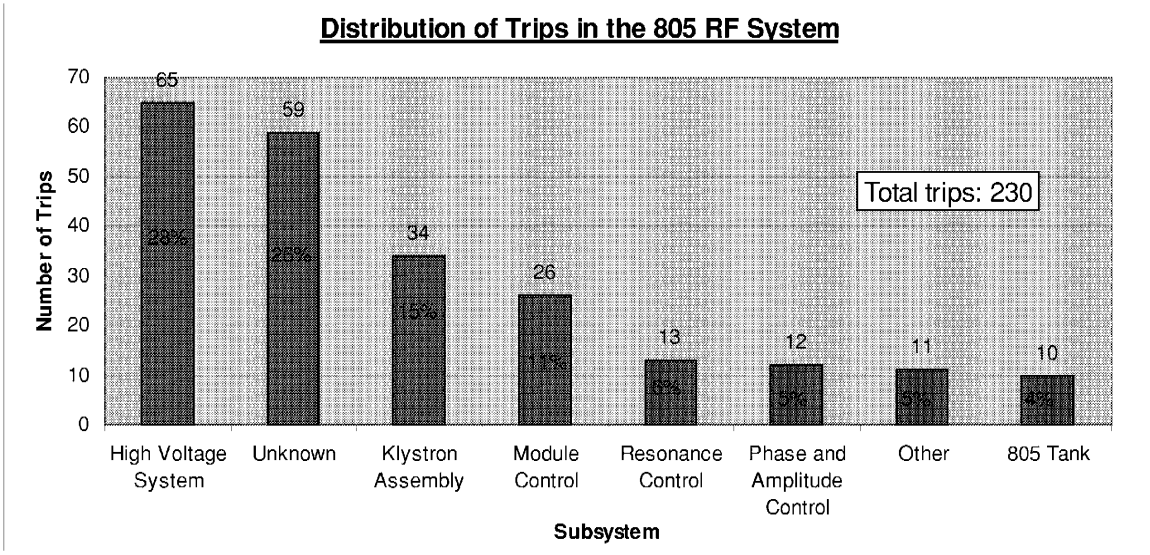

Figure A4.1 Distribution of Trips in the 805 RF System

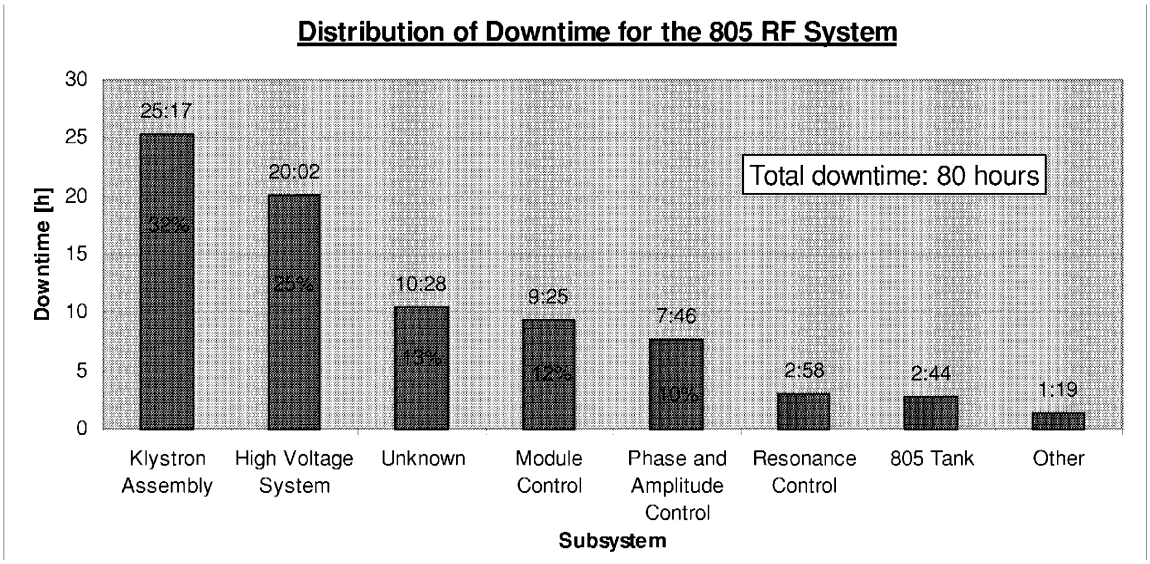

Figure A4.2 Distribution of Downtime for the 805 RF System

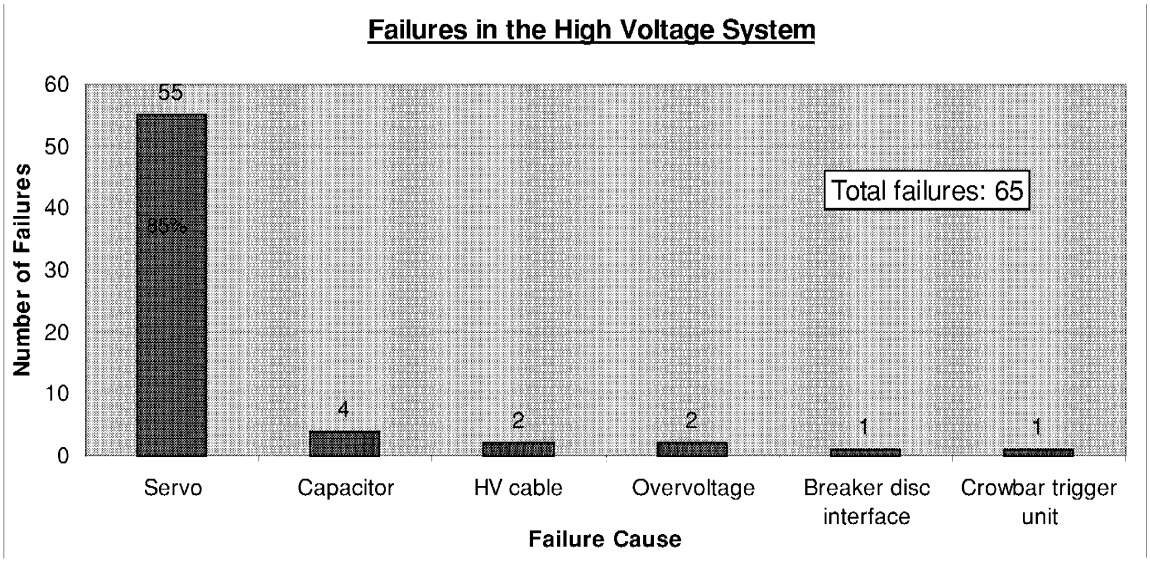

Figure A4.3 Failures in the High Voltage System

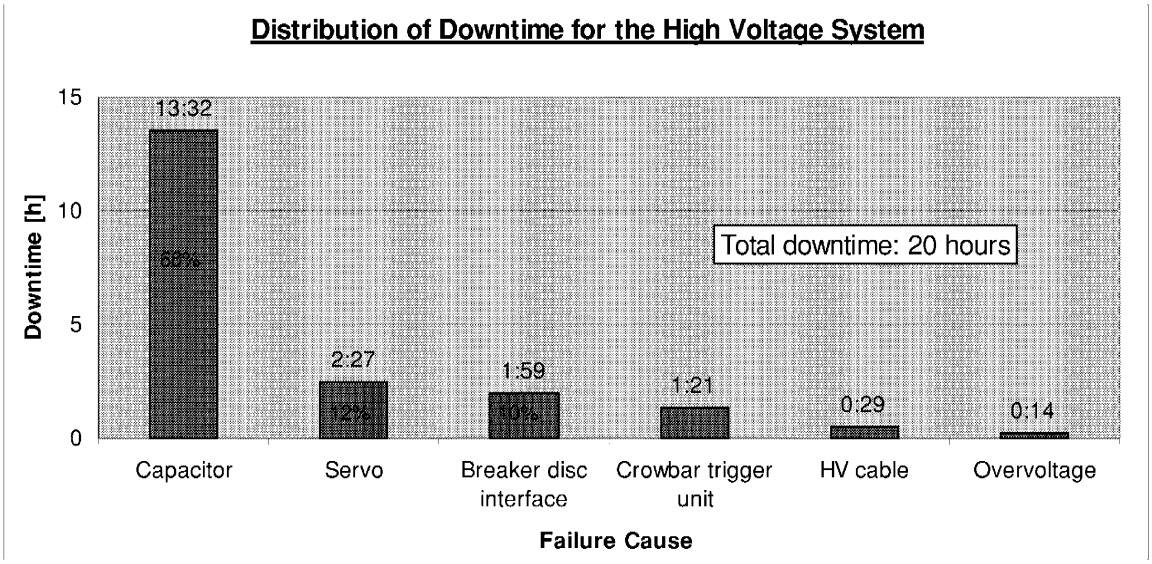

Figure A4.4 Distribution of Downtime for the High Voltage System

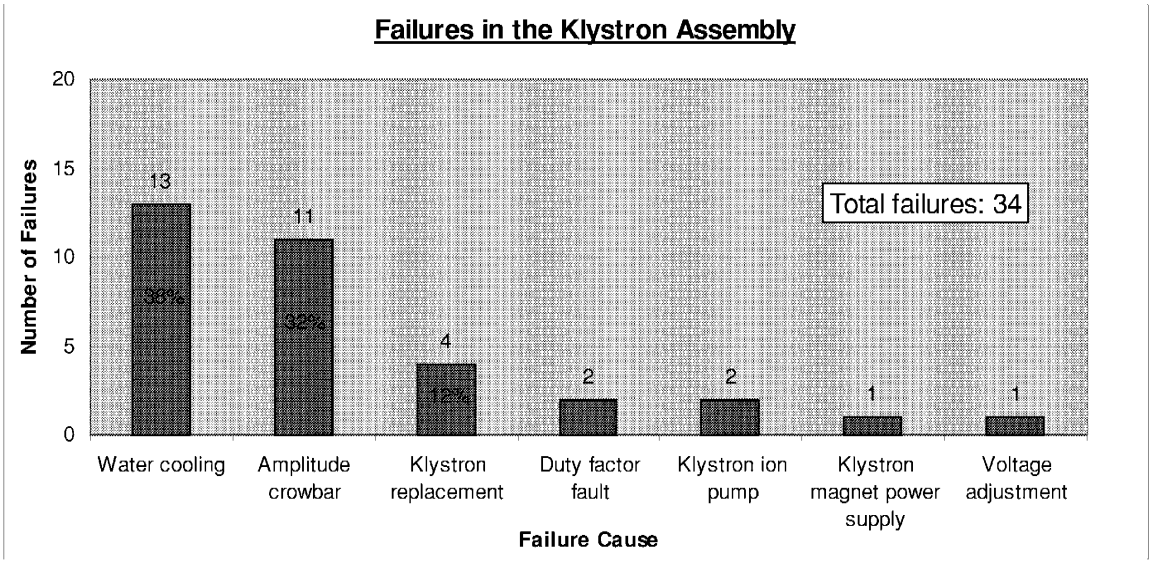

Figure A4.5 Failures in the Klystron Assembly

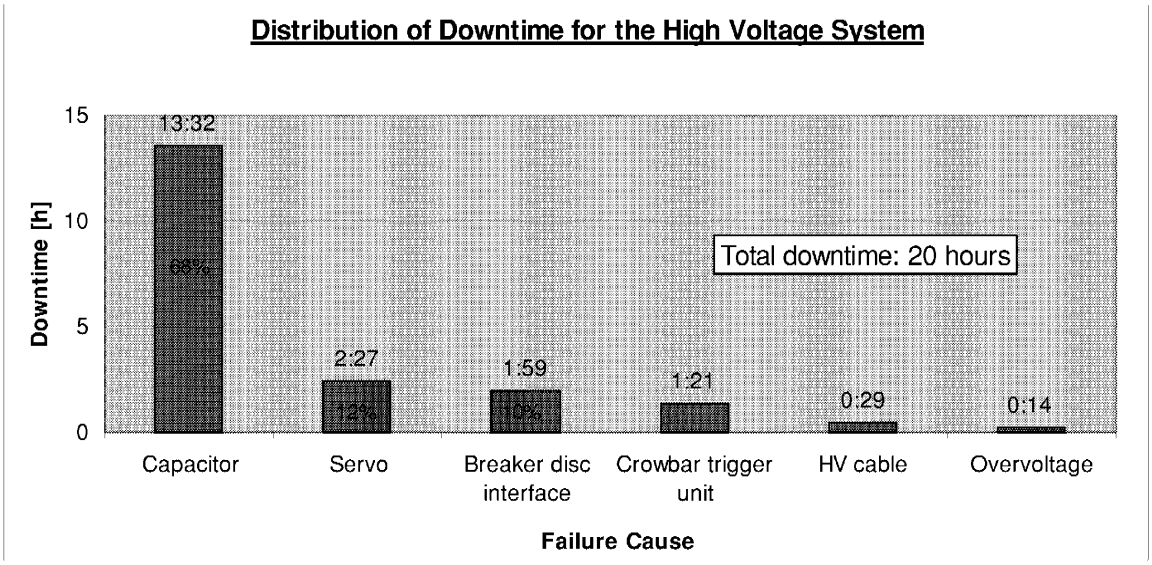

Figure A4.6 Distribution of Downtime for the Klystron Assembly

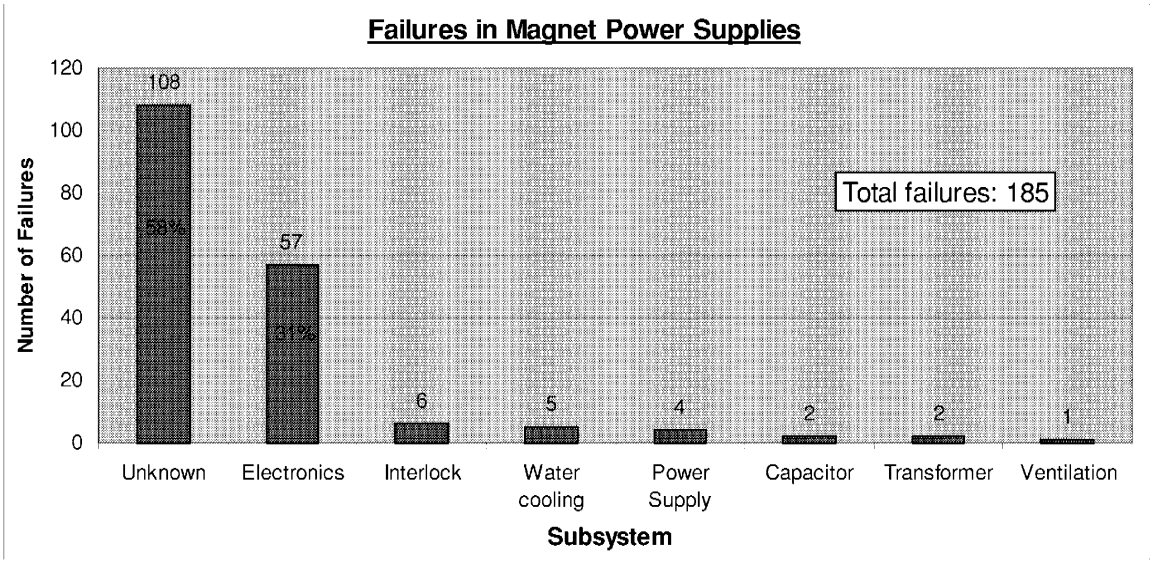

Figure A4.7 Failures in Magnet Power Supplies

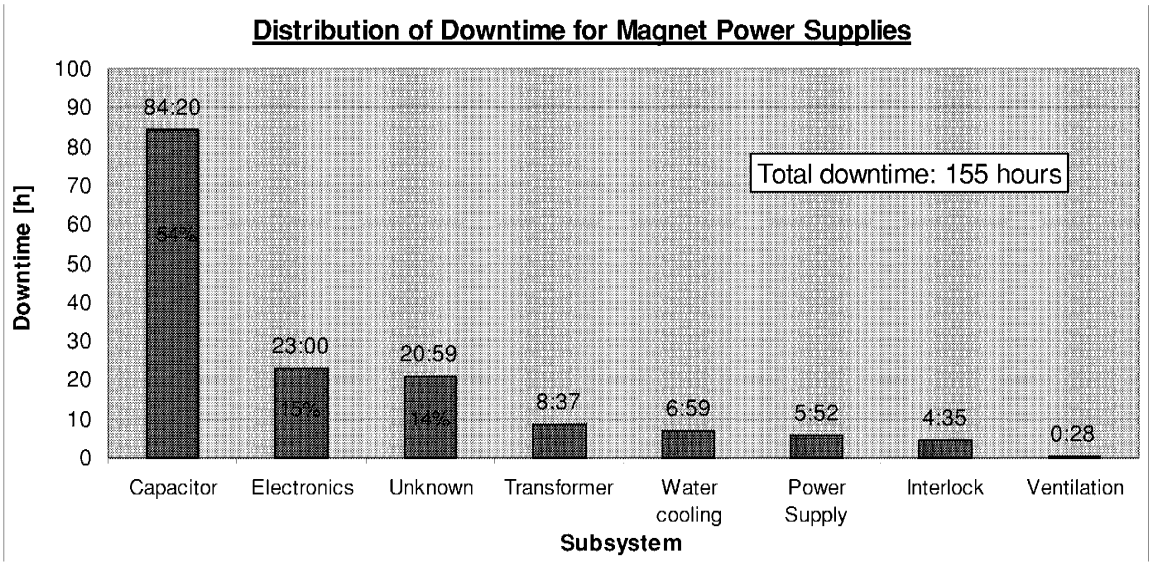

Figure A4.8 Distribution of Downtime for Magnet Power Supplies

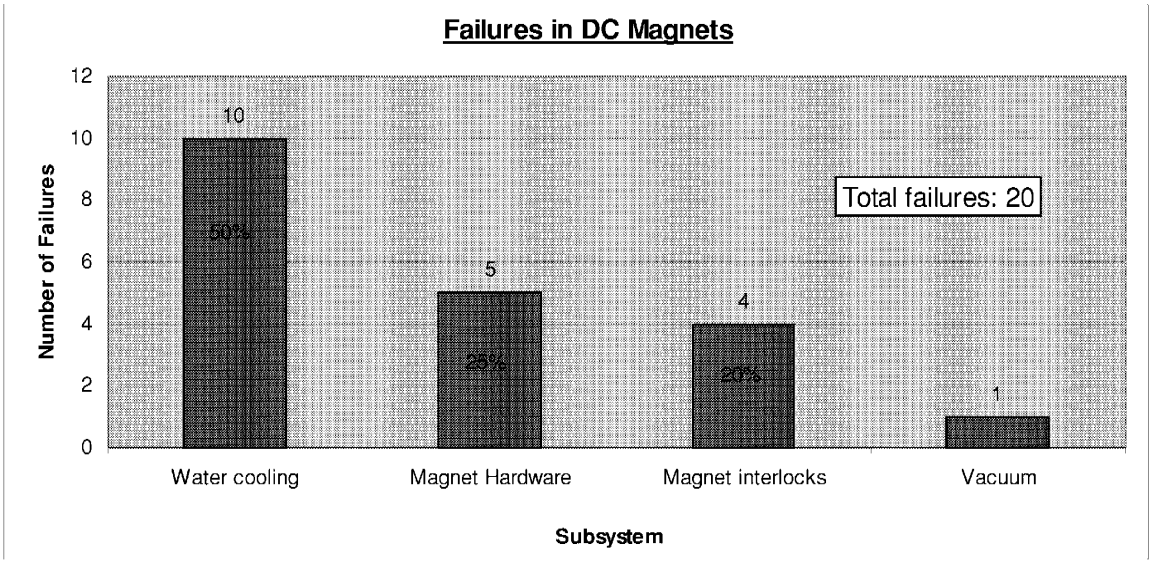

Figure A4.9 Failures in DC Magnets

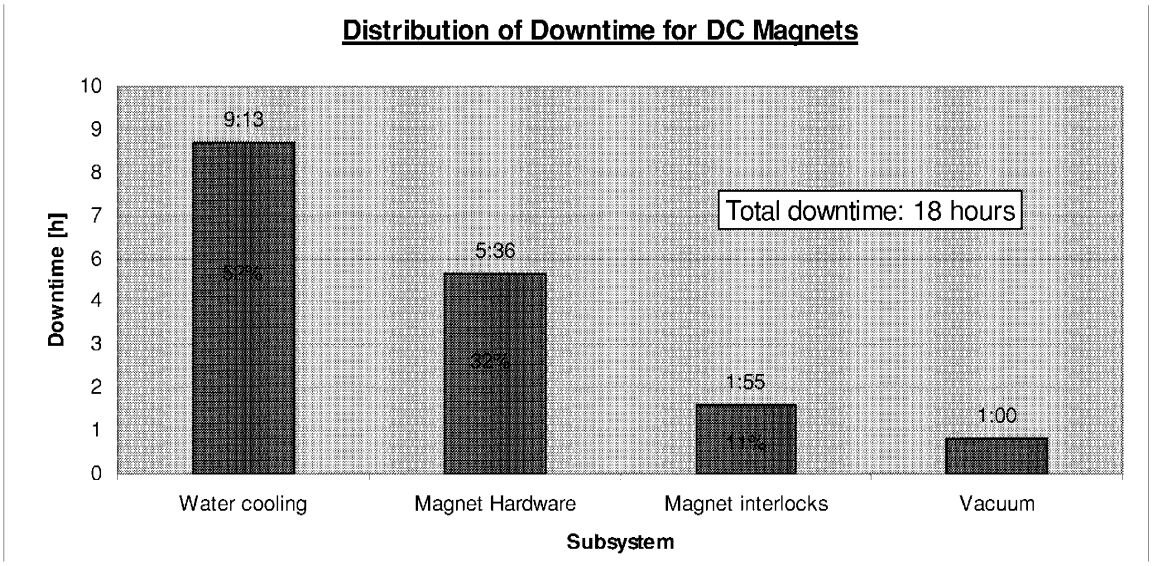

Figure A4.10 Distribution of Downtime for DC Magnets

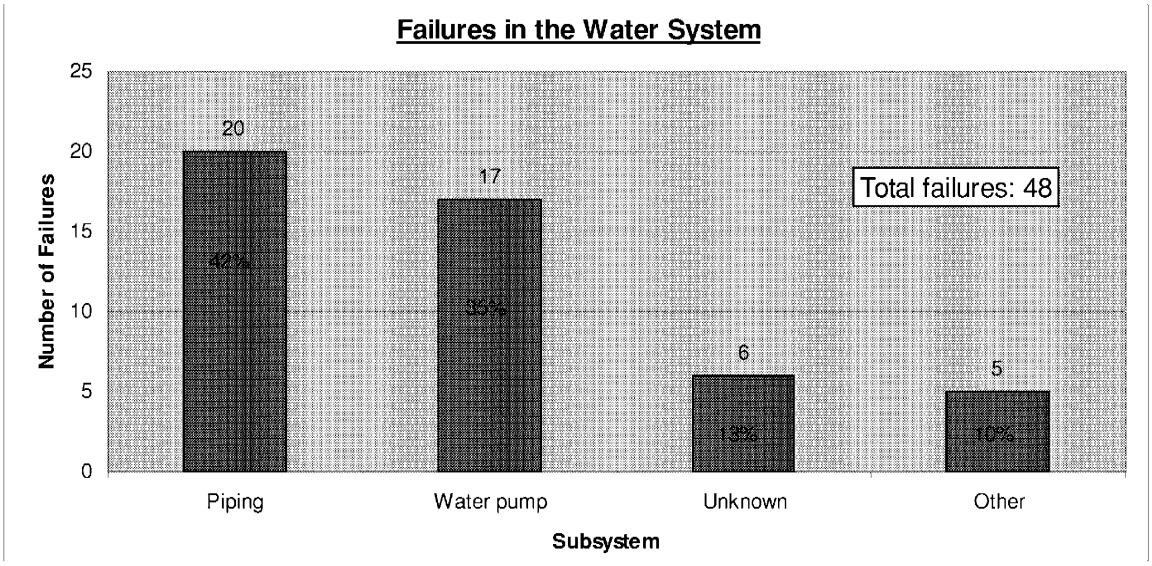

Figure A4.11 Failures in the Water System

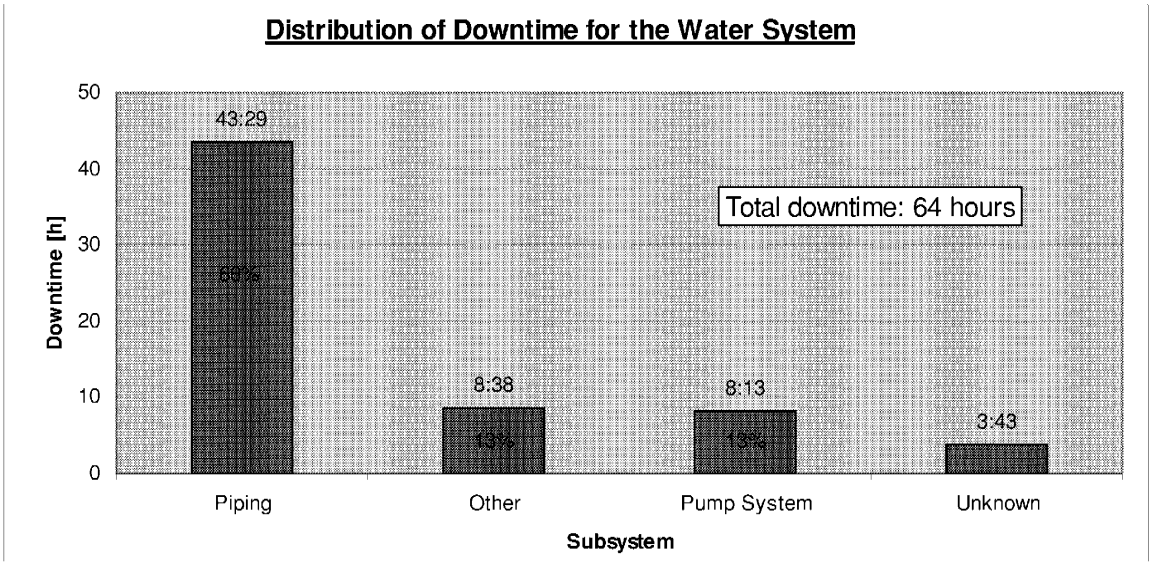

Figure A4.12 Distribution of Downtime for the Water System

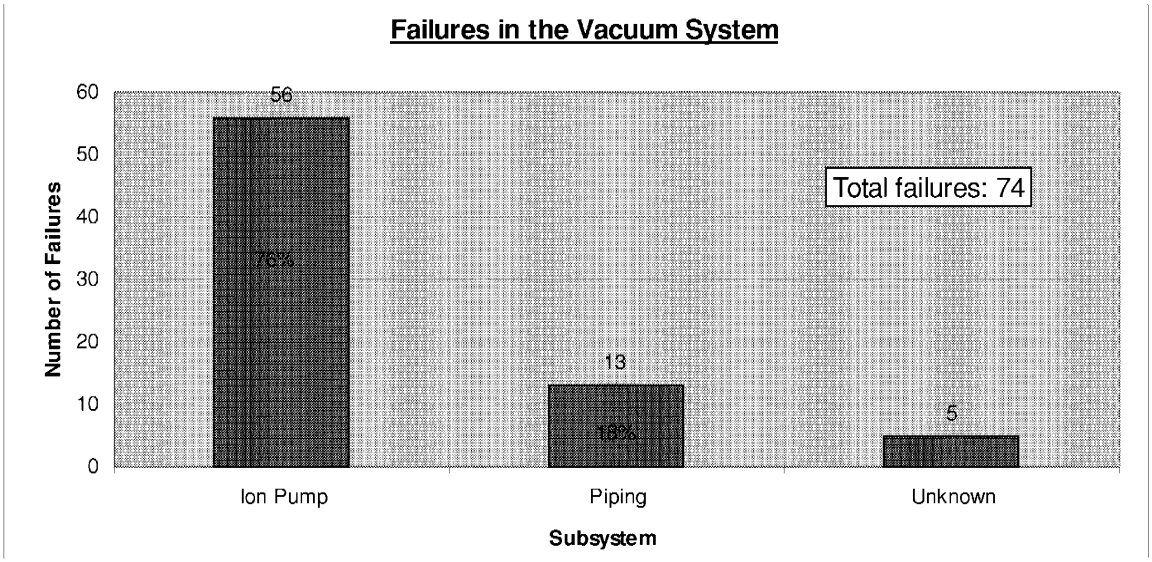

Figure A4.13 Failures in the Vacuum System

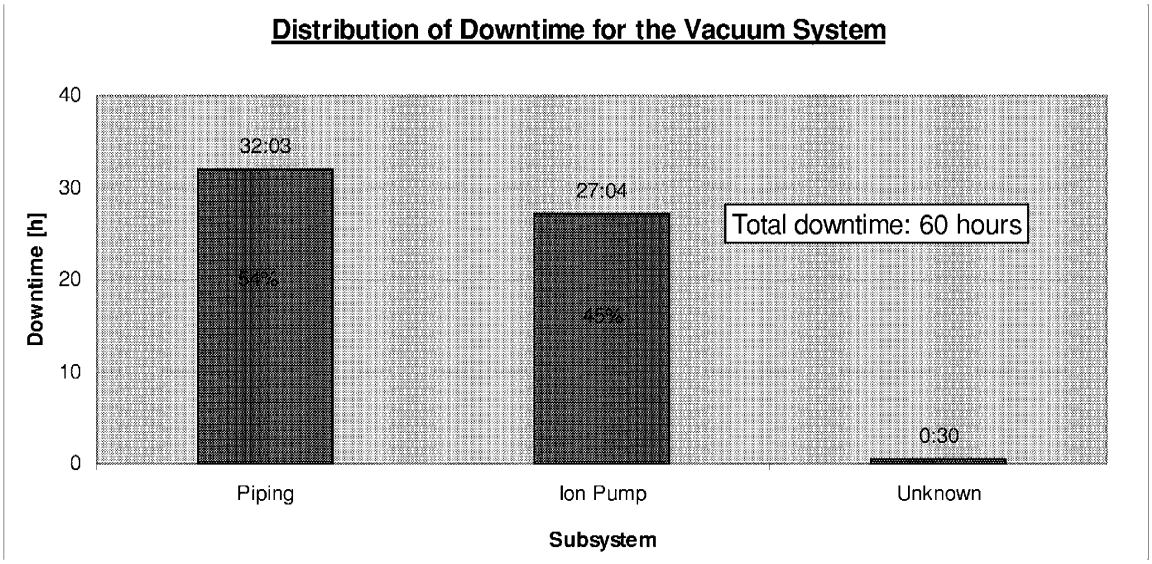

Figure A4.14 Distribution of Downtime for the Vacuum System

Appendix 5
A5 Instantaneous Beam Current

Appendix 5

A5.1 Instantaneous beam current

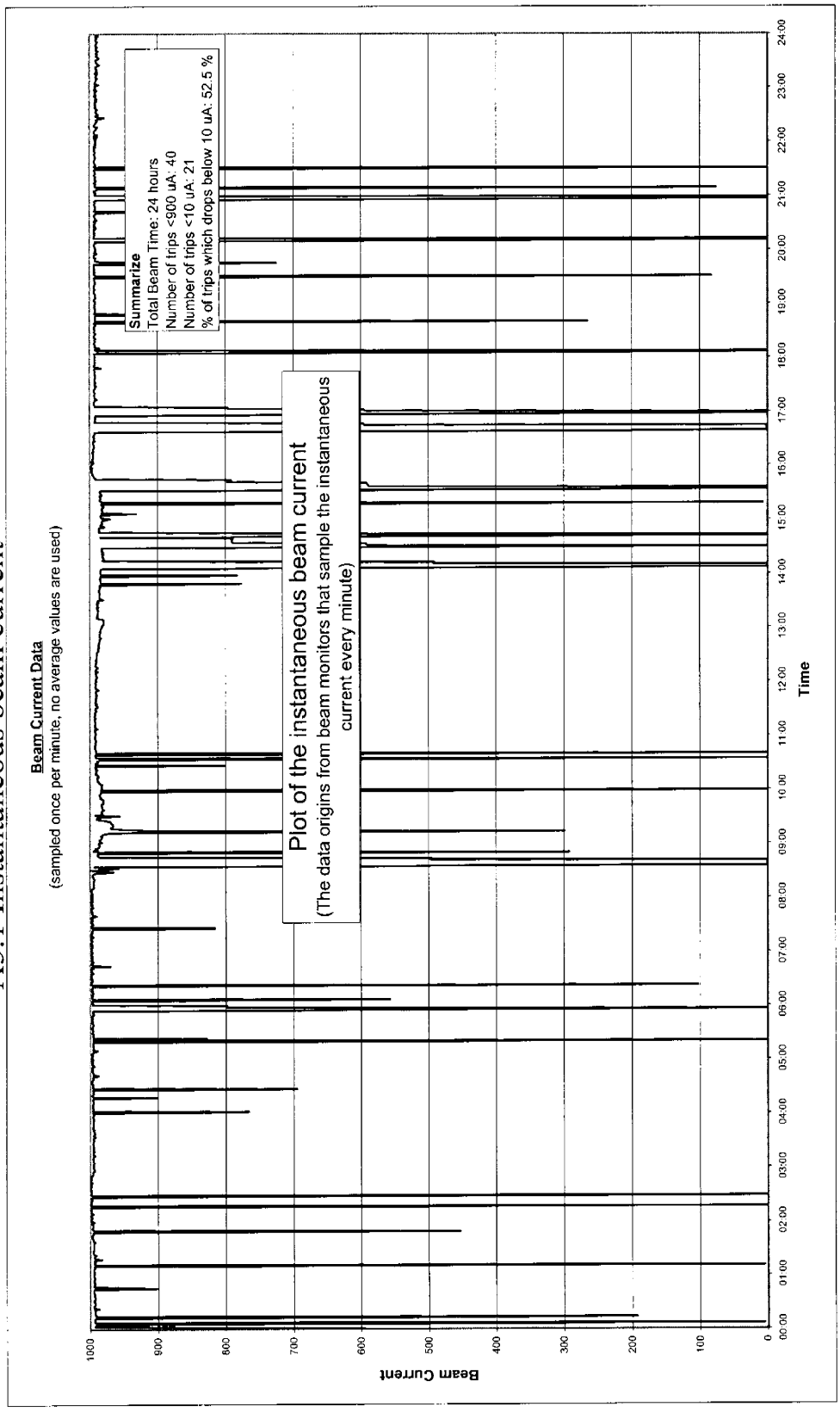

APPENDIX 5

REACTOR NEUTRON INDUCED MATERIAL DAMAGE IN SUBCRITICAL SYSTEMS

BY

CHARLOTTA SANDERS

LICENTIATE DISSERTATION AT THE
ROYAL INSTITUTE OF TECHNOLOGY

DEP. NUCLEAR & REACTOR PHYSICS
ROYAL INSTITUTE OF TECHNOLOGY
S-100 44 Stockholm, Sweden

Thesis for the degree of Technical Licentiate in Reactor & Neutron Physics presented at the Royal Institute of Technology in 1998.

Abstract

In the design of nuclear reactor cores for transmutation of nuclear waste, special demands have been placed on cladding and construction material. The highly energetic neutron spectrum that is needed for an effective transmutation of actinides and fission products may be implemented by the use of heavy liquid metal coolants, such as lead/bismuth. The average neutron elastic collision energy in a heavy metal cooled reactor core may be as high as 400 - 500 keV, which is about three times higher than the typical value for a sodium cooled breeder reactor. In the present study, the energy available for lattice displacements in cladding materials was calculated with NJOY as a function of incident neutron energy. Quenched cascade defect fractions were calculated within the binary collision approximation using the simulation code MARLOWE in the energy range 1-1000 keV. The fraction of lattice defects surviving correlated recombination was then estimated using results of recent molecular dynamics simulations. A comparison with standard NRT DPA values show that the latter should be used with considerable caution in the description of defect production in fast neutron spectra. Consequently, experimental data on void swelling and embrittlement in sodium cooled reactors cannot be trivially scaled to heavy metal cooled systems using ratios of NRT DPA, as has been customary in previously published works.

Keywords

Defect Production, Radiation Damage, Fast Spectrum, Nuclear Waste Transmutation, Ferritic Martensitic Steel

LIST OF PAPERS

This thesis is based on the following paper:

I. *C. Sanders and J. Wallenius*
Fission Neutron Induced Defect Production in Heavy Metal Cooled Reactors
Submitted to Journal of Reactor Technology.

The author

Contents

CHAPTER 1. INTRODUCTION

The demands of energy in the world today are ever increasing. It has been proven that where there is enough energy provided, health care is better, food is more affordable, more children are educated, life spans are longer and the quality of life is better. Therefore, it is essential that nuclear energy can be preserved as an energy source. One obstacle facing nuclear energy is the highly radioactive waste, which is generated during power production. In order for nuclear power to realize its full potential, there must be safe and efficient ways of taking care of the waste. In order to both be able to take care of the waste and to sustain the growing energy demands, a new approach to nuclear energy is needed. Accelerator driven Transmutation of Waste (ATW) could offer a new breakthrough in the field of nuclear energy. The ATW accelerator burns the nuclear waste in a subcritical reactor driven by neutrons from a spallation target subject to the impact of a proton beam. This reduces the toxicity of waste while providing, because of its subcriticality, a safer system.

This report is outlined in the following manner. Chapter 2 and 3 give a brief explanation of the transmutation concept and the Accelerator Driven System (ADS) that provides the option of transmutating nuclear waste. Chapter 4 briefly presents the current investigation, which is referred to as the Sing-Sing Core (SSC) project, motivated by efforts to find environmental friendly and safe management of spent nuclear fuel by means of transmutation. In the design of nuclear reactor cores for transmutation of nuclear waste, special demands have been placed on cladding and construction materials. Chapter 5 outlines the study focusing on irradiation damages in ferritic martensitic steel induced by fission neutrons.

CHAPTER 2. TRANSMUTATION OF NUCLEAR WASTE

2.1 Introduction

Spent nuclear fuel contains large quantities of long-lived radio-toxic transuranics and fission products. From a geologic storage point of view, there is a potential problem if there are any possibilities of release to the environment. One way of preventing these toxic elements of being released into the environment is to eliminate them by transmutation. Through transmutation, one element can be converted into another by changing the structure of the atomic nuclei. This way

the actinides and the fission products can be eliminated to a large extent and, consequently, significantly reduce the geologic storage inventory and toxicity.

2.2 Nuclear Waste

Natural uranium consists of 99.3% uranium-238 and 0.7% uranium-235. Fuel used in modern light water-cooled nuclear power plants consist of 97% ^{238}U and 3% ^{235}U. It is mainly ^{235}U that fission, while ^{238}U has a very low probability of fissioning compared to neutron capture. When ^{238}U captures a neutron, Plutonium-239 is produced according to equation 1:

$$n + {}^{238}U \rightarrow {}^{239}U \rightarrow {}^{239}Np + e^- \rightarrow {}^{239}Pu + e^- \qquad (1)$$

In a similar way americium, neptunium and curium are produced, which are the main constituents of the long-lived toxic waste. These isotopes are unstable and they also have a very long half-life. Some toxic fission products, like ^{99}Tc, have a half-life of 200000 years. By transmutation, ^{99}Tc can be converted to ^{100}Ru, which is both stable and unharmful. The reaction that takes place is the following:

$$n + {}^{99}Tc \rightarrow {}^{100}Tc \rightarrow {}^{99}Ru + e^- \qquad (2)$$

2.3 Neutron Economy

Large neutron availability is necessary for transmutation of waste, otherwise the transmutation will not be as efficient. The neutron economy can be improved by using a coolant with heavy nuclei and/or by adding an external neutron source. By exchanging water coolant for liquid heavy-metal coolant the neutrons maintain high velocities and can, therefore, fission also heavy nuclei with even number of neutrons. An added external neutron source achieves a series of nuclear reactions in the reactor without the necessity of a self-sustaining chain reaction, i.e. the reactor can be subcritical. This kind of system, that provides increased safety margins because the external neutron source controls the heat development, is commonly referred to as an Accelerated Driven System (ADS).

CHAPTER 3. ACCELERATOR DRIVEN SYSTEMS

3.1 Introduction

Several options of transmutation methods have been proposed. Among the most feasible systems are those that utilizes high power proton accelerators, i.e., an Accelerated Driven System (ADS). Some of ADS's advantages are:

- While producing power, up to 99 % of the nuclear fuel is burnt
- Allows for plutonium free fuel (i.e. minor actinide only)
- Offers safety due to its subcriticality

Existing commercial nuclear power plants do not offer these features. Through ADS, the nuclear fuel can be utilized to a much larger fraction reducing geological storage of long-lived actinides and fission products. ADS also have, in addition to the traditional reactor safety control functions, the possibility of more easily shutting down by turning off the accelerator (see details below) which makes it a very safe system, provided that the accelerator reliability is sufficiently high.

3.2 Accelerator driven Transmutation of Waste (ATW)

Because an ADS is subcritical, the system doesn't rely on delayed neutrons for power control and power change. The ADS system is driven by an externally generated neutron source, the accelerator, which delivers a highly energetic proton beam to strike a target (Fig.1). The target is proposed to be made out of tungsten or lead-bismuth compositions, which both feature low absorption of neutrons. When the high-energy particle beam strikes the target, a high intensity neutron source (spallation neutrons) is being created. This process is referred to as *spallation* and it ensures a large neutron availability, which is needed to effectively transmute the waste. Next, the spallation neutrons go into a subcritical blanket surrounding the target. The blanket contains the nuclear waste and, due to the system's subcriticality, it can burn any type of waste composition. In the blanket, the neutrons are multiplied by fission reactions transmuting waste isotopes into stable or short-lived nuclei [15].

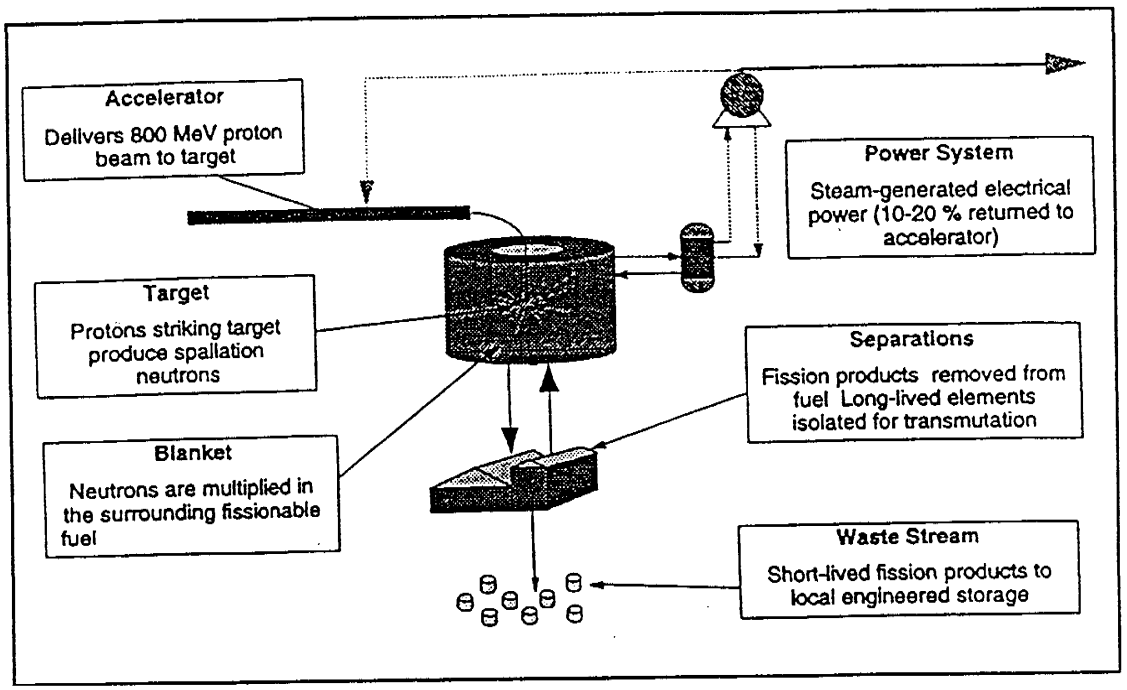

Figure 1. Schematic of an ADS.

CHAPTER 4. THE SING-SING CORE (SSC) STUDY

4.1 Introduction

The frame of our investigation, which we call the Sing-Sing Core (SSC) project, is motivated by efforts to find environmental friendly and safe management of spent nuclear fuel by means of transmutation. The aim of the project is to find a core configuration that minimizes flux and power gradients at a given total fission power over the full length of a burn-up cycle. The SSC-project will result in a design of a sub-critical core with purpose of transmuting long-lived nuclear waste from Swedish nuclear power plants. Currently, the Swedish nuclear waste management policy involves burial of the waste in underground geological formations (bedrock). There are several concerns about the operation of the geological underground depositories primarily regarding safety and non-proliferation issues. Thus, the research was mainly focused on reducing the amount of actinides and long-term radiotoxicity of fission products in the spent fuel coming from the commercial nuclear power plants.

4.2 The Design of the Core

The Sing-Sing Core design is limited to solid fuel forms, even though fast spectrum liquid fuel, like molten chlorides, also feature very attractive properties from the point of view of neutron economy and separation chemistry. The gradient in power density, although, for homogeneous fuel compositions severely limits the total power and thus the grade of burn-up.

When considering the issue of construction materials, experiences from fast reactor program show that Zirconium is not ideal. Different types of steel are usually designed for specific neutron spectra and radiation doses. In the SSC study, various types of steel are to be investigated as to minimize radiation damages in terms of annual defect production. For the optimized fuel composition, the induced defect production per spallation neutron will set the upper limit of neutron source strength.

Figure 2 shows the geometry of the Sing-Sing subcritical core.

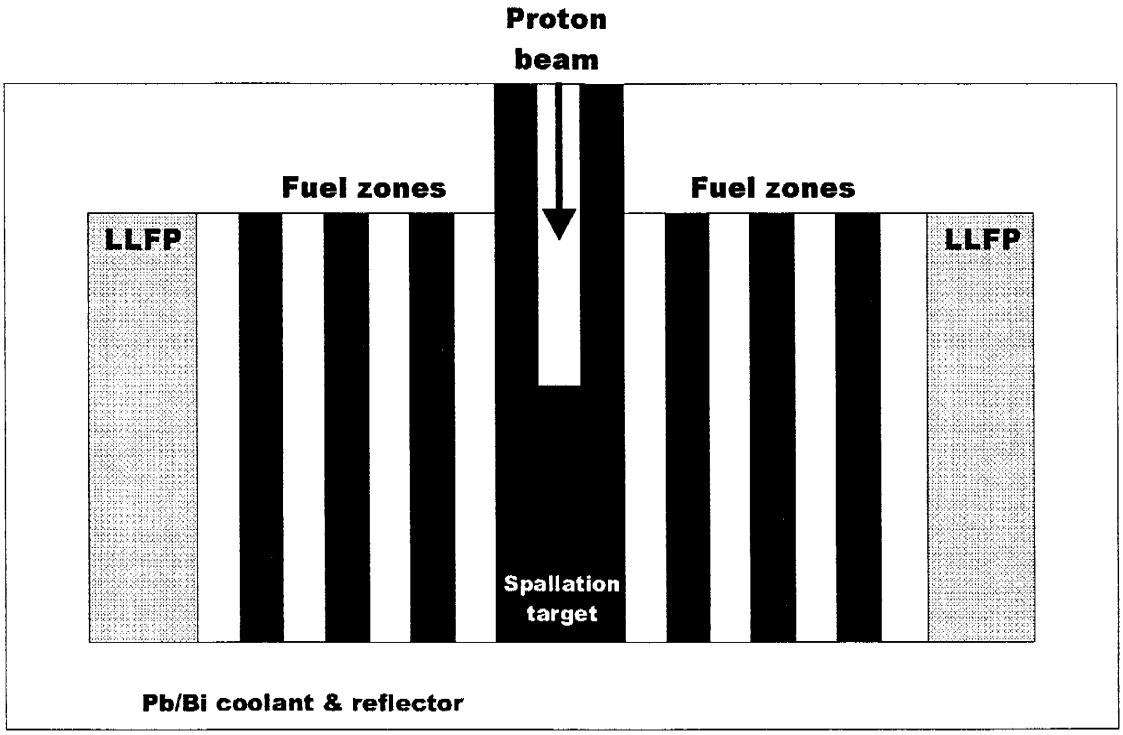

Figure 1: A schematic view of the SSC for transmutation of nuclear waste. The spallation target is assumed to consist of liquid Pb/Bi, having a diameter of 60 cm. The core itself was approximated with homogenized fuel zones of 10 cm thickness, each containing 45% coolant, 20% Ferritic Martensitic steel and 35% 238U/TRU fuel. In the first configuration investigated, five fuel zones with constant TRU-fraction equal to 21% were adopted, while in the second seven fuel zones with TRU-fraction increased from 13% in the innermost fuel zone up to 30% in the periphery were modeled.

CHAPTER 5. DEFECT PRODUCTION

5.1 Introduction

While ideas of transmuting long-lived radiotoxic isotopes present in spent nuclear fuel appeared over 30 years ago [1], research programs were until recently mainly focused on conceptual studies. With the consensus that has appeared during the last few years of the necessity of applying fast neutron spectrum systems for achieving sufficient transmutation efficiency [2-5], more attention has to be paid to material's analysis and radiation damage issues.

High burn-up fractions are necessary for obtaining small secondary waste streams in the reprocessing of the high level waste. As the burn-up level is generally limited by radiation damage of the fuel itself as well as to the cladding, additional experimental and theoretical investigations of the induced radiation damage are mandatory.

It is well known that steels used as fuel cladding and duct material in liquid metal cooled reactors begin to swell at differing neutron spectrum dependent threshold values. Nickel based austenitic steels generally exhibit high swelling rates above a few tenths of standard NRT DPA, while tempered ferritic martensitic (FM) steels have shown to be very resistant to swelling up to and above 150 NRT DPA [6]. The chemical compatibility of certain FM-steels with a liquid lead/bismuth environment is well known from the long experience of the Russian submarine reactor park. Hence, FM-steels are now considered to be the optimum choice for construction materials in waste transmutation systems, where the very fast neutron spectrum arising from potential use of heavy liquid metal coolants would yield high transmutation rates of both actinides and fission products [7].

It is not well established to what degree the low swelling rate in tempered ferritic martensitic steels is due to the inherently lower dislocation bias discussed in [8], specific bcc lattice dislocation types [9] or high self-diffusion rates [10]. However, the progress in recoil cascade simulations made during the last decade has led to a deepened understanding of defect production in neutron irradiated metals [11-13]. Unfortunately, this understanding has not yet fully dissipated into the nuclear engineering community, leading to not so well founded statements on radiation damage issues in the literature [14-16].

In this study, an effort is made to introduce the recent land winnings in microscopic defect production theory into the nuclear engineering field applied to waste transmutation systems. We start by recapitulating important definitions and implications of modern microscopic defect

production theory. Then we use the data processing code NJOY [17] to calculate the available damage energy cross section for a ferritic martensitic-like steel as function of incident neutron energy. The quenched cascade defect fraction for the corresponding primary recoil energy is calculated within the binary collision approximation (BCA) using the simulation code MARLOWE [18-20]. The shortcomings of the BCA model is discussed, and results of MD-simulations are used to estimate the true fraction of surviving defects.

5.2 Theory

The definition of standard NRT (Norgett, Robinson & Torrens) DPA [21] is based on the Kinchin & Pease assumption [22] that the number of stable defects (vacancy-interstitial pairs) ν_{NRT}, emerging from a displacement cascade, is growing linearly with the "available damage energy" E_{dam}. The available damage energy E_{dam} is the energy of the primary knocked on atom energy E_{PKA} less the energy transferred to electronic excitations [23]:

$$\nu_{NRT} = 0.8\frac{E_{dam}}{2E_d} \qquad (3)$$

where the displacement energy E_d is the average energy supplied to displaced atoms ending up as stable interstitials. The factor 0.8 was introduced to express the influence of the scattering not being of hard sphere type, while the factor of 1/2 accounted for replacement collisions taking place. The replacement collisions takes place when atoms with energy in the interval $E_d < E < 2 E_d$ are put to rest at a lattice site, as a result of displacing the target atom. E_d was assumed to be constant for a given material, with recommended values being 30 eV for copper and 40 eV for iron, nickel and chromium. The NRT DPA has become the industry standard for quantifying radiation damage.

However, experimental investigations in the last two decades have shown that the relationship between available damage energy in displacement cascade and the resulting number of stable defects is *non-linear* [11]. The NRT DPA turns out to correspond more closely to the number of stable defects created at zero Kelvin for low energy primary recoils (where the defect density during the displacement cascade is too low for defects to interact). With increasing PKA energy, defects in the displacement cascade starts to interact and recombine. In modern defect production theory, the quenched cascade defect fraction (QDF) is defined as the number of stable defects emerging from the cascade at zero Kelvin *rdative* to the NRT DPA value [11].

5.3 Results

The simulation code MARLOWE was employed for calculating the number of stable defects for primary recoil energies in the range 34 eV – 40 keV, corresponding to incident neutron energies in the range of 1 – 1000 keV. Ferritic Martensitic steels originally have tetragonal body centered structure, but after annealing they revert to body centered cubic (bcc) structure. We employed a model material having bcc structure with Fe and Cr atoms situated on random lattice sites. The MARLOWE code generated the collision cascades in static single crystals for Fe and Cr. In addition, collision cascades where also generated for the 90%Fe-10%Cr alloy. The bcc lattice constant of Fe was 0.2866 nm, 0.288 nm in Cr and 0.287 nm in the model steel. The projectiles were followed until their kinetic energy fell below (E_c) 5 eV in both materials. It is well known that atoms are bound in solids with energies above 5 eV. Therefore, it can be expected that in order to displace an atom within the solid, energy exceeding 5 eV is required. The thermal displacements of the lattice atoms where considered by employing a Debye temperature for Fe of 462 K.

Since MARLOWE does not take into account neither collective effects nor local melting of the lattice, the code will overestimate the actual defect production for recoil energies above 1 keV. Hence we will use the results of MD-simulations instead of MARLOWE's BCA model for our purposes. We define the defect production cross section, σ_{def}, as follows:

$$\sigma_{\mathrm{DEF}} = \sigma_{\mathrm{dam}} \frac{\nu_{\mathrm{NRT}}}{E_{\mathrm{dam}}} \eta \qquad (4)$$

where η is the 'cascade efficiency', defined as $\eta \equiv$ QDF [11,13]. Using values of η from reference [13] for pure iron, figure 3 displays the resulting σ_{def} as a function of incident neutron energy.

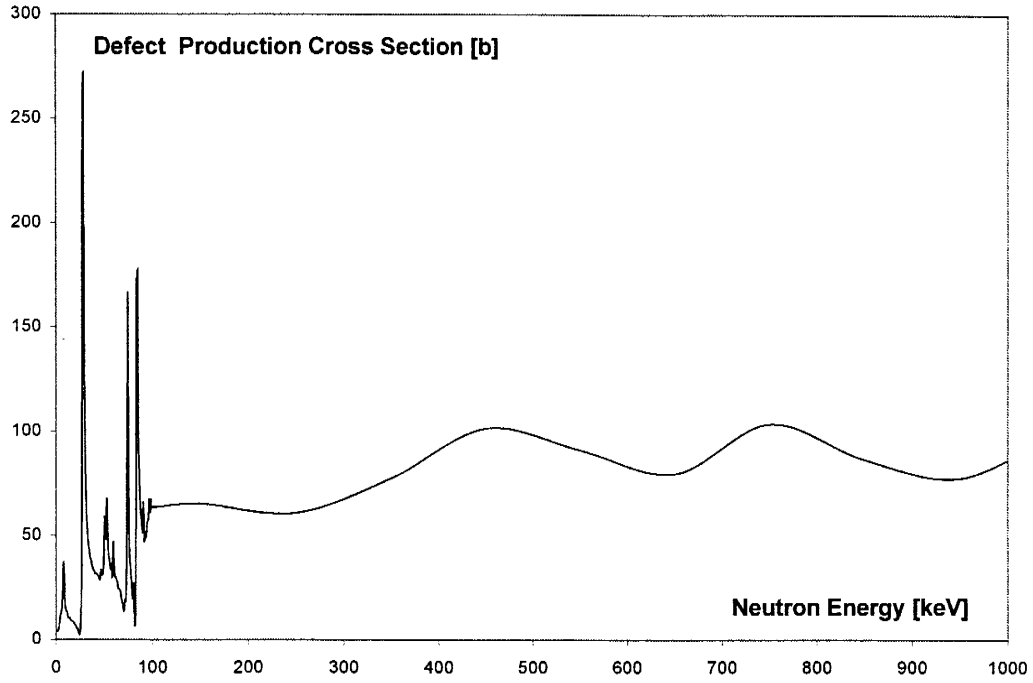

Figure 3. The *defect production cross section versus neutron energy calculated using the NJOY code.*

5.4 Conclusions

Irradiation damage related to fission neutrons in high power heavy metal cooled reactors will severely limit the life-time of the construction material and must be carefully modeled. In the presented study, the energy available for lattice displacements in cladding materials was calculated with NJOY, as a function of incident neutron energy. Quenched cascade defect fractions were calculated within the binary collision approximation using the simulation code MARLOWE in the energy range 1-1000 keV. The fraction of lattice defects surviving correlated recombination was then estimated using results of recent molecular dynamics simulations. Because MARLOWE does not take into account collective effects nor local melting of the lattice, the results of MD-simulations was also used in order to calculate the defect production cross section. Also, comparisons with standard NRT DPA values show that the latter should be used with considerable caution in the description of defect production in fast neutron spectra.

ACKNOWLEDGEMENT

I would like to express my appreciation to Jan Wallenius of the Royal Institute of Technology for all his advice and help. Further, I would like to thank Clas Grägg of Studsvik Core Analysis for his advice and help with the NJOY runs. Special thanks are also due to Mark T. Robinson, formerly of ORNL, for his very helpful emails regarding the MARLOWE code. Finally, I am appreciative to Waclaw Gudowski of the Royal Institute of Technology and the directors of Studsvik Nuclear for giving me the opportunity to do this work.

REFERENCES

[1] M. Steinberg, G. Watsak, B. Manowitz, Neutron Burning of Long-Lived Fission Products for Waste Disposal, BNL -8558, Brookhaven National Laboratory (1964).

[2] T. Sasa et al, in Proceedings of the international conference on future nuclear systems, Global 97, 425 (1997)

[3] M. Salvatores et al, in Proceedings of the international conference on future nuclear systems, Global 97, 428 (1997).

[4] C. Rubbia, Fast Neutron Incineration in the Energy Amplifier as Alternative to Geologic Storage, CERN/LHC/97-01, CERN (1997).

[5] F. Venneri et al, Disposition of Nuclear Waste Using Sub-critical Accelerator-Driven Systems, LA-UR 98-985, Los Alamos National Laboratory (1998).

[6] J. Boutard, Radiation Effects on Window Structural Material, proceedings of an ISTC-559 meeting in Obninsk (1998).

[7] Salvatores et al, in Proceedings of the international conference on future nuclear systems, Global 97, 561 (1997).

[8] J.J. Sniegowski and W.G. Wolfer, Proc. Topical Conf. Ferritic Alloys for Use in Nuclear Energy Technologies, Warrendale, The Metallurgical society of AIME (1984) 579.

[9] E.A Little et al, Proc. Roy. Soc., London A372, 565 (1980).

[10] G.R. Odette, J. Nucl. Mater. 155-157, 921-927 (1988)

[11] S.J. Zinkle and B.N. Singh, J. Nucl. Mater. 199 (1993) 173.

[12] A.F. Calder and D.J. Bacon, J. Nucl. Mater. 207 (1993) 25.

[13] W.J. Phythian et al., J. Nucl. Mater.223 (1995) 245.

[14] M.S. Wechsler, C. Lin and W.F. Sommer, in AIP proceedings 346, eds. E. Arthur, A. Rodriguez, S. Schriber (1995) 466.

[15] C. Rubbia et al, in Accelerator Driven Systems, Editor W. Gudowski, IAEA-TECDOC-985, IAEA (1997).

[16] H. Takahashita and H. Takahashi, Nucl. Inst. Meth. A 399 (1997) 421.

[17] The NJOY nuclear data processing system, version 91, LA-12740-M. Editors R.E. MacFarlane and D.W. Muir, Los Alamos National Laboratory (1994).

[18] M. Robinson, Nuc. Instr. and Meth. B67, 396, (1992).

[19] M.T. Robinson, J. Nucl. Mater. 216, (1994) 1.

[20] M. Robinson, user's guide to MARLOWE ,version 14, Oak Ridge National Laboratory (1997).

[21] Standard Practice for Neutron Radiation Damage by Charged Particel Irradiation, Annual book of ASTM standards vol 12.02, p 137, ASTM (1997).

[22] G.H. Kinchin and R.S. Pease, Prog. in Phys.,1-51 (1964).

[23] J. Lindhard, M. Scharff and H.E. Schiött, Kungl. Dan. Vidensk. Selsk. Mat. Fys. Medd. 33 (1963) 14.

Fission neutron induced defect production in heavy metal cooled reactors

Charlotta Sanders and Jan Wallenius
Department of Nuclear & Reactor Physics
Royal Institute of Technology
Stockholm, Sweden

Abstract

The highly energetic neutron spectrum that is required for an effective transmutation of actinides and fission products places special demands on cladding and construction material. The average neutron elastic collision energy in a heavy metal cooled reactor core suitable for transmutation may be as high as 400 - 500 keV, which is about three times higher than the typical value for a sodium cooled reactor. In the present study, the energy available for lattice displacements in cladding materials was calculated with NJOY as a function of incident neutron energy. Quenched cascade defect fractions were calculated within the binary collision approximation using the simulation code MARLOWE in the primary recoil energy range 0.03 - 30 keV. Comparison with experiment and recent molecular dynamics simulations showed that MARLOWE is inadequate for recoil energies above 1 keV. Hence, the number of surviving lattice defects was estimated using molecular dynamics predictions. Comparison with standard NRT DPA values for annual defect production in the cladding material of a lead/bismuth cooled sub-critical core shows that the concept of NRT DPA should be used with considerable caution. Consequently, experimental data on defect production in sodium cooled reactors cannot be trivially scaled to heavy metal cooled systems using ratios of NRT DPA, as has been customary in previously published works.

Keywords: Defect Production, Radiation Damage, Fast Spectrum, Nuclear Waste Transmutation

Introduction

While ideas of transmuting long-lived radiotoxic isotopes present in spent nuclear fuel appeared over 30 years ago [1], research programs were until recently mainly focused on conceptual studies. With the consensus that has appeared during the last few years of the necessity of applying fast neutron spectrum systems for achieving sufficient transmutation efficiency [2-5], more attention has to be paid to material's analysis and radiation damage issues.

High burn-up fractions are necessary for obtaining small secondary waste streams in the reprocessing of the high level waste. As the burn-up level is generally limited by radiation damage of the fuel itself as well as to the cladding, additional experimental and theoretical investigations of the induced radiation damage are mandatory.

It is well known that steels used as fuel cladding and duct material in liquid metal cooled reactors begin to swell at differing neutron spectrum dependent threshold values. Nickel based austenitic steels generally exhibit high swelling rates above a few tenths of standard NRT DPA, while tempered ferritic martensitic (FM) steels have shown to be very resistant to swelling up to and above 150 NRT DPA [6]. The chemical compatibility of certain FM-steels with a liquid lead/bismuth environment is well known from the long experience of the Russian submarine reactor park. Hence, FM-steels are now considered to be the optimum choice for construction materials in waste transmutation systems, where the very fast neutron spectrum arising from potential use of heavy liquid metal coolants would yield high transmutation rates of both actinides and fission products [7].

It is not well established to what degree the low swelling rate in tempered ferritic martensitic steels is due to the inherently lower dislocation bias discussed in [8], specific bcc lattice dislocation types [9] or high self-diffusion rates [10]. However, the progress in recoil cascade simulations made during the last decade has led to a deepened understanding of defect production in neutron irradiated metals [11-13]. Unfortunately, this understanding has not yet fully dissipated into the nuclear engineering community, leading to not so well founded statements on radiation damage issues in the literature [14-16].

In the present paper, we make an effort to introduce the recent land winnings in microscopic defect production theory into the nuclear engineering field applied to waste transmutation systems. This will be important in view of the fact that the magnitude of the surviving defect number is not growing linearly with available damage energy. That is, ratios between NRT DPA values for different types of neutron spectra will not give a correct picture of the ratio between lattice defect production in sodium and lead/bismuth cooled FM-steel cladding. First, important definitions and implications of modern microscopic defect production theory are recapitulated. Following, the data processing code NJOY [17] was used to calculate the available damage energy cross section for a ferritic martensitic-like steel as function of incident neutron energy. The quenched cascade defect fraction for the corresponding primary recoil energy is calculated within the binary collision approximation (BCA) using the simulation code MARLOWE [18-20]. The shortcomings of the BCA model is discussed, and results of MD-simulations are used to estimate the true fraction of surviving defects. Finally, we fold the defect production cross with the neutron spectrum of a lead/bismuth cooled sub-critical waste transmutation system and relate the resulting defect production rate to standard NRT DPA values.

Theory

The definition of standard NRT (Norgett, Robinson & Torrens) DPA [21] is based on the Kinchin & Pease assumption [22] that the number of stable defects (vacancy-interstitial pairs) $\nu_{NRT,}$ emerging from a displacement cascade, is growing linearly with the "available damage energy" E_{dam}. The available damage energy E_{dam} is the energy of the primary knocked on atom energy E_{PKA} less the energy transferred to electronic excitations [23]:

$$\nu_{NRT} = 0.8\frac{E_{dam}}{2E_d} \qquad (1)$$

where the displacement energy E_d is the average energy supplied to displaced atoms ending up as stable interstitials. The factor 0.8 was introduced to express the influence of the scattering not being of hard sphere type, while the factor of 1/2 accounted for replacement collisions taking place. Replacement collisions appear when atoms with energy in the interval $E_d < E < 2\ E_d$ are put to rest at a lattice site, as a result of displacing the target atom previously located at the site. E_d was assumed to be constant for a given material, with recommended values being 30 eV for copper and 40 eV for iron, nickel and chromium. The NRT DPA has become the industry standard for quantifying radiation damage.

However, experimental investigations in the last two decades have shown that the relationship between available damage energy in displacement cascade and the resulting number of stable defects is *non-linear* [11]. The NRT DPA turns out to correspond more closely to the number of stable defects created at zero Kelvin for low energy primary recoils (where the defect density during the displacement cascade is too low for defects to interact). With increasing PKA energy, defects in the displacement cascade starts to interact and recombine. In modern defect production theory, the quenched cascade defect fraction (QDF) is defined as the number of stable defects emerging from the cascade at zero Kelvin *relative* to the NRT DPA value [11]. Molecular dynamics (MD) simulations show that QDF decreases from a value closer to one at low PKA-energies down to 0.2 in copper for E_{PKA} = 14 keV and 0.35 for the same energy in iron [13].

At non-zero temperatures, thermal diffusion of vacancies and interstitials will take place. The surviving defect fraction (SDF) is defined as the number of defects surviving correlated recombination of Frenkel pairs due to thermal diffusion *relative* to the NRT DPA value [11]. At temperatures typical for the outer surface of reactor claddings (400 - 900K) measurements [24] and MD-simulations indicate that SDF may be as low as ~0.12 in copper. The calculated value in iron at 600K is SDF ~ 0.25 [12,13]. Note that SDF is higher in iron than in copper, leading to *higher* defect production rates at elevated temperatures in iron, in spite of its higher NRT displacement threshold energy.

Void swelling rates are given by difference in absorption rate of migrating vacancies and interstitials at void embryos [11]. Similarly, embrittlement due to radiation hardening is given by the concentration of interstitial clusters acting as obstacles for the motion of dislocation loops. While the clustering fraction and migration rates in principle are possible to calculate, in practice these entities have shown to be rather elusive, especially so in alloys. Hence there is still a quantitative gap between the macroscopic radiation damage setting limits to burnup fractions in reactors on one side, and the newly extended understanding of how lattice defects are produced.

Damage energy

The data processing code NJOY[17] was used to calculate the available damage energy cross section for a model material approximating tempered ferritic-martensitic (FM) steels. The model material consisted of 90% Fe and 10% Cr. The ENDF/B-VI neutron cross section and recoil spectrum library was used. In NJOY, the distribution of neutron target recoil energies is calculated with contributions taken into account from elastic and inelastic scattering as well as absorption (capture, fission). The fraction $P(E_{PKA})$ of the recoil energy E_{PKA} that is available for lattice damage after subtracting energy transferred to target electron excitation, is found by multiplying E_{PKA} with the Robinson partitioning function [17]:

$$P(E_{PKA}) = \frac{E_{PKA}}{1 + F_L(3.4008\varepsilon^{1/6} + 0.40244\varepsilon^{3/4} + \varepsilon)}, \quad E_{PKA} > 25\,\text{eV} \qquad (2)$$
$$P(E_{PKA}) = 0, \quad E_{PKA} < 25\,\text{eV}$$

where ε and F_L are expressed as

$$\varepsilon = \frac{E_{PKA}}{E_L}$$

$$E_L = 30.72\, Z_{PKA} Z_L (Z_{PKA}^{2/3} + Z_L^{2/3})^{1/2} \frac{A_{PKA} + A_L}{A_L}$$

$$F_l = \frac{0.0793 Z_{PKA}^{2/3} Z_L^{1/2} (A_{PKA} + A_L)^{3/2}}{(Z_{PKA}^{2/3} + Z_L^{2/3})^{3/4} A_{PKA}^{3/2} A_L^{1/2}}$$

and the index L denotes lattice nuclei.

The available damage energy E_{dam} for a given incident neutron energy is calculated by averaging over the recoil spectrum. The damage energy cross section σ_{dam} is obtained by multiplying E_{dam} with the total cross section (sum of elastic, inelastic and absorption cross-sections) and averaging over the material components. Figure 1 shows E_{dam} for natural Fe, Cr and our model material for incident neutron energies up to 100 keV. Several resonances in the elastic scattering cross section show up in the damage energy cross section. In figure 2, the resulting ratio of E_{dam} to E_{PKA} as function of incident neutron energy is displayed. It is seen that up to ten percent of the PKA recoil energy is transferred to electron excitations at neutron energies up to 100 keV.

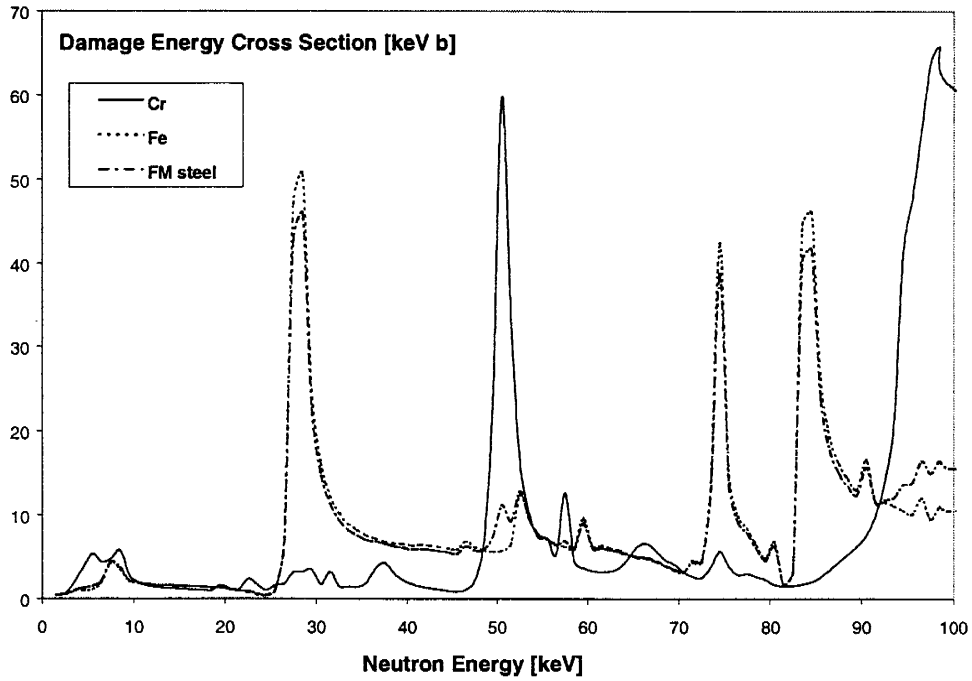

Figure 1. *Damage energy cross section for incident neutron energies up to 100 keV for chrome, iron, and ferritic martensitic model steel calculated with NJOY.*

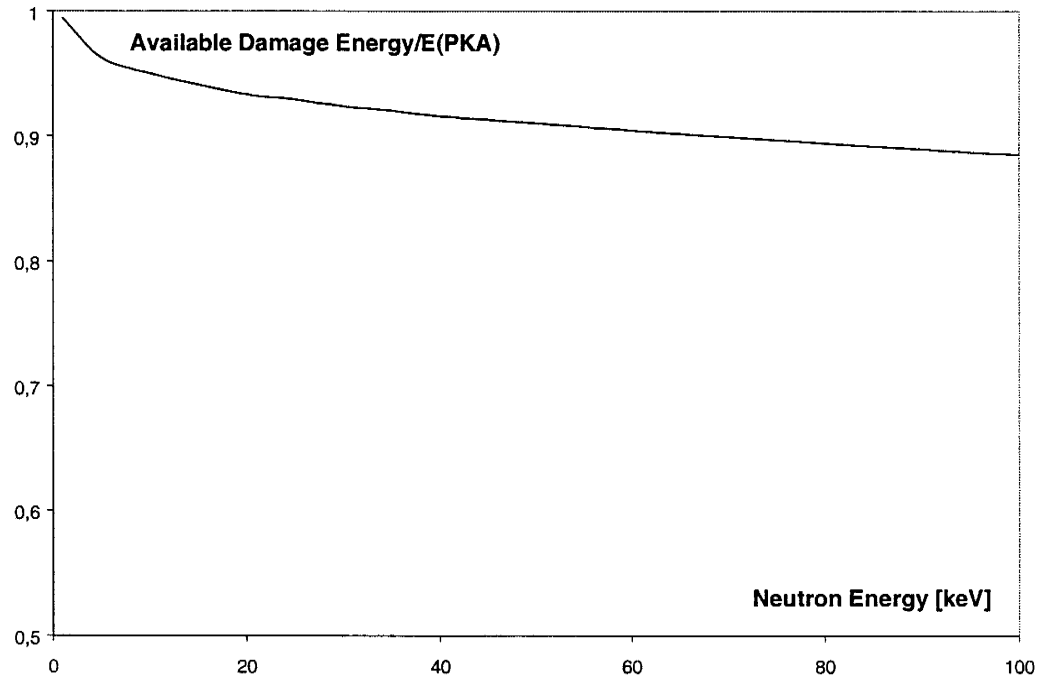

Figure 2. *Ratio of available damage energy to initial recoil energy E_{dam}/E_{PKA} for the model FM steel.*

Displacement cascade

At low energies, the interaction of a primary recoil atom with the surroundings may be described by the binary collision approximation, i.e., one assumes that the energy in a collision between the recoil and the lattice target atom is transferred to the target atom *only*. If this energy is larger than the lattice binding energy (typically of the order of 5 eV) the target atom will be *displaced*, and one may talk about a displacement cascade. If the kinetic energy of the atom is within the range $E_d < E < 2E_d$ where E_d is the energy required to create a stable defect, a subsequent cascade collision transferring energy larger than E_d will lead to the projectile stopping at the vacant lattice site appearing. Hence the total number of displaced atoms does not increase.

For higher recoil energies one should take into account the possibility of collective displacements of regions of crystal [11, 12]. By this mechanism, interstitials appear far away from the center of the displacement cascade, leaving vacancies behind in the displacement core. Further the phenomenon of "thermal spiking" must be considered, i.e. the energy transferred to lattice vibrations might lead to a local temperature exceeding the melting point of the solid. In this case, local disorder may lead to aggregation of vacancy clusters, which stabilize when cooling takes place. If the local temperature of the core is lower than the melting point, much less vacancy clustering will take place.

The temporal evolution of the displacement cascade consists of several overlapping stages [11]. During the *collisional phase*, which lasts for approximately 0.1 ps, all collisions transferring energy $> E_d$ occur. During the following ten picoseconds the cascade is quenched, its kinetic energy being dissipated in the lattice, causing rearrangement of the atoms in the cascade region. The displacement mixing factor DMF is defined as the number of lattice site rearrangements relative to the NRT displacement and may be as large as ~100 for energetic PKA cascades. In the next stage, the *relaxation and cascade cooling phase*, annihilation, in-cascade clustering, and replacement events takes place. This phase lasts for about 100 ps. The number of defects surviving annihilation in displacement cascades at zero Kelvin, relative to the NRT DPA value, is labeled quenched cascade defect fraction (QDF). Due to the above mentioned collective and thermal spike effects, QDF decreases by a factor of four when primary recoil energy is raised from 0.1 keV up to 10 keV in both fcc and bcc type metals [13].

At elevated temperatures, thermal diffusion and reduced temperature gradient between cascade core and surrounding lattice will result in increased recombination of defects [11]. The surviving fraction of defects (SDF) relative to NRT DPA is measured to be as low as 0.13 in copper at 300K [24] and calculated to be 0.25 in iron at 600 K

There are two kinds of recovery of migrating defects; correlated (recombination with its own vacancy pair) and uncorrelated (recombination with a vacancy from another Frenkel pair). SDF corresponds to the fraction of NRT DPA remaining after correlated recombination has taken place in the cascade. SDF is, therefore, a measure of the fraction of defects that escape intra-cascade annihilation. They may subsequently migrate and react with other defects in the matrix. The SDF's can be divided into isolated point defects and clustered defects. These have different migrating properties, and hence macroscopic damage rates (radiation hardening, void swelling) depend on the ratio between surviving isolated and clustered defects.

Results

For low recoil energies the binary collision approximation should be valid. We have employed the simulation code MARLOWE for calculating the number of stable defects for primary recoil energies in the range 0.03 – 30 keV, corresponding to incident neutron energies in the range of 1 – 1000 keV. Ferritic Martensitic steels originally have tetragonal body centered structure, but after annealing they revert to body centered cubic (bcc) structure. We employed a model material having bcc structure with Fe and Cr atoms situated on random lattice sites. The MARLOWE code generated the collision cascades in static single crystals for Fe and Cr. In addition, collision cascades where also generated for the 90% Fe-10%Cr disordered alloy. The bcc lattice constant of Fe was 0.2866 nm, 0.288 nm in Cr and 0.287 nm in the model steel. The projectiles were followed until their kinetic energy fell below the lattice binding energy ~ 5 eV in both materials. Further, 500 primaries were initially launched for each PKA energy. Thermal displacements of the lattice atoms where taken into account by employing a Debye temperature for Fe of 462 K.

In Figure 3 we show the number of stable vacancy-interstitial pairs versus neutron energy for the model material. Note that these figures correspond to the quenched cascade fraction (QDF) rather than the surviving defect fraction (SDF), since MARLOWE does not treat thermal diffusion. Also note that the binary collision approximation employed by MARLOWE will not be valid for recoil energies above 1 keV, corresponding to neutron energy of 30 keV.

In Figure 4 the entity $Q \equiv E_{dam}/\nu$, where ν is the number of distant Frenkel pairs [18], is plotted as a function of incident neutron energy. As seen it is only weakly dependent of energy, which is a sign of the inability of the BCA model to account for collective effects. Converting Q into an effective displacement threshold energy, we note that MARLOWE yields a value E_d ~ 15 eV, which is significantly lower than the NRT DPA value of 40 eV for iron. This is however consistent with molecular dynamics simulations which predict higher QDF in iron (bcc-lattices) and in copper (fcc-lattices) in spite of the NRT DPA value of ν being higher for iron than for copper [13]. According to the standard, similar recoil energies in iron should yield 25% less defects than in copper, while MD-simulations yield that the magnitude of defects in iron is 50% higher than in copper.

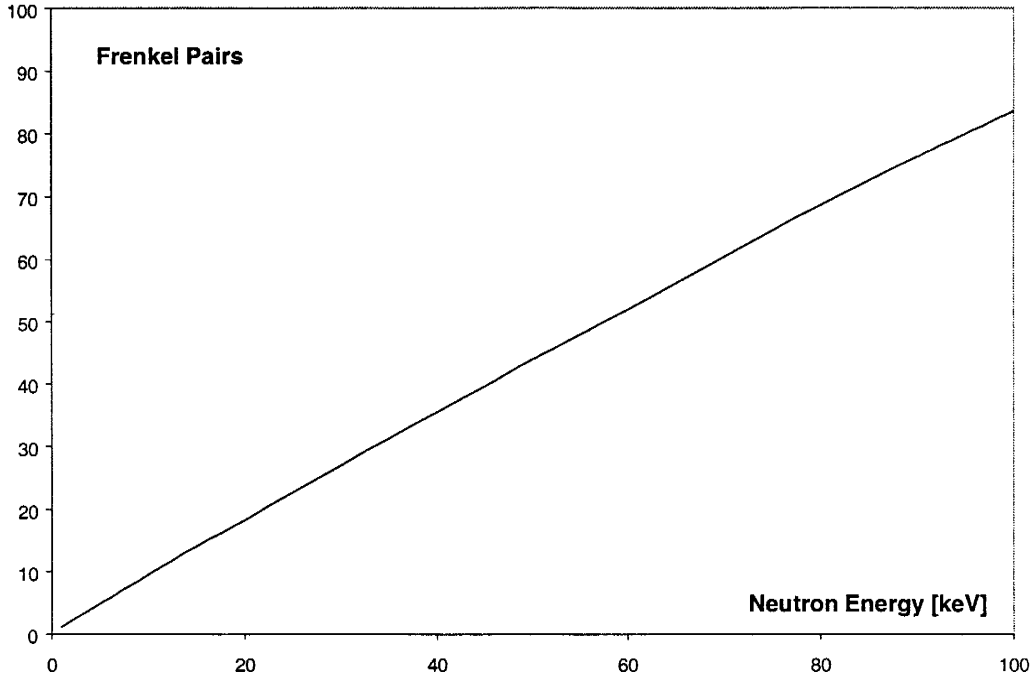

Figure 3. *Number of vacancies produced by neutrons (as a function of its energy) in a model ferritic martensitic steel calculated with MARLOWE.*

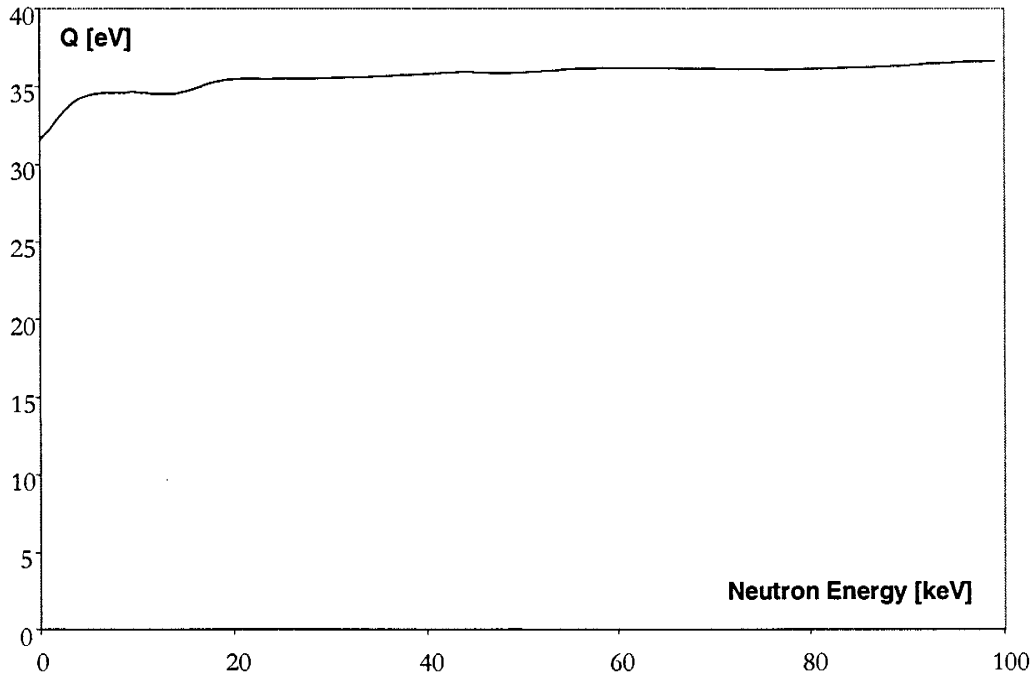

Figure 4. *Q (energy per created defect) versus incident neutron energy in the 'FM' model steel as given by MARLOWE.*

Since MARLOWE does not take into account neither collective effects nor local melting of the lattice, the code will overestimate the actual defect production for recoil energies above 1 keV. Hence we will use the results of MD-simulations instead of MARLOWE's BCA model for our purposes. We define the defect production cross section, $\sigma_{def,}$ as follows:

$$\sigma_{def} = \sigma_{dam} \frac{\nu_{NRT}}{E_{dam}} SDF \qquad (3)$$

where SDF is the Surviving Defect Fraction. In [13] SDF was calculated for cascades in pure iron at three different temperatures and recoil energies up to 13.5 keV. We extrapolated the results for T = 600K by fitting the function $SDF(E_{PKA}) = a\,(E_{PKA})^b$ as suggested in [25]. The resulting curve is shown in figure 5. Figure 6 displays the resulting σ_{def} as a function of incident neutron energy up to 5 MeV. As seen, the defect production cross section grows more slowly for high energies. This is in clear contradiction to the employment of a constant displacement threshold energy used in the definition of NRT DPA [21]. Even though there exists a weak PKA energy dependence in NRT DPA due to the decrease of E_{dam}/E_{PKA} , NRT DPA grows much faster with incident neutron energy [25].

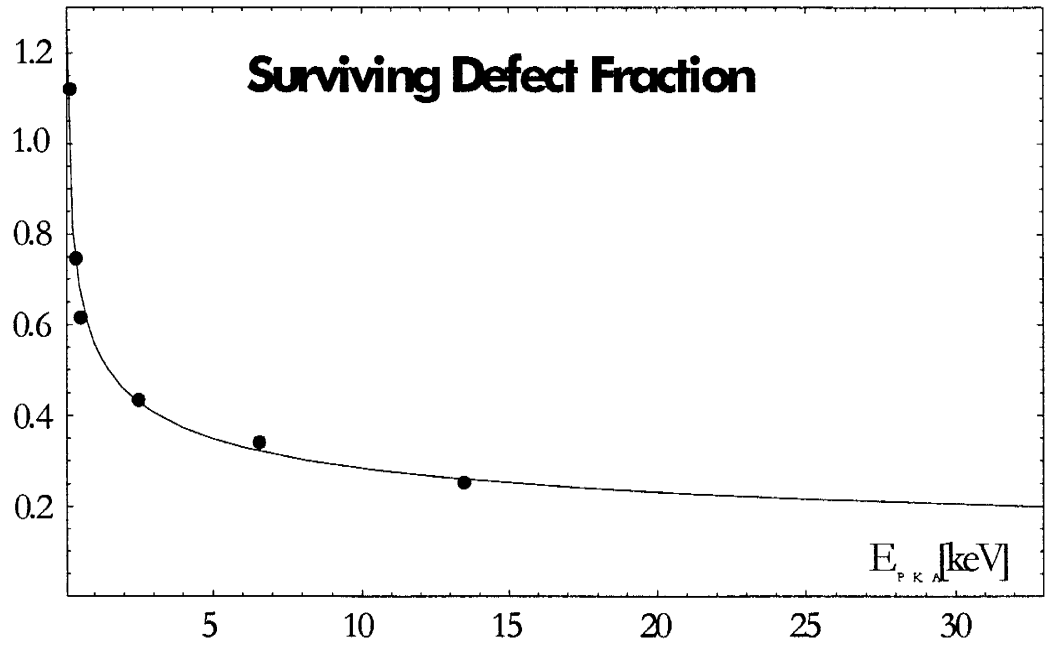

Figure 5: *The fraction of surviving defects, relative to* NRT DPA, *as function of primary recoil energy. Filled circles denote results of MD-simulations [13], and the curve is the fit function* $SDF(E_{PKA}) = 0.565/(E_{PKA})^{0.3}$

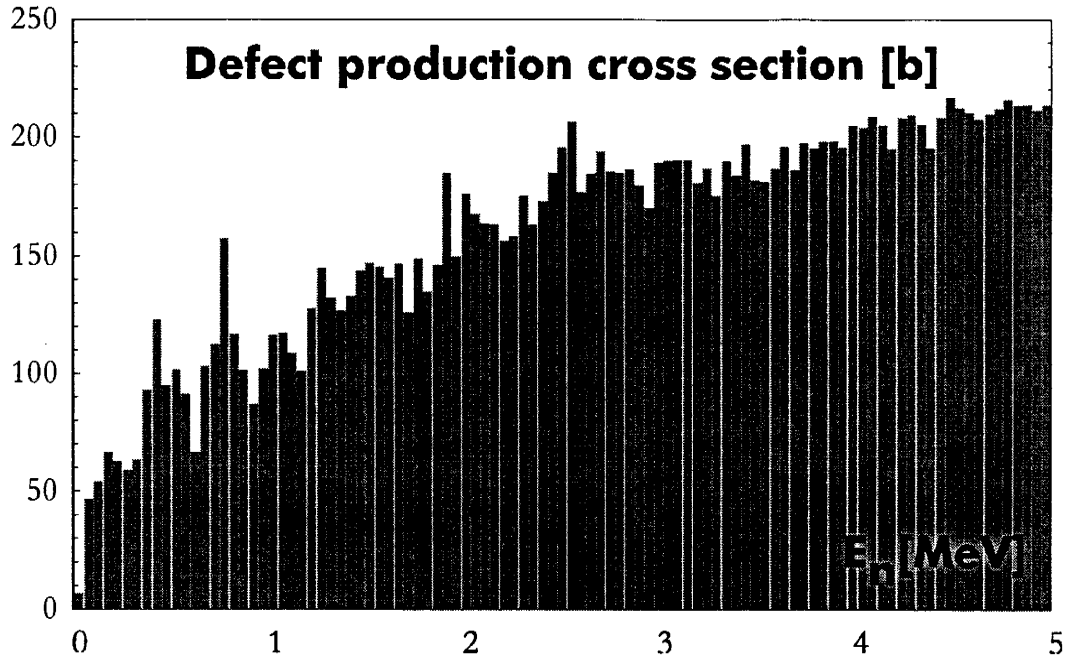

Figure 6. *Defect production cross section versus incident neutron energy. The growth as function of energy is significantly smaller than that of NRT DPA.*

Defect production in sub-critical core cladding material

We applied the defect production cross section calculated above to estimate the defect production rate in cladding material of a sub-critical lead/bismuth cooled core designed for transmutation of Swedish LWR spent fuel. The spallation target of the sub-critical system was assumed to consist of liquid lead/bismuth at a temperature of 600K, having a radius of 30 cm. The core was divided into seven cylindrical zones having different ratios of spent fuel transuranics (TRU) and U-238, for the manifold purpose of a) flattening the power density profile, b) increasing the average neutron energy in the core for better transmutation performance and c) flattening the defect production profile. Oxide fuel form was adopted in the present calculation. A proton beam power of 30 MW was assumed with a neutron yield of 25 neutrons per proton. The TRU content was adjusted to yield a multiplication eigenvalue k_λ = 0.96 in the core, corresponding to a source neutron multiplication constant k_s = 0.95. The total power of the system then became 1500 MWth, with an average power density of ~520 W/cm^3. The neutron flux and power densities were calculated with the continuous energy Monte Carlo simulation code MCNP [26]. Table 1 summarizes characteristics of the neutron flux obtained. In figure 7 we display the resulting annual defect production rate obtained by integrating the product of neutron flux and defect product cross section over energy, for comparison with NRT DPA expectations. It can be seen that the average neutron flux energy in the periphery of the core is 38% higher than in the vicinity of the target. This directly leads to higher fission to capture cross section ratios in the periphery, as well as a flattening out of the defect production profile. Note that even though the average neutron flux is a factor of two smaller in the periphery, the defect production rate is 0.57 of that in the target vicinity. The ratio of NRT DPA rates is as large as 0.61, but as we have argued throughout this paper, the faster spectrum in the periphery will not create as many defects as one expects from scaling NRT DPA with average neutron energy. As seen from figure 5, SDF is extremely sensitive to the value of primary recoil

Zone	TRU fraction	Neutron flux [10^{15} cm^{-2} s^{-1}]	Power density [W/cm^3]	Average neutron flux energy [keV]	Fraction of flux above 500 keV	Annual SDF*NRT DPA	Annual NRT DPA
1	0.130	2.42	499	338	0.200	4.16	16.2
2	0.149	2.20	505	356	0.204	3.85	15.2
3	0.166	2.06	521	378	0.215	3.71	14.8
4	0.185	1.93	540	401	0.228	3.60	14.5
5	0.205	1.77	543	425	0.243	3.41	14.0
6	0.240	1.52	541	455	0.260	3.05	12.7
7	0.300	1.16	505	467	0.260	2.37	9.9

Table 1: *Characteristics of the 1500 MWth lead/bismuth cooled sub-critical core investigated.*

energies in the region E_{PKA} = 0 – 3 keV, corresponding to incident neutron energies of 0 - 100 keV in cladding materials. In lead/bismuth cooled cores like the present only about 15% of the total defect production derives from this part of the neutron spectrum. Hence the accuracy of our fit to calculated defect productions may not be that critical. Note however that a large fraction of the neutron spectrum in a sodium cooled system will be located in this energy region. Therefore one may expect that defect production rates characterized by NRT DPA in materials irradiated with sodium moderated neutrons will *not* be trivially scalable to lead/bismuth cooled systems. It will be necessary to calculate actual surviving defect production rates, taking into account collective displacement, thermal diffusion and local melting effects. Further, it is likely that averaging over primary recoil energies before predicting neutron induced lattice damage may not be a good approximation, considering the relatively large impact of low energy recoils.

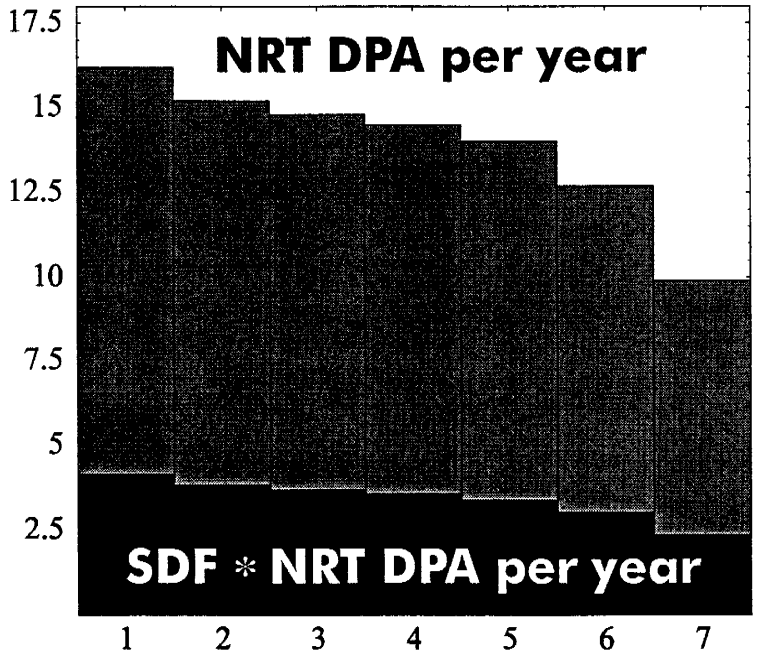

Figure 7: *Defect production per atom per year in the ferritic steel claddings of a 1500 MWth subcritical waste transmutation fuel elements. Zone 1 to 7 denote increasing enrichment as function of radius according to table 1. Note the vast difference in magnitude between NRT DPA per year compared to the number of surviving defects.*

Conclusions

Irradiation damage related to fission neutrons in high power heavy metal cooled reactors will limit the life-time of cladding and construction material and must be carefully modeled. In the presented study, the energy available for lattice displacements in cladding materials was calculated with NJOY, as a function of incident neutron energy. Quenched cascade defect fractions were calculated within the binary collision approximation using the simulation code MARLOWE in the primary recoil energy range 0.03 – 30 keV. Comparison with molecular dynamics simulations shows that the present version of MARLOWE does not yield adequate results for primary recoil energies above 1 keV. This may be explained by MARLOWE's inability to account for collective effects and local melting of the lattice. The results of MD-simulations were thus used in order to calculate defect production cross sections, which for recoil energies larger than a few keV turns out to be a factor of four smaller than what is predicted by the standard NRT DPA model. Even though the standard displacement rate in the construction material of a 1500 MWth sub-critical lead/bismuth cooled core turns out to be about 15 NRT DPA per year, the actual defect production will be less than four vacancy-interstitial pairs per atom per year. Consequently, NRT DPA values must be used with considerable caution in the comparison of defect production in fast neutron spectra, especially so if any of the recoil spectra has a maximum in the vicinity of a few keV.

Acknowledgments

The authors would like to thank Kamil Tucek for help in various matters and Waclaw Gudowski for preparing MCNP cross section data files. This work was financially supported by Studsvik Nuclear AB and the Swedish Fuel and Waste Management Board (SKB).

References

[1] M. Steinberg, G. Watsak, B. Manowitz, Neutron Burning of Long-Lived Fission Products for Waste Disposal, BNL -8558, Brookhaven National Laboratory (1964).

[2] T. Sasa et al, in Proceedings of the international conference on future nuclear systems, Global 97, 425 (1997)

[3] M. Salvatores et al, in Proceedings of the international conference on future nuclear systems, Global 97, 428 (1997).

[4] C. Rubbia, Fast Neutron Incineration in the Energy Amplifier as Alternative to Geologic Storage, CERN/LHC/97-01, CERN (1997).

[5] F. Venneri et al, Disposition of Nuclear Waste Using Sub-critical Accelerator-Driven Systems, LA-UR 98-985, Los Alamos National Laboratory (1998).

[6] J. Boutard, Radiation Effects on Window Structural Material, proceedings of an ISTC-559 meeting in Obninsk (1998).

[7] Salvatores et al, in Proceedings of the international conference on future nuclear systems, Global 97, 561 (1997).

[8] J.J. Sniegowski and W.G. Wolfer, Proc. Topical Conf. Ferritic Alloys for Use in Nuclear Energy Technologies, Warrendale, The Metallurgical society of AIME (1984) 579.

[9] E.A Little et al, Proc. Roy. Soc., London A372, 565 (1980).

[10] G.R. Odette, J. Nucl. Mater. 155-157, 921-927 (1988)

[11] S.J. Zinkle and B.N. Singh, J. Nucl. Mater. 199 (1993) 173.

[12] A.F. Calder and D.J. Bacon, J. Nucl. Mater. 207 (1993) 25.

[13] W.J. Phythian et al., J. Nucl. Mater.223 (1995) 245.

[14] M.S. Wechsler, C. Lin and W.F. Sommer, in AIP proceedings 346, eds. E. Arthur, A. Rodriguez, S. Schriber (1995) 466.

[15] C. Rubbia et al, in Accelerator Driven Systems, Editor W. Gudowski, IAEA-TECDOC-985, IAEA (1997).

[16] H. Takahashita and H. Takahashi, Nucl. Inst. Meth. A 399 (1997) 421.

[17] The NJOY nuclear data processing system, version 91, LA-12740-M. Editors R.E. MacFarlane and D.W. Muir, Los Alamos National Laboratory (1994).

[18] M. Robinson, Nuc. Instr. and Meth. B67, 396, (1992).

[19] M.T. Robinson, J. Nucl. Mater. 216, (1994) 1.

[20] M. Robinson, user's guide to MARLOWE, version 14, Oak Ridge National Laboratory (1997).

[21] Standard Practice for Neutron Radiation Damage by Charged Particel Irradiation, Annual book of ASTM standards vol 12.02, p 137, ASTM (1997).

[22] G.H. Kinchin and R.S. Pease, Prog. in Phys.,1-51 (1964).

[23] J. Lindhard, M. Scharff and H.E. Schiött, Kungl. Dan. Vidensk. Selsk. Mat. Fys. Medd. 33 (1963) 14.

[24] S.J. Zinkle, J. Nucl. Mater. 155-157 (1988) 1201.

[25] D.J. Bacon, A.F. Calder and F. Gao, Radiation Effects and Defects in Solids, 141 (1997) 283.

[26] MCNP - A general Monte Carlo N-Particle transport code, version 4B, LA-12625-M. Editor J.F. Briesmeister. Los Alamos National Laboratory (1997).